MECHANICAL CHARACTERIZATION OF HYDROXYAPATITE, THERMOELECTRIC MATERIALS AND DOPED CERIA

By

Xiaofeng Fan

A DISSERTATION

Submitted to
Michigan State University
in partial fulfillment of the requirements
for the degree of

Materials Science and Engineering - Doctor of Philosophy

2013

ABSTRACT

MECHANICAL CHARACTERIZATION OF HYDROXYAPATITE, THERMOELECTRIC MATERIALS AND DOPED CERIA

By

Xiaofeng Fan

For a variety of applications of brittle ceramic materials, porosity plays a critical role structurally and/or functionally, such as in engineered bone scaffolds, thermoelectric materials and in solid oxide fuel cells. The presence of porosity will affect the mechanical properties, which are essential to the design and application of porous brittle materials.

In this study, the mechanical property versus microstructure relations for bioceramics, thermoelectric (TE) materials and solid oxide fuel cells were investigated. For the bioceramic material hydroxyapatite (HA), the Young's modulus was measured using resonant ultrasound spectroscopy (RUS) as a function of (i) porosity and (ii) microcracking damage state. The fracture strength was measured as a function of porosity using biaxial flexure testing, and the distribution of the fracture strength was studied by Weibull analysis.

For the natural mineral tetrahedrite based solid solution thermoelectric material ($Cu_{10}Zn_2As_4S_{13}$ - $Cu_{12}Sb_4S_{13}$), the elastic moduli, hardness and fracture toughness were studied as a function of (i) composition and (ii) ball milling time. For ZiNiSn, a thermoelectric half-Heusler compound, the elastic modulus – porosity and hardness – porosity relations were examined.

For the solid oxide fuel cell material, gadolina doped ceria (GDC), the elastic moduli including Young's modulus, shear modulus, bulk modulus and Poisson's ratio were measured by RUS as a function of porosity. The hardness was evaluated by Vickers indentation technique as a function of porosity.

The results of the mechanical property versus microstructure relations obtained in this study are of great importance for the design and fabrication of reliable components with service life and a safety factor. The Weibull modulus, which is a measure of the scatter in fracture strength, is the gauge of the mechanical reliability. The elastic moduli and Poisson's ratio are needed in analytical or numerical models of the thermal and mechanical stresses arising from in-service thermal gradients, thermal transients and/or mechanical loading. Hardness is related to a material's wear resistance and machinability, which are two essential considerations in fabrication and application.

Dedicated to my father, Jianmin Fan
You are, and will always be in my heart

ACKNOWLEDGMENTS

I would like to give my sincere thanks to Professor Eldon Case, for his guidance and support on my way of pursuing the doctoral degree. Your insightful advice and profound knowledge enlightened me academically; your dedication to work, your ethicality and integrity as a researcher influenced me and would be my lifetime treasure. I also thank Professor Melissa Baumann, Professor Laura McCabe, Professor Tim Hogan and Professor Jeffery Sakamoto for their help and suggestions during the completion of my degree.

Also, I have received countless help from my co-workers during my study at MSU. I would like to thank Robert Schmidt, Jennifer Ni, Yutian Shu, Fei Ren, Andrew Morrison, Travis Thompson, Qing Yang, Hui Sun, Xu Lu, Iulia Gheorghita and Luis Guerrero. I really appreciated all your help and suggestions during my research.

TABLE OF CONTENTS

LIST OF TABLES

LIST OF FIGURES

CHAPTER 1

INTRODUCTION

For a wide variety of brittle ceramic material applications, porosity plays a critical role structurally and/or functionally. Porous ceramics are widely used in filtration [Zievers 1991, Guizard 2002], absorption [Drisko 2009], separation [Araki 2005], catalyst supporting [Opre 2005], thermal insulation [Clyne 2006] and as lightweight structural components [Fu 2011]. For example, porous bioceramic hydroxyapatite is used as bone scaffold materials [Hench 1991], and highly porous ceramics such as doped ceria are critical components used in solid oxide fuel cells [Samson 2012].

The presence of porosity in ceramics will affect the mechanical properties, including fracture strength [Park 2009], Young's modulus [Fan 2012, Ni 2009], shear modulus [Ren 2009, Ni 2009], hardness [Hoepfner 2003] and fracture toughness [Rice 1996]. These mechanical properties determine the capability of a material to resist external or internal stresses. For instance, the thermal stress produced due to temperature difference is proportional to the Young's modulus [Kaliakin 2002]. Hardness determines how fast the material will be worn out in service [Leyland 2000]. The brittleness of the material, which is a function of the Young's modulus, hardness and toughness, is directly related to the machinability of the material [Quinn 1997]. Thus, a thorough understanding of the mechanical properties as a function of porosity is essential to the design and application of porous brittle ceramics.

This dissertation includes mechanical property – microstructure relations for bioceramic, solid oxide fuel cell material and thermoelectric (TE) materials. Chapters 4 – 7 focused on the bioceramic material, hydroxyapatite (HA). For the first time, the Weibull modulus for HA

with porosity ranging from green porosity to nearly full density was investigated. Relations for the fracture strength – porosity, Young's modulus – porosity, and Young's modulus – microcracking damage state were studied for HA specimens. Chapters 8 and 9 explored the elastic modulus – porosity and hardness – porosity relations for gadolina doped ceria used in solid oxide fuel cells. Chapters 10 and 11 focused on the thermoelectric materials, namely the natural mineral tetrahedrite based material and the half-Heusler compound, respectively. The elastic moduli, hardness and fracture toughness of the tetrahedrite based solid solution material were studied as a function of composition and ball milling time. The elastic modulus – porosity and hardness – porosity relations for half-Heusler compound was examined in Chapter 11.

REFERENCES

REFERENCES

[Araki 2005] K. Araki, J. W. Halloran, Porous ceramic bodies with interconnected pore channels by a novel freeze casting technique, J. Am. Ceram. Soc. 88, 1108–1114, 2005.

[Clyne 2006] T.W. Clyne, I.O. Golosnoy, J.C. Tan, A.E. Markaki, Porous materials for thermal management under extreme conditions, Philos. T. Roy. Soc. A 364, 125-146, 2006.

[Drisko 2009] G. L. Drisko, V. Luca, E. Sizgek, N. Scales, R. A. Caruso, Template synthesis and adsorption properties of hierarchically porous zirconium titanium oxides, Langmuir, 25, 5286–5293, 2009.

[Fan 2012] X. Fan, E.D. Case, F. Ren, Y. Shu, M.J. Baumann, Part II: Fracture strength and elastic modulus as a function of porosity for hydroxyapatite and other brittle materials. J. Mech. Behav. Biomed. 8, 99-110, 2012.

[Fu 2011] Q. Fu, E. Saiz, A. P. Tomsia, Bioinspired strong and highly porous glass scaffolds, Adv. Funct. Mater. 21, 1058–1063, 2011.

[Guizard 2002] C. Guizard, A.Ayral, A. Julbe, Potentiality of organic solvents filtration with ceramic membranes. A comparison with polymer membranes, Desalination, 147, 275–280, 2002.

[Hench 1991] L. L. Hench, J. K. West, Principles of Electronic Ceramics, Wiley, New York, 190.

[Hoepfner 2003] T.P. Hoepfner, E.D. Case, The influence of the microstructure on the hardness of sintered hydroxyapatite, Ceramics International. Ceram. Int. 29, 699-706, 2003.

[Kaliakin 2002] V.N. Kaliakin, In Introduction to Approximate Solution Techniques, Numerical Modeling, and Finite Element Methods, Marcel Dekker, New York, 2002.

[Leyland 2000] A. Leyland, A. Matthews, On the significance of the H/E ratio in wear control: a nanocomposite coating approach to optimised tribological behaviour, Wear, 246, 1–11, 2000.

[Ni 2009] J.E. Ni, F. Ren, E.D. Case, E.J. Timm, Porosity dependence of elastic moduli in LAST (Lead-antimony-silver-tellurium) thermoelectric materials. Mater. Chem. Phy. 118, 459 – 466, 2009.

[Opre 2005] Z. Opre, J.D. Grunwaldt, M. Maciejewski, D. Ferri, T. Mallat, A. Baiker, Promoted Ru-hydroxyapatite: designed structure for the fast and highly selective oxidation of alcohols with oxygen. J. Catal. 230, 406-419, 2005.

[Park 2009] Y.H. Park, T. Hinoki, A. Kohyama, Development of multi-functional NITE-porous SiC for ceramic insulators, J. Nuclear Mater. 386–388, 1014-1017, 2009.

[Quinn 1997] J.B. Quinn, G.D. Quinn, Indentation brittleness of ceramics: A fresh approachJ

Mater. Sci. 32, 4331-4346, 1997.

[Ren 2009] F. Ren, E.D. Case, A. Morrison, M. Tafesse, M.J. Baumann, Resonant ultrasound spectroscopy measurement of Young's modulus, shear modulus and Poisson's ratio as a function of porosity for alumina and hydroxyapatite, Philos. Mag. 89, 1163-1182, 2009.

[Rice 1996] R. W. Rice, Evaluation and extension of physical property-porosity models based on minimum solid area, J. Mater. Sci. 31, 102-118, 1996.

[Samson 2012] A.J. Samson, P. Hjalmarsson, M. Sogaard, J. Hjelm, N. Bonanos, Highly durable anode supported solid oxide fuel cell with an infiltrated cathode, J. Power Sources 216, 124-130, 2012.

[Zievers 1991] J.F. Zievers, P. Eggerstedt, E.C. Zievers, Porous ceramics for gas filtration, Am. Ceram. Soc. Bull. 70, 108-111, 1991.

CHAPTER 2

BACKGROUND

1. Hydroxyapatite and its applications

Hydroxyapatite (HA, $Ca_{10}(PO_4)_6(OH)_2$) is widely studied as a candidate for hard tissue (bone and teeth) engineering scaffold due to its similarity to natural bone minerals [Hench 1991]. HA can form a direct bond to the bone, showing excellent biocompatibility, osteoconductivity and bioactivity [Hench 1991].

Both dense and porous HA have extensive scopes of applications due to HA's particular physical and chemical properties. In HA crystals, the positive calcium ions and negative phosphate groups provide multiple sites for specific adsorption of gases, proteins, viruses and bacteria [Mahabole 2005, Ohtsuki 2010, Yang 2007 a, 2007 b]. Silver nanoparticles deposited onto porous bulk HA have been used to determine the concentration of adsorbed protein via changes in the localized surface plasmon resonance of the silver nanoparticles [Ohtsuki 2010]. Porous HA with a bimodal pore size distribution (large pores: 40 μm; small pores: 3 μm) can filter microorganisms from water and gas [Yang 2007 a, Yang 2007 b]. When water or gas flows through the highly permeable porous HA filters, microbes are absorbed on the walls of large pores or blocked by the small pores [Yang 2007 a, Yang 2007 b]. In terms of the gas sensing properties of HA, Mahabole [Mahabole 2005] found that OH^- groups in HA are adsorption sites for CO, so that when CO gas flows through a porous HA pellet, the electrical conductivity changes with adsorption level of CO on HA [Mahabole 2005].

The calcium ions in HA can actively exchange with other cations such as Cd, Pb, Co

and Cr [Yin 2010], thus making HA useful in environmental, sensing and catalytic applications. Three dimensional HA structures consisting of spherical macropores with uniform 0.8 μm diameters were fabricated by burning out polystyrene spheres [Srinivasan 2006]. The structures were then immersed in waste water containing cadmium and lead [Srinivasan 2006]. Cadmium was captured via ion exchange with calcium, while lead formed an insoluble phase with HA by a dissolution/precipitation reaction [Srinivasan 2006].

In another study, the concentration of CO_2 gas was monitored by electrical conductivity changes in porous cast HA films [Nagai 1988]. The change of electrical conductivity as a function of CO_2 concentration was assumed to be due to the formation of surface layers with high electrical resistance on the HA pores [Nagai 1988]. In an additional application, yttrium ions exchanged with calcium ions in porous HA generate OH^- vacancies. The concentration OH^- vacancies changes as a function of the ambient water vapor concentration, thus changes in electrical conductivity are directly related to changes in humidity [Owada 1989].

Ion exchanged HA also is widely studied as support platforms for transition metal ions catalysts [Opre 2005, Mori 2003, Mori 2004, Venugopal 2003]. The advantages of using HA as support are: (i) active transition metal ions can be immobilized in HA due to ion exchange and (ii) the HA support is stable and avoids possible side reactions induced by the support itself [Opre 2005, Mori 2003, Mori 2004, Venugopal 2003]. In a study by Wang [Wang 2010], HA nanowire arrays were prepared by template-assisted electrodeposition, then horseradish peroxidise (HRP) cyanide sensors were cast onto the surfaces of multiple glassy carbon substrates.

2. Thermoelectric materials

Thermoelectric (TE) materials have attracted great attention in recent years due to their potential to convert waste heat into electricity. The safety, sustainability, and reliability make TE materials stand out compared to other energy sources such as fossil fuels, nuclear energy, wind and solar energy.

The power generation function of TE materials is based on the Seebeck effect [Chen 2003]. When two different materials are joined together with a temperature gradient between them, then an electrical current will be developed such that the magnitude of the current is proportional to the temperature difference. As demonstrated in Figure 2.1a, a thermoelectric couple of a n -type and a p-type semiconductor material connected together, an electric current is formed due to the moving of the electrons and the holes in the n -type and p-type semiconductors respectively under the temperature gradient.

Conversely, a temperature gradient can be developed when a potential is applied to the same n-type and p-type configuration (Figure 2.1a). This phenomenon is called the Peltier effect [Snyder 2002], which is the basis for TE refrigeration devices.

When TE materials are incorporated into devices, they are built into modules that contain dozens of the thermoelectric couples (Figure 2.1b) arranged into an array that is electrically in series and thermally in parallel.

The efficiency of TE materials is characterized by a dimensionless figure of merit (ZT, $ZT = S^2\sigma T/\kappa$), where S is the Seebeck coefficient, σ is the electrical conductivity, T is the absolute temperature, and κ is the thermal conductivity [Zebarjadi 2012]. More efficiency can be achieved with higher ZT. For conventional bulk TE materials studied, the ZT value is less than or around unity [Zebarjadi 2012].

The concept of an ideal TE material is an “electron crystal, phonon glass”, which

(a)

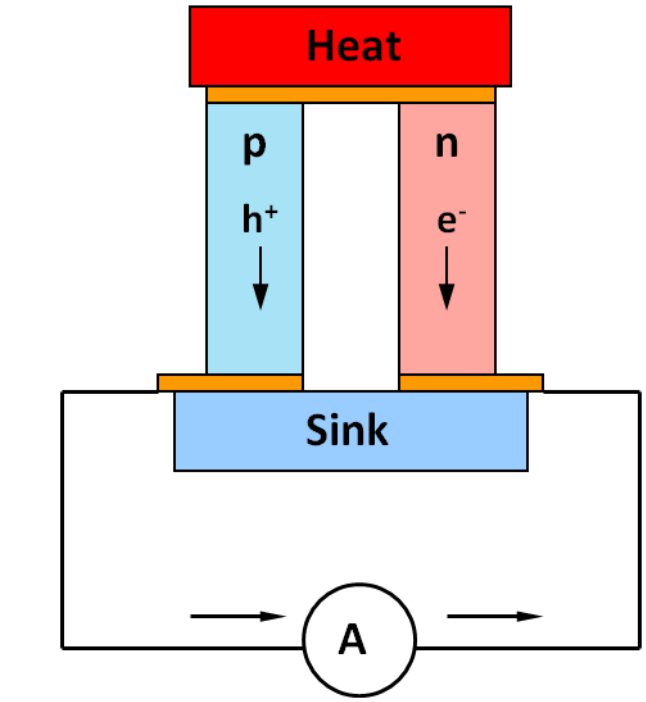

(b)

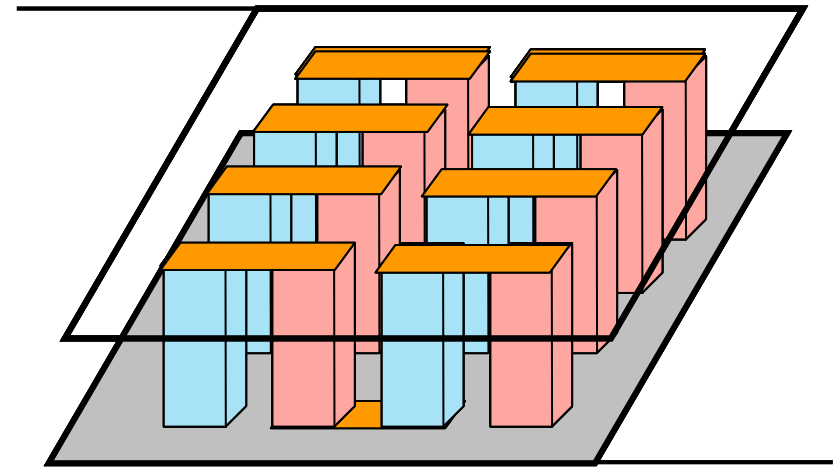

Figure 2.1. Illustration of (a) a thermoelectric couple of an n -type and a p-type semiconductor material connected together; (b) thermoelectric module of an array of thermoelectric couples. For interpretation of the references to color in this and all other figures, the reader is referred to the electronic version of this dissertation.

maximizes the electrical transport while hinders the thermal transport [Slack 1995]. Strategies towards improving ZT include tuning the electronic properties by doping [Hsu 2004] and band engineering [Heremans 2008]; lowering the thermal conductivity by nanostrucuring [Poudel 2008]. Nanostructuring has been studied intensively recently due to its ability to decouple the Seebeck coefficient and the electrical conductivity, and offer additional phonon scattering to reduce the thermal conductivity [Kanatzidis 2010]. Nanostructuring has been performed over length scales from atomic-scale lattice defects like dislocations and vacancies [He 2010], nanoscale precipitates [Pei 2011a], nano-inclusions [Zhao 2008] to mesoscale interfaces like grain boundaries [Joshi 2008].

Current studied TE materials include, but are not limited to, chalcogenides [Pei 2011b], clathrates [Shi 2010], oxides [Koumoto 2006], skutterudites [Nolas 1999], half-Heuslers [Uher 1999], and silicides [Yani 2007]. Each TE material system has an optimal performance over a certain temperature range with individual merits compared to other systems.

3. Solid oxide fuel cells

Solid oxide fuel cells (SOFCs) are capable of producing electricity through electrochemical reactions [Minh 1993]. Similar to other types of fuel cells, SOFCs consist of two electrodes and the electrolyte materials. The difference between SOFCs and other fuels cell is that SOFCs have solid oxide electrolyte materials (ceramics). Compared to other fuel cells, the advantages of SOFCs include long-term stability, high efficiency and less environmental effect [Zhu 2003]. However, the operating temperatures for SOFCs are relatively high, which poses challenges to maintain mechanical and chemical stability.

Doped cerium dioxides are studied for potential application in SOFCs due to the high ionic conductivity and low cost. Gadolinia doped ceria (GDC), is commonly used in SOFCs.

Its dense form is applied as membrane or diffusion blocking material; the porous GDC, finds applications in anode catalyst [Sauvet 2001], anode mixed ionic electronic conductor (MIEC) [Goodenough 2007], oxygen storage material [Trovarelli 1996], composite cathode oxygen ion conductor [Murray 2001] in SOFCs. Nano-composite cathodes (NCC's) of porous GDC surface-decorated with nano-sized MIEC catalyst particles have received much interest due to their high electrochemical performance [Nicholas 2010, 2012] and electrochemical/microstructural durability [Samson 2012] at intermediate (500-700^{o}C) temperatures.

4. The importance of studying mechanical properties

In general, before any material or any component is put into application, the mechanical properties should be studied thoroughly to ensure the mechanical integrity during use. In applications, stresses will arise both internally and externally, due to thermal expansion mismatch [Jeon 2000], thermal gradient [Kamaya 2011], thermal transient [Zhou 2011], and mechanical loading and manufacturing [Zhou 2012]. For example, when HA scaffolds are implanted in human bodies, the stress from everyday activity like running and walking may induce microcracks in scaffolds [Zioupos 1994]. In waste heat harvesting applications, TE materials are operated at cycles of low to high temperatures. The stresses arising from cyclic thermal gradients, thermal transients, thermal expansion mismatch among TE materials, interconnects and heat sources, may generate and growth of cracks, degradation of properties, and consequently failure of the entire TE system [Case 2012]. In addition, when used in automobile applications, the mechanical vibrations will also cause mechanical degradation or even failure. In SOFC applications, the mismatch of coefficient of thermal expansion (CTE) mismatch between the cell layers (electrolyte, cathode, current collector) may lead to stress

increase or even fracture [Jiang 2012]. Also, the materials in this study (HA, TE materials and GDC) are all brittle materials, which means that relatively little energy will be absorbed before the fracture of the materials when subjected to stress.

For commercial use, good mechanical reliability and predictable performance is required, especially when failure may cause fatal damage. Fracture strength is a direct indicator of how the material will survive under certain load [Wachtman 2009]. In designing a component, knowing the scatter in fracture strength is of equal importance as knowing the mean fracture strength, since the whole system will fail in the weakest part [Wachtman 2009]. The Weibull modulus is a gauge for the distribution of fracture strength [Trustrum 1979] (Chapter 3, Section 3).

Young's modulus and Poisson's ratio are crucial parameters in the stiffness matrix in modelling the materials subject to thermal and mechanical loading, and to model load transfer between different stacked layers [Larson 2013]. Hardness is directly related to the material's machinability [Boccaccini 1997] and wear resistance [Leyland 2000], which are two important considerations in design and manufacturing. Fracture toughness is the measure of the material's resistance to crack propagation, and is extremely important in designing any brittle materials [Wachtman 2009].

5. Mechanical properties as functions of microstructure

The mechanical properties, including elastic moduli, fracture strength, Weibull modulus, hardness and fracture toughness are not only functions of the material itself, but are also affected by the microstructure of the material, such as porosity, composition, microcracking, and other factors such as damage state and temperature. Porosity is commonly observed in a wide range of ceramic materials. Some pores are left behind after sintering, while some pores

are introduced in on purpose by methods like partial sintering [Fan 2012], addition of sacrificial fugitives [Ren 2005] and fabrication using replica templates [Carbajo 2002]. Porous ceramics are of significant interest both for functional or structural applications in areas such as filtration [Zievers 1991, Guizard 2002], absorption [Drisko 2009], separation [Araki 2005], catalyst supports [Opre 2005, Mori 2003], thermal insulation [Clyne 2006] and lightweight structural components [Fu 2011].

For synthetic HA bone scaffolds, it is of great importance to incorporate the bimodal porosity similar to natural bones to enhance bone ingrowth [Hsu 2007]. Bimodal porosity is observed in natural bones, with macropores at the diameters of several hundred microns and micropores at the diameters of tens of microns [Hench 1991]. These bimodal pores are biologically essential for blood and nutrient circulations. Studies have shown that early attachment of bone cells to the bioceramic scaffold was enhanced as a result of the microporosity in the scaffold [El-Ghannam 2004]. Moreover, the newly formed natural bone cells tend to grow into the macropores of the scaffold and finally replace the resorbable scaffold [El-Ghannam 2004].

A number of mechanical properties are sensitive to porosity, including the flexural fracture strength [Park 2009], compressive fracture strength [Sammis 1986, Nielsen 1990], the Young's modulus [Fan 2012b, Ni 2009], shear modulus [Ren 2009, Ni 2009] and hardness [Hoepfner 2003].

In addition to the mechanical properties, porosity also affects a variety of physical properties, including thermal and electrical properties. For example, thermal conductivity [Park 2009, Sulistyo 2010] and thermal diffusivity [Park 2009] are both functions of porosity. For electrical properties, the dielectric constant [Hoepfner 2002, Geis 2002], dielectric

breakdown voltage [Hench 1990, Geis 2002], and electrical conductivity [Shimizi 2009, Sulistyo 2010] are all functions of porosity.

In sintered ceramic materials, generally microcracking can be formed due to three mechanisms: (i) thermal expansion anisotropy (TEA) [Case 2005], (ii) thermal expansion mismatch (two phases) [Todd 2004] and (iii) externally applied mechanical loads [Zhou 2012]. TEA applies to non-cubic polycrystalline materials with different thermal expansion coefficients along crystallographic axes. Grains expanding and shrinking at different rate during heating and cooling generate stress. The interplay of stored elastic strain energy and surface energy determines microcracking formation. Microcracks are generated when grain size reaches the critical grain size. The critical grain size, G_{cr}, can be estimated [Cleveland 1978]

$$G_{cr} = \frac{14.4\gamma_f}{E(\Delta T)^2(\Delta\alpha_{max}^2)} \quad (1)$$

where γ_f is the fracture surface energy, E is the Young's modulus of the material, ΔT is the temperature difference during sintering, and $\Delta\alpha_{max}$ is the maximum difference in the thermal expansion coefficients along different crystallographic axes.

For example, HA belongs to the hexagonal system with a space group P63/m, with thermal expansion coefficients that are different along the "a" axis and "c" axis of HA. Using γ_f of 0.48 J/m^2, E of 113 GPa, ΔT of 1000^{o}C and $\Delta\alpha_{max}$ of 7.4x10^{-6}/^{o}C, Hoepfner and Case estimated the critical grain size of HA as 1.1 μm [Hoepfner 2004]. The presence of microcracks affects a wide range of properties, including mechanical properties such as Young's modulus [Fan 2012c], hardness [Perera 2010], fracture strength [Diaz 2008] and

fracture toughness [Kratschmer 2011]. Other physical properties such as electrical conductivity [Hilpert 2004], thermal diffusivity [Deroo 2010] and dielectric constant [Morito 2005] are also a function of microcracking damage state.

5.1 Fracture strength as a function of porosity

Fracture strength is the stress at which a test specimen fractures [Wachtman 2009]. The experimental fracture strength is usually determined from the stress-strain curve during a fracture test (tensile test, compression test, flexure test). For brittle materials, the stress-strain curve usually remains linear before the fracture takes place, meaning that no apparent plastic deformation before fracture [Wachtman 2009].

The theoretical strength of a single crystal material can be approximated as [Wachtman 2009]

$$\sigma_{th} = \sqrt{\frac{E\gamma}{a_0}} \tag{2}$$

where E is the Young's modulus of the material, γ is the surface energy, and a_0 is the equilibrium distance between atomic centers.

For brittle polycrystalline materials, fracture strength is affected by flaw size which is related to porosity [Park 2009, Fan 2012], microcracking [Diaz 2008], grain size [Hirosaki 1993], surface finish [Nakamura 2010] of the test specimens. In addition, fracture strength is affected by fracture testing technique [Cordell 2009].

The discussion on the fracture strength – porosity relationship dates back to the fifties. In 1953, Ryshkewitch [Ryshkewitch 1953] suggested the following equation to describe the porosity dependence of the strength, σ,

$$\sigma = \sigma_0 \exp(-nP) \tag{3}$$

where σ_0 is the strength for nonporous body, P is the volume fraction porosity and n is a unitless, material-dependent constant.

In 1958, Schriller [Schiller 1958] gave a porosity-relative strength relationship that included the concept of a critical porosity, P_c, such that [Schiller 1958],

$$\frac{\sigma}{\sigma_0} = \left[1 - \left(\frac{P}{P_c}\right)^q\right]\left[1 + k\left(\frac{P}{P_c}\right)^n\right] \quad (4)$$

where k, q and n are empirically determined parameters. P_c is the critical porosity that for $P > P_c$, the above equation is no longer valid.

In 1959, Millard [Millard 1959] proposed a relationship such that

$$\sigma = S_0\left(1 - \frac{P}{P_{cr}}\right)\frac{P_{cr}}{P} \quad (5)$$

where S_0 is a constant with unit of the strength, P_{cr} is the critical porosity defined as the porosity of the loose powder.

In 1972, Carnaglia [Carnaglia 1972] suggested that the strength-porosity relationship could be written in terms of a function of the relative Young's modulus E/E_0, such that

$$\frac{\sigma}{\sigma_0} = \left[(1-P)\frac{E}{E_0}\right]^{1/2} \quad (6)$$

Based on mathematical model, Hrma [Hrma 1974] gave the relative strength as a function of the volume fraction porosity normalized by a critical porosity, P_c, such that

$$\frac{\sigma}{\sigma_0} = 1 - \left(\frac{P}{P_c}\right)^n \quad (7)$$

Equations 3-7 can all describe the strength-porosity relationship very well to a critical

porosity value, P_c, where for $P > P_c$, the strength decreases more rapidly than is predicted by equations 3-7.

A slightly modified equation provides better fitting to the strength-porosity data [Fan 2012b]

$$\frac{\sigma}{\sigma_0} = A \cdot \left(1 - \frac{P}{P_g}\right)^n = A \cdot \phi \qquad (8)$$

where σ is fracture strength of the porous ceramic, σ_0 is fracture strength of the theoretically dense ceramic, A and n are dimensionless constants. The degree of densification, ϕ, is defined as $(1-P/P_g)$, where P_g is the porosity at green porosity.

5.2 Elastic moduli as functions of porosity, microcracking and composition

Elastic moduli are fundamental properties of a material, measuring the stiffness of the material. Theoretically, Young's modulus represents the second derivative of the binding energy with respect to strain [Wachtman 2009]. Experimentally, Young's modulus can be measured from the linear portion of a stress-strain curve during a mechanical testing.

Young's modulus is a fourth rank tensor, which consists of 81 stiffness constants [Nye 1985]. The 81 stiffness constants can be reduced to 21 independent stiffness constants after applying the symmetry considerations. The number of independent stiffness constants can be further reduced when considering the symmetry of a particular crystal structure. For example, in cubic crystal structure, the 4 threefold rotation axis reduces the number of independent stiffness constants to three [Nye 1985].

As mentioned above, since the Young's modulus represents the second derivative of the binding energy, the theoretical Young's modulus is only a function of the atomic binding

energy [Wachtman 2009]. In real materials, the elastic modulus is also a function of many other factors, including porosity [Fan 2012], microcracking [Fan 2012c] and composition [Radovic 2006].

For polycrystalline materials, the stress generated in a specimen subjected to a strain arising from mechanical loading can be expressed as [Wachtman 2009]

$$\sigma = E\,\varepsilon \tag{9}$$

For TE materials used in harvesting waste energy, the temperature-dependent Young's modulus, E(T), Poisson's ratio, ν(T), and thermal expansion, α(T), are required for both the analytic and finite element analysis of the stress, induced by thermal gradients or thermal transients [Kaliakin 2002, Martin 1973] such that

$$\sigma(T) = \frac{E(T)\alpha(T)\Delta T}{(1-\nu(T))} \tag{10}$$

where ΔT is the temperature gradient or the temperature change during the thermal cycling.

5.2.1 Elastic moduli versus porosity

In terms of characterizing the behaviour of Young's modulus as a function of porosity, the equation proposed by Spriggs in 1961 has widely been used to predict the Young's modulus of porous brittle materials [Spriggs 1961]

$$E = E_0 \exp(-b_E P) \tag{11}$$

where E and E_0 are the Young's modulus at porosity P and zero, and b_E is a material constant that is dependent on the pore character in the materials [Rice 1998].

In 1987, a new semi-empirical equation was derived by Phani [Phani 1987] to describe the porosity dependence of Young's modulus

$$E = E_0 (1 - aP)^n \tag{12}$$

where a and n are both dimensionless constants, where $a = 1/P_c$ and P_c as the critical porosity at which Young's modulus is zero. According to Phani [Phani 1987], equation 12 is valid for any range of porosity.

Lam [Lam 1994] in 1994 and Hardy [Hardy 1995] in 1995 suggested that the relative Young's modulus, E/E_0, of porous ceramics can be described as

$$\frac{E}{E_0} = \left(1 - \frac{P}{P_g}\right) \tag{13}$$

where E is Young's modulus of the porous ceramic, E_0 is the Young's modulus of the theoretically dense ceramic, and P_g is the porosity at green density. The right hand side of equation (equation 13) is defined as the degree of densification.

A slightly modified equation provides better fitting to the modulus-porosity data, in a similar manner to the relative fracture strength (equation 8)

$$\frac{E}{E_0} = A \cdot \left(1 - \frac{P}{P_g}\right)^n \tag{14}$$

where A and n are dimensionless constants. The degree of densification, ϕ, is defined as $(1-P/P_g)$, where P_g is the porosity at green porosity.

For porosity dependence of Poisson' ratio, υ, here is not a single trend found to work in general. The compilation of Poisson's ratio versus porosity data for fifteen different materials including oxides and non-oxides showed that as the porosity increased, Poisson's ratio may increase, decrease or stay almost constant [Boccaccini 1994].

5.2.2 Elastic moduli versus microcracking

Near surface microcracking can be generated by external mechanical loads and post processing such as grinding, cutting and polishing [Zhou 2012]. During sintering of polycrystalline materials, microcracks can be formed through the whole body due to thermal expansion anisotropy [Case 2005], thermal expansion mismatch [Todd 2004] and Martensitic-type crystallographic phase change [Deville 2004].

The presence of microcracking affects the Young's modulus of the material in a linear manner. Theoretical research by Budiansky and O'Connell [Budiansky 1976], Salganik [Salganik 1974], Hoenig [Hoenig 1979] and Laws and Brockenbrough [Laws 1987] have suggested the following relationship to describe the effect of microcracking on Young's modulus, such that

$$E = E_N (1 - f \varepsilon) \quad (15)$$

where E_N is the Young's modulus for non-microcracked specimen, f is the crack orientation function, and ε is the crack damage parameter, which is a function of the crack number density and the crack radius. For circular microcracks of uniform radius c, ε is defined as $\varepsilon = N c^3$, where N is the volumetric crack number density.

5.2.3 Elastic moduli versus composition

In a solid solution system, the replacement of one atom by another element will change the binding energy, which in turn changes the elastic moduli. Studies on the elastic moduli dependence on composition in solid solution system have shown linear [Ren 2007] (also known as the Vegard's law [Vegard 1921]) or parabolic relationships [Mokhtari 2004, Kanoun 2005, Ren 2007].

An empirical equation has been successfully used to describe the property change as a

function of fractional composition, x ($0 \leqslant x \leqslant 1$), in solid solution system, such that

$$A = A_0 + (A1 - A_0)x + k\,x\,(1\text{-}x) \quad (16)$$

where A_0 = the value of A at x = 0, A_1 = the value of A at x = 1, and k is a parameter (sometimes called the "bowing parameter") which has the same unit as A, where A can be material properties including Young's modulus, shear modulus and hardness. k is a measure of the deviation of A from the linear rule of mixture model. The k values for elastic modulus depend on the lattice mismatch strain in the solid solution system [Bernard 1986, Mokhtari 2004].

5.3 Hardness as a function of porosity and indentation load

Hardness shows how a material will react to plastic deformation when a force is applied [Wachtman 2009]. Hardness is directly related to the two essential factors for fabrication and mechanical stability, namely, the wear resistance [Zeng 2005, Krakhmalev 2006] and machinability [Kamboj 2003, Wang 2002]. For example, when HA is used as dental restoration materials, the wear resistance requires careful consideration [Angker 2006]. For thermoelectric devices, the TE material will be diced into hundreds of small pillars and assembled in array to form a TE module [Wesolowski 2012]. The machinability of the TE materials is an important concern in fabrication.

As is the case with many other material properties, hardness is affected by porosity [Hoepfner 2003], grain size [Xu 1995] and composition [Ren 2008]. Inclusions [Canakci 2011] and precipitates [Liao 2011] are also commonly discussed microstructural features that affect hardness.

5.3.1 Hardness versus porosity

An empirical exponential relationship similar to equation 11 is widely used to

characterize the hardness dependence on porosity [Hoepfner 2003]

$$H = H_0 \exp(-b_H P) \quad (17)$$

where H_0 is the hardness for zero porosity materials, b_H is a material constant measuring the degree of hardness change with respect to porosity.

5.3.2 Load dependence on hardness

The indentation load can be varied for each measurement. In some cases, the hardness value is independent on the indentation load [Ni 2010, White 2011]. For some ceramics [Bull 1989, Sangwal 2009] and metals [Pharr 2010], the measured hardness values decreased with increasing applied load. This phenomenon is called the indentation size effect (ISE) [Nix 1998], which is caused by elastic recovery and work hardening during indentation, surface dislocation pinning in metals [Gong 1999]. Reversed indentation size effect (RISE) has also been reported [Sangwal 2000] where hardness decreases with decreasing load. In RISE, the specimens undergo relaxation instead of elastic recovery in unloading [Sangwal 2000].

5.4 Fracture toughness as a function of porosity

Fracture toughness is a measure of material's resistance to crack initiation and propagation [Wachtman 2009]. When the stress intensity factor is great than fracture toughness, rapid crack growth will take place. It is an important property in design and application for brittle materials. A study by Rice [Rice 1996] showed that fracture toughness decreased exponentially with increasing porosity, similar to other properties such as elastic moduli and hardness. For fracture toughness determined by Vickers indentation, as the porosity exceeds 0.1, no radial cracks will be generated during the indentation due to the presence of porosity. In these cases, tensile test, bend test and double-cantilever beam test can be performed to determine the fracture toughness.

REFERENCES

REFERENCES

[Angker 2006] L. Angker, M.V. Swain, Nanoindentation: Application to dental hard tissue investigations, J. Mater. Res. 21, 1893-1905, 2006.

[Araki 2005] K. Araki, J. W. Halloran, Porous ceramic bodies with interconnected pore channels by a novel freeze casting technique, J. Am. Ceram. Soc. 88, 1108–1114, 2005.

[Bernard 1986] J.E. Bernard, A. Zunger, Optical bowing in zinc chalcogenide semiconductor alloys, Phys. Rev. B 34, 5992-5995, 1986.

[Boccaccini 1994] A.R. Boccaccini, Dependence of ceramic fracture properties on porosity – comment, J. Mater. Sci. Lett. 13, 1035-1037, 1994.

[Boccaccini 1997] A.R. Boccaccini, Machinability and brittleness of glass-ceramics, J. Mater. Process. Tech. 65, 302–304, 1997.

[Budiansky 1976] B. Budiansky, R.J. O'Connell, Elastic-moduli of a cracked solid, Int. J. Solids Struct. 12, 81-97, 1976.

[Bull 1989] S. J. Bull, T. F. Page, E. H. Yoffe, An explanation of the indentation size effect in ceramics, Philoso. Mag. Lett. 59, 281-288, 1989.

[Canakci 2011] A. Canakci, Microstructure and abrasive wear behaviour of B_4C particle reinforced 2014 Al matrix composites, J. Mater. Sci. 46, 2805–2813, 2011.

[Carbajo 2002] M.C. Carbajo, A. Gomez, M.J. Torralvo, E.Enciso, Macroporous silica and titania obtained using Poly[styrene-co-(2-hydroxyethyl methacrylate)] as template, J. Mater. Chem. 12, 2740-2746, 2002.

[Carnaglia 1972] S.C. Carniglia, Working model for porosity effects on the uniaxial strength of ceramics. J. Am. Ceram. Soc. 55, 610-618, 1972.

[Case 2005] E.D. Case, I.O. Smith, M.J. Baumann, Microcracking and porosity in calcium phosphates and the implications for bone tissue engineering, Mater. Sci. Eng. A, 390, 246-254, 2005.

[Case 2012] E. D. Case, Thermal fatigue and waste heat recovery via thermoelectrics, J. Electron. Mater. 41, 1811-1819, 2012.

[Chen 2003] G. Chen, M.S. Dresselhaus, G. Dresselhaus, J.P. Fleurial, T. Caillat, Recent developments in thermoelectric materials, Int. Mater. Rev. 48, 45-66, 2003.

[Cleveland 1978] J. J. Cleveland, R. C. Bradt, Grain size/microcracking relations for pseudobrookite oxides, J. Am. Ceram. Soc. 61, 478-481, 1978.

[Clyne 2006] T.W. Clyne, I.O. Golosnoy, J.C. Tan, A.E. Markaki, Porous materials for

thermal management under extreme conditions, Philos. T. Roy. Soc. A 364, 125-146, 2006.

[Cordell 2009] J.M. Cordell, M.L. Vogl, A.J.W. Johnson, The influence of micropore size on the mechanical properties of bulk hydroxyapatite and hydroxyapatite scaffolds, J. Mech. Behav. Biomed. 2, 560-570, 2009.

[Deroo 2010] F. Deroo, J.Y. Kim, Detection of damage in concrete using diffuse ultrasound, J. Acoust. Soc. Am. 127, 3315 – 3318, 2010.

[Deville 2004] S. Deville, G. Guenin, J. Chevalier, Martensitic transformation in zirconia: Part II. Martensite growth, Acta Materialia 52, 5709–5721, 2004.

[Diaz 2008] L.A. Diaz, R. Torrecillas, F. Simonin, G. Fantozzi, Room temperature mechanical properties of high alumina refractory cass with spinel, periclase and dolomite additions, J. Eur. Ceram. Soc. 28, 2853-2858, 2008.

[Drisko 2009] G. L. Drisko, V. Luca, E. Sizgek, N. Scales, R. A. Caruso, Template synthesis and adsorption properties of hierarchically porous zirconium titanium oxides, Langmuir, 25, 5286–5293, 2009.

[El-Ghannam 2004] A.R. El-Ghannam, Advanced bioceramic composite for bone tissue engineering: Design principles and structure-bioactivity relationship, J. Biomed. Mater. Res. A 69A, 490-501, 2004.

[Fan 2012] X. Fan, E.D. Case, F. Ren, Y. Shu, M.J. Baumann, Part I: Porosity dependence of the Weibull modulus for hydroxyapatite and other brittle materials. J. Mech. Behav. Biomed. 8, 21-36, 2012.

[Fan 2012b] X. Fan, E.D. Case, F. Ren, Y. Shu, M.J. Baumann, Part II: Fracture strength and elastic modulus as a function of porosity for hydroxyapatite and other brittle materials. J. Mech. Behav. Biomed. 8, 99-110, 2012.

[Fan 2012c] X. Fan, E. D. Case, M. J. Baumann, The effect of indentation-induced microcracks on the elastic modulus of hydroxyapatite, J Mater. Sci. 47, 6333–6345, 2012.

[Fu 2011] Q. Fu, E. Saiz, A. P. Tomsia, Bioinspired strong and highly porous glass scaffolds, Adv. Funct. Mater. 21, 1058–1063, 2011.

[Geis 2002] S. Geis, J. Fricke, P. Lobmann, Electrical properties of PZT aerogels, J. Eur. Ceram. Soc. 22, 1155-1161, 2002.

[Gong 1999] J. Gong, J. Wu, Z. Guan, Examination of the indentation size effect in low-load Vickers hardness testing of ceramics, J. Eur. Ceram. Soc. 19, 2625-2631, 1999.

[Goodenough 2007] J.B. Goodenough, Y.-H. Huang, Alternative anode materials for solid oxide fuel cells, J. Power Sources 173, 1-10, 2007.

[Guizard 2002] C. Guizard, A.Ayral, A. Julbe, Potentiality of organic solvents filtration with

ceramic membranes. A comparison with polymer membranes, Desalination, 147, 275–280, 2002.

[Hardy 1995] D. Hardy, D.J. Green, Mechanical properties of a partially sintered alumina, J. Eur. Ceram. Soc. 15, 769-715, 1995.

[He 2011] J.Q. He, S.N. Girard, M.G. Kanatzidis, V.P. Dravid, Microstructure-lattice thermal conductivity correlation in nanostructured $PbTe_{0.7}S_{0.3}$ Thermoelectric Materials, Adv. Funct. Mater. 20, 764–772, 2011.

[Hench 1990] L.L. Hench, J.K. West, Principles of Electronic Ceramics, Wiley, New York, 1990.

[Hench 1991] L. L. Hench, J. K. West, Principles of Electronic Ceramics, Wiley, New York, 190.

[Heremans 2008] J. P. Heremans, V. Jovovic, E. S. Toberer, A. Saramat, K. Kurosaki, A. Charoenphakdee, S. Yamanaka, G. J. Snyder, Enhancement of thermoelectric efficiency in PbTe by distortion of the electronic density of states, Science 321, 554–557, 2008.

[Hilpert 2004] T. Hilpert, E. Ivers-Tiffee, Correlation of electrical and mechanical properties of zirconia based thermal barrier coatings, Solid State Ionics 175, 471-476, 2004.

[Hirosaki 1993] N. Hirosaki, Y. Akimune, Effect of grain growth of β-silicon nitride on strength, Weibull modulus, and fracture toughness. J. Am. Ceram. Soc. 76, 1892-1894, 1993.

[Hoenig 1979] A. Hoenig, Elastic-moduli of a non-randomly cracked body, Int. J. Solids Struct. 15, 137-154, 1979.

[Hoepfner 2002] T.P. Hoepfner, E.D. Case, The porosity dependence of the dielectric constant for sintered hydroxyapatite. J. Biomed. Mater. Res. 60, 643-650, 2002.

[Hoepfner 2003] T.P. Hoepfner, E.D. Case, The influence of the microstructure on the hardness of sintered hydroxyapatite, Ceramics International. Ceram. Int. 29, 699-706, 2003.

[Hoepfner 2004] T. P. Hoepfner, E. D. Case, An estimate of the critical grain size for microcracks induced in hydroxyapatite by thermal expansion anisotropy, Mater. Lett. 58, 489-492, 2004.

[Hrma 1974] P. Hrma, V. Satava, Model for strength of brittle porous materials, J. Am. Ceram. Society, 57, 71–73, 1974.

[Hsu 2004] K. F. Hsu, S. Loo, F. Guo, Wei. Chen, J. S. Dyck, C. Uher, T. Hogan, E. K. Polychroniadis, M. G. Kanatzidis, Cubic $AgPb_mSbTe_{2+m}$: Bulk thermoelectric materials with high figure of merit, Science 303, 818-821, 2004.

[Hsu 2007] Y. H. Hsu, I. G. Turner, A. W. Miles, Fabrication of porous bioceramics with porosity gradients similar to the bimodal structure of cortical and cancellous bone, J. Mater.

Sci. Mater. M. 18, 2251-2256, 2007.

[Jeon 2000] H.C Jeon, J.H Leem, Y.S Ryu, T.W Kang, T.W Kim, Effect of lattice mismatch and thermal expansion on the strain of CdTe/GaAs heterostructures, Appl. Surf. Sci. 156, 110–114, 2000.

[Jiang 2012] Q. Jiang, J. Cheng, R. Wang, Y. Fan, J. Gao, Novel triple-phase composite cathode materials for proton-conducting solid oxide fuel cells, J. Power Sources 206, 47–52, 2012.

[Joshi 2008] G. Joshi, H. Lee, Y. Lan, X. Wang, G. Zhu, D. Wang, R. W. Gould, D. C. Cuff, M. Y. Tang, M. S. Dresselhaus, G. Chen, Z. Ren, Enhanced thermoelectric figure-of-merit in nanostructured p-type silicon germanium bulk alloys, Nano Lett., 8, 4670–4674, 2008.

[Kaliakin 2002] V.N. Kaliakin, In Introduction to Approximate Solution Techniques, Numerical Modeling, and Finite Element Methods, Marcel Dekker, New York, 2002.

[Kamaya 2011] M. Kamaya, Crack growth under high-cycle thermal fatigue loading: effects of stress gradient and relaxation in a crack network, J. Pressure Vessel Technol. 133, 061203, 2011.

[Kamboj 2003] R.K. Kamboj, S. Dhara, P. Bhargava, Machining behaviour of green gelcast ceramics, J. Eur. Ceram. Soc. 23, 1005-1011, 2003.

[Kanatzidis 2010] M. G. Kanatzidis, Nanostructured thermoelectrics: The new paradigm? Chem. Mater. 22, 648-659, 2010.

[Kanoun 2005] M. B. Kanoun, S. Goumri-Said, A. E. Merad, H. Mariette,Ab initio study of structural parameters and gap bowing in zinc-blende $Al_xGa_{1-x}N$ and $Al_xIn_{1-x}N$ alloys, J. Appl. Phys. 98, 063710, 2005.

[Koumoto 2006] K. Koumoto, I. Terasaki, R. Funahashi, Complex oxide materials for potential thermoelectric applications, MRS Bull. 31, 206–210, 2006.

[Krakhmalev 2006] P.V. Krakhmalev, J. Bergstrom, Tribological behavior and wear mechanisms of $MoSi_2$-base composites sliding against AA6063 alloy at elevated temperature, Wear 260, 450-457, 2006.

[Kratschmer 2011] T. Kratschmer, C.G. Aneziris, Improved thermal shock performance of sintered Mg-partially stabilized zirconia with alumina and titania additions, Int. J. Appl. Ceram. Technol. 8, 398-410, 2011.

[Lam 1994] D.C.C. Lam, F.F. Lange, A.G. Evans, Mechanical properties of partially dense alumina produced from powder compacts. J. Am. Cer. Soc. 77, 2113 –2117, 1994.

[Larson 2013] M.G. Larson, Finite Element Method: Theory, Implementation, and Applications, Springer-Verlag Berlin Heidelberg, 2013.

[Laws 1987] N. Laws, J.R. Brockenbrough, The effect of micro-crack systems on the loss of stiffness of brittle solids, Int. J. Solids Struct. 23, 1247-1268, 1987.

[Leyland 2000] A. Leyland, A. Matthews, On the significance of the H/E ratio in wear control: a nanocomposite coating approach to optimised tribological behaviour, Wear, 246, 1–11, 2000.

[Liao 2011] Y. Liao, I. Baker, Evolution of the microstructure and mechanical properties of eutectic $Fe_{30}Ni_{20}Mn_{35}Al_{15}$, J. Mater. Sci. 46, 2009–2017, 2011.

[Mahabole 2005] M.P. Mahabole, R.C. Aiyer, C.V. Ramakrishna, B. Sreedhar, R.S. Khairnar, Synthesis, characterization and gas sensing property of hydroxyapatite ceramic, Mater. Sci. B 28, 535-545, 2005.

[Martin 1973] H.C. Martin, G.F. Carey, In Introduction to Finite Element Analysis, McGraw-Hill, New York, 1973.

[Millard 1959] D.J.Br. Millard, Relationship between strength and porosity for coal compacts, J. Appl. Phys. 10, 287-290, 1959.

[Minh 1993] N. Q. Minh, Ceramic Fuel Cells, J. Am. Ceram. Soc. 76, 563–588, 1993.

[Mokhtari 2004] A. Mokhtari, H. Akbarzadeh, First principles investigation of the electronic and structural properties of $Mg_{3x}Be_{3-3x}N_2$ ternary alloy, J. Phys. Condens. Mat. 16, 6063-6074, 2004.

[Mori 2003] K. Mori, T. Hara, T. Mizugaki, K. Ebitani, K. Kaneda, Hydroxyapatite-bound cationic ruthenium complexes as novel heterogeneous Lewis acid catalysts for Diels-Alder and aldol reactions. J. Am. Chem. Soc. 125, 11460-11461, 2003.

[Mori 2004] K. Mori, T. Hara, T. Mizugaki, K. Ebitani, K. Kaneda, Hydroxyapatite-supported palladium nanoclusters: A highly active heterogeneous catalyst for selective oxidation of alcohols by use of molecular oxygen. J. Am. Chem. Soc. 126, 10657-10666, 2004.

[Morito 2005] K. Morito, T. Suzuki, Effect of internal residual stress on the dielectric properties and microstructure of sputter-deposited polycrystalline (Ba,Sr)TiO_3 thin films J. Appl. Phys. 97, 104107, 2005.

[Murray 2001] E.P. Murray, S.A. Barnett, (La,Sr)MnO_3-(Ce,Gd)$O_{(2-x)}$ composite cathodes for solid oxide fuel cells, Solid State Ionics 143, 265-273, 2001.

[Nagai 1988]M. Nagai, T. Nishino, T. Saeki, A new type of CO_2 gas sensor comprising porous hydroxyapatite ceramics, Sensor. Actuator. 15, 145-151, 1988.

[Nakamura 2010] Y. Nakamura, S. Hojo, H. Sato, The effect of surface roughness on the

Weibull distribution of porcelain strength. Dent. Mater. J. 29, 30-34, 2010.

[Ni 2009] J.E. Ni, F. Ren, E.D. Case, E.J. Timm, Porosity dependence of elastic moduli in LAST (Lead-antimony-silver-tellurium) thermoelectric materials. Mater. Chem. Phy. 118, 459 – 466, 2009.

[Ni 2010] J.E. Ni, E.D. Case, K.N. Khabir, R.C. Stewart, C-I. Wu, T.P. Hogan, E.J. Timm, S.N. Girard, M.G. Kanatzidis, Room temperature Young's modulus, shear modulus, Poisson's ratio and hardness of PbTe–PbS thermoelectric materials, Mater. Sci. Eng. B 170, 58-66, 2010.

[Nicholas 2010] J.D. Nicholas, S.A. Barnett, Measurements and modeling of $Sm_{0.5}Sr_{0.5}CoO_{3-x}$-$Ce_{0.9}Gd_{0.1}O_{1.95}$ SOFC cathodes produced using infiltrate solution additives, J. Electrochem. Soc. 157, B536-B541, 2010.

[Nicholas 2012] J.D. Nicholas, L. Wang, A.V. Call, S.A. Barnett, Use of the simple infiltration microstructure polarization loss estimation (SIMPLE) model to predict the measured polarization resistance of infiltrated nano-composite solid oxide fuel cell cathodes, Phys. Chem. Chem. Phys. 14, 15379-15392, 2012.

[Nielsen 1990] L.F. Nielsen, Strength and stiffness of porous materials, J. Am. Ceram. Soc. 73, 2684-2689, 1990.

[Nix 1998] W.D. Nix, H. Gao, Indentation size effects in crystalline materials: a law for strain gradient plasticity, J. Mech. Phys. Solids 46, 411-425, 1998.

[Nolas 1999] G. S. Nolas, D. T. Morelli, T. M. Tritt, Skutterudites: A phonon-glass-electron crystal approach to advanced thermoelectric energy conversion applications, Annu. Rev. Mater. Sci. 29, 89-116, 1999.

[Nye 1985] J. F. Nye, Physical Properties of Crystals: Their representation by Tensors and matrices, Clarendon Press, Oxford, 1985.

[Ohtsuki 2010] C. Ohtsuki, Y. Ichikawa, H. Shibata, G. Kawachi, T. Torimoto, S. Ogata, Sensing of protein adsorption with a porous bulk composite comprising silver nanoparticles deposited on hydroxyapatite, J. Mater. Sci-Mater. M 21, 1225-1232, 2010.

[Opre 2005] Z. Opre, J.D. Grunwaldt, M. Maciejewski, D. Ferri, T. Mallat, A. Baiker, Promoted Ru-hydroxyapatite: designed structure for the fast and highly selective oxidation of alcohols with oxygen. J. Catal. 230, 406-419, 2005.

[Owada 1989] H. Owada, K. Yamashita, T. Umegaki, T. Kanazawa, M. Nagai, Humidity-sensitivity of yttrium substituted apatite ceramics. Solid State Ionics 35, 401-404, 1989.

[Park 2009] Y.H. Park, T. Hinoki, A. Kohyama, Development of multi-functional NITE-porous SiC for ceramic insulators, J. Nuclear Mater. 386–388, 1014-1017, 2009.

[Pei 2011a] Y. Pei, J. Lensch-Falk, E.S. Toberer, D.L. Medlin, G.J. Snyder, High

thermoelectric performance in PbTe due to large nanoscale Ag_2Te precipitates and La doping, Adv. Funct. Mater. 21, 241–249, 2011.

[Pei 2011b] Y. Pei, A. LaLonde, S. Iwanaga, G.J. Snyder, High thermoelectric figure of merit in heavy hole dominated PbTe, Energy Environ. Sci. 4, 2085–2089, 2011.

[Perera 2010] F.H. Perera, F.J. Martinez-Vazquez, P. Miranda, A.L. Ortiz, A. Pajares, Clarifying the effect of sintering conditions on the microstructure and mechanical properties of β-tricalcium phosphate, Ceram. Int. 36, 1929-1935, 2010.

[Phani 1987] K. K. Phani, S. K. Niyogi, Young's modulus of porous brittle solids, J. Mater. Sci. 22, 257-263, 1987.

[Pharr 2010] G.M. Pharr, E.G. Herbert, Y. Gao, The indentation size effect: a critical examination of experimental observations and mechanistic interpretations, Annu. Rev. Mater. Res. 40, 271–292, 2010.

[Poudel 2008] B. Poudel, Q. Hao, Y. Ma, Y.C. Lan, A. Minnich, B. Yu, X. Yan, D.Z.Wang, A. Muto, D. Vashaee, X.Y. Chen, J.M. Liu, M.S. Dresselhaus, G. Chen, Z.F. Ren, High-thermoelectric performance of nanostructured bismuth antimony telluride bulk alloys, Science 320, 634–638, 2008.

[Radovic 2006] M. Radovic, M.W. Barsoum, A. Ganguly, T. Zhen, P. Finkel, S.R. Kalidindi, E. Lara-Curzio, On the elastic properties and mechanical damping of Ti_3SiC_2, Ti_3GeC_2, $Ti_3Si_{0.5}Al_{0.5}C_2$ and Ti_2AlC in the 300–1573 K temperature range, Acta Materialia 54, 2757-2767, 2006.

[Ren 2005] F. Ren, I. O. Smith, M.J. Baumann, E. D. Case, Three-dimensional microstructural characterization of porous hydroxyapatite using confocal laser scanning microscopy, Int. J. Appl. Ceram. Technol., 2, 200–211, 2005.

[Ren 2007] F. Ren , E. D. Case , E. J. Timm & H. J. Schock, Young's modulus as a function of composition for an n-type lead–antimony–silver–telluride (LAST) thermoelectric material, Philos. Mag. 87, 4907-4934, 2007.

[Ren 2008] F. Ren, E.D. Case, E.J. Timm, H.J. Schock, Hardness as a function of composition for n-type LAST thermoelectric material, J Alloys Compd. 455, 340–345, 2008.

[Ren 2009] F. Ren, E.D. Case, A. Morrison, M. Tafesse, M.J. Baumann, Resonant ultrasound spectroscopy measurement of Young’s modulus, shear modulus and Poisson’s ratio as a function of porosity for alumina and hydroxyapatite, Philos. Mag. 89, 1163-1182, 2009.

[Rice 1996] R. W. Rice, Evaluation and extension of physical property-porosity models based on minimum solid area, J. Mater. Sci. 31, 102-118, 1996.

[Rice 1998] R.W. Rice, Porosity of Ceramics, Marcel Dekker, Inc., New York, 1998.

[Ryshkewitch 1953] E. Ryshkewitch, Compression strength of porous sintered alumina and zirconia, J. Am. Ceram. Soc. 36, 65–68, 1953.

[Salganik 1974] R.L. Salganik, Mechanics of bodies with many cracks, Mech. Solids 8, 135-143, 1974.

[Sammis 1986] C.G. Sammis, M.F. Ashby, The fracture of brittle porous solids under compressive stress states, Acta Mater. 34, 511-526, 1986.

[Samson 2012] A.J. Samson, P. Hjalmarsson, M. Sogaard, J. Hjelm, N. Bonanos, Highly durable anode supported solid oxide fuel cell with an infiltrated cathode, J. Power Sources 216, 124-130, 2012.

[Sangwal 2000] K. Sangwal, On the reverse indentation size effect and microhardness measurement of solids, Mater. Chem. Phys. 63, 145–152, 2000.

[Sangwal 2009] K. Sangwal, Review: Indentation size effect, indentation cracks and microhardness measurement of brittle crystalline solids – some basic concepts and trends, Cryst. Res. Technol. 44, 1019-1037, 2009.

[Sauvet 2001] A.L. Sauvet, J. Fouletier, Catalytic Properties of new anode materials for solid oxide fuel cells operated under methane at intermediary temperature, J. Power Sources 101, 259-266, 2001.

[Schiller 1958] K.K. Schiller, Porosity and strength of brittle solids (with particular reference to gypsum), mechanical properties of non-metallic brittle materials, Intersciemce Pub. Inc., New York, 1958.

[Shi 2010] X. Shi, J. Yang, S. Bai, J.Yang, H. Wang, M. Chi, J. R. Salvador, W. Zhang, L. Chen, W. Wong-Ng, On the design of high-efficiency thermoelectric clathrates through a systematic cross-substitution of framework elements, Adv. Funct. Mater. 20, 755–763, 2010.

[Shimizi 2009] S. Shimizi, T. Yamaguchi, Y. Fujishiro, M. Awan, Effect of microstructure on the conductivity of porous $(La_{0.8}Sr_{0.2})_{0.99}MnO_3$, J. Ceram. Soc. Japan 117, 895-898, 2009.

[Slack 1995] G. A. Slack, CRC Handbook of Thermoelectrics, edited by D. M. Rowe, Chemical Rubber, Boca Raton, FL, 1995.

[Snyder 2002] G. J. Snyder, J-P Fleurial, T. Caillat, R.Yang, G.Chen, Supercooling of Peltier cooler using a current pulse, J. Appl. Phys. 92, 1564-1569, 2002.

[Spriggs 1961] R.M. Spriggs, Expression for effect of porosity on elastic modulus of polycrystalline refractory materials, particularly aluminum oxide, J. Am. Ceram. Soc. 44, 628-629, 1961.

[Srinivasan 2006] M. Srinivasan, C. Ferraris, T. White, Cadmium and lead ion capture with three dimensionally ordered macroporous hydroxyapatite, Environ. Sci. Technol. 40, 7054-

7059, 2006.

[Sulistyo 2010] J. Sulistyo, T. Hata, H. Kitagawa, P. Bronsveld, M. Fujisawa, K. Hashimoto, Y. Imamura, Electrical and thermal conductivities of porous SiC/SiO2/C composites with different morphology from carbonized wood. J. Mater. Sci. 45, 1107-1116, 2010.

[Todd 2004] R.I. Todd, B. Derby, Thermal stress induced microcracking in alumina–20% SiCp composites, Acta Materialia, 52, 1621-1629, 2004.

[Trovarelli 1996] A. Trovarelli, Catalytic properties of ceria and CeO_2-containing materials, Catal. Rev. Sci. Eng. 38, 439-509, 1996.

[Trustrum 1979] K. Trustrum, A. De S. Jayatilaka, On estimating the Weibull modulus for a brittle material, J. Mater. Sci. 14, 1080-1084, 1979.

[Uher 1999] C. Uher, J. Yang, S. Hu, D. T. Morelli, G. P. Meisner, Transport properties of pure and doped MNiSn (M=Zr, Hf), Phys. Rev. B 59, 8615-8621, 1999.

[Vegard 1921] L. Vegard. Die Konstitution der Mischkristalle und die Raumfüllung der Atome. Zeitschrift für Physik, 5, 17, 1921.

[Venugopal 2003] A. Venugopal, M.S. Scurrell, Hydroxyapatite as a novel support for gold and ruthenium catalysts - Behaviour in the water gas shift reaction. Appl. Catal. a-Gen 245, 137-147, 2003.

[Wachtman 2009] J.B. Wachtman, W.R. Cannon, M.J. Matthewson, Mechanical Properties of Ceramics, 2nd ed., Wiley Interscience, New York, 2009.

[Wagner 1992] H.D. Wagner, S. Weiner, On the relationship between the microstructure of bone and its mechanical stiffness, J. Biomech. 25, 1311-1320, 1992.

[Wang 2010] S. Wang, Y. Lei, Y. Zhang, J. Tang, G. Shen, R. Yu, Hydroxyapatite nanoarray-based cyanide biosensor, Anal. Biochem. 398, 191–197, 2010.

[Wesolowski 2012] D.E. Wesolowski, R.S. Goeke, A.M. Morales, S.H. Goods, P.A. Sharma, M.P. Saavedra, K.R. Reyes-Gil, W.C.G. Neel, N.Y.C. Yang, C.A. Apblett, Development of a Bi_2Te_3-based thermoelectric generator with high-aspect ratio, free-standing legs, J. Mater. Res. 27, 1149-1156, 2012.

[White 2011] R.M. White, J.M. Kunkle, A.V. Polotai, E.C. Dickey, Microstructure and hardness scaling in laser-processed B4C–TiB2 eutectic ceramics, J. Eur. Ceram. Soc. 31, 1227–1232, 2011.

[Xu 1995] H. H. K. Xu, S. Jahanmir, Effect of grain size on scratch damage and hardness of alumina, J Mater. Sci. Lett. 14, 736-739, 1995.

[Yang 2007a] L. Yang, X. S. Ning, K.X. Chen, H.P. Zhou, Preparation and properties of

hydroxyapatite filters for microbial filtration, Ceram. Int. 33, 483-489, 2007.

[Yang 2007b] L. Yang, X. S. Ning, Q.F. Xiao, K.X. Chen, H.P. Zhou, Development and characterization of porous silver-incorporated hydroxyapatite ceramic for separation and elimination of microorganisms, J. Biomed. Mater. Res. B 81B, 50-56, 2007.

[Yani 2007] J. Tani, H. Kido, Thermoelectric properties of Sb-doped Mg_2Si semiconductors, Intermetallics 15, 1202-1207, 2007.

[Yin 2010] S.X. Yin, D.E. Ellis, First-principles investigations of Ti-substituted hydroxyapatite electronic structure, Phys. Chem. Chem. Phys. 12, 156-163, 2010.

[Zebarjadi 2011] M. Zebarjadi, K. Esfarjani, M. S. Dresselhaus, Z. F. Ren, G. Chen, Perspectives on thermoelectrics: from fundamentals to device applications, Energy Environ. Sci., 5, 5147-5162, 2012.

[Zeng 2005] J. Zeng, Y. Sato, C. Ohkubo, T. Hosoi, In vitro wear resistance of three types of composite resin denture teeth, J. Prosthet. Dent. 94, 453-457, 2005.

[Zhao 2008] L-D. Zhao, B-P. Zhang, J-F. Li, M. Zhou, W-S. Liu, J. Liu, Thermoelectric and mechanical properties of nano-SiC-dispersed Bi2Te3 fabricated by mechanical alloying and spark plasma sintering, J. Alloy. Compd. 455, 259–264, 2008.

[Zhou 2011] Z. Zhou, X. Xu, A. Y. Leung, Z. Guan, Transient thermal stress intensity factors for Mode I edge-cracks, Nucl. Eng. Des. 241, 3613–3623, 2011.

[Zhou 2012] S.S. Zhou, X.L. Gao, G.W. Griffith, Stress analysis and structural optimization of a three-layer composite cladding tube under thermo-mechanical loads, J. Eng. Mater.-T. ASME 134, 031001, 2012.

[Zhu 2003] W.Z. Zhu, S.C. Deevi, Development of interconnect materials for solid oxide fuel cells, Mater. Sci. Eng. A 348, 227-243, 2003.

[Zievers 1991] J.F. Zievers, P. Eggerstedt, E.C. Zievers, Porous ceramics for gas filtration, Am. Ceram. Soc. Bull. 70, 108-111, 1991.

[Zioupos 1994] P. Zioupos, J. D. Currey， The extent of microcracking and the morphology of microcracks in damaged bone, J. Mater. Sci. 29, 978-986, 1994.

CHAPTER 3

EXPERIMENTAL PROCEDURES

This chapter is a general outline of the techniques and equipments used in this study.

1. Specimen preparation

All of the hydroxyapatite (HA, $Ca_{10}(PO_4)_6(OH)_2$) specimens discussed in Chapters 4, 5, 6 and 7 in this dissertation were made from biomedical grade commercial HA powders (Taihei Chemical Industrials Co., Osaka, Japan), with a vendor-specified average powder particle size of 1 – 3 μm. Each specimen was fabricated by cold die uniaxially pressing (Carver Inc., Wabash, IN) of ~2.5 grams of HA powder into disk-shaped compact at 33 MPa for 1 minute using a steel pellet die with a diameter of 32 mm.

The as-pressed HA specimens were followed by pressure-less sintering in air in an electrical resistance furnace (CM Inc., Model #0100277, Bloomfield, NJ), at a heating/cooling rate of 10^oC/min. The sintering temperatures and sintering times were varied deliberately in order to obtain specimens with a wide range of porosities, from near zero porosity to near green porosity. During the sintering process, specimens were placed on an alumina crucible covered with 2 – 3 mm thick layer of HA loose powder, and the HA specimens were covered with a layer of 2 – 3 mm HA loose powder on top. The powder bed assured an even thermal distribution and helped to avoid warping of specimens during sintering.

The volume fraction porosity, P, of the as-sintered specimens was calculated from the specimen mass along with the average specimen diameter and thickness, assuming a theoretical density of 3.156 g/cm^3 for HA [CRC 2009]. The specimen mass was measured

using an electronic balance (Denver Instrument Company, Arvada, CO), with a vendor-specified precision of ±0.001 gram. The diameter and thickness were measured three times using digital caliper (Davis Calibration, Carol Stream, IL, with a vendor-specified precision of ±0.01 mm) and an average value was calculated and used in the porosity calculation.

For grain size evaluation and indentation studies, the as-sintered HA specimens were then polished using 600 grit SiC abrasive paper followed by polishing using diamond paste with grit size from 90 μm, 30 μm, 15 μm, 9 μm, 6 μm, 1 μm down to 0.5 μm (Buehler Ecomet 3 variable speed grinder/polisher, Lake Bluff, IL), until a mirror-like finish was obtained. During the polishing process, specimens were ultrasonically cleaned (VWR B3500A-MT, Radnor, PA) for 10 minutes before shifting down to a smaller grit.

2. Biaxial flexural testing

As-sintered HA specimens were fractured using biaxial flexural testing (Figure 3.1) performed on a universal testing machine (Model 4206, Instron, Norwood, MA) via a ring-on-ring configuration (Figures 3.2a and 3.2b, ASTM 2003). The diameter of the support ring is 20 mm, and the diameter of the loading ring is 10 mm (Figures 3.2a and 3.2b). A piece of rubber tape was placed between the support ring and the test specimen in order to eliminate any contact stress or friction (Figures 3.2a and 3.2b). An adhesive Teflon tape was attached onto the upside face of the specimen, for the purpose to hold the remnants of the specimen after fracture (Figures 3.2a and 3.2b). The crosshead loading speed was 1 mm/min.

After fracture, the remnants of the specimens were used for fractographic examination to determine the validity of the fracture testing. The crack pattern corresponding to a valid test is recognized as cracks initiating from the inner area of the loading ring; while an invalid fracture testing is recognized as a diametral crack across the specimen that initiated from the

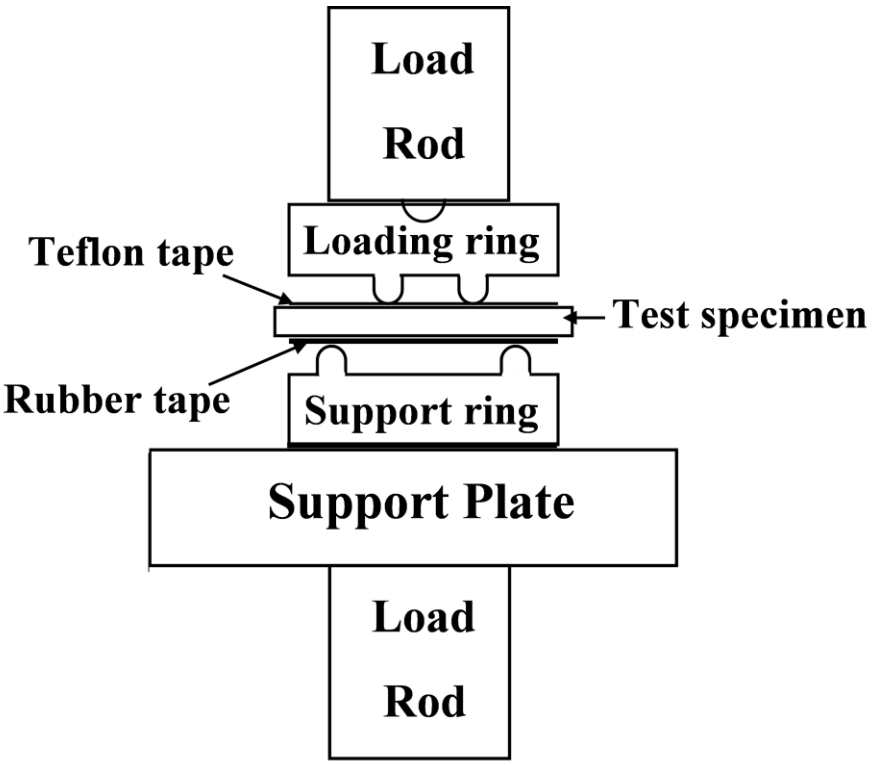

Figure 3.1. Cross-section view of the biaxial flexural testing set up.

(a)

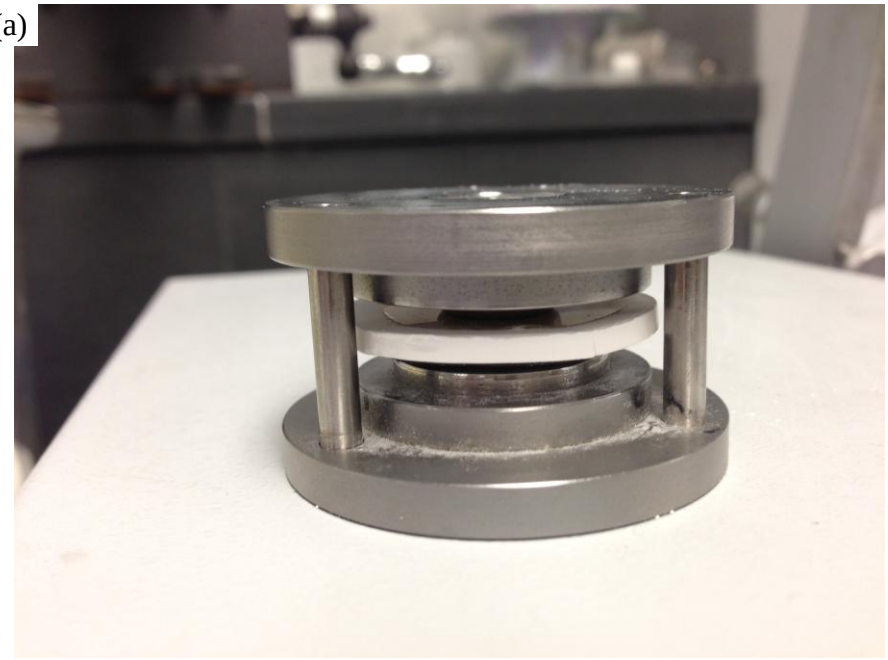

(b)

Figure 3.2. Digital image of the ring-on-ring fixture used in the biaxial flexure testing in this study; (a) assembled fixture with support ring underneath and loading ring on top of the specimen; (b) support ring (left), loading ring (right), rubber tape (middle, top), specimen with adhesive Teflon tape (middle, bottom).

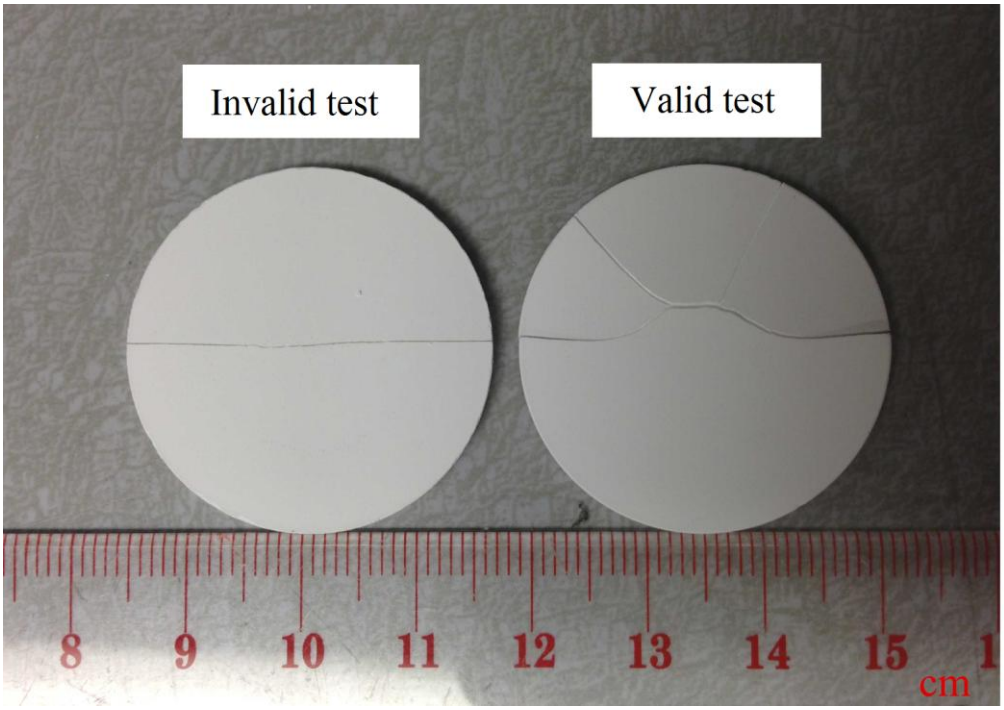

Figure 3.3. Digital image of specimens showing crack patterns that correspond to valid and invalid fracture test.

specimen edge (Figure 3.3, ASTM 2003). Only data of validly fractured specimens were included in the study.

The fracture strength, σ, was calculated using the following equation [ASTM 2003]

$$\sigma = \frac{3F}{2\pi h^2}\left[(1-\nu)\frac{D_S^2 - D_L^2}{2D^2} + (1+\nu)\ln\left(\frac{D_S}{D_L}\right)\right] \quad (1)$$

where F is the load at failure, h and D are the thickness and the diameter of the test specimen, D_S and D_L are the diameters of the support ring and the loading ring, ν is the Poisson's ratio of the material.

Compared to other flexure test methods, including three point and four point flexure tests, the advantages of the biaxial flexure test include the following: no extensive polishing is needed before testing; the fracture is not affected by edge flaws or the slight warping of specimens during sintering [Wachtman 2009].

3. Weibull analysis

In fracturing a group of brittle specimens fabricated in the same manner, the fracture strength distribution does not follow a normal distribution. Instead, a Weibull distribution typically fits the data well, Weibull statistics are based on the weakest link theory [Wachtman 2009]. The distribution of the largest flaws (the weakest link) determines the distribution of the fracture strengths in a brittle material. While knowing the mean strength is important, knowing the distribution of strength is even critical in the design of products fabricated from brittle materials.

The Weibull modulus is related to an applied stress at which a given fraction of specimens will fail. For example, if one is designing products made from brittle materials, and requires that less than 1 specimen out of 1000 specimens will fail in use, then the

Weibull modulus can be used to estimate the stress that would cause this fraction of failure. Weibull modulus is directly linked to material reliability, in a way that the less scatter in the strength leads to a higher Weibull modulus, meaning the more reliable a component is.

A high Weibull modulus value, for example, m = 20, indicates a narrow distribution of the largest flaws and the fracture strengths [Wachtman 2009]. Carefully processed structural ceramics such as SiC [Zhan 1999] and Si_3N_4 [Hirosaki 1993] can exhibit high m values. On the other hand, a low Weibull modulus value, say, 5 and below, implies that strengths can vary over a wide range, which is associated with a broad distribution of flaw size. In the extreme, a Weibull modulus value will be infinite if the fracture strength of each specimen is identical. On the contrary, a Weibull modulus value approaching zero would correspond to an infinite scatter among the strength values of the group of specimens. The Weibull modulus is affected by many factors such as porosity [Chao 1992], surface finish [Nakamura 2010a], and test techniques [Cordell 2009], which is discussed in detail in Chapter 4, Appendix B.

The general form of Weibull distribution for fracture strength is expressed in the following equation [Wachtman 2009]:

$$P_f = 1 - \exp\left[-\int_V \left(\frac{\sigma}{\sigma_c} \right)^m dV \right] \quad (2)$$

where P_f is the cumulative probability of failure, V is the specimen volume subject to stress, the scale parameter σ_c is called the characteristic strength, the shape parameter *m* is named the Weibull modulus [Wachtman 2009]. For specimens with constant volume, Equation (2) can be simplified to

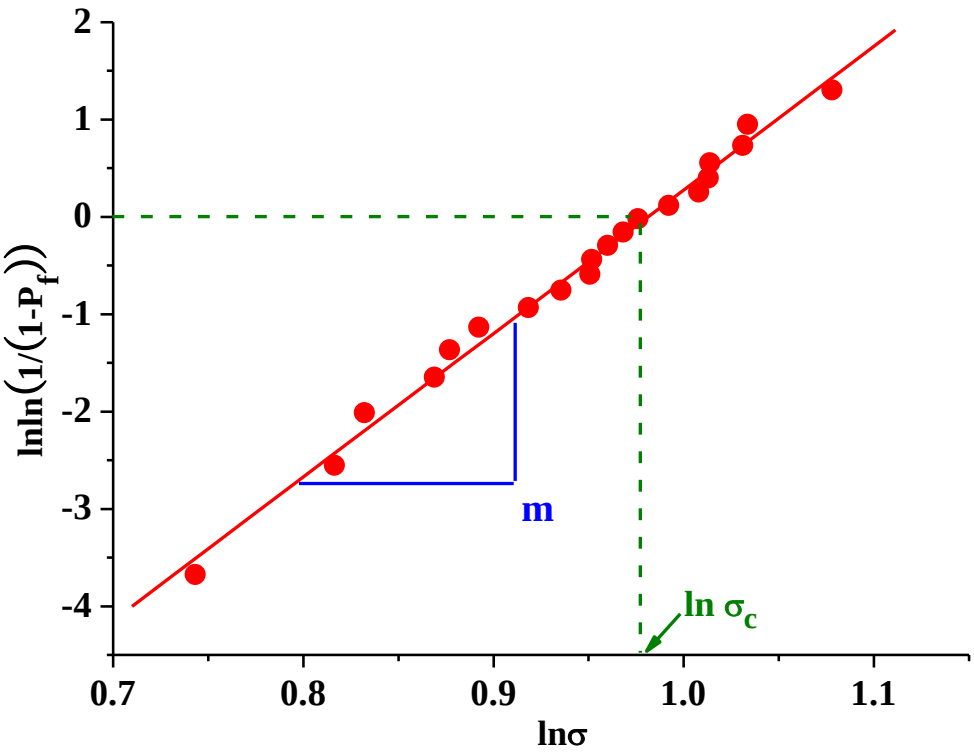

Figure 3.4. An example of the Weibull plot. The slope of the linear least-squares fit, m, is the Weibull modulus. The characteristic strength, σ_c, can be calculated from the least-squares fit at $\ln\ln(1/(1- P_f)) = 0$.

$$P_f = 1 - \exp\left[-\left(\frac{\sigma}{\sigma_c}\right)^m\right] \quad (3)$$

By taking the double logarithm of equation (3), the two-parameter Weibull equation can be rewritten as

$$\ln\ln\left(\frac{1}{1-P_f}\right) = m\ln\sigma - m\ln\sigma_c \quad (4)$$

To determine the Weibull modulus of a group of specimens (all specimens have the same volume and are tested under identical conditions), the fracture strength of each specimen are ranked in order, starting from the lowest to the highest. If we assign 'i' as the rank order for each specimen and 'N' is the total number of the specimens in the group, and then the cumulative probability of failure, P_f , can be expressed as (i – 0.5)/N. Plotting $\ln\ln(1/(1 - P_f))$ versus $\ln\sigma$ will result in a straight line with the slope m, given that the data follow Weibull distribution (Figure 3.4). The characteristic strength, σ_c, can be calculated from the least-squares fit at $\ln\ln(1/(1- P_f)) = 0$. At characteristic strength, σ_c, the value of P_f is 0.63, which means 63% of specimens will fail at σ_c.

4. Microstructural examination

Microstructural examination of specimens was conducted via scanning electron microscopy (SEM) (JEOL 6400V, JEOL Corp. Japan or Carl Zeiss Microscopy, LLC, Thornwood, NY) on selected surfaces of selected specimens, including fractured surfaces, polished surfaces, thermally etched surfaces and indented surfaces. Prior to examination, a gold coating was sputtered on the examined surfaces of non-conductive specimens using a

gold sputter (EMSSCOPE SC500, Ashford, Kent, UK) to enhance electrical conductivity. An accelerating voltage of 15 – 20 kV and a working distance of 5 - 15 mm were used.

Thermal etching was done on polished specimens by heating at temperatures 100^{o}C below the sintering temperatures for 1 hour in an electrical resistance furnace (CM Inc., Model #0100277, Bloomfield, NJ). The small grooves appearing at the grain boundaries are due to surface diffusion.

The grain size was determined using the linear-intercept method. Multiple straight lines were randomly superimposed over the SEM micrograph. Approximately 200 intercepts of the lines and the grain boundaries were counted. Grain size was obtained via dividing the true line length by the number of intercepts. A stereographic projection factor of 1.5 was used in the mean grain size calculation [Case 1981, Underwood 1968].

5. Elastic modulus measurements

There are many techniques in the literature to measure the elastic moduli [Wachtman 2009, Radovic 2004]. Basically, the techniques can be categorized into two groups: the static methods and the dynamic methods.

Static methods are based on the direct measurements of the stress – strain curve during mechanical testing (tensile, compressive, flexural) [Wachtman 2009]. Then the elastic moduli are determined from the slope of the linear part on the stress – strain curve. The disadvantages of the stress – strain curve method include (i) a required specimen shape and dimension, (ii) required careful surface processing, (iii) relative poor precision compared to dynamic methods [Radovic 2004].

Another widely used static method is the nanoindentation technique [Oliver 2004]. The elastic moduli can be determined from the slope of the linear unloading part of the load –

displacement curve. High precision can be achieved on well-prepared, relatively hard specimens with homogenous microstructure [Radovic 2004]. However, the pre-obtained Poisson's ratio value is required in the Young's modulus calculation using nanoindentation, which poses a difficulty that either the Poisson's ratio value is not accessible or the value is not accurate.

Dynamic methods can also be categorized into two groups: the pulse methods [Rogers 2000] and the resonance methods [Migliori 1996, 2005]. Dynamic methods possess remarkable merits compared to the static methods, with the advantages of minimum specimen preparation, ease of specimen shapes and sizes, and high precision.

Pulse methods are based on the relationship between the sound velocities traveling in a material and the elastic constants of the material [Rogers 2000]. By measuring the transit time for longitudinal and transversal ultrasonic waves along with the dimensions and mass of the specimens, the elastic moduli can then be calculated. The elastic moduli determined this way are in a given direction or set of directions.

To date, the resonant ultrasound spectroscopy (RUS) method has been considered a very good method for measuring the elastic moduli. In principle, the specimen is excited by a range of driving frequencies, and the natural resonant vibrations of the specimen are recorded. The entire matrix of elastic constants can then be determined with high precision from the single resonant frequency spectrum.

RUS has been successfully used to measure the elastic moduli for a number of materials including single-crystals [Yoneda 2012], polycrystalline bulk metals [Hurley 2010, Kaplan 2009], ceramics [Ren 2009, Seiner 2012], composites [Gorsse 2003, Vdovychenko 2006] and thin film materials [Nakamura 2010b, Tan 2010].

The application of RUS method requires some experience. Some aspects need to be considered during RUS analysis. First, an initial guess of the elastic moduli is required to ensure converge in the final solution. A close initial guess can be made by reference of similar materials in the literature, and the initial guess can be modified based on the shift between measured frequency peaks and predicted frequency peaks. Another concern lies in the accuracy of the specimen dimensions. Since the calculation of the mechanical vibration modes is based on the geometry of the specimens (in this study, either disk-shaped or bar-shaped), it is of great importance to cut and polish the specimen as close to a perfect disk or bar shape.

In this study, the Young's, shear, bulk modulus and Poisson's ratio of the specimens were measured by RUS (RUSpec, Quasar International, Albuquerque, NM, USA). Two types of configuration were used, namely, the three-transducer configuration (Figure 3.5a) mainly used for disk-shaped specimens and the two-transducer configuration (Figure 3.5b) for bar-shaped specimens. For the three-transducer configuration, a disk-shaped specimen was places on the tripod, where one piezoelectric transducer emits an ultrasonic signal through a range of frequencies, while the other two piezoelectric transducers pick up and record the mechanical resonance peaks of the specimen as a function of frequency (Figure 3.5a). For the two-transducer configuration, the body diagonal or the face diagonal of the bar-shaped specimen was lined up and held between the two piezoelectric transducers, where one transducer excites and the other being the pick up transducer. The two transducers are spring loaded, which allow free vibration of the specimen (Figure 3.5b).

In each measurement, about 30 to 50 sharp mechanical resonant peaks were recorded for analysis (Figure 3.6). After each measurement, the specimen was rotated a small angle on the

(a)

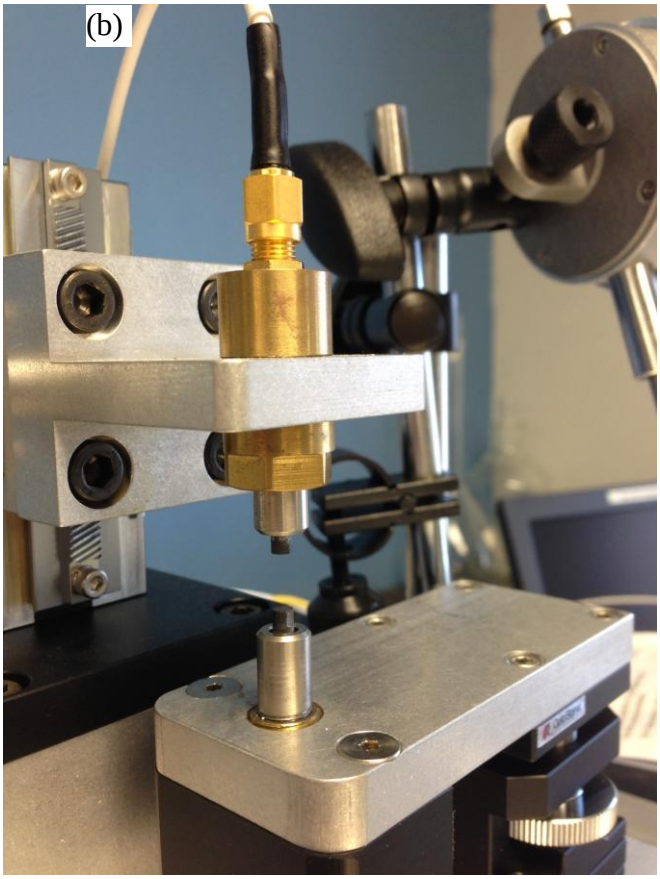

Figure 3.5. Digital images of (a) three-transducer configuration and (b) two-transducer configuration of the RUS apparatus.

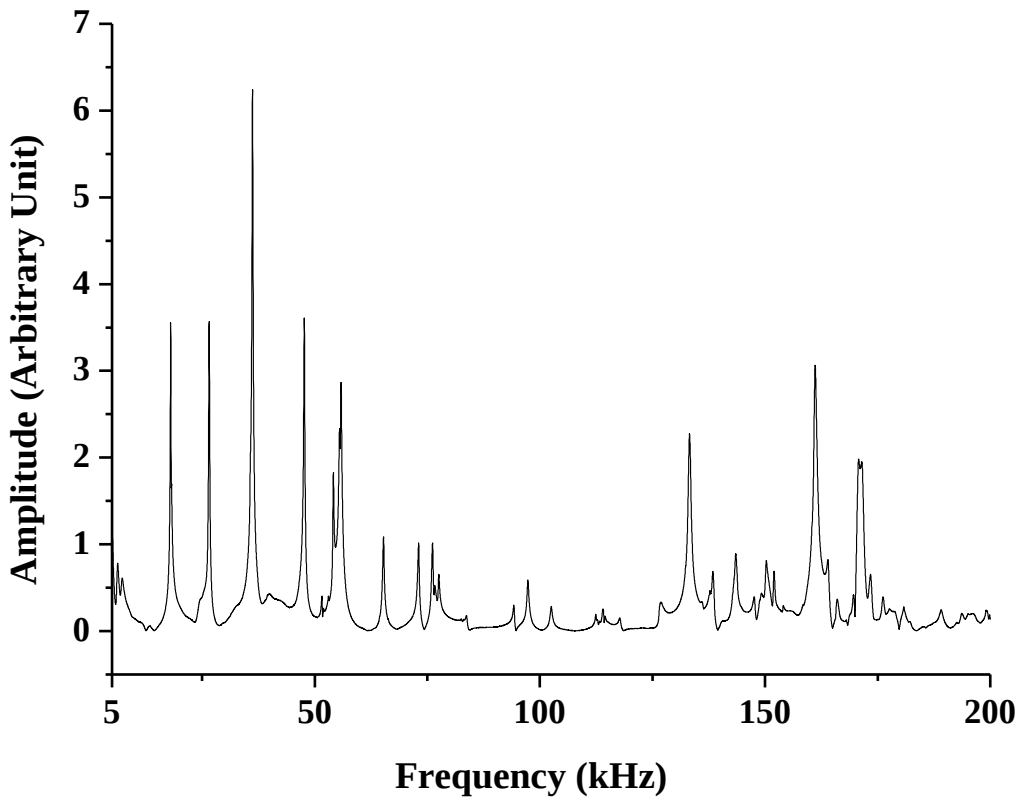

Figure 3.6. A typical RUS spectrum.

tripod or held along another face/body diagonal on the two-transducer configuration before another measurement was performed. The purpose of doing so is to detect possible missing vibrational modes due to the placement of the transducers at the vibration antinode. For disk-shaped specimens, some vibration frequency peaks are degenerate due to the geometric symmetry of the specimens.

The elastic stiffness tensor was then calculated using the resonant frequencies along with the mass, geometry and dimensions of the specimen. For all the specimens discussed in this dissertation, they are polycrystalline solids with randomly oriented grains, which implies isotropic elastic behavior (two independent elastic constants). The independent elastic constants were calculated via a commercial software (RPModel, Quasar International, Albuquerque, NM, USA) that performs an algorithm using a weighted error minimization between the initial input and calculated resonance frequencies until it is converged. The program also generated the root mean square (RMS) error of the fit, and only measurements with RMS error less than 0.5 % were used to ensure a relative accurate calculation.

6. Hardness and fracture toughness measurements

Both the hardness, H, and the fracture toughness, K_C, were measured using the Vickers indentation technique. Vickers indentation is a non-destructive technique that requires minimum sample preparation, and has been widely used in hardness and fracture toughness evaluation [Barsoum 1997, Quinn 1997]. A diamond indenter, with square-based pyramid shape was applied.

Hardness shows a material's resistance to plastic deformation. The hardness measured by Vickers indentation can be calculated from the following relationship [Wachtman 2009]

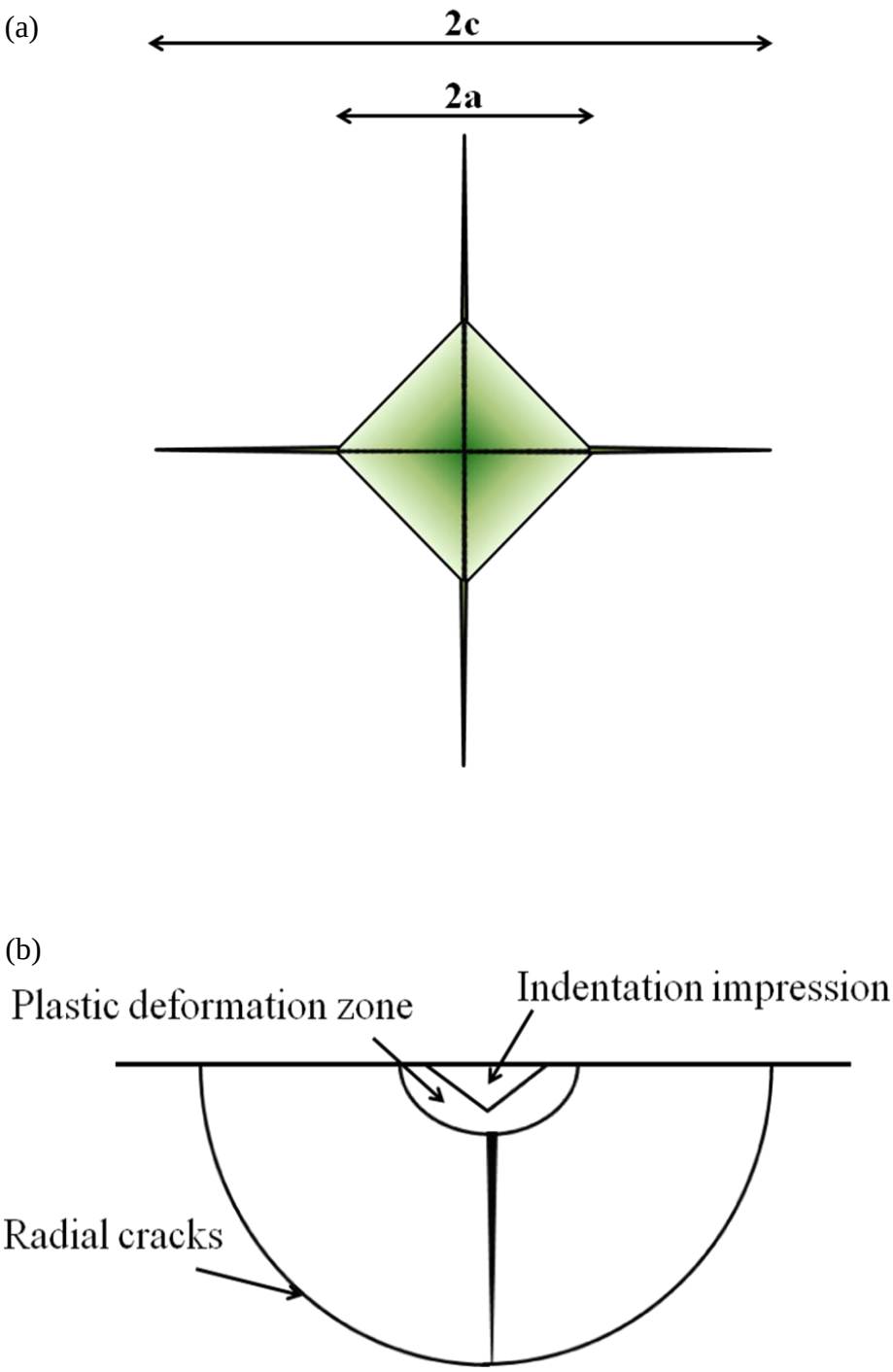

Figure 3.7. Diagram of the Vickers indentation impression and radial cracks system, (a) viewed on top; (b) viewed by side.

$$H = \zeta \frac{1.8544 P_L}{(2a)^2} \quad (5)$$

where P_L is the indentation load, ζ is the calibration factor and $2a$ is the diagonal length of the indentation impression (Figures 3.7a and 3.7b).

In this study, a Vickers indenter (Shimadzu HMV 2000, Kyoto, Japan) with load range from 5 g to 2000 g was used. Each hardness value was calculated from the average of 10 indentations. The Vickers indenter was calibrated using a HV 790 steel standard calibration block (Yamamoto Scientific Tools Lab Co. LTD, Chiba, Japan). The calibration factors, ζ, were determined from the average hardness value obtained from ten indentations on the calibration block for each load.

In brittle materials, the residual stresses during the indentation will cause the formation of the semi-elliptical cracks [Lube 2001], known as radial cracks (Figures 3.7a and 3.7b). Using the crack length, the fracture toughness can be estimated via the Vickers indentation technique using equation (6) [Anstis 1981]

$$K_C = \delta \left(\frac{E}{H} \right)^{1/2} \frac{P_L}{c^{3/2}} \quad (6)$$

where E is the Young's modulus determined from RUS, H is the hardness calculated from equation (5), P_L is the indentation load and 2c is the radial crack length (Figures 3.7a and 3.7b) and the calibration constant, δ, $\delta = 0.016$ [Anstis 1981].

REFERENCES

REFERENCES

[Anstis 1981] G.R. Anstis, P. Chantikul, B.R. Lawn, D.B. Marshall, A critical evaluation of indentation techniques for measuring fracture toughness: I, direct crack measurements, J. Am. Ceram. Soc. 64, 533-538, 1981.

[ASTM 2003] ASTM C1499-05, Standard test method for monotonic equibiaxial flexural strength of advanced ceramics at ambient temperature, 2003.

[Barsoum 1997] M.W. Barsoum, Fundamentals of Ceramics, The McGraw – Hill Companies, Inc., New York, 1997.

[Case 1981] E.D. Case, J.R. Smyth, V. Monthei, Grain-size determinations, J. Am. Ceram. Soc. 64, C24 – C25, 1984.

[Chao 1992] L.Y. Chao, D.K. Shetty, Extreme-value statistics analysis of fracture strengths of a sintered silicon-nitride failing from pores, J. Am.Ceram. Soc. 75, 2116-2124, 1992.

[Cordell 2009] J.M. Cordell, M.L. Vogl, A.J.W. Johnson, The influence of micropore size on the mechanical properties of bulk hydroxyapatite and hydroxyapatite scaffolds, J. Mech. Behav. Biomed. 2, 560-570, 2009.

[CRC 2009] CRC Handbook of Chemistry and Physics, 90th ed., CRC press, four-55, 2009.

[Gorsse 2003] S. Gorsse, D.B. Miracle, Mechanical properties of Ti-6Al-4V/TiB composites with randomly oriented and aligned TiB reinforcements, Acta Mater. 51, 2427-2442, 2003.

[Hirosaki 1993] N. Hirosaki, Y. Akimune, M. Mitomo, Effect of grain growth of β-silicon nitride on strength, weibull modulus, and fracture toughness, J. Am. Ceram. Soc., 76, 1892–1894, 1993.

[Hurley 2010] D.H. Hurley, S.J. Reese, S.K. Park, Z. Utegulov, J.R. Kennedy, K.L. Telschow, In situ laser-based resonant ultrasound measurements of microstructure mediated mechanical property evolution, J. Appl. Phys. 107, 063510, 2010.

[Kaplan 2009] G. Kaplan, T.W. Darling, K.R. McCall, Resonant ultrasound spectroscopy and homogeneity in polycrystals, Ultrasonics 49, 139-142, 2009.

[Lube 2001] T. Lube, Indentation crack profiles in silicon nitride, J. Eur. Ceram. Soc. 21, 211–218, 2001.

[Migliori 1996] A. Migliori, T. W. Darling, Resonant ultrasound spectroscopy for materials studies and non-destructive testing, Ultrasonics 34, 473-476, 1996.

[Migliori 2005] A. Migliori, J. D. Maynard, Implementation of a modern resonant ultrasound spectroscopy system for the measurement of the elastic moduli of small solid specimens, Rev.

Sci. Instrum. 76, 121301, 2005.

[Nakamura 2010a] Y. Nakamura, S. Hojo, H. Sato, The effect of surface roughness on the Weibull distribution of porcelain strength, Dent. Mater. J. 29, 30-34, 2010.

[Nakamura 2010b] N. Nakamura, T. Nakashima, H. Ogi, M. Hirao, M. Nishiyama, Fast recovery of elastic constant in thin films studied by resonant-ultrasound spectroscopy, J. Appl. Phys. 107, 103541, 2010.

[Oliver 2004] W.C. Oliver, G.M. Pharr, Measurement of hardness and elastic modulus by instrumented indentation: Advances in understanding and refinements to methodology, J. Mater. Res., 19, 3-20, 2004.

[Quinn 1997] J.B. Quinn, G.D. Quinn, Indentation brittleness of ceramics: a fresh approach, J. Mater. Sci. 32, 4331 – 4346, 1997.

[Radovic 2004] M. Radovic, E. Lara-Curzio, L. Riester, Comparison of different experimental techniques for determination of elastic properties of solids, Mater. Sci. Eng. A368, 56–70, 2004.

[Ren 2009] F. Ren, E.D. Case, A. Morrison, M. Tafesse, M.J. Baumann, Resonant ultrasound spectroscopy measurement of Young's modulus, shear modulus and Poisson's ratio as a function of porosity for alumina and hydroxyapatite, Phil. Mag. 89, 1163-1182, 2009.

[Rogers 2000] J.A. Rogers, A.A. Maznev, M.J. Banet, K.A. Nelson,Optical generation and characterization of acoustic waves in thin films: Fundamentals and applications, Annu. Rev. Mater. Sci. 30, 117-157, 2000.

[Seiner 2012] H. Seiner, P. Sedlak, L. Bodnarova, A. Kruisova, M. Landa, A. de Pablos, M. Belmonte, Sensitivity of the resonant ultrasound spectroscopy to weak gradients of elastic properties, J. Acoust. Soc. Am. 131, 3775-3785, 2012.

[Underwood 1968] E. E. Underwood, A. R. Colcord, R.C.,Waugh, in Ceramic Microstructures, R.M. Fulrath and J.A. Pask eds., John Wiley and Sons, New York, 1968.

[Vdovychenko 2006] O.V. Vdovychenko, V.S. Voropaev, A.N. Slipenyuk, Effect of microstructure on Young's Modulus of extruded Al-SiC composites studied by resonant ultrasound spectroscopy, J. Mat. Sci. 41, 8329-8338, 2006.

[Wachtman 2009] J. B. Wachtman, W. R. Cannon, M. J. Matthewson, Mechanical Properties of Ceramics, 2nd ed., Wiley Interscience, New York, 2009.

[Yoneda 2012] A. Yoneda, T. Cooray, A. Shatskiy, Single-crystal elasticity of stishovite: New experimental data obtained using high-frequency resonant ultrasound spectroscopy and a Gingham check structure model, Phys. Earth Planet. In. 190–191, 80–86, 2012.

[Zhan 1999] G-D Zhan, M. Mitomo, Microstructural control for strengthening of silicon carbide ceramics, J. Am. Ceram. Soc., 82, 2924–2926, 1999.

CHAPTER 4

POROSITY DEPENDENCE OF THE WEIBULL MODULUS FOR HYDROXYAPATITE AND OTHER BRITTLE MATERIALS

X. Fan, E. D. Case, F. Ren, Y. Shu and M. J. Baumann
Department of Chemical Engineering and Materials Science, Michigan State University, East Lansing, MI, 48824

Published in: J Mechanical Behavior of Biomedical Materials, 8:21-36, 2012.

Abstract

Porous brittle materials are used as filters, catalyst supports, solid oxide fuel cells and biomedical materials. However the literature on the Weibull modulus, m, versus volume fraction porosity, P, is extremely limited despite the importance of m as a gauge of mechanical reliability. In Part I of this study, m is determined for 441 sintered hydroxyapatite (HA) specimens fractured in biaxial flexure for $0.08 \leq P \leq 0.62$. In this study, we analyze a combined data set collected from literature that represents work from a total 17 different research groups (including the present authors), eight different materials and more than 1560 oxide and non-oxide specimens, the m versus P plot is "U - shaped" with a wide band of m values for $P < 0.1$ (Region I) and $P > 0.55$ (Region III), and a narrower band of m values in the intermediate porosity region of $0.1 < P < 0.55$ (Region II). The limited range of m ($\sim 4 < m < 11$) in Region II has important implications since Region II includes the P range for the majority of the applications of porous brittle materials. Part II of this study focuses on the P dependence of the mean fracture strength, $<\sigma_f>$, and the Young's modulus E for the HA

specimens tested in Part I along with literature data for other brittle materials. Both $<\sigma_f>$ and E are power law functions of the degree of densification, ϕ, where $\phi = 1 - P/P_G$ and P_G is the green (unfired) porosity.

1. Introduction

Most thermal, electrical and mechanical properties of solids are affected by porosity. For example, porosity affects thermal conductivity [Hu 2010a, Park 2009, Sulistyo 2010] and thermal diffusivity [Park 2009]. For electrical properties, the dielectric constant [Case 2006, Geis 2002, Hoepfner and Case 2002, Yang 2010], dielectric breakdown voltage [Geis 2002, Hench and West 1990], and electrical conductivity [Geis 2002, Shimizi 2009, Sulistyo 2010] are all functions of porosity. In terms of mechanical properties, the flexural fracture strength [Park 2009], compressive fracture strength [Hu and Wang 2010b, Nielsen 1990, Sammis and Ashby 1986], fracture surface energy [Vandeperre, 2004, Case and Smyth, 1981], Young's modulus [Ni 2009, Ren 2009], shear modulus [Ni 2009, Ren 2009] and hardness [Hoepfner and Case 2003] also are porosity dependent.

However, the literature data on the P dependence of the Weibull modulus, m, is quite limited, despite the fact that m is an important gauge of the mechanical reliability of brittle materials. While many studies in the literature evaluate m for brittle specimens with volume fraction porosities, P, of roughly 0.1 or less, few studies give Weibull modulus versus P results for $P > 0.1$ and the data is especially sparse for $P > 0.3$.

For a very wide range of brittle material applications, porosity is required for the

materials to function in the desired manner. In fact, for many applications of porous materials, P ranges from about 0.2 to 0.5 [Liu2010]. For engineered bone materials, porosity is required for the HA to mimic the function of natural bone [Baumann2008, Ren2005]. Other example of applications of porous HA include use as microbe filters [Yang 2007a, Yang 2007b], sensors [Mahabole2005, Nagai1988, Owada1989] and catalytic supports [Ohtsuki2010], where a number of these environmental, sensing and catalytic applications of porous HA [da Silva2006, Mori2003, Mori2004, Nishikawa 2003, Opre2005, Srinivasan2006, Venugopal and Scurrell 2003, Yin and Ellis 2010] are based on HA's ion exchange capabilities. In general, coatings and dielectric layers (both dense and porous) of HA also have been explored for biomedical and microwave applications [Hontsu1997, Silva2003, Silva2005], such as biocompatible coatings on implanted medical devices [Hontsu1997].

In addition to HA, porous brittle materials such as alumina, silica, mullite, zeolites and Ni-YSZ cermets also have been used for gas separation [Sommer and Melin 2005, Zeng2009], water filtration [Corneal2010, Karnik2005], heavy metal immobilization [Barba and Callejas 2006, Twigg and Richardson 2007], catalytic supports [Bein 1996, de Lange1995, Groschel 2005, Lambert and Gonzalez 1991] and anodes for solid oxide fuel cells (SOFC) [Jung2006].

This study is presented in two parts. Part I deals with the porosity dependence of the Weibull modulus, m, of brittle materials. Part II examines the average fracture strength, $<\sigma_f>$, and the Young's modulus, E, of brittle materials as functions of porosity. For both Part I and Part II, HA powders were sintered to achieve a range of volume fraction porosity, P, from P =

0.08 to P = 0.62. All HA specimens in the experimental phase of this study were fractured in biaxial flexure using a ring-on-ring (ROR) fixture.

The Weibull modulus, m, (Part I), the average fracture strength, $<\sigma_f>$ and Young's modulus, E, (Part II) were analyzed in conjunction with appropriate data from the literature. The number of HA specimens (n = 540) fractured in this study is more than twice the combined number of HA specimens in porosity-Weibull modulus studies previously reported in the literature.

Although individual m versus P studies in the literature were not as extensive (in terms of numbers of specimens fractured), this study analyzes literature data from 17 different research groups for eight different materials, including HA in this study, six literature studies of HA [Cordell2009, Meganck 2005, Murray1995, Lopes 1999, Ruys1995, Villora2004] as well as data from other oxides: zirconia (ZrO_2, [Pissenberger and Gritzner 1995]), titania (TiO_2, [Kishimoto 1991]), alumina (Al_2O_3, [Chao 1991], [Nanjangud 1995]) and mullite ($2SiO_2 \cdot 3Al_2O_3$, [Vales1999]) and non-oxides (silicon, [Borrero-Lopez2009], [Brodie and Bahr 2003], [Paul2006]), silicon nitride (Si_3N_4, [Hirosaki and Akimune 1993], [Vales1999]) and LASTT ($Ag_{0.9}Pb_9Sn_9Sb_{0.6}Te_{20}$ semiconducting thermoelectric materials, [Ren 2006]).

2. Experimental Procedure

2.1 Specimen preparation

All the hydroxyapatite (HA) specimens in this study were fabricated from biomedical grade commercial powder (Taihei Chemical Industrials Co., Osaka, Japan). The powder was uniaxially pressed into disk-shaped compacts at 33 MPa and then sintered in air from 550^{o}C

to 1360^{o}C from 12 minutes to 4 hours (Table 4.1). The specimen mass was measured using an electronic balance (Denver Instrument Company, Arvada, CO, with a vendor-specified precision of ±0.001 gram). For each specimen, three measurements of the specimen's diameter and thickness were made using digital caliper (Davis Calibration, Carol Stream, IL, with a vendor-specified precision of ±0.01 mm). The porosity of the sintered specimens (Table 4.1) was calculated from the specimen mass along with mean specimen diameter and thickness, assuming a theoretical density of 3.156 g/cm^{3} for HA [CRC 2009]. The current study includes 23 groups of HA specimens with volume fraction porosity, P, values ranging between approximately 0.08 and 0.62 (Table 4.1). From 20 to 24 specimens were prepared for each porosity group, yielding a total number of 540 specimens.

2.2 X-ray diffraction

To examine the phase purity of the HA specimens, X-ray diffraction (XRD) was performed on the as-received commercial powder as well as specimens sintered at 1100^{o}C for 2 h, 1200^{o}C for 1 h and 1360^{o}C for 4 h. Specimens sintered at 1360^{o}C were examined as both bulk and pulverized specimen. All XRD patterns were collected on a rotating anode diffractometer (Rigaku 20B, Rigaku Corp., Japan) using Cu K_{α} radiation between 10^{o} and 60^{o} 2θ with a step size of 0.02^{o}. Bulk specimens were scanned at a rate of 0.5^{o} 2θ per minute, whereas powder specimens were scanned at a rate of 2^{o} 2θ per minute.

2.3 Scanning electron microscopy

Microstructural examination was conducted on polished and thermally etched surfaces of HA specimens via scanning electron microscopy (SEM) (JEOL 6400V, JEOL Corp.

Table 4.1. For the disk-shaped HA specimens included in this study, the specimen label, sintering temperature, T, sintering time, the specimen dimensions, the volume fraction porosity P, the number of valid specimens N, the mean fracture strength $<\sigma_f>$, the characteristic strength σ_c, and the Weibull modulus m. Each specimen was cold die pressed at 33 MPa and sintered in air in an electrical resistance furnace.

Label	T (^{o}C)	Time (mins)	Thickness (mm)	Diameter (mm)	P	N	$<\sigma_f>$ (MPa)	σ_c (MPa)	m
P-08	1360	240	1.84±0.05	23.4±0.1	0.08±0.01	20	91±16	97±15	6.8
P-09	1350	120	1.85±0.02	23.8±0.1	0.33±0.01	18	62±5	63.6±4.9	15.0
P-13	1360	27	1.89±0.02	24.0±0.1	0.13±0.01	18	58±7	61±9	9.2
P-17	1360	12	1.92±0.01	24.3±0.1	0.17±0.01	24	69±10	74±8	8.4
P-21	1250	85	2.00±0.03	24.6±0.1	0.21±0.01	14	42±5	44.4±4.3	9.8
P-24	1220	60	1.92±0.02	25.2±0.2	0.24±0.01	15	39±8	42.2±8.2	6.1
P-30	1200	110	2.00±0.03	25.9±0.1	0.30±0.01	17	33±4	34.5±3.5	9.8
P-33	1200	60	2.09±0.03	26.2±0.1	0.33±0.01	18	33±4	35.2±4.0	8.8
P-36	1200	60	2.13±0.05	26.4±0.1	0.36±0.02	18	34±8	37.7±6.5	4.4
P-35	1200	30	2.03±0.04	26.8±0.2	0.35±0.01	12	29±4	31.3±3.9	7.5
P-39	1175	55	2.14±0.03	27.2±0.1	0.39±0.01	19	23±3	24.3±3.7	10.5
P-42	1150	40	2.08±0.02	28.1±0.2	0.42±0.01	19	22±3	22.7±3.0	9.4
P-46	1125	60	2.15±0.03	28.6±0.3	0.46±0.02	20	23±4	24.5±4.3	6.6
P-46	1100	120	2.19±0.02	28.4±0.1	0.46±0.01	20	17±2	17.3±1.9	11.5
P-51	1075	120	2.27±0.02	29.2±0.1	0.51±0.01	23	12±2	12.6±1.6	8.2
P-55	1050	120	2.32±0.03	30.1±0.1	0.55±0.01	21	8±1	8.4±1.0	9.5
P-60	1000	120	2.42±0.02	32.2±0.03	0.60±0.01	21	4.5±0.5	4.8±0.3	10.1
P-62	900	120	2.47±0.02	32.0±0.02	0.62±0.01	21	3.5±0.3	3.6±0.2	15.5
P-62	800	120	2.49±0.02	32.2±0.01	0.62±0.01	19	3.3±0.3	3.4±0.2	12.2
P-62	700	120	2.50±0.02	32.2±0.01	0.62±0.01	19	2.0±0.2	2.1±0.2	10.4
P-62	600	120	2.48±0.03	32.2±0.01	0.62±0.01	21	1.4±0.1	1.4±0.1	12.7
P-62	550	120	2.47±0.03	32.1±0.01	0.62±0.01	22	1.3±0.1	1.3±0.2	10.6
P-61	green	0	2.50±0.02	32.2±0.01	0.61±0.01	22	0.6±0.03	0.6±0.05	21.2

Japan). Thermal etching was done by heating the specimens in air in a conventional box furnace at temperatures 100^{o}C below the sintering temperatures for 1 hour. After thermal etching, a gold coating of approximately 20 nm thick was sputtered on the HA specimens using a gold sputter (EMSSCOPE SC500, Ashford, Kent, UK) before SEM examination. Each SEM image was taken using a working distance of 15 mm and an accelerating voltage of 15 kV. The grain size analysis was performed using the linear-intercept method. Multiple straight lines were randomly superimposed over the SEM micrographs and approximately 200 intercepts between the lines and the grain boundaries were counted to determine the mean grain size. A stereographic projection factor of 1.5 was used in the mean grain size calculation [Case1981, Underwood 1968].

Microstructural examination was also conducted on fracture surfaces of HA specimens via SEM using the same procedure described above.

2.4 Biaxial flexural testing

Biaxial flexural testing (BFT) was performed on a universal testing machine (Model 4206, Instron, Norwood, MA) using a ring-on-ring (ROR) test fixture [ASTM 2003]. The diameters of the loading ring and the supporting ring were 10 mm and 20 mm, respectively. In this study, each as-sintered specimen was fractured at a crosshead speed of 1 mm/min.

3. Results and Discussion

3.1 Phase analysis for the HA specimens in this study

The XRD patterns for the initial HA powder as well as bulk specimens sintered at

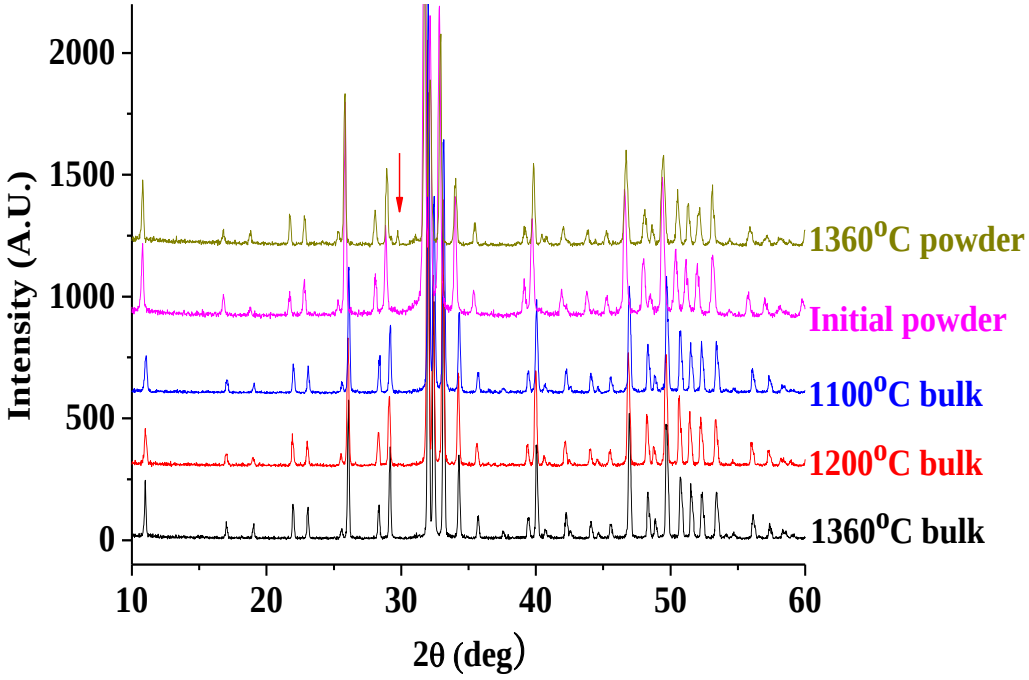

Figure 4.1. XRD patterns of the initial commercial HA powder and HA specimens sintered at 1100°C, 1200°C and 1360°C, where the arrow above the XRD pattern marks the position of the faint peak associated with β - TCP in the XRD pattern for initial powders. (A.U. stands for arbitrary units).

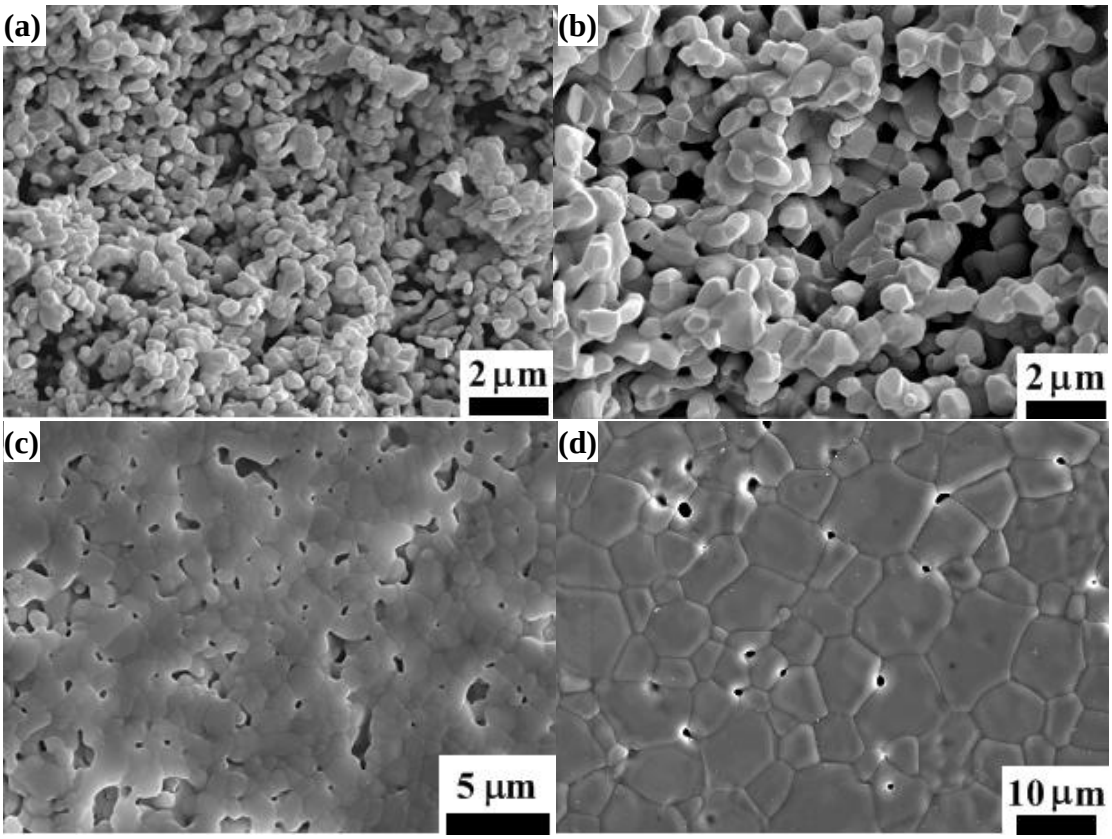

Figure 4.2. SEM micrographs of (a) fracture surfaces for HA specimens with porosity of 0.42; (b) fracture surfaces for HA specimens with porosity of 0.30; (c) polished and thermally etched surfaces for HA specimens with porosity of 0.24 and (d) polished and thermally etched surfaces for HA specimens with porosity of 0.08.

1100^{o}C, 1200^{o}C and 1360^{o}C showed no detectible secondary phases (Figure 4.1). The XRD pattern of specimens sintered at 1360^{o}C and ground into powder showed a faint peak at 2θ ~ 31^{o} (indicated by the arrow in Figure 4.1). This additional peak is likely associated with β-tricalcium phosphate (β-TCP), where β-TCP is one of the minor products of the decomposition of HA at high temperature [Sueter 1972].

3.2 Microstructural evolution of HA specimens included in this study

In general, during solid state sintering of powder compacts, the pore size and morphology evolves through three stages: (1) an initial stage when necks start to form and grow between powder particles, (2) an intermediate stage where tubular pores appear along the grain boundaries and (3) a final stage at which the tubular pores break up into isolated quasi-spherical pores typically located at the triple points of grains [Barsoum 1997, German 1996].

This typical microstructural evolution was observed for the HA powders sintered in this study (Figures 4.2a –4.2d). At P = 0.42, during the initial sintering stage (Figure 4.2a), the powder particles begin to neck and an open network of pores is present. At P = 0.30, when the sintering was between the initial stage and the intermediate stage (Figure 4.2b), a relatively open pore network still exists between particles. During the intermediate sintering stage, not only the most densification occurred, but also the pore size, number density of pores, and pore morphology underwent significant changes. At P = 0.24, tubular pores were observed along the grain boundaries (Figure 4.2c), which corresponds to the intermediate sintering stage [Barsoum 1997, German 1996]. In the final sintering stage, isolated spherical

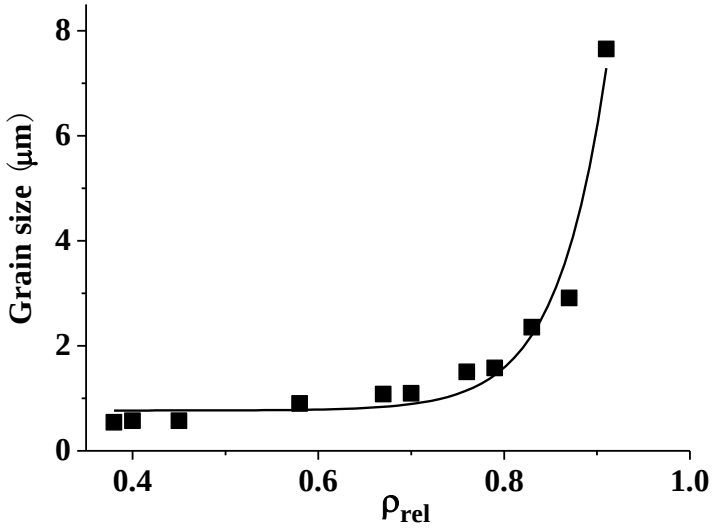

Figure 4.3. Grain size versus relative density, ρ_{rel}, trajectory for HA specimens included in this study, representing eleven values of ρ_{rel} ranging from 0.38 to 0.91.

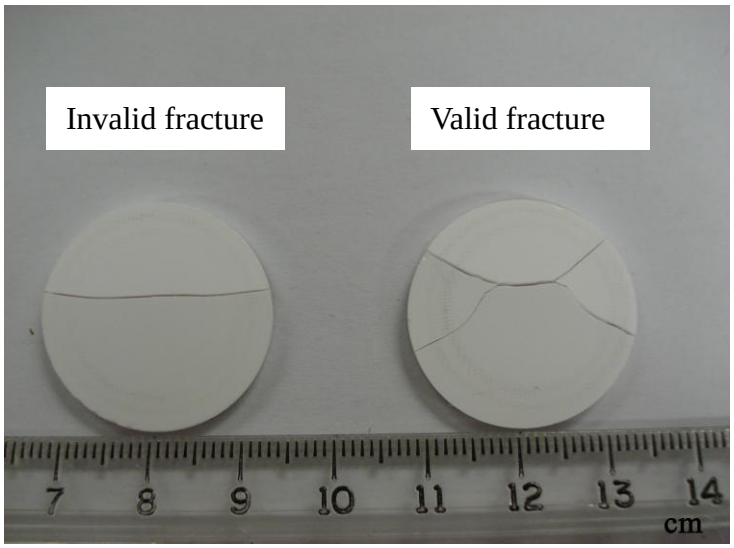

Figure 4.4. Digital photographs of specimens showing valid and invalid fracture patterns for HA specimens fractured via biaxial flexure (the ring-on-ring technique) in this study. "Valid" and "invalid" are defined in ASTM C1499-05 [ASTM 2003], where invalid ring-on-ring fractures involve failure from edge flaws.

or quasi-spherical pores were observed at grain boundaries or within grains (Figure 4.2d), while the porosity decreased to 0.08.

The grain size versus density trajectory of the HA specimens showed a typical behavior [Barsoum 1997, Berry and Harmer 1986], with limited grain growth for specimens with relative densities less than about 0.8 to 0.9 (Figure 4.3). In this study, the grain size measurements (Figure 4.3) covered the entire P range of 0.09 to 0.62, which corresponds to the relative density, ρ_{rel}, range of 0.91 – 0.38. For ρ_{rel} values between approximately 0.38 and 0.8, the grain size slowly increases from about 0.5 μm to 1.5 μm (Figure 4.3), and this density range includes 19 out of the 23 sets of specimens included in this study (Table 4.1). Thus, for about 85 percent of the HA data in this study, the grain size of the specimens is within the relatively restricted range from 0.5 μm to 1.5 μm.

3.3 Measurement of the Weibull modulus for the HA specimens in this study

For the 23 groups of HA specimens in this study (Table 4.1), a total number of 540 disks, tested using the ROR configuration [ASTM 2003], yielded 441 valid tests (Figure 4.4). According to ASTM C1499-05 [ASTM 2003], fractures that initiated from the specimen edges and extended diametrally across the specimen (Figure 4.4) were invalid and were not included in the strength calculations in this study. Figure 4.4 also gives an example of a valid ROR fracture pattern [ASTM 2003].

A two-parameter Weibull analysis was applied to the fracture strength data in this study using the following equation

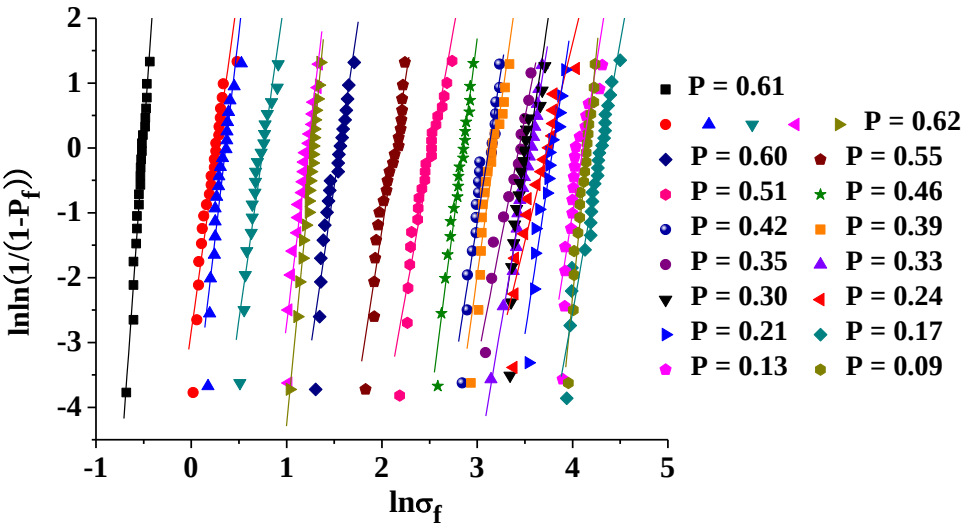

Figure 4.5. For the HA specimens fractured by biaxial flexure in this study, the Weibull plots (equation (1)) for each of the HA groups, where each group had a different volume fraction porosity, P. (Table 4.1 lists the P values of each group of specimens in this study).

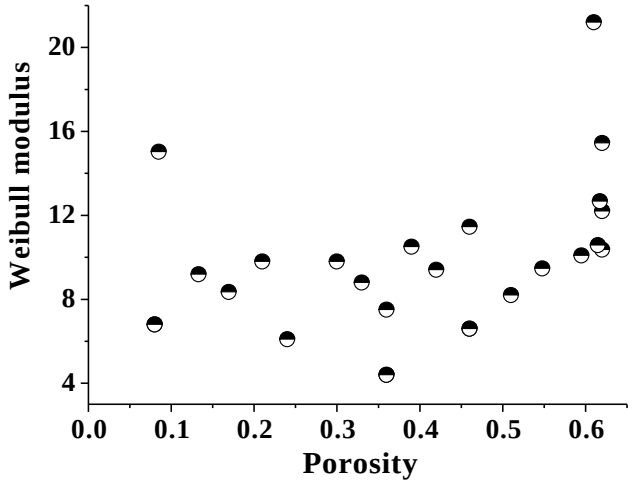

Figure 4.6. Weibull modulus as a function of volume fraction porosity, P, for the HA specimens in this study. (The numbers in parentheses indicate the total number of specimens fractured in a given study).

$$\ln\ln\left(\frac{1}{1-P_f}\right) = m\ln\sigma_f - m\ln\sigma_c \quad (1)$$

where P_f is the probability of failure, m is the Weibull modulus, σ_f is the fracture strength and σ_C is the characteristic strength [Wachtman 2009]. Weibull plots of the 23 groups of HA specimens are shown in Figure 4.5; while details of the Weibull analysis is given in Appendix A.

The average fracture strength, $<\sigma_f>$, the characteristic strength, σ_c, and the Weibull modulus, m, of the 23 groups of HA specimens were summarized in Table 4.1. Both $<\sigma_f>$ and σ_c decreased monotonically with increasing porosity (Table 4.1), while m varied from 4.4 to 21.2 (Figure 4.6). In Part II of this study, we discuss the porosity dependence of fracture strength and Young's modulus for the HA specimens included in this study along with other HA and non-HA specimens from the literature.

3.4 Porosity effect on Weibull modulus

3.4.1 Weibull modulus as a function of porosity for HA

In addition to the HA specimens sintered and fractured in this study, we used HA data from six other research groups [Cordell2009, Meganck 2005, Murray1995, of volume fraction porosity, P. Details of the materials, processing and testing of HA from literature are summarized in Table 4.2. It is worthwhile to note that the number of HA specimens fractured in this study is greater than the total number of specimens fractured in all six studies currently available in the literature [Cordell2009, Meganck 2005, Murray1995, Lopes 1999, Ruys1995, Villora2004].

Table 4.2. For the HA studies from the literature: shape forming techniques, specimen dimensions, grain size G.S., strength testing techniques, loading rate, surface finish, SF, number of specimens N, porosity P, the mean fracture strength $<\sigma_f>$, the characteristic strength σ_c and Weibull modulus m.

Ref.	Shape forming tech.	Specimen dimension	G.S. (μm)	Testing tech. & loading rate	SF	N	P	$<\sigma_f>$ (MPa)	σ_c (MPa)	m
Meganck	Cold Pressed	32 mm [b]	7.9	Piston-on-3 ball 0.5 mm/min	1 μm	10	0.02	130± 12	134.9 ±0.4	11.9
Lopes	Cold Pressed	25 x 2.5 mm [c]	N/S	Ring-on-ring 5 mm/min	N/S	12	0.12	~28	N/S	5.8
			0.9			12	0.07	~50		5.2
			1.2			12	0.05	~55		3
			2.4			12	0.06	~46	~ 50	5.6
Ruys	Cold Pressed	13 x 2 mm [c]	N/S	Ball-on-ring	5 μm	20	0.45	~28	N/S	6.9
						20	0.24	~73		7.9
						20	0.07	~80		6.5
						20	0.09	~55		3.4
Villora	Cold Pressed	8 x ~ 4 x ~8 mm	N/S	Diametr-al comp. 10 mm/min	d	28	0.42	35	39	3.7
	Extrusion					28	0.55	24	25	6
	Slip Cast					28	0.65	27	32	2
Cordell [a]	Cold pressed	~6.48 x 13 mm	N/S	Comp. Strain rate: 0.002 s^{-1}	15 μm	30	0.4	110± 18	118.2	5.8
						30	0.41	70.9± 8.8	73.9	8.7
	Extruded	3 x 4 x 45 mm bar		4-p bend Strain rate: 0.002 s^{-1}		30	0.46	21.8± 2.3	22.7	10.3
						30	0.46	18.6± 2.5	19.1	7.2
Murray	Uniaxial cold pressed	16.7 x 1.2 - 1.5 mm [c]	N/S	Standard shell test	d	15	0.28	69.7	N/S	7.6
						15	0.06	170.6		13.5

Table 4.2 (cont'd).

[a] In [Cordell 2009], PMMA spheres with diameters of 5.96 μm and 16.2 μm added to the powders burned out during sintering leaving large pores with diameters similar to the PMMA sphere diameters. This results in a bimodal pore size distribution. Specimens in the other references in this table have unimodal pore size distribution.

[b] Diameter of disc-shaped specimens

[c] Diameter and thickness of disc-shaped specimens

[d] As-fabricated

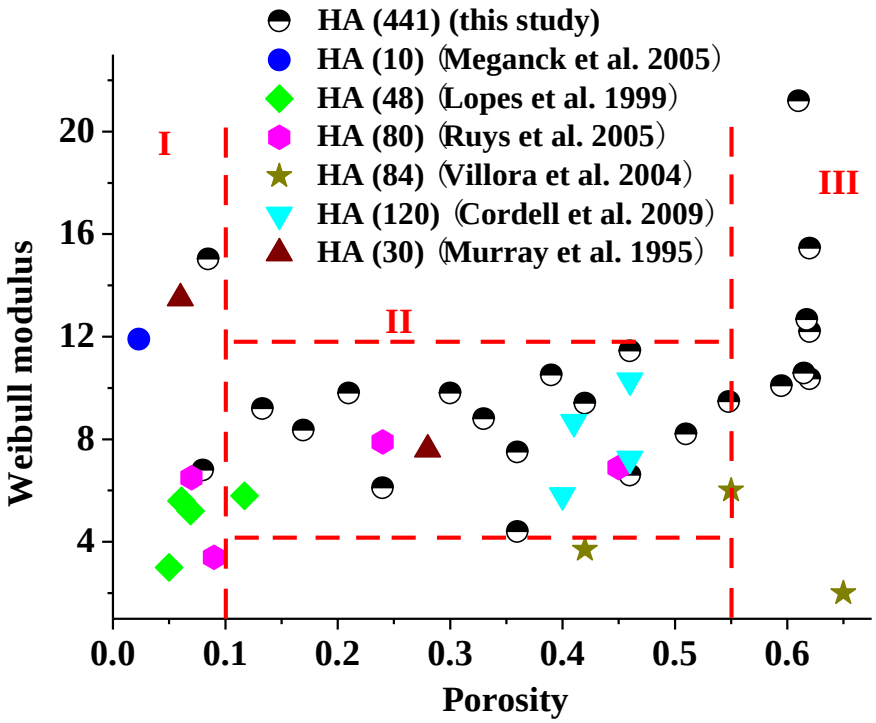

Figure 4.7. Weibull modulus as a function of P for HA (this study, Cordell2009, Meganck 2005, Murray1995, Lopes 1999, Ruys1995, Villora2004]. (The numbers in parentheses indicate the total number of specimens fractured in a given study).

For the HA data we can divide the m versus P behavior into three regions (Figure 4.7). In Region I ($P < 0.1$), there is considerable scatter in the m versus P data (Figure 4.7). In this study, for $P = 0.08$, the Weibull modulus was 15 while for $P = 0.08$, the Weibull modulus was 6. In region II ($0.1 < P < 0.55$), the m values fall into a relatively narrow band from ~ 4 to ~ 11. In region III ($P > 0.55$), m tends to increase with increasing P but there is scatter in the data especially near the green density P value of 0.62 (Table 4.1). For green (unfired) HA powder compacts, the Weibull modulus is as high as 21 (this study).

3.4.2 Weibull modulus as a function of porosity for HA from this study, HA from the literature and seven additional brittle materials from the literature

The combined data set includes the m versus P data for HA [this study, Cordell2009, Meganck 2005, Murray1995, Lopes 1999, Ruys1995, Villora2004] plus the m versus P data for other oxides (zirconia [Pissenberger and Gritzner 1995], titania [Kishimoto 1991], alumina [Chao 1991, Nanjangud 1995] and mullite [Vales1999]) and non-oxides (silicon [Borrero-Lopez2009, Brodie and Bahr 2003, Paul2006], silicon nitride [Hirosaki and Akimune 1993, Nanjangud 1995, Vales1999] and LAST-T semiconducting thermoelectric materials [Ren 2006]) from the literature (Figure 4.8). Details of the materials, processing and testing of the other oxides [Kishimoto 1991, Nanjangud 1995, Pissenberger and Gritzner 1995, Vales1999] and the non-oxides [Borrero-Lopez2009, Brodie and Bahr 2003, Hirosaki and Akimune 1993, Nanjangud 1995, Paul2006, Ren 2006, Vales1999] are summarized in Tables 4.3 and 4.4, respectively.

It is extremely important to note that for the combined data set, the mean fracture

strengths, $<\sigma_f>$, of the dense forms of these materials can differ from one another by up to more than a factor of 5. For example, the fracture strength for HA with P = 0.023 is 130 MPa [Meganck 2005] (Table 4.2), while the fracture strength of silicon nitride with P = 0.01 is 689 MPa [Hirosaki and Akimune 1993] (Table 4.4). Nevertheless, despite the large range in the $<\sigma_f>$ values, the m versus P values of the combined data set (Figure 4.8) are consistent with the trends observed for the HA (Figure 4.7). This underscores the fact that m versus porosity trends depicted in Figure 4.8 apply to an extremely diverse set of materials.

The Weibull modulus versus P data for the combined data set (Figure 4.8) shows a large scatter in region I (P < 0.1) and less scatter in region II (0.1 < P < 0.55). In Region II the band of m values between 4 and 11 includes data from this study (14 m values) as well as data from eight additional studies including four different materials: HA [Lopes one m value [Lopes 1999], Ruys two m values [Ruys1995], Villora one m value [Villora2004], Cordell four m values [Cordell2009], Murray one m value [Murray1995]), Nb and Ta doped zirconia (Pissenberger one m value [Pissenberger and Gritzner 1995]), titania (Kishimoto three m values [Kishimoto 1991]) and alumina (Nanjangud two m values [Nanjangud1995]). All of the m data for the non-oxides lies in Region I (P < 0.1) with m values ranging from ~ 2 to 53 (Figure 4.8).

The m versus P behavior observed in Region II and Region III (Figures 4.6 –4.8) has not been previously reported. For HA and other brittle materials, the m versus P data available in the literature for P > 0.47 is especially limited. The authors are only aware of two groups of Weibull modulus data for P > 0.47, namely specimens from the Villora HA study

Table 4.3. For the oxides other than HA from the literature: materials, shape forming techniques, specimen dimensions, grain size G.S., strength testing techniques, loading rate, surface finish, SF, number of specimens in each group N, porosity P, the mean fracture strength $<\sigma_f>$, the characteristic strength σ_c and Weibull modulus m.

Ref.	Materials and shape forming tech.	Specimen dimen.	G.S. (μm)	Testing tech. & loading rate	SF	N	P	$<\sigma_f>$ or σ_c (MPa)	m
Nanjangud	Commercial available alumina extruded bars	62 mm x 10 mm x 4 mm	N/S	4-p bend 25.4 mm/min	N/S	20 -30	0.38	25.9 [c]	8.4
							0.27	111.4 [c]	8.1
							0.08	262.7 [c]	9.3
							0.03	293.4 [c]	13
Kishimoto	Commercial titanium dioxide powders. Uniaxially Pressed	5 mm x 20 mm x 0.19 mm	1.1	3-p bend	N/S	34	0.4	63 [f]	8.4
			1			32	0.3	71 [f]	5.3
			1			21	0.2	129 [f]	5.7
			1			31	0.1	288 [f]	4.3
Pissenberger	Niobia and tantala doped zirconia. Isostatically pressed at 8 kPa	4 mm x 3 mm x 30 mm	N/S	3-p bend	d	N/S			
	10.0%, 0.0%, 1.99 μm [a]						0.24	48 [f]	4.9
	14.2%, 0.0%, 15.2 μm [a]						0.06	172 [f]	5.1
	18.0%, 0.0%, 1.91 μm [a]						0.1	126 [f]	5.2
	0.0%, 10.0%, 1.61 μm [a]						0.05	127 [f]	6.2

Table 4.3 (cont'd).

	0.0%, 14.2%, 1.89 μm [a]						0.02	173 [f]	10
	0.0%, 18.0%, 1.71 μm [a]						0.03	199 [f]	4.9
	10.0%, 0.0%, 0.38 μm [a]						0.05	184 [f]	5.9
	14.2%, 0.0%, 0.43 μm [a]						0.02	216 [f]	8.5
	18.0%, 0.0%, 0.44 μm [a]						0.01	194 [f]	9.2
	0.0%, 10.0%, 0.34 μm [a]						0.01	210 [f]	8.8
	0.0%, 14.2%, 0.47 μm [a]						0.01	224 [f]	14
	0.0%, 18.0%, 0.55 μm [a]						0.02	217 [f]	14
Vales	Commercial mullite	45x4x3 mm	~ 5	4-p bend 5 mm/min	d	20	0.075	N/S	13
Chao	Commercial-grade sintered alumina	45x4x3 mm	6	3-p bend	d	~33	~ 0.07	385.9 [c]	5.4
		45x4x3 mm		4-p bend				353.4 [c]	3.8
		50.8x 3.175 in [b]		Biaxial flexure				338.8 [c]	2.3

[a] Weight percentage of doped niobia and tantala, particle size

[b] Diameter and thickness of disc-shaped specimens

[c] The characteristic strength σ_c

[d] Polished

[f] The mean fracture strength $\langle\sigma_f\rangle$

[Villora2004] (representing 56 fractured specimens) and data for nine groups of specimens from this study (representing 189 fractured specimens). If one extends the P range out to Region III ($P > 0.55$), then only a single m value from Villora's study [Villora2004] remains. However, Villora's specimens are multiphase specimens of HA and SiO_2 that also include animal bones, waste diatom filters and paper industrial sludge [Villora2004]. Thus, while the other porous brittle materials analyzed in this study consisted of partially sintered single phase materials (this study, Borrero-Lopez2009, Brodie and Bahr 2003, Chao 1991, Cordell2009, Hirosaki and Akimune 1993, Kishimoto 1991, Lopes 1999, Meganck 2005, Murray1995, Nanjangud1995, Paul2006, Pissenberger and Gritzner 1995, Ruys1995, Vales1999, Villora2004], Villora's specimens are in contrast quite heterogeneous. The multiphase nature of Villora's specimens could lead to microcracking which could also affect the flaw populations and hence the value of the Weibull modulus.

3.5 Physical interpretations of the three regions in the m versus P plots

A critical question here concerning the m versus P behavior shown in Figures 4.6 –4.8 is "What physical mechanisms may be responsible for the observed behaviors?" For the entire range of P in Figures 4.6 –4.8, the Weibull modulus behavior is almost certainly fundamentally linked to the evolution of the porosity during sintering as discussed briefly in Section 3.2. Given that, then what may be the particular links between the evolution of porosity and the m versus P behavior? It is important to note that if the Weibull modulus versus porosity data (Figure 4.8) were to be plotted for each material in isolation, there are too few data points to determine a trend.

Table 4.4. For the non-oxides other than HA from the literature: powder specification, shape forming techniques, specimen dimensions, grain size G.S., strength testing techniques, loading rate, surface finish, SF, number of specimens in each group N, porosity P, the mean fracture strength $<\sigma_f>$, the characteristic strength σ_c and Weibull modulus m.

Ref.	Materials and shape forming tech.	Specimen dimen.	G.S.	Testing tech. & loading rate	SF	N	P	$<\sigma_f>$ or σ_c (MPa)	m
Borrero-Lopez	Poly-silicon wafer. Cut from commercial wafer	12.5 cm x 12.5 cm x 199±4 μm	Tens of mm	Twist test 5 mm / min	As-cut	30	~0	131[f]	14.4
				4-p bend 5 mm / min		30	~0	76[f]	1.6
								161.2[f]	11.5
Ren	$Ag_{0.9}Pb_9Sn_9$ -$Sb_{0.6}Te_{20}$ Cast	22 mm x 3 mm[a]	700 μm	Ball-on-ring 0.5 mm / min	1 μm	15	~ 0.01	~15[f] 15.3[c]	3.2
Chao	Commercial-grade silicon nitride	45 x 4 x 3.175 mm	N/S	4-p bend	600 grit	30	~ 0.09	768.5[c]	10.1
		34 x 4 x 3.175 mm		3-p bend				908.1[c]	15.7
		50.8 mm x3.17 mm[a]		Biaxial flexure				717.1[c]	12.0

Table 4.4 (cont'd).

Hirosaki	β-Si_3N_4 powder Die pressed at 20 MPa, isostatically pressed at 200 MPa	6 x 6 x 50 mm	Matrix 0.2-2 x 1-5 μm[a] Elongated grains 2-20 x10-300 μm[a]	3-p bend 0.5 mm / s	800 grit	15	~ 0.01	689 [f]	53
						15	~ 0.01	599 [f]	25
						15	~ 0.01	515 [f]	19
Paul	(100) p-type silicon wafer	5 x 10 mm x 525 μm	Single crystal	3-p bend	N/S	25	0	247 [c]	3.5
		5 x 10 mm x 250 μm						435 [c]	2.5
		5 x 10 mm x 100μm						648 [c]	4.5
		5 x 10 mm x 50μm						726 [c]	4.5
Vales	Si_3N_4 with ~ 4 % residual Si	45 x 4 x 3 mm	Acicular, 1 to 5 μm	4-p bend 5 mm / min	Polis-hed	20	0.037	N/S	7

Table 4.4 (cont'd).

Brodie	Commercial bulk poly-silicon, Chemical vapor deposition	24.6 mm x ~ 5 mm[a]	1 x 10[b]	Tension test 0.01 mm/s	N/S	20	0	N/S	7.1
			3 x 15[b]						6.1
			2 x 10[b]						4.8
			2 x 10[b]						5.0
			3 x 15[b]						6.9
			5 x 30[b]						4.8
			~ 3						6.7
			5 – 20[b]						8.0

[a] Diameter and thickness of disc-shaped specimens

[b] The grain aspect ratios (relative lengths minor axis X major axis) listed for the elongated grains in specimens

[c] The characteristic strength σ_c

[f] The mean fracture strength $\langle\sigma_f\rangle$

In this discussion, we begin with Region II since it plays a key role in the m versus P behavior and since it's important to many of the applications of brittle, porous materials

3.5.1 Region II

Region II ($0.1 < P < 0.55$, Figures 4.6 - 4.8) is important in several ways. First, the P range from roughly 0.2 to 0.5 includes the P values that are employed in most applications of porous brittle materials, including filters, SOFC, catalyst supports and biomedical materials [Liu 2010].

Also, the details of the m versus P behavior of m in Region II reveal phenomena that have not been discussed earlier in the limited m versus P literature. In particular, the combined data set depicted in Figure 4.8 includes a total of 32 m values: 14 m values for HA [this study], 10 m values for other HA studies, and 8 values for three other oxides, namely zirconia, titania and alumina (Table 4.5). In contrast to Regions I and III, in Region II the m values occur in a relatively narrow band from about 4 to 11. The "banded" nature of the m versus P data in Region II is underscored by the fact that there are no statistically significant differences among <m>, the mean m values for each of the data groupings in Table 4.5. The statistical analysis was carried out using one-way ANOVA with $p < 0.03$ considered to be statistically significant.

Although there are no statistically significant differences in the <m> for Region II (Table 4.5 and Figure 4.8), we note that the processing, testing, and the materials themselves differ considerably (Tables 4.1 –4.4). For the HA specimens in this study (Table 4.1), the material, the material vendor, the initial powder particle size, the powder pressing technique, the

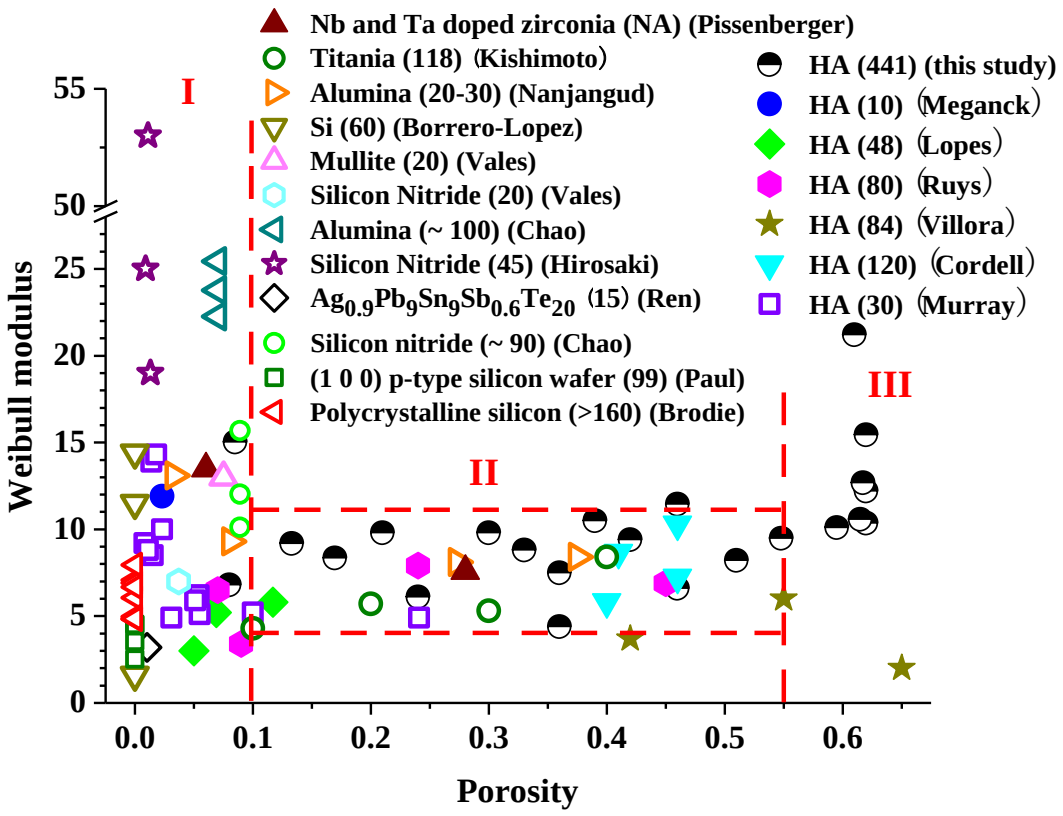

Figure 4.8. Combined data set for Weibull modulus as a function of P for HA [this study, Cordell2009, Meganck 2005, Murray1995, Lopes 1999, Ruys1995, Villora2004], oxides (alumina [Chao 1991, Nanjangud 1995], zirconia [Pissenberger and Gritzner 1995], titania [Kishimoto 1991], mullite [Vales1999]) and non-oxides (silicon [Borrero-Lopez2009, Brodie and Bahr 2003, Paul2006], silicon nitride [Hirosaki and Akimune 1993, Nanjangud 1995, Vales1999], LAST-T [Ren 2006]) from literature. (The numbers in parentheses indicate the total number of specimens fractured in a given study).

sintering furnace, the specimen geometry, testing machine and loading rate were all kept constant during the entire study, whereas in contrast for the other data in Region II (Table 4.5), many of these variables differed among the research groups (Tables 4.2 –4.4).

How then can we reconcile the banded nature of the Region II data despite differences in the materials, testing and processing, especially since in Appendix B we cite literature that demonstrates that m is in fact a function of the materials, testing and processing? First, as is true for the vast majority of the research involving m, the particular studies that focus on processing and testing effects on m (Appendix B) were performed almost entirely for specimens with $P < 0.1$ (Region I). Thus information for the effects of processing and testing on m is not currently available in the literature for specimens with P values within Regions II and III.

A second key point is that the universality in the m versus P behavior (manifest in the banded nature of Region II, Figure 4.8) may reflect the universality of microstructural evolution that occurs during the powder sintering process. This universality is consistent with the striking similarities among the microstructure evolution observed during sintering of many ceramic [Barsoum 1997] and metallic [German 1994, 1996] powders. In particular, during the intermediate stage of sintering (which roughly corresponds to Region II), tubular pores along grain boundaries evolve from the connected pore phase in Region III and toward isolated spherical pores in Region I [Barsoum 1997, German 1994, 1996]. Thus, the 3-dimensional arrangement of tubular pores associated with the intermediate sintering stage (and hence Region II) may overwhelm effects of processing and testing, including such

parameters as processing-induced surface flaws, along with the temporal (loading rate, for example) and spatial distributions of stress within the specimen. Therefore, the results seem to agree well with established theories of microstructural development in ceramics.

Also, in general a high m value (say, m > 20) indicates relatively little scatter in fracture strength while a low m value (for instance, m less than 3 or 4) indicates significant scatter in σ_f, which degrades mechanical reliability [Wachtman 2009]. Thus in particular, the banded nature of Region II ($4 < m < 11$) requires designers of such components to include high safety factors. Furthermore, the broad-ranging nature of the Region II database (Table 4.5), which includes HA data from this study, HA data from five additional literature studies and data for alumina, titania, and zirconia may indicate a difficulty in obtaining any brittle, porous material sintered from powdered compacts with Weibull moduli outside the range of $4 < m < 11$. However, m values between 2 and 4 have been reported for dense commercial silicon wafers [Borrero-Lopez2009, Paul2006], thus designers in the microelectronics industry have been able to produce serviceable products from brittle components that have even lower Weibull moduli than the porous, brittle materials in Region II.

3.5.2 Region I

In Region I, the m versus P behavior is dramatically different than the banded nature of Region II, since m is as large as 53 and as small as 2 for the data included in Region I (Figure 4.8). The spread in the m data in Region I is likely influenced by (i) the various processing and testing parameters discussed in Appendix B and (ii) defects such as surface scratches or cracks caused by grinding and cutting.

Table 4.5. For the m versus P data included in Region II (Figure 4.8), the number of m data points, m_N as well as the mean and standard deviation of m, <m> and m_{STD}, respectively. The data ranges defined by <m> $\pm$ m_{STD} overlap for every entry in the table, signifying that there are no statistically significant differences among <m> for the various data groupings listed in this table.

Material	m_N	<m>	m_{STD}	References
HA	14	8.55	1.88	This study
HA from other studies	10	6.99	1.82	Cordell2009, Lopes 1999, Murray1995, Ruys1995, Villora2004
Zirconia, titania, alumina	8	6.29	1.72	Zirconia [Pissenberger and Gritzner 1995], titania [Kishimoto 1991], alumina [Nanjangud1995]
All data, except HA from study	18	6.68	1.76	[a]
Entire data set in Region II	32	7.50	2.02	[b]

[a] The references include each of those listed in the table for the HA from other studies plus zirconia, titania and alumina.

[b] The references include each of those indicated in footnote [a] plus this study.

Thus for the relatively dense specimens in Region I ($P < 0.1$), surface cracks arising from processing (machining and cutting) rather than pores may be the dominant flaws although in Region II pores likely dominate the m versus P behavior (Section 3.5.1). Processing-induced flaws are not porosity dependent and are unpredictable from specimen to specimen, which coupled with the effects of differences in test and processing techniques (Tables 4.2 - 4.4) make the significant scatter of the Weibull modulus data in Region I reasonable.

3.5.3 Region III

Region III, where $P > 0.55$, corresponds to an initial sintering stage in which only limited interparticle necking occurs rather than densification. [Barsoum 1997, German 1996]. A relative uniformity in the dominate flaw distribution in Region III (the connected pore phase that permeates the space between the "necked" particles) could thus lead to less scatter in the fracture strength data itself and hence higher Weibull modulus values than the more anisotropic grain-edge, tubular pores that dominate the pore phase in much of Region II (intermediate sintering stage).

However, in contrast to Region II, where the m values fall between approximately 4 and 11 (Figure 4.8 and Table 4.5), in Region III the "band" of m values is from about 11 to 23 (Figure 4.8 and Table 4.1). The wider band of values of m values in Region III is likely related to powder processing issues such as the presence or absence of agglomerates. Furthermore, the mean fracture strength decreases monotonically as P increases (Table 4.1), again emphasizing the de-coupled nature of the mean strength (a measure of the center of the

strength distribution) and the Weibull modulus, which is a function of the dispersion in the individual strength values.

For Region III, it is important to note that except for one m value from a study of HA/SiO_2 composites by Villora [Villora2004], the current authors were unable to find in the literature Weibull modulus data for $P > 0.55$ for HA or any brittle material. Thus all but one of the m versus P data in Region III (Figure 4.8) was obtained from the HA specimens fractured in this study. The increase in m in Region III from the values observed in Region II is at first surprising, but one must recall that the average strength and m are in general decoupled.

The evolution of dominant flaws associated with the evolution of porosity between regions determines the observed m versus P behavior. In Region I, surface cracks developed during processing may be the dominant flaws. These porosity independent flaws coupled with the effects of differences in test and processing techniques lead to the significant scatter of the Weibull modulus data in Region I. In region II, the tubular pores along the grain boundaries likely overwhelm effects of processing and testing and become the dominant flaws. In Region III, the connected open pores result in a relative uniformly distributed flaws and thus higher Weibull modulus. In addition, pore clustering and pore anisotropy may have significant effects which could be the subject of future studies.

In contrast to the behavior of m versus P for the entire spectrum of P (Regions I, II and III), in Table 4.1 (and as will be discussed in far more detail in Part II of this paper), we observe that the average fracture strength and Young's modulus (Part II) decrease

monotonically with increasing P. For the HA specimens sintered and fractured in this study, the uniformity in the material, processing and testing of the HA specimens in Region III makes it unlikely that the parameters discussed in Appendix B are responsible for the relatively wide range of m values observed in this study. Also, as was the case for the specimens in Region II, no studies currently exist in the literature to indicate whether or not the studies on specimens from Region I (Appendix B) have any applicability to the m versus P behavior for specimens in Region III.

3.5.4 Transitions among the regions

The transition from Region I to Region II at $P \approx 0.1$ may be related to a change in fracture mode. For example, Flinn [Flinn 2000] found that for $0.15 < P < 0.40$ (where $P = 0.40$ was the highest P value in their study), the fracture mode for partially sintered alumina specimens was predominantly intergranular. However, for $P < 0.15$, the fraction of transgranular fracture increased as P decreased [Flinn 2000]. Thus the P value corresponding to the transition in fracture mode observed by Flinn [Flinn 2000] for their porous alumina specimens corresponds roughly to the P value for the transition from Region I to Region II behavior (Figures 4.7 and 4.8 in this study) Thus a change in fracture mode may be linked to the Region I – Region II boundary, although further study is needed to explore this concept.

At $P \sim 0.55$ there is a second transition in m versus P behavior, where the limited m range of Region II changes to the rapidly increasing m values of Region III (Figures 4.7 and 4.8). The Region II → Region III transition behavior may reflect the transition from the initial sintering stage (Region III) to the intermediate sintering stage (Region II). The change in

pore morphology may also be related to the fracture mode. Perhaps in the very high porosity ranges ($P > 0.55$), the fracture surfaces tend to be somewhat " rougher" than in Region II, which may lead to a return (in Region III) toward the higher m values that were characteristic of Region I. In the future, the authors plan to use confocal laser scanning microscopy (CLSM) to quantify the surface roughness of fracture surfaces over a broad range of P for the HA specimens fractured in this study.

Furthermore, in Part II we shall show that a single mathematical form involving a power law function of (1- P) describes both the fracture strength and elastic modulus as a function of P for P values extending from unfired powder compacts to near theoretical density. Thus, the current study involving the "U-shaped" behavior for m versus P in porous materials is in contrast to the behavior of both fracture strength and Young's modulus versus P (Part II). The overall scarcity of m versus P data in the literature is likely the reason that the Region II and Region III behavior has not been identified until now.

For the full data set, the demarcations between Regions I and II as well as between Regions II and III were determined by eye based on the trends shown in Figure 4.8. Future work could include determining a statistical or analytical basis for selecting values of P that demarcates the Regions I, II and III.

4. Summary and Conclusions

In this study, a total of 540 HA specimens were sintered and fractured. In addition, more than 1560 specimens data of HA, other oxides and non-oxides from the literature were compared and analyzed, making this study the most extensive Weibull modulus study in the

open literature (Figure 4.8). It should be emphasized that in Figure 4.8, the m versus P literature data is included from 17 different research groups for a total of 8 different materials.

A three-region, "U" shaped plot of m versus P data was observed for HA and a combined data set including HA, other oxides and non-oxides from the literature which shows a wide band of m values for Region I ($P < 0.1$) and Region III ($P > 0.55$), and a narrower band of m values in Region II ($0.1 < P < 0.55$) (Figure 4.8). Since Figure 4.8 includes HA data from this study as well as data for brittle oxides and non-oxides for 16 other research groups, this trend may hold for a wide range of brittle materials.

The experimental data from this study and eight other research groups with m versus P data in Region II (Figure 4.8) show that Weibull modulus values fall in the range between about 4 and 11 regardless of the composition, grain size, testing techniques or surface finish of the specimens. Thus, in Region II the Weibull moduli are likely not dominated by the processing and testing parameters discussed in Appendix B, since the specimens included in Region II (Figure 4.8, Table 4.5) do vary widely in terms of both processing and testing (Tables 4.2 and 4.3). In particular, unlike the more dense specimens in Region I, failure of the Region II specimens is likely decoupled from the statistics of surface flaws that might be induced by handling since again the limited range in m in Region II would seem to preclude a large influence from such effects. Thus, instead of processing or testing techniques (Appendix B), the banded nature of the m versus P behavior for the several materials given in Figure 4.8 and Table 4.5 is may stem from the near universality in the pore evolution during

sintering, namely the evolutions of anisotropic (tubular) pores during the intermediate sintering stage.

Nested within Region II is the P range (from about 0.2 to 0.4) which includes the P values required for many of the biomedical and other applications of brittle, porous materials (Section 1). Thus the m versus P behavior in Region II has very significant technical implications. For volume fraction porosities between 0.1 and 0.55, a medium to high scatter in the fracture strength is to be expected, thus requiring the designers of such components to include high safety factors in their designs.

For the precursor to Region II, namely Region III ($P > 0.55$), the authors were able to find only one data point in the literature that corresponds to Region III, namely a single m value from a study by Villora [Villora2004], for a HA/silica composite material. The general trend that for Region III, the m values are greater than in Region II may be related to evolution of pore morphology in the initial and intermediate sintering stages, respectively, or to differences in fracture mode in term associated with the differing pore morphologies. The trend of higher m values in Region III than in Region II is somewhat surprising and further study is needed to explore this behavior.

5. Acknowledgements

The authors acknowledge the financial support of the National Science Foundation, Division of Materials Research Grant DMR-0706449. In addition, the authors acknowledge the use of the Electron Microscopy facilities at the Center for Advanced Microscopy, Michigan State University. Ring-on-ring loading fixtures were fabricated in the Physics

Department Machine Shop in Michigan State University.

APPENDICES

APPENDIX A

WEIBULL ANALYSIS

Weibull statistics have been widely used to analyze fracture strength data of brittle materials, as well as the spread in the distribution of data for other physical quantities. The Weibull distribution has been applied to distributions of other types of mechanical property data, including Young's modulus [Chen2010, Sarkar 2011] and hardness [Sarkar 2011] in addition to applications as diverse as wind speed distributions in meteorology [Gabriel2011]. In this study we apply Weibull analysis only to fracture strength data.

The general form of the Weibull distribution for fracture strength can be expressed as [Wachtman 2009]:

$$P_f = 1 - \exp\left[-\int_V \left(\frac{\sigma}{\sigma_C} \right)^m dV \right] \tag{A1}$$

where P_f is the probability of failure, V is the specimen volume subject to (tensile) stress, the scale parameter σ_c is called the characteristic strength, and the shape parameter m is the Weibull modulus [Wachtman 2009]. For tensile tests performed on specimens with constant volume, equation (A1) can be simplified to

$$P_f = 1 - \exp\left[-\left(\frac{\sigma}{\sigma_c} \right)^m \right] \tag{A2}$$

or

$$\ln \ln \left(\frac{1}{1-P_f} \right) = m \ln \sigma - m \ln \sigma_c \tag{A3}$$

Under multiaxial stress conditions (as in the case of an ROR test, where the stress is equibiaxial), equation (A1) becomes much more complicated, which requires numerical evaluation of the integral term [Chao 1991, Chao and Shetty 1992). However, if the specimens fail due to surface flaws in a given test configuration, equation (A3) can then be rewritten as

$$P_f = 1 - \exp\left[- \int_S \left(\frac{\sigma}{\sigma_c} \right)^m dS \right] \tag{A4}$$

where S is the surface area subject to stress. For ROR testing, the equibiaxial stress is constant within the loading ring perimeter on the tension side of the specimen. If the fracture origins fall within the loading ring perimeter on the tension surface, then equation (A4) can be simplified as

$$P_f = 1 - \exp\left[- \left(\frac{\sigma}{\sigma_c} \right)^m S_0 \right] \tag{A5}$$

where S_0 is the surface area circumscribed by the loading ring. For a fixed loading ring diameter, S_0 in equation (A5) can be "absorbed" into σ_c, which in turn results in equation (A2).

Thus, the two-parameter Weibull analysis can be applied to the ROR test with a fixed loading ring diameter if the fractures are caused by surface distributed flaws. Also, all of the HA specimens fractured in this study were fractured in the as-sintered condition, that is, none

of the specimens were polished. The lack of polishing might increase the probability of specimen failure via surface flaws.

APPENDIX B

FACTORS OTHER THAN POROSITY WHICH AFFECT THE WEIBULL MODULUS

The Weibull modulus varies with porosity as described by the "U" shaped m versus P plot (Figure 4.8) in Section 3.4.2. Tables 4.2 through 4.4 in this study show the wide range of processing and testing conditions associated with the literature data presented in Figure 4.8. This range of processing and testing conditions needs to be considered, since in general the scatter in m values at a given porosity (Figure 4.8) may result from specimen agglomerates [Murray1995], processing techniques and microstructure [Villora2004], strength testing techniques [Chao 1991, Cordell2009], pore size and pore shape [Chao 1992], spatial distribution of pores [Chao 1991], loading rate [Andrews2010], grain size [Kim1995] as well as surface finish [Nakamura2010]. In this appendix, we briefly discuss the magnitude of the changes in m that have been observed for each of the factors listed above.

Eliminating agglomerates via emulsion-refining before sintering improved the mechanical reliability of sintered HA specimens [Murray1995], where the as-sintered agglomerate-free specimens had an m of 13.5, compared to the dramatically lower m value of 7.6 of sintered specimens with agglomerates [Murray1995]. In another microstructure and processing technique study, Villora [Villora2004] formed specimens from powdered animal bones, waste diatom filters and paper industrial sludge using cold pressing, extrusion and slip casting. Then with a single time-temperature sintering profile Villora [Villora2004]

obtained partially densified specimens with porosities of 0.42, 0.55 and 0.65, respectively [Villora2004]. The m values for the cold pressed, extruded and slip cast specimens were 3.7, 6 and 2, respectively. Differences in composition and processing likely lead to microstructural variations that in turn resulted in the observed range of m values [Villora2004].

Cordell demonstrated the importance of the strength testing technique on m via (i) compression and (ii) four-point bend tests on HA specimens that included fugitive (pore forming) PMMA microspheres [Cordell2009]. Compression tested HA specimens sintered with 16.2 μm PMMA microsphere inclusions had an m value of 8.7 compared to m = 5.8 for HA specimens sintered with 5.96 μm PMMA microsphere inclusions [Cordell2009], indicating a higher m value for larger pores. Conversely, for the four-point bend test, specimens with larger pores had m = 7.24 compared to m = 10.3 for specimens with smaller pores. The different m values for four-point bend and compression may result from the differing stress distributions induced within the specimens during testing.

A silicon nitride specimens studied by Chao indicated a dependence of m on pore size and shape [Chao 1992], where larger, irregularly shaped pores were more likely to act as fracture origins compared to smaller, equiaxed pores, although no numerical values of m were reported [Chao 1992]. A second study by Chao explored the relationship of m and the spatial distribution of pores in alumina and silicon nitride [Chao 1991] for specimens fractured using three-point bend, four-point bend and biaxial flexure testing. For alumina, the three strength testing techniques agreed well with each other, such that m = 23.8 for

four-point bend, m = 25.4 for three-point bend and m = 22.3 for biaxial flexure testing [Chao 1991]. However, for silicon nitride specimens, m = 10.1 for four-point bend, m = 15.7 for three-point bend and m = 12.0 for biaxial flexure testing [Chao 1991]. Chao [Chao 1991] noted that fracture originated from surface flaws in alumina but from subsurface pores in silicon nitride, thus the spatial distribution of pores likely influences the link between m and a given test technique.

Andrews found that when fracture is induced by surface flaws in dense silicon nitride, loading rates of 30 MPa/s, 0.3 MPa/s and 0.003 MPa/s gave m values of 26.7 to 15.4 and 6.9, respectively [Andrews2010]. Also, as the loading rate decreased, the specimens with surface flaws became more susceptible to slow crack growth [Andrews2010].

Kim [Kim1995] showed a coupling between grain size and m. Using identical test techniques, silicon nitride specimens with grains one μm in diameter and 5.3 μm long had m values ranging from 23 to 30, while m was 17 for specimens with grains 2 μm in diameter and 12 μm long. Kim [Kim1995] attributed the measured differences in m to a narrower critical flaw size distribution for the smaller grain size.

Nakamura's study of porcelain specimens with glazed surfaces and surfaces roughened using 1000, 600 and 100 abrasive grit [Nakamura2010] shows that m depends on surface finish. For the glazed specimens, m ~16 and for the abraded specimens, the m values were from 11 to 13 [Nakamura2010]. However, among the abraded specimens no obvious correlation between m and grit size was reported [Nakamura2010].

Each mechanism discussed in this appendix may affect m differently for this study and

for each of the eighteen studies from the literature (Tables 4.2, 4.3, and 4.4) that are plotted as the combined data set in Figure 4.8. Thus, despite this considerable diversity in the processing, testing and material properties among the studies in the combined data set (that represents a total of more than 1560 specimens including HA, other oxides and non-oxides), a universal three-region U-shaped behavior was observed in m versus P plot (Figure 4.8), within which we observed a strip of m values between about 4 and 11 for a wide intermediate porosity region (Region II, Figure 4.8).

Furthermore, for this study, the composition, initial powder particle size, the furnace and furnace atmosphere used to densify the specimens, the specimen geometry, the test technique, specimen surface finish and the loading rate were all held fixed. Nevertheless, the scatter in m versus P in this study is comparable to the scatter in m versus P observed in the data from the literature, implying that at least for Region II, the porosity rather than the processing or test conditions are the dominant factor determining the m value.

REFERENCES

REFERENCES

[Andrews 2010] Andrews, M. J., Wereszczak, A. A., Breder, K., Ferber, M. K., Kirkland, T. P., 2010. Investigations of the Weibull Modulus as a Function of Stressing Rate, in 22nd Annual Conference on Composites, Advanced Ceramics, Materials, and Structures: B: Ceramic Engineering and Science Proceedings, D. Bray, ed., Volume 19, Issue 4, John Wiley & Sons, Inc., Hoboken, NJ, USA.

[ASTM 2003] ASTM C1499-05, Standard Test Method for Monotonic Equibiaxial Flexural Strength of Advanced Ceramics at Ambient Temperature, 2003.

[Barba 2006] Barba, F., Callejas, P., 2006. Calcium phosphate silicate ceramics for heavy metal immobilization and antibacterial activity in waste water. J. Mater. Sci. 41, 5227-5230.

[Barsoum 1997] Barsoum, M. W., 1997. Fundamentals of Ceramics, The McGraw – Hill Companies, Inc., New York.

[Baumann 2008] Baumann, M. J., Smith, I. O., Case, E. D., 2008. in Developments in Porous, Biological and Geopolymer Ceramics (Ceram. Eng. Sci. Proc., Vol. 28, IS. 9), Wiley InterScience, New York, pp. 197-207.

[Bein 1996] Bein, T., 1996. Synthesis and applications of molecular sieve layers and membranes. Chem. Mater. 8, 1636-1653.

[Berry 1986] Berry, K.A., Harmer, M.P., 1986. Effect of MgO Solute on microstructure development in $A1_2O_3$. J. Am. Ceram. Soc. 69, 143 – 149.

[Borrero-Lopez 2009] Borrero-Lopez, O., Vodenitcharova, T., Hoffman, M., Leo, A. J., 2009. Fracture strength of polycrystalline silicon wafers for the photovoltaic industry. J. Am. Ceram. Soc. 92, 2713 - 2717.

[Brodie 2003] Brodie, R.C., Bahr, D.F., 2003. Fracture of polycrystalline silicon. Mater. Sci. Eng. A 351, 166 - 173.

[Case 2006] Case, E. D., 2006. Microwave Processing of Ceramics, Encyclopedia of Chemical Processing (ECHP), Sunggyu Lee, Ed., Marcel Dekker Inc, New York, NY.

[Case 1981] Case, E. D., Smyth, J. R., Monthei, V., 1981. Grain-size determinations. J. Am. Ceram. Soc. 64, C24 – C25.

[Case and Smyth 1981] Case, E. D., Smyth, J. R., 1981. Fracture Energy of Monoclinic Gd_2O_3, J. Mater. Sci., 16, 3215-3217.

[Chao 1991] Chao, L.Y., Shetty, D. K., Leo, J., 1991. Reliability analysis of structural ceramics subjected to biaxial flexure. J. Am. Ceram. Soc. 74, 333 - 344.

[Chao 1992] Chao, L.Y., Shetty, D. K., 1992. Extreme-value statistics analysis of fracture strengths of a sintered silicon-nitride failing from pores. J. Am.Ceram. Soc. 75, 2116-2124.

[Chen 2010] Chen, Q., Mao, W. G., Zhou, Y. C., Lu, C., 2010. Effect of Young's modulus evolution on residual stress measurement of thermal barrier coatings by X-ray diffraction. Appl. Surf. Sci. 256, 7311 - 7315.

[Cordell 2009] Cordell, J.M., Vogl, M.L., Johnson, A.J.W., 2009. The influence of micropore size on the mechanical properties of bulk hydroxyapatite and hydroxyapatite scaffolds. J. Mech. Behav. Biomed. 2, 560-570.

[Corneal 2010] Corneal, L., Masten, S. J., Davies, S.H.R., Tarabara, V. V., Byun, S., Baumann, M. J., 2010. AFM, SEM and EDS characterization of manganese oxide coated ceramic water filtration membranes. J. Membrane Sci. 360, 292 - 302.

[CRC 2009] CRC Handbook of Chemistry and Physics, 90th ed., CRC press, four-55, 2009.

[da Silva 2006] da Silva, O.G., da Silva, E.C., da Fonseca, M.G., Arakaki, L.N.H., Airoldi, C., 2006. Hydroxyapatite organofunctionalized with silylating agents to heavy cation removal. J Colloid Interf. Sci. 302, 485-491.

[de Lange 1995] de Lange, R.S.A., Hekkink, J.H.A., Keizer, K., Burggraaf, A.J., 1995. Permeation and Separation Studies on Microporous Sol-Gel Modified Ceramic Membranes. Microporous Mater. 4, 169-186.

[Flinn 2000] Flinn, B. D., Bordia, R. K., Zimmermann, A., Rodel, J., 2000. Evolution of defect size and strength of porous alumina during sintering. J. Eur. Ceram. Soc. 20, 2561 - 2568.

[Gabriel 2011] Gabriel, F., Luis, R. A., Cremasco, C. P., Seraphim, O. J., de L. Caneppele, F., 2011. Analytical and geometric characterization of general methodology of determination of Weibull distribution for wind regime and its applications. Eng. Agric. 31, 56 - 66.

[Geis 2002] Geis, S., Fricke, J., Lobmann, P., 2002. Electrical properties of PZT aerogels. J. Eur. Ceram. Soc. 22, 1155 - 1161.

[German 1996] German, R. M., 1996. Sintering Theory and Practice, John Wiley & Sons, Inc., New York.

[Groschel 2005] Groschel, L., Haidar, R., Beyer, A., Colfen, H., Frank, B., Schomacker, R.,

2005. Hydrogenation of propyne in palladium-containing polyacrylic acid membranes and its characterization. Ind. Eng. Chem. Res. 44, 9064-9070.

[Hench 1990] Hench, L. L., West, J. K., 1990. Principles of Electronic Ceramics, Wiley, New York.

[Hirosaki 1993] Hirosaki, N., Akimune, Y., 1993. Effect of Grain Growth of p-Silicon Nitride on Strength, Weibull Modulus, and Fracture Toughness. J. Am. Ceram. Soc. 76, 1892 - 1894.

[Hoepfner 2002] Hoepfner, T. P., Case, E. D., 2002. The porosity dependence of the dielectric constant for sintered hydroxyapatite. J. Biomed. Mater. Res. 60, 643 - 650.

[Hoepfner 2003] Hoepfner, T. P., Case, E. D., 2003. The influence of the microstructure on the hardness of sintered hydroxyapatite, Ceramics International. Ceram. Int. 29, 699 - 706.

[Hontsu 1997] Hontsu, S., Matsumoto, T., Ishii, J., Nakamori, M., Tabata, H., Kawai, T., 1997. Electrical properties of hydroxyapatite thin films grown by pulsed laser deposition. Thin Solid Films 295, 214-217.

[Hu 2010] Hu, L. F., Wang, C. A., 2010. Effect of sintering temperature on compressive strength of porous yttria-stabilized zirconia ceramics. Ceram. Int. 36, 1697 - 1710.

[Hu 2010] Hu, L.F., Wang, C.A., 2010. Porous yttria-stabilized zirconia ceramics with ultralow thermal conductivity. J. Mater. Sci. 45, 3242 3246.

[Jung 2006] Jung, S., Gross, M.D., Gorte, R.J., Vohs, J.M., 2006. Electrodeposition of Cu into a Highly Porous Ni/YSZ Cermet. J. Electrochem. So. 153, A1539 – A1543.

[Karnik 2005] Karnik, B. S., Davies, S.H.R., Chen, K.C., Jaglowski, D.R., Baumann, M.J., Masten, S.J., 2005. Effects of ozonation on the permeate flux of nanocrystalline ceramic membranes. Water Res. 39, 728 - 734.

[Kim 1995] Kim, Y.W., Mitomo, M., Hirosaki, N., 1995. R-Curve Behavior and Microstructure of Sintered Silicon-Nitride. J. Mater. Sci. 30, 5178-5184.

[Kishimoto 1991] Kishimoto, A., Koumoto, K., Yanagida, H., Nameki, M., 1991. Microstructure Dependence of Mechanical and Dielectric Strengths .1. Porosity. Eng. Fract. Mech. 40, 927-930.

[Lambert 1999] Lambert, C.K., Gonzalez, R.D., 1999. Activity and selectivity of a Pd/gamma-Al_2O_3 catalytic membrane in the partial hydrogenation reactions of acetylene and 1,3-butadiene. Catal. Lett. 57, 1-7.

[Liu 2010] Liu, X., Martin, C. L., Delette, G., Bouvard, D., 2010. Elasticity and strength of

partially sintered ceramics. J. Mech. Phys. Solids 58, 829 - 842.

[Lopes 1999] Lopes, M.A., Monteiro, F.J., Santos, J.D., 1999. Glass-reinforced hydroxyapatite composites: Secondary phase proportions and densification effects on biaxial bending strength. J. Biomed. Mater. Res. 48, 734-740.

[Mahabole 2005] Mahabole, M.P., Aiyer, R.C., Ramakrishna, C.V., Sreedhar, B., Khairnar, R.S., 2005. Synthesis, characterization and gas sensing property of hydroxyapatite ceramic. Mater. Sci. B 28, 535-545.

[Meganck 2005] Meganck, J.A., Baumann, M.J., Case, E.D., McCabe, L.R., Allar, J.N., 2005. Biaxial flexure testing of calcium phosphate bioceramics for use in tissue engineering. J. Biomed. Mater. Res. A 72. 115-126.

[Mori 2003] Mori, K., Hara, T., Mizugaki, T., Ebitani, K., Kaneda, K., 2003. Hydroxyapatite-bound cationic ruthenium complexes as novel heterogeneous Lewis acid catalysts for Diels-Alder and aldol reactions. J. Am. Chem. Soc. 125, 11460-11461.

[Mori 2004] Mori, K., Hara, T., Mizugaki, T., Ebitani, K., Kaneda, K., 2004. Hydroxyapatite-supported palladium nanoclusters: A highly active heterogeneous catalyst for selective oxidation of alcohols by use of molecular oxygen. J. Am. Chem. Soc. 126, 10657-10666.

[Murray 1995] Murray, M.G.S., Wang, J., Ponton, C.B., Marquis, P.M., 1995. An Improvement in Processing of Hydroxyapatite Ceramics. J. Mater. Sci. 30, 3061-3074.

[Nagai 1988] Nagai, M., Nishino, T., Saeki, T., 1988. A New Type of Co2 Gas Sensor Comprising Porous Hydroxyapatite Ceramics. Sensor Actuator 15, 145-151.

[Nakamura 2010] Nakamura, Y., Hojo, S., Sato, H., 2010. The effect of surface roughness on the Weibull distribution of porcelain strength. Dent. Mater. J. 29, 30-34.

[Nanjangud 1995] Nanjangud, S.C., Brezny, R., Green, D.J., 1995. Strength and Young’s Modulus Behavior of a Partially Sintered Porous Alumina. J. Am. Ceram. Soc. 78, 266-268.

[Ni 2009] Ni, J. E., Ren, F., Case, E. D., Timm, E. J., 2009. Porosity dependence of elastic moduli in LAST (Lead-antimony-silver-tellurium) thermoelectric materials. Mater. Chem. Phy. 118, 459 - 466.

[Nielsen 1990] Nielsen, L. F., 1990. Strength and stiffness of porous materials. J. Am. Ceram. Soc. 73, 2684 - 2689.

[Nishikawa 2003] Nishikawa, H., 2003. Surface changes and radical formation on hydroxyapatite by UV irradiation for inducing photocatalytic activation. J. Mol. Catal.

a-Chem. 206, 331-338.

[Ohtsuki 2010] Ohtsuki, C., Ichikawa, Y., Shibata, H., Kawachi, G., Torimoto, T., Ogata, S., 2010. Sensing of protein adsorption with a porous bulk composite comprising silver nanoparticles deposited on hydroxyapatite. J. Mater. Sci-Mater. M 21, 1225-1232.

[Opre 2005] Opre, Z., Grunwaldt, J.D., Maciejewski, M., Ferri, D., Mallat, T., Baiker, A., 2005. Promoted Ru-hydroxyapatite: designed structure for the fast and highly selective oxidation of alcohols with oxygen. J. Catal. 230, 406-419.

[Owada 1989] Owada, H., Yamashita, K., Umegaki, T., Kanazawa, T., Nagai, M., 1989. Humidity-Sensitivity of Yttrium Substituted Apatite Ceramics. Solid State Ionics 35, 401-404.

[Park 2009] Park, Y. H., Hinoki, T., Kohyama, A., 2009. Development of multi-functional NITE-porous SiC for ceramic insulators. J. Nuclear Mater. 386–388, 1014 - 1017.

[Paul 2006] Paul, I., Majeed, B., Razeeb, K. M., Barton, J., 2006. Statistical fracture modeling of silicon with varying thickness. Acta Mater. 54, 3991 - 4000.

[Pissenberger 1995] Pissenberger, A., Gritzner, G., 1995. Preparation and Properties of Niobia-Doped and Tantala-Doped Orthorhombic Zirconia. J. Mater. Sci. Lett. 14, 1580-1582.

[Ren 2009] Ren, F. Case, E. D., Morrison, A., Tafesse, M., Baumann, M. J., 2009. Resonant ultrasound spectroscopy measurement of Young's modulus, shear modulus and Poisson's ratio as a function of porosity for alumina and hydroxyapatite. Philos. Mag. 89, 1163 - 1182.

[Ren 2006] Ren, F., Case, E. D., Timm, E. J., Jacobs, M. D., Schock, H. J., 2006. Weibull analysis of the biaxial fracture strength of a cast p-type LAST-T thermoelectric material. Phil. Mag. Lett. 86, 673 - 682.

[Ren 2005] Ren, F., Smith, I. O., Baumann, M. J., Case, E. D., 2005. Three-Dimensional Microstructural Characterization of Porous Hydroxyapatite Using Confocal Laser Scanning Microscopy (CLSM), Int. J. Appl. Ceram. Tec. 2, 200 - 211.

[Ruys 1995] Ruys, A.J., Wei, M., Sorrell, C.C., Dickson, M.R., Brandwood, A., Milthorpe, B.K., 1995. Sintering Effects on the Strength of Hydroxyapatite. Biomaterials 16, 409-415.

[Sammis 1986] Sammis, C. G., Ashby, M. F., 1986. The fracture of brittle porous solids under compressive stress states. Acta Mater. 34, 511 - 526.

[Sarkar 2011] Sarkar, S., Dey, A., Das, P. K., Mukhopadhyay, A. K., Kumar, A., 2011. Evaluation of micromechanical properties of carbon/carbon and carbon/carbon–silicon carbide composites at ultralow load. Int. J. Appl. Ceram. Technol. 8, 282 - 297.

[Shimizi 2009] Shimizi, S., Yamaguchi, T., Fujishiro, Y., Awan, M., 2009. Effect of microstructure on the conductivity of porous $(La_{0.8}Sr_{0.2})_{0.99}MnO_3$. J. Ceram. Soc. Japan 117, 895 - 898.

[Silva 2003] Silva, C.C., Almeida, A.F.L., De Oliveira, R.S., Pinheiro, A.G., Goes, J.C., Sombra, A.S.B., 2003. Dielectric permittivity and loss of hydroxyapatite screen-printed thick films. J. Mater. Sci. 38, 3713-3720.

[Silva 2005] Silva, C.C., Rocha, H.H.B., Freire, F.N.A., Santos, M.R.P., Saboia, K.D.A., Goes, J.C., 2005. Hydroxyapatite screen-printed thick films: optical and electrical properties. Mater. Chem. Phys. 92, 260-268.

[Sommer 2005] Sommer, S., Melin, T., 2005. Performance evaluation of microporous inorganic membranes in the dehydration of industrial solvents. Chem. Eng. Process 44, 1138-1156.

[Srinivasan 2006] Srinivasan, M., Ferraris, C., White, T., 2006. Cadmium and lead ion capture with three dimensionally ordered macroporous hydroxyapatite. Environ. Sci. Technol. 40, 7054-7059.

[Sueter 1972] Sueter, A.M.J.H., 1972, Existence region of calcium hydroxyapatite and the equilibrium with co-existing phases at elevated temperatures, Reactivity of Solids, pp. 806-812, J. S. Anderson, M. W. Roberts, Eds., Chapman and Hall, London.

[Sulistyo 2010] Sulistyo, J., Hata, T., Kitagawa, H., Bronsveld, P., Fujisawa, M., Hashimoto, K., Imamura, Y., 2010. Electrical and thermal conductivities of porous SiC/SiO2/C composites with different morphology from carbonized wood. J. Mater. Sci. 45, 1107 - 1116.

[Twigg 2007] Twigg, M.V., Richardson, J.T., 2007. Fundamentals and applications of structured ceramic foam catalysts. Ind. Eng. Chem. Res. 46, 4166-4177.

[Underwood 1968] Underwood, E. E., Colcord, A. R., Waugh, R.C., 1968. in Ceramic Microstructures, R.M. Fulrath and J.A. Pask eds., John Wiley and Sons, New York, p.25.

[Vales 1999] Vales, F., Rezakhanlou, R., Olagnon, C., 1999. Determination of the fracture mechanical parameters of porous ceramics from microstructure parameters measured by quantitative image analysis. J. Mat. Sci. 34, 4081 - 4088.

[Vandeperre 2004] Vandeperre, L. J., Wang J., Clegg, W. J., 2004. Effects of porosity on the measured fracture energy of brittle materials, Philos. Mag. 84, 3689-3704.

[Venugopal 2003] Venugopal, A., Scurrell, M.S., 2003. Hydroxyapatite as a novel support for gold and ruthenium catalysts - Behaviour in the water gas shift reaction. Appl. Catal. a-Gen 245, 137-147.

[Villora 2004] Villora, J.M., Callejas, P., Barba, M.F., Baudin, C., 2004. Statistical analysis of the fracture behaviour of porous ceramic Raschig rings. J. Eur. Ceram. Soc. 24, 589-594.

[Wachtman 2009] Wachtman, J. B., Cannon, W. R., Matthewson, M. J., 2009. Mechanical Properties of Ceramics, 2nd ed., Wiley Interscience, New York.

[Yang 2010] Yang, A., Wang, C.A., Guo, R., Huang, Y., Nan, C.W., 2010. Effects of sintering behavior on microstructure and piezoelectric properties of porous PZT ceramics. Ceram. Int. 36, 549 - 554.

[Yang 2007a] Yang, L., Ning, X. S., Chen, K. X., Zhou, H. P., 2007a. Preparation and properties of hydroxyapatite filters for microbial filtration. Ceram. Int. 33, 483 - 489.

[Yang 2007b] Yang, L., Ning, X. S., Xiao, Q. F., Chen, K. X., Zhou, H. P., 2007b. Development and characterization of porous silver-incorporated hydroxyapatite ceramic for separation and elimination of microorganisms. J. Biomed. Mater. Res. B 81B, 50 - 56.

[Yin 2010] Yin, S.X., Ellis, D.E., 2010. First-principles investigations of Ti-substituted hydroxyapatite electronic structure. Phys. Chem. Chem. Phys. 12, 156-163.

[Zeng 2009] Zeng, Q., Zu, Y.B., Fan, C.G., Chen, C.S., 2009. CO_2-tolerant oxygen separation membranes targeting CO_2 capture application. J. Membrane Sci. 335, 140-144.

CHAPTER 5

FRACTURE STRENGTH AND ELASTIC MODULUS AS A FUNCTION OF POROSITY FOR HYDROXYAPATITE AND OTHER BRITTLE MATERIALS

X. Fan, E. D. Case, F. Ren, Y. Shu and M. J. Baumann
Department of Chemical Engineering and Materials Science, Michigan State University, East Lansing, MI, 48824

Published in: J Mechanical Behavior of Biomedical Materials, 8:99-110, 2012.

Abstract

Part I of this paper discussed the Weibull modulus, m, versus porosity, P, behavior of brittle materials, including HA. While the Weibull modulus m deals with the scatter in fracture strength data, this paper (Part II) focuses on two additional key mechanical properties of porous materials, namely the average fracture strength, $<\sigma_f>$, and the Young's modulus, E, for P in the interval from P ≈ zero to P ≈ P_G (the porosity of the unfired compacts). The $<\sigma_f>$ versus P data for HA from this study and the literature data for alumina, yttria stabilized zirconia (YSZ) and silicon nitride are described well by functions of ϕ, where $\phi = 1 - P/P_G$ = the degree of densification. A similar function of ϕ applies to the <E> versus P behavior of HA from this study and data from the literature for alumina, titanium and YSZ. All of the data analyzed in this study (Part II) are based on partially and fully sintered powder compacts (excluding green powder compacts), thus the $<\sigma_f>/\sigma_0$ versus ϕ and $<E>/E_0$ versus ϕ relationships may apply only to such specimens.

1. Introduction

In previous chapter, the Weibull modulus, m, versus volume fraction porosity, P, behavior was examined for 441 cold-die pressed and sintered hydroxyapatite (HA) disk-shaped specimens. The HA specimens were fractured in biaxial flexure using a ring-on-ring (ROR) fixture for $0.08 \leq P \leq 0.62$. A "U" shaped m versus P plot was obtained for this study's fractured HA specimens as well as for combined data sets that included HA data from the literature along with oxide and non-oxide data from the literature.

In this study we examine the porosity dependence of the average fracture strength, $<\sigma_f>$, and the average Young's modulus, <E>. For $<\sigma_f>$ versus P, we analyze data for HA (this study], alumina [Nanjangud 1995], yttria stabilized zirconia (YSZ) [Deng 2002] and silicon nitride [Yang 2003]. In addition, Young's modulus versus P data are examined for HA [this study, Ren 2009], alumina [Hardy and Green 1995, Nanjangud 1995, Ren 2009], titanium [Oh 2003], and YSZ [Deng 2002]. Both the fracture strength and Young's modulus dependence on P can be expressed in terms of a power law dependence on the degree of densification, ϕ, where $\phi = (1 - P/P_G)$ and P_G is the porosity of a green (unfired) powder compact.

Of key importance is the complementary nature of Parts I and II of this study. Part I considered the Weibull modulus, m, of a wide range of materials where m is a measure of the spread of the distribution of strength values. In addition to m, the average strength (the mean of the strength distribution) and the Young's modulus (which characterizes the stress-strain response of a brittle material prior to fracture) also are fundamental mechanical properties.

Construction of the stiffness matrix for finite element method calculation of stress and strain, for example, requires Young's modulus data [Martin 1973]. Unlike the Weibull modulus, the average strength and Young's modulus decrease smoothly and monotonically with increasing P.

2. Background

2.1 Strength-porosity relationships for brittle solids

Nearly sixty years ago, Ryshkewitch [Ryshkewitch 1953] and Duckworth [Duckworth 1953] suggested that the porosity dependence of the fracture strength, σ_f, of brittle materials could be represented as

$$\sigma_f = \sigma_0 \exp(-bP) \quad (1)$$

where σ_0 is the fracture strength for the theoretically dense (P = 0) material, P is the volume fraction porosity and b is a unitless, material-dependent constant.

Rice [Rice 1998] stated that the constant b in equation (1) typically ranges from about 4 to 6 in part of a comprehensive review text on porosity in ceramics. In addition, Rice [Rice 1998] emphasized that equation (1) describes very well the strength-porosity relationships governing the strength of ceramics, but only up to a critical porosity, P_C. For $P > P_C$, Rice [Rice 1998] noted that the strength decreases more rapidly than is described by equation (1). However, Rice did not present a method for predicting P_C.

Prior to Rice's work [Rice 1998], a number of researchers considered a similar concept of a critical porosity. In 1958, Schriller [Schriller 1958] gave a porosity-relative strength relationship based on a mathematical model that included the concept of a critical porosity,

P_C, such that

$$\sigma_f = q \log \frac{P_C}{P} \tag{2}$$

where σ_f is the fracture strength, q is a quality factor depending on the preparation of the mix and impurities. In this case, the critical porosity corresponds to zero fracture strength of a material.

In 1959, Millard [Millard 1959] also employed the concept of a critical porosity in a σ_f versus P relationship such that

$$\sigma_f = S_0 \left(1 - \frac{P}{P_C}\right) \frac{P_C}{P} \tag{3}$$

where Millard [Millard 1959] defined S_0 as a constant "having units of strength" and P_C as a critical porosity equal to porosity of a loose powder.

In this study, we fit the relative average fracture strength, $<\sigma_f>/\sigma_0$, to the following function form

$$\frac{<\sigma_f>}{\sigma_o} = A_\sigma \left(1 - \frac{P}{P_G}\right)^n = A_\sigma (\phi)^n \tag{4}$$

where $<\sigma_f>$ is average fracture strength of a group of porous ceramics with a fixed value of P, σ_0 is fracture strength of the theoretically dense (P = 0) ceramic, P_G is the porosity of the powder compact and $\phi = (1 - P/P_G)$ is defined as the degree of densification.

In the work by Rice [Rice 1998], Schriller [Schriller 1958] and Millard [Millard 1959], there is an implicit assumption that the green or unfired state corresponds to a critical or initial point of strength in the partially sintered specimens. However, the bonding

mechanisms among particles that bind together the green powder compact are different than the bonding between grains in partially sintered/fully sintered bodies [Barsoum 1997, Flatt 2004, Hornbaker 1997, Libowitzky 1999]. Thus, the "initial point" of strength (σ_G at $P = P_G$) may be difficult to define unambiguously.

The P = 0 value of the fracture strength, σ_0, is a function of parameters such as the defect state, the nature of loading, and other factors [Rice 1998]. However, for the partially sintered bodies examined in this study, even when $P \rightarrow 0$, equation (4) and the corresponding equation for Young's modulus (equation (10) that is discussed in the next section) describe remarkably well the porosity dependence of the relative strength and Young's modulus data, respectively.

2.2 Young's modulus as a function of porosity

In an analogy to Ryshkewitch's [Ryshkewitch 1953] and Duckworth's [Duckworth 1953] expression for the P dependence of the relative fracture strength (equation (1)), in 1961 Spriggs proposed that the porosity dependence of Young's modulus could be written as [Spriggs 1961]

$$E/E_0 = \exp(-bP) \quad (5)$$

where E is the Young's modulus at a given volume fraction porosity P, E_0 is the value of E for theoretically dense materials and b is a material-dependent constant. For $bP << 1$, $E/E_0 = \exp(-bP)$ can be approximated as

$$E/E_0 = (1 - bP) \quad (6)$$

In 1987 Phani [Phani and Niyogi 1987] proposed a semi-empirical equation

$$E/E_0 = (1 - aP)^n \quad (7)$$

where a is defined as the unitless "packing geometry factor" and the constant n depends on grain morphology and pore geometry. Phani's [Phani and Niyogi 1987] Young's modulus versus P equation (equation (7)) is thus roughly analogous in form to equation (3), the strength-porosity equation proposed in 1959 by Millard [Millard 1959]. Phani [Phani and Niyogi 1987] defined the constant in equation (7) as $a = 1/P_C$ and P_C as the critical porosity at which Young's modulus is zero. According to Phani [Phani and Niyogi 1987], $E = E_0 (1 - aP)^n$ is valid for any range of porosity. Note that equations (5), (6) and (7) are all essentially identical for small values of P and for n near unity. As we shall discuss in Section 4, n is in fact near unity for the materials analyzed in this study, and the predictions of equations (5) and (7) diverge with increasing P.

In 1994 Lam [Lam 1994] developed a linear relationship of the relative Young's modulus, E/E_0, of porous ceramics based on Phani's work [Phani and Niyogi 1987], such that

$$\frac{E}{E_0} = \left(1 - \frac{P}{P_G}\right) = \phi \quad (8)$$

where E is Young's modulus of the porous ceramic, E_0 is the Young's modulus of the theoretically dense ceramic, P is the volume fraction porosity. P_G and ϕ are as defined following equation (4).

Nanjangud [Nanjangud 1995] and Hardy [Hardy and Green 1995] in 1995 referred to Lam's 1994 paper [Lam 1994] to obtain the expression

$$\frac{E - E'}{E_0 - E'} = \left(1 - \frac{P}{P_G}\right) = \phi \tag{9}$$

where E' is the Young's modulus value for the green, cold-pressed porosity state.

In this study, we use a slightly modified equation that provides a higher R^2 (coefficient of determination) for the least-squares fit to a given <E> versus P data set, namely

$$\frac{< E >}{E_0} = A_E\left(1 - \frac{P}{P_G}\right)^q = A_E(\phi)^q \tag{10}$$

where <E> is the average Young's modulus of a group of porous ceramics with a fixed value of P. Also A_E and q are dimensionless constants. Equation (10) is equivalent to Phani's equation [Phani and Niyogi 1987] if one sets $A_E = 1$ and $a = 1/P_G$.

3. Experimental Procedure

3.1 Specimen preparation and biaxial flexure testing

Details of specimen preparation and biaxial flexure testing technique were given in Part I of this paper. The fracture strength, σ_f, was calculated using the following equation as suggested by the ASTM standard C1499-05 [ASTM 2003]

$$\sigma_f = \frac{3F}{2\pi h^2}\left[(1-\nu)\frac{D_S^2 - D_L^2}{2D^2} + (1+\nu)\ln\left(\frac{D_S}{D_L}\right)\right] \tag{11}$$

where F is the load at failure, h and D are the thickness and the diameter of the disk-shaped test specimen, D_S and D_L are the diameters of the supporting ring and the loading ring, respectively. A Poisson's ratio, ν, of 0.27 [Ren 2009] was used in the above calculation.

3.2 Scanning electron microscopy

Scanning electron microscopy (SEM) was used to examine the size and morphology of

the initial HA powders. A small amount of the HA powder was dispersed for 10 minutes in ethanol (190 Proof, Becon Laboratory, Inc.) using an ultrasonic bath (Bransonic ultrasonic cleaner, 1510R-MT, Branson Ultrasonics Corporation, CT). Immediately after removing the HA/ethanol mixture from the ultrasonic bath, a droplet of the mixture was placed onto a metal stub covered with carbon tape. The ethanol was allowed to evaporate over 24 hours before the specimen surfaces were sprayed with pressurized air to remove loose powder particles. The powder sample was then gold-coated and examined by SEM. Details of the gold-coating and the SEM experimental procedures were given in Part I of this paper.

3.3 Elastic modulus measurements of HA

The Young's modulus of the as-sintered HA specimens were measured by Resonant Ultrasound Spectroscopy (RUS) (RUSpec, Quasar International, Albuquerque, NM, USA). The HA specimens were placed on a tripod arrangement of three piezoelectric transducers. A driving transducer (operating over a frequency range of 10 to 250 kHz in this case) generated a sinusoidal mechanical vibration that was sensed by the two pick-up transducers [Ren 2008]. The peaks recorded by the pick-up transducers (Figure 5.1) correspond to the mechanical resonance modes of the specimen. Using the recorded resonance frequencies and the mass, shape and dimensions of the specimens, the Young's modulus, E, as well as the shear modulus, G, and Poisson's ratio, ν were calculated using a commercial software package (RPModel®, Quasar International, Albuquerque, NM, USA).

4. Results and Discussion

4.1 Microstructural analysis of the initial HA powder

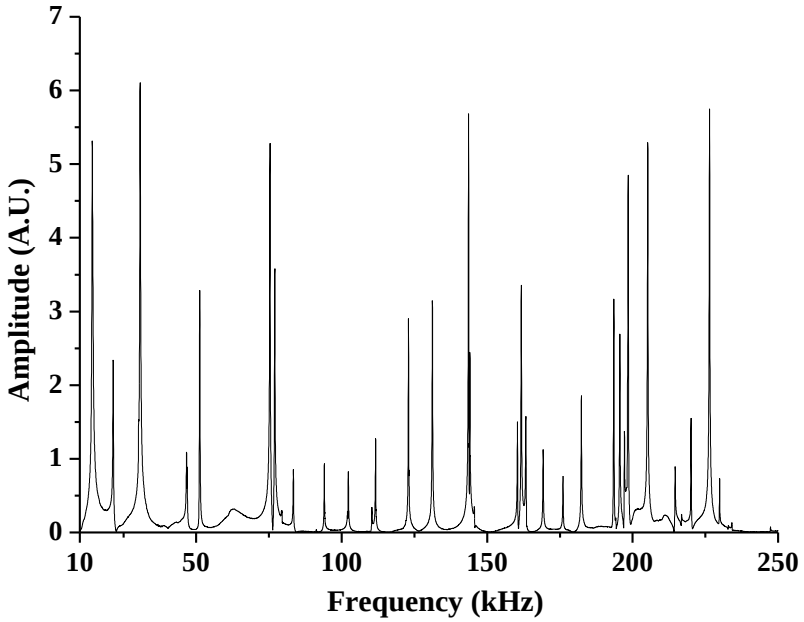

Figure 5.1. The RUS spectrum obtained for as-sintered HA specimen sintered at 1200^{o}C for 60 min. A.U. stands for arbitrary units.

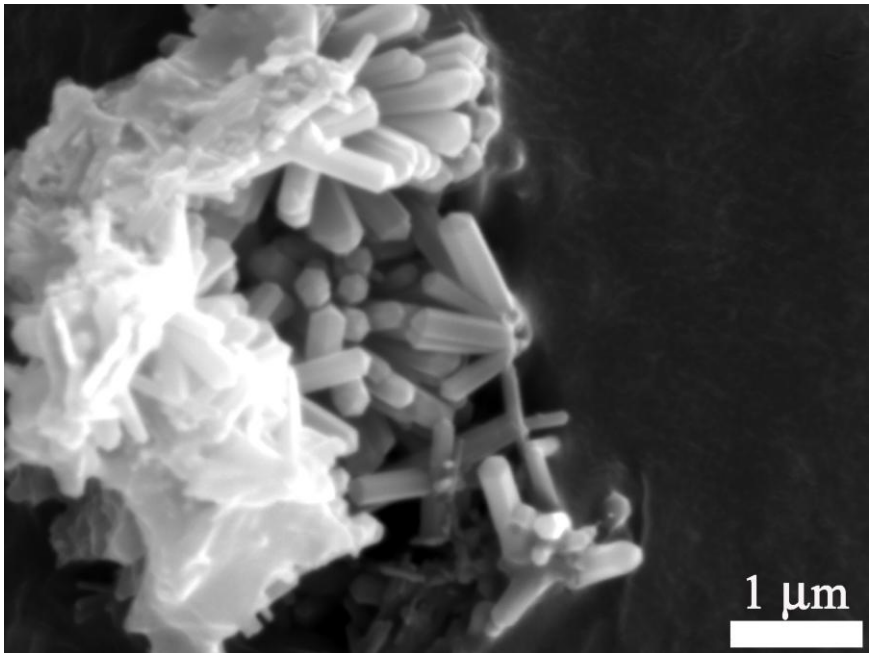

Figure 5.2. SEM micrographs of initial HA powder showing rod-shaped particles and agglomerates.

SEM analysis showed the initial HA powder particles to be approximately 0.8 μm in length and rod-shaped, with an aspect ratio of ~ 3 (Figure 5.2). These primary powder particles formed irregularly-shaped agglomerates ranging from several microns to roughly 10 microns across (Figure 5.2).

Based on measurements of the specimen mass and dimensions, the green density of the HA specimens was approximately 38% of theoretical density, which corresponds to a volume fraction porosity of $P_G = 0.62$. While P_G for nearly equiaxed powders is typically between roughly 0.4 and 0.5 [German 1994], the relatively high value of $P_G = 0.62$ for the HA powder compacts in this study is likely a consequence of the rod-like shape of the starting HA powders (Figure 5.2).

Rod-like particles do not pack as closely as spherical or quasi-spherical particles, thus powder compacts formed from rod-shaped particles tend to have fewer initial particle contacts, larger initial pores and a higher green porosity [German 1994]. In addition to the rod-shaped particles, the irregularly-shaped agglomerates observed in the as-received powders (Figure 5.2) also likely increase P_G. Thus, given the rod-like powder particles and the agglomerates included in the as-received HA powder, the measured P_G value of 0.62 is reasonable.

4.2 Strength versus porosity for HA and other brittle materials

4.2.1 Fracture strength versus P for the HA included in this study

For the HA specimens included in this study, the average fracture strength was plotted on a logarithmic scale as a function of porosity in order to show clearly the changes in

Table 5.1. Strength at zero porosity, σ_0, number of data points, N, fitting parameters, A_σ and n, for the least-squares fit of $<\sigma_f>/\sigma_0$ versus degree of densification, ϕ, data to equation (4) with coefficient of determination, R^2, for HA [this study], alumina [Nanjangud 1995], YSZ [Deng 2002] and Si_3N_4 [Yang 2003]. The combined data set includes all of the data from each of the four studies [this study, Deng 2002, Nanjangud 1995, Yang 2003].

References	Material	σ_0 (MPa)	N	A_σ	n	R^2
HA in this study	HA	80[a]	17	1.00 ± 0.004	1.08 ± 0.007	0.989
Nanjangud 1995	Alumina	380[b]	11	1.14 ± 0.02	1.04 ± 0.03	0.997
Deng 2002	YSZ	800[c]	8	1.01 ± 0.03	1.53 ± 0.11	0.992
Yang 2003	Si_3N_4	850[d]	8	0.85 ± 0.21	0.77 ± 0.18	0.860
Combined data set	All listed above	e	44	0.95 ± 0.03	1.02 ± 0.06	0.948

[a] The σ_0 value was estimated from the extrapolation of the strength versus porosity plot (Figure 5.3 in this study)

[b] The σ_0 value was estimated from the extrapolation of the strength versus porosity plot (Figure 5.1 in [Nanjangud 1995])

[c] The σ_0 value was estimated from the extrapolation of the strength versus porosity plot (Figure 5.2a in [Deng 2002])

[d] The σ_0 value was given in [Yang 2003]

[e] The normalized strength of each data set of the four materials listed above versus degree of densification was combined into a single data set and the combined data set were least-squares fit to equation (4)

strength at high porosities (Figure 5.3). In this study, the HA specimens were sintered at temperatures from 550^{o}C to 1360^{o}C with sintering times from 12 min to 4 hours (Table 5.1, Part 1). In particular, for the HA specimens sintered between 550^{o}C and 1000^{o}C, the volume fraction porosity, P, was very close to the green porosity, P_G. Although the P value changed little over the sintering temperature range from 550^{o}C and 1000^{o}C, the strength increased by a factor of 3 due to the development of imterparticle necking. The concept of the initial formation and growth of interparticle necks with little or no increase in density is consistent with the observations and models discussed by Barsoum [Barsoum 1997], German [German 1996] and Kinergy [Kinergy 1976]. Thus, the mean fracture strength decreases monotonically with increasing P for HA in this study, while in contrast for Part I of this study, a "U – shaped" Weibull modulus, m, versus P trend was found for HA as well as seven other oxides and non-oxides in the literature.

The differences between the $<\sigma_f>$ versus P trend and the m versus P trend reflect the fundamental differences in the statistical meaning of the mean strength $<\sigma_f>$, which is a measure of the central tendency of the strength distribution, and the Weibull modulus, m, which measures the spread in a strength distribution. Thus, $<\sigma_f>$ and m can vary independently. In an entirely analogous way, if one determines the average of a distribution, then one does not necessarily have information about the standard deviation, since the mean and standard deviation, in general, are independent quantities, with one related to the "center" of the distribution and the other related to the spread of the distribution. Appendix A

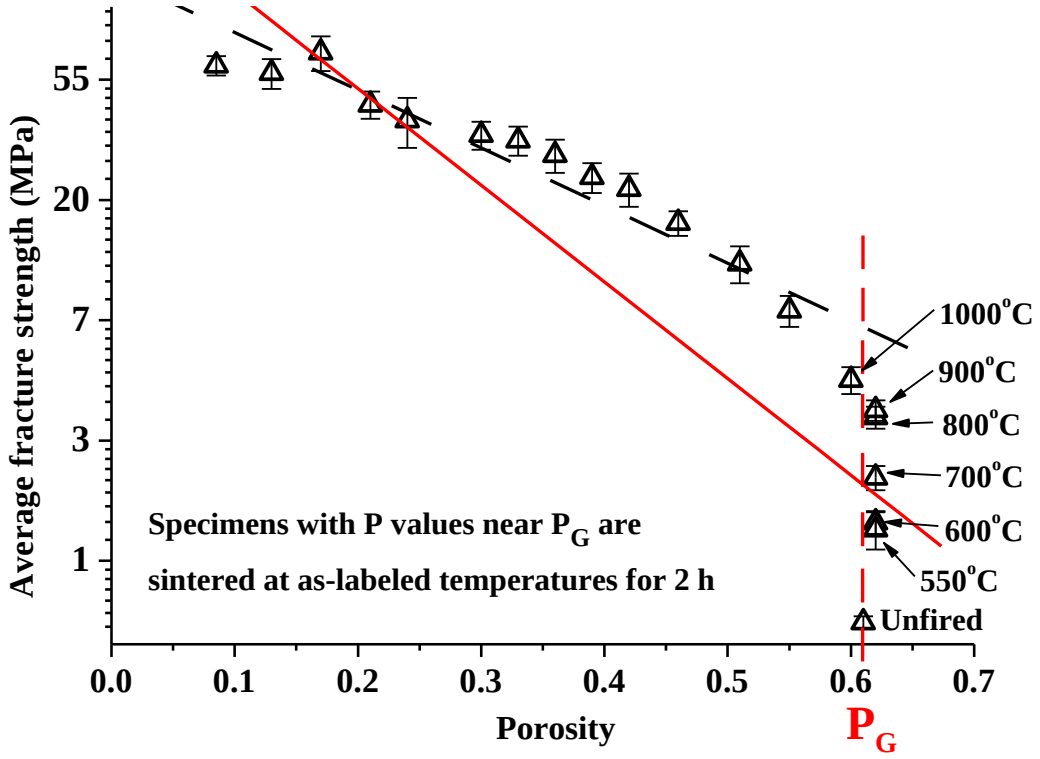

Figure 5.3. Average fracture strength, $\langle\sigma_f\rangle$, of HA [this study] as a function of porosity, P. The solid line represents a least-squares fit of the $\langle\sigma_f\rangle$ versus P data to equation (1) in the entire P range of $0.08 < P < 0.62$. The dashed line represents a least-squares fit of data to equation (1) in the restricted P range of $0.08 < P < 0.55$. For specimens with P values near P_G, the sintering temperature is indicated for each plotted data point. The formation and growth of interparticle necks increase in the fracture strength while not appreciably changing P. Table 4.1 of Chapter 4 gives a complete list of the sintering temperatures and times for each group of specimens shown in this figure.

discusses particular studies that highlight the different behaviors for the $<\sigma_f>$ versus porosity and m versus porosity.

Nine groups of HA specimens with high porosities ($0.47 < P < 0.62$) were fabricated, fractured and analyzed in this study. To the authors' knowledge, no strength data for HA with $P > 0.47$ are available in the literature except for two data points from Villora's study [Villora 2004], where Villora's specimens were composites containing both crystalline HA and SiO_2 phases.

In this study a least-squares fit of all the fracture strength HA data to equation (1) yielded a poor coefficient of determination, R^2, value of 0.786 (Figure 5.3). However, a least-squares fit restricted to a subset of data (with $P < 0.6$) yielded a higher R^2 value of 0.915 (Figure 5.3).

However, in contrast to using equation (1) for the least-squares fit of $<\sigma_f>$ versus P for this study's HA data, when the least-squares fit to equation (4) was instead performed on $<\sigma_f>/ \sigma_0$ versus ϕ for the entire porosity range, an R^2 value of 0.989 was obtained (Figure 5.4). Thus as demonstrated by comparing Figures 5.3 and 5.4, equation (4) describes the $<\sigma_f>/ \sigma_0$ versus P behavior of HA [this study] over the entire range of porosity included in this study; while the exponential strength-porosity relationship represented by equation (1) only fits $<\sigma_f>/ \sigma_0$ versus P data well for P values less than about 0.6.

For the HA specimens in this study that were sintered in air at temperatures between 550^oC and 1000^oC (Part I, Table 5.1), the specimens' volume fraction porosity was essentially constant at 0.62. However, the mean specimen strength more than tripled,

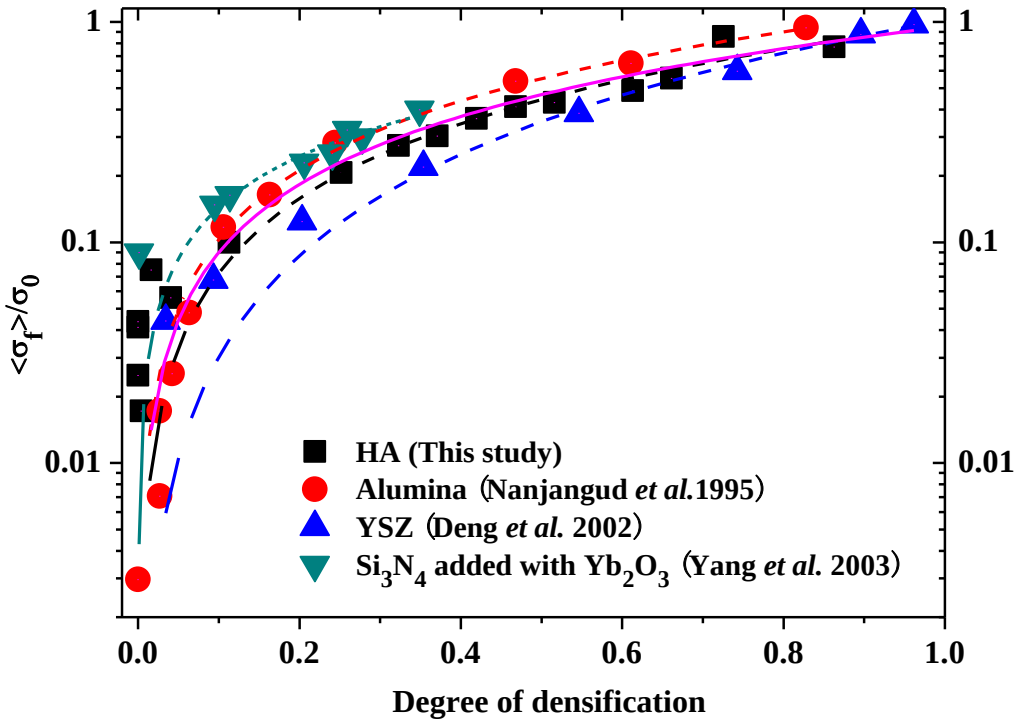

Figure 5.4. Relative fracture strength $\langle\sigma_f\rangle/\sigma_0$ as a function of degree of densification, ϕ, for HA [this study], and literature values of alumina [Nanjangud 1995], YSZ [Deng2002] and silicon nitride [Yang2003]. Each dashed curve represents a least-squares fit to equation (4) for each data set. The solid curve represents a least-squares fit to equation (4) for the combined data sets. The parameters for the least-squares fit of the relative strength versus degree of densification data to equation (4) are listed in Table 5.1.

from 1.3 MPa for specimens fired at 550^{o}C to 4.5 MPa for specimens fired at 1000^{o}C (Table 5.1 in Part I of this paper). The increase in specimen strength without an accompanying increase in specimen density likely results from powder particle necking, where necking is a common phenomenon associated with the initial stage of sintering [Barsoum 1997, German 1996]. With increasing sintering temperature, the dimensions of the interparticle necks progressively increase [Barsoum 1997, Kingery 1976]. As suggested by Nanjangud [Nanjangud 1995] in their study of partially sintered alumina, the increasing dimension of interparticle necks is consistent with increasing fracture strength.

4.2.2 Mechanisms for strength and Young's modulus of green powder compacts

The HA specimens in this study that were tested in the green (unfired) state (P~0.61) had a very low average fracture strength of 0.6 MPa. In contrast to the partially sintered HA specimens, interparticle necking does not occur in the unfired powder compact since at room temperature the mass diffusion needed to develop interparticle necks [Barsoum 1997] is negligible. Thus, instead of interparticle necking, other mechanisms must account for the observed fracture strength of the green powder compacts. These mechanisms likely include van der Waals attractions [Flatt 2004], hydrogen bonding [Libowitzky 1999], electrostatic interactions as well as the cohesive forces between particles generated through capillarity [Hornbaker 1997]. In addition to these molecular level mechanisms, there may also be contributions to mechanical strength based on mesoscopic level mechanisms, such as a mechanical interlocking among powder particles [German 1984]. Such mechanical effects may be enhanced by rod-shaped HA powder particles included in this study.

Powder compacts and porous specimens exposed to atmospheric humidity may absorb moisture from the air. Particle-particle interactions between dry (especially microscopic-scale and smaller) particles are dominated by van der Waals bonding [Flatt 2004, Fung2009, Quintanilla 2006, Yang 2007, Yu 2003] while interactions between wet particles are dominated by capillarity [Fung2009, Yang 2007, Yu 2003]. For unfired particle compacts in materials with crystal structures (such as HA) that contain hydroxyl groups and oxygen ions, hydrogen bonds may also be present [Libowitzky 1999, Stelte 2011]. Electrostatic interactions also may contribute to bonding between particles of dielectric (not electrically conducting) materials such as HA, where the electrostatic interaction between the Ca ions and the phosphate groups likely play a role in binding green HA powder compacts.

In this study, an indication that water may play a role in binding together the particles in the green compacts arises from the fact that the green (unfired) HA specimens had a volume fraction porosity of about 0.61, while the specimens sintered at 550^{o}C to 1000^{o}C had a volume fraction porosity of about 0.62. The slightly lower apparent volume fraction porosity for the green HA compacts aged in air compared to the partially sintered specimens is likely due to water forming liquid bridges at particle contact points and/or accumulating in the voids between particles [Mitarai and Nori 2006].

Thus, there are many possible binding mechanisms for brittle, non-conducting powder compacts such as HA compacts included in this study. However, these binding modes are fundamentally different from the mechanism of interparticle necking produced by diffusive transport during sintering. Therefore, while it makes physical sense that the powder compacts

possess a non-zero fracture strength, the fracture strength of green compacts is likely dependent on the ambient environment and should not be considered as a “zero point” in the evolution of strength versus sintering temperature and time since the process of strengthening via diffusion (sintering) involves the growth of necks between adjacent particles and thus is physically very different than processes such as Van der Waals bonding and capillarity that contribute to the strength of green powder compacts.

Recall that in Sections 2.1 and 2.2 of this study, each of equations 2 - 4 for the dependence of strength on P as well as equations 7 - 10 for the E versus P behavior involved either the green density, P_G, or a critical porosity, P_C. Furthermore, P_C (equations 2 and 3) was defined somewhat similarly to P_G. Also, although not specifically included in either equation (1) or equation (5), Rice [Rice 1998] discussed the concept of a critical porosity, P_C, such that for $P > P_C$ the exponential equations (1) and (5) no longer described the strength or Young's modulus versus P behavior, respectively, although Rice did not specify a means of determining P_C. This section points out although P_G or P_C is fundamentally connected to the models described in Section 2, the physical mechanisms that give rise to the strength and elastic modulus for green (unfired) specimens are almost certainly different than the mechanisms that are important after interparticle necking begins. Nevertheless, the P value at which the strength and elastic modulus values are likely dominated by the formation and growth of interparticle necks is likely very close to P_G, so that using the porosity of the green compact as P_G likely does not cause significant errors specifically in equations (4) and (10),

which were used in this paper to describe the P (ϕ) dependence of fracture strength and elastic modulus.

4.2.3 Relative mean fracture strength, $<\sigma_f>/\sigma_0$, as a function of degree of densification, ϕ, from literature

Among the limited number of σ_f versus P studies in the literature that include P values ranging from roughly green (unfired) density to near full density are: Nanjangud's alumina study [Nanjangud 1995], the current authors' HA research [this study], Deng's YSZ work [Deng 2002] and Yang's silicon nitride study [Yang 2003] (Figure 5.4). Since none of these four data sets [Deng 2002, Nanjangud 1995, Yang2003, this study] included experimental data for theoretically dense specimens, the σ_0 values (where for each material, σ_0 is the σ_f value at P = 0) were estimated from the extrapolation of the strength versus porosity plots (Table 5.1) in each reference [Deng 2002, Nanjangud 1995, Yang2003, this study].

When the combined data are plotted in terms of log ($<\sigma_f>/\sigma_0$) versus degree of densification, ϕ, the four data sets [Deng 2002, Nanjangud 1995, Yang 2003, this study] follow the same trend (Figure 5.4). A least-squares fit of the combined average strength versus ϕ data to equation (4) yielded $A_\sigma = 0.95 \pm 0.03$, $n = 1.02 \pm 0.06$ and $R^2 = 0.948$ (Table 5.1 and Figure 5.4).

For the $<\sigma_f>/\sigma_0$ versus ϕ data plotted in Figure 5.4 [Deng2002, Nanjangud 1995, Yang2003, this study], information concerning the material, porosity, shape forming technique, sintering conditions, fracture testing technique and loading rate are summarized in Table 5.2. Since each of the factors given in Table 5.2 can affect fracture strength, it is

Table 5.2. Materials, particle size, shape forming technique, specimen dimensions, green porosity, fracture testing technique and loading rate for the HA specimens in this study and the materials from the literature [Deng 2002, Nanjangud 1995, Yang 2003] included in this study's analysis on $<\sigma_f>/\sigma_0$ versus degree of densification, ϕ.

References	Materials	Particle size (μm)	Shape forming technique	Specimen dimensions	Green porosity (P_G)	Fracture test tech. & loading rate
Nanjangud 1995	Commercial green extruded alumina	N/S	Extruded	Rods: ~ 7.5 x 75 mm [a] Bars: 62 x 10 x 4 mm	~ 42%	4 point bend 25.4 mm/min
Deng 2002	Yttria - stabilized tetragonal ZrO_2 granules	0.028	Single - ended pressing at 30 MPa and 75 MPa	3 x 4 x 40 mm	60 % at 30 MPa and 56 % at 75 MPa	3 point bend 0.5 mm/min
Yang 2003	95.5 % α - Si_3N_4, 1.3 wt. % oxygen, 1 to 7.5 wt. % Yb_2O_3 added	0.55	Uniaxially pressed at 20 MPa	3 x 4 x 40 - 50 mm	55 - 58 %	3 point bend 0.5 mm/min
This study	Commercial HA powder	10.20	Uniaxially cold pressed at 27 MPa	23.8 - 32.2 x 1.85 - 2.55 mm [b]	~ 62 %	Biaxial flexure 1 mm/min

[a] Diameter and length of rod-shaped specimens

[b] Diameter and thickness of disc-shaped specimens

important to consider the differences among the studies [Deng 2002, Nanjangud 1995, Yang 2003, this study] in terms of these processing and testing factors.

4.3 Relative Young's modulus as a function of ϕ for HA and other brittle materials

As is the case for $<\sigma_f>$ as a function of P, there are a limited number of studies in the literature that provide Young's modulus versus P data for values of P extending from near green density to approximately full density. The few materials for which there are studies that do include a wide range of <E> versus P data are alumina [Hardy and Green 1995, Nanjangud 1995, Ren 2009], HA [Ren 2009], titanium [Oh 2003] and YSZ [Deng 2002].

In this study, we least-squares fit the relative Young's modulus, $<E>/E_0$, versus the degree of densification,ϕ data to equation (10) from four different materials: alumina [Hardy and Green 1995, Nanjangud 1995, Ren 2009], HA [this study, Ren 2009], titanium metal [Oh 2003] and 3 mol% YSZ [Deng 2002] (Figure 5.5). The materials' green porosity P_G, the Young's modulus at theoretical density, E_0, and the fitting No single study in the current literature provides a comparison among $<E>/E_0$ versus ϕ data for several different materials. However, in this study we demonstrate that equation (10) describes well the $<E>/E_0$ versus ϕ data behavior of multiple data sets (Figure 5.5). In particular, Ren's HA specimens [Ren 2009] were fabricated and tested in the same way as the HA specimens in this study and as expected, the $<E>/E_0$ versus ϕ results (Figure 5.5) are quite similar between this study and Ren's study [Ren 2009]. However, the Ren study included <E> versus P data only for $P < 0.5$ while this study included data for P up to 0.62.

Table 5.3. Experimentally determined values of green porosity, P_G, Young's modulus corresponding to theoretically dense materials, E_0, number of data points, N, and least-squares fitting parameters, A_E and q, for the fit of E/E_0 versus degree of densification, ϕ, to equation (10) with coefficient of determination, R^2 for HA [this study, Ren 2009], alumina [Nanjangud 1995, Hardy 1995, Ren 2009], titanium [Oh 2003] and YSZ [Deng 2002].

Reference	Material	P_G	E_0 (GPa)	N	A_E	q	R^2
This study	HA	0.62	120[a]	10	0.84 ± 0.07	1.20 ± 0.12	0.979
Ren 2009	HA	0.62	120[a]	15	0.95 ± 0.01	1.38 ± 0.02	0.998
Ren 2009	Alumina	0.47	402.8[b]	9	0.93 ± 0.03	0.92 ± 0.07	0.979
Hardy 1995	Alumina	0.46	402.8[b]	13	1.01 ± 0.08	0.83 ± 0.11	0.905
Nanjangud 1995	Alumina	0.42	402.8[b]	35	0.97 ± 0.02	0.90 ± 0.03	0.988
Oh2003	Titanium	0.36	114.6[c]	25	0.78 ± 0.03	0.64 ± 0.05	0.948
Oh2003	Titanium	0.36	105[d]	25	0.85 ± 0.03	0.64 ± 0.05	0.948
Deng 2002	YSZ	0.56	234.8[e]	7	0.87 ± 0.02	1.19 ± 0.06	0.995

[a] Aggregate average Young's modulus from single crystal data [Landolt and Bornstein 1979].

[b] Aggregate average Young's modulus from single crystal data [Wachtman 1960].

[c] Aggregate average Young's modulus from single crystal data [Fisher and Renken 1964].

[d] E_0 was estimated from the extrapolation of the E vs. P plot (Figure 5.3 in [Oh 2003])

[e] Calculated from aggregate average E from single crystal zirconia stabilized with 2.8 mol% and 3.4 mol % yttria [Ingel and Lewis 1988].

In the three studies of partially sintered alumina by Nanjangud [Nanjangud 1995], Hardy [Hardy and Green 1995] and Ren [Ren 2009], the Young's modulus data was normalized by E_0, value of E at P = 0. Hardy [Hardy and Green 1995] and Nanjangud [Nanjangud 1995] fit their <E> versus P data to equation (9), while Ren [Ren 2009] fit the <E> versus P data to equations (5) and (6). Nevertheless, the studies by [Nanjangud 1995], Hardy [Hardy and Green 1995] focused only on the partially sintered alumina included in their own studies. Ren [Ren 2009] not only studied partially sintered alumina and HA but also compared (i) the $<E>/E_0$ versus P behavior for their alumina specimens to literature data for alumina and (ii) the $<E>/E_0$ versus P behavior for their HA specimens to literature data for HA. However, Ren [Ren 2009] did not systematically compare their alumina and HA data.

4.4 Physical interpretation of the descriptions of $<E>/E_0$ and as a function of degree of densification, ϕ

In terms of the success that equations (10) and (4) have, respectively, in describing the Young's modulus, $<E>/E_0$ versus ϕ behavior (Figures 5.5) and the fracture strength, $<\sigma_f>/\sigma_0$ versus ϕ behavior (Figure 5.4) for each of the materials analyzed in this study, the physical interpretation of that success must begin with a consideration of the data that has been examined in this study. Each of the materials included in the fracture strength (Figure 5.4) and the Young's modulus (Figures 5.5) analysis were single phase, partially sintered powder compacts without pore forming agents (Tables 5.2 and 5.4a), indicating that the specimens in each study likely had a unimodal pore size distribution [Rice 1998].

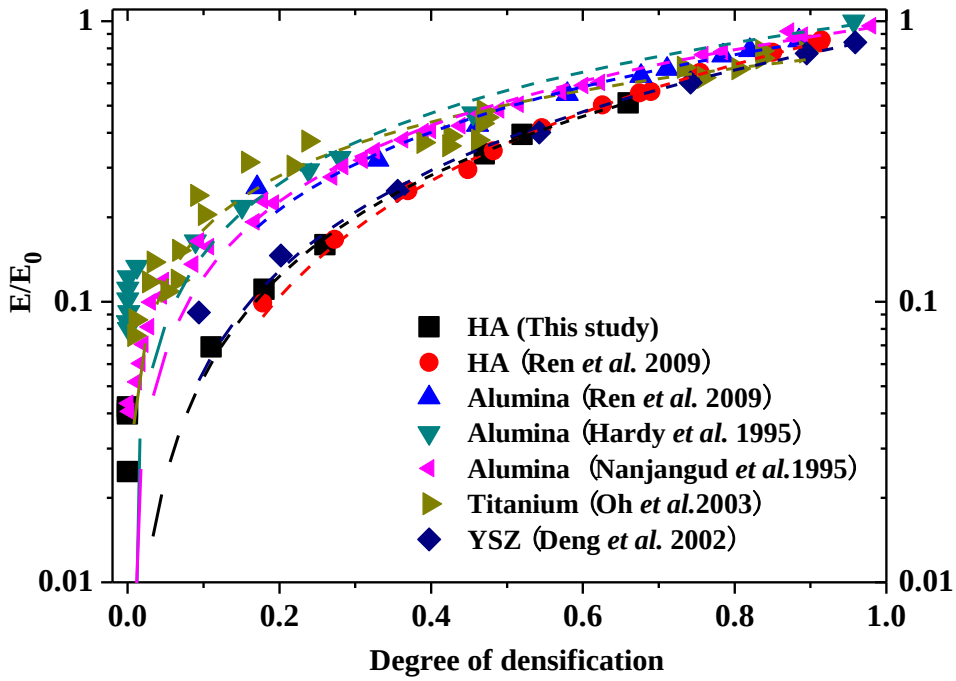

Figure 5.5. Relative Young's modulus, $\langle E \rangle / E_0$, versus ϕ for HA [this study], HA from literature [Ren 2009] alumina [Hardy and Green 1995, Nanjangud 1995, Ren 2009], titanium [Oh 2003] and YSZ [Deng 2002]. Each dashed curve represents a least-squares fit of $\langle E \rangle / E_0$ versus ϕ data to equation (10). The parameters for the least-squares fit of the data sets to equation (10) are listed in Table 5.3.

Table 5.4a. Processing details for HA [Ren 2009], alumina [Hardy 1995, Ren 2009] and titanium [Oh 2003] included in this study's analysis E/E_0 versus degree of densification, ϕ. Processing information for additional data in the E/E_0 analysis for alumina [Nanjangud 1995], YSZ [Deng 2002] and HA [this study] is included in Table 5.2.

References	Materials, purity and vendor	Powders	Green porosity (P_G)	Shape forming technique	Sintering temperatures
HA Ren 2009	Commercial HA powder (Taihei Chemical Industrials Co., Osaka, Japan)	Average particle size: 1 - 3 μm	~ 62 %	Uniaxially cold pressed at 33 MPa	1125^{o}C to 1360^{o}C for 1 h to 6 h
Alumina Ren 2009	Commercial alumina powders (Baikowski RC-HP, Malakoff, TX)	Vendor-specified average powder particle size of 0.3 μm	~ 47 %	Uniaxially cold pressed at 23 MPa	1200^{o}C to 1475^{o}C for 1 h to 4 h
Alumina Hardy 1995	Commercially available alumina (Malakoff Industries, TX) >99.99% purity	Median particle size of 0.38 μm	~ 46 %	Uniaxially pressed at 45 MPa	800^{o}C to 1600^{o}C for 2 h
Ti Oh 2003	Commercially available Ti powders fabricated by plasma rotating electrode process and the gas atomization process. Gas atomized Ti powders supplied by Sumitomo Titanium Corp.	300 – 500 μm (mean diameter 374 μm); 150 – 250 lm (mean diameter 189 μm) and 45 – 150 lm (mean diameter 65 μm)	~ 36 %	Pressed at 70 MPa for 0.6 ks then pressurelessly sintered in vacuum at 1173 K, 1373 K and 1573 K, for 7.2 ks. Also sintered under uniaxial punch pressure of 5 or 10 MPa at 1173 K for 7.2 ks and 1 MPa at 1223 K for 7.2 ks.	

Table 5.4b. Details of the Young's modulus, E, measurement techniques for HA [this study] and for the materials from the literature (HA [Ren 2009], alumina [Nanjangud 1995, Hardy 1995, Ren 2009], titanium [Oh 2003] and YSZ [Deng 2002]) included this study's analysis of E/E_0 versus degree of densification, ϕ. The measurement technique is significant since the isothermal moduli (determined by static or quasistatic testing) is typically about 10 percent lower that the adiabatic moduli (determined by dynamic testing) on the same material.

Reference	Materials	E measurement techniques	Type of E measurement
This study	HA	Resonant ultrasound spectroscopy	Dynamic
Ren 2009	HA	Resonant ultrasound spectroscopy	Dynamic
Ren 2009	Alumina	Resonant ultrasound spectroscopy	Dynamic
Hardy 1995	Alumina	Ultrasonic velocity technique	Dynamic
Nanjangud 1995	Alumina	Ultrasonic velocity technique	Dynamic
Oh2003	Ti	Evaluated via the compression test in an elastic range of deformation up to a maximum 1000 N with an applied load of 0.5 N per step	Quasistatic
Deng 2002	YSZ	Pulse-echo method	Dynamic

Table 5.5. Porosity range, strength at zero porosity, σ_0, Young's modulus at zero porosity, $E_{0,}$ number of data points, N, fitting parameters, A and r, and coefficient of determination, R^2 for the least-squares fit of the normalized strength - Young's modulus data to equation (12), for the three data sets (HA [this study], alumina [Nanjangud 1995] and YSZ [Deng 2002]) which included both σ and E data on the same material.

Reference	Material	P range	σ_0 (MPa)	E_0 (GPa)	N	A	r	R^2
This study	HA	0.21 – 0.62	80	120	10	0.954 ± 0.050	0.856± 0.046	0.990
Nanjangud 1995	Alumina	0.07 – 0.42	380	402.75	10	1.282 ± 0.039	1.201± 0.053	0.995
Deng 2002	YSZ	0.02 – 0.49	800	234.8	7	0.962 ± 0.019	1.253± 0.059	0.996

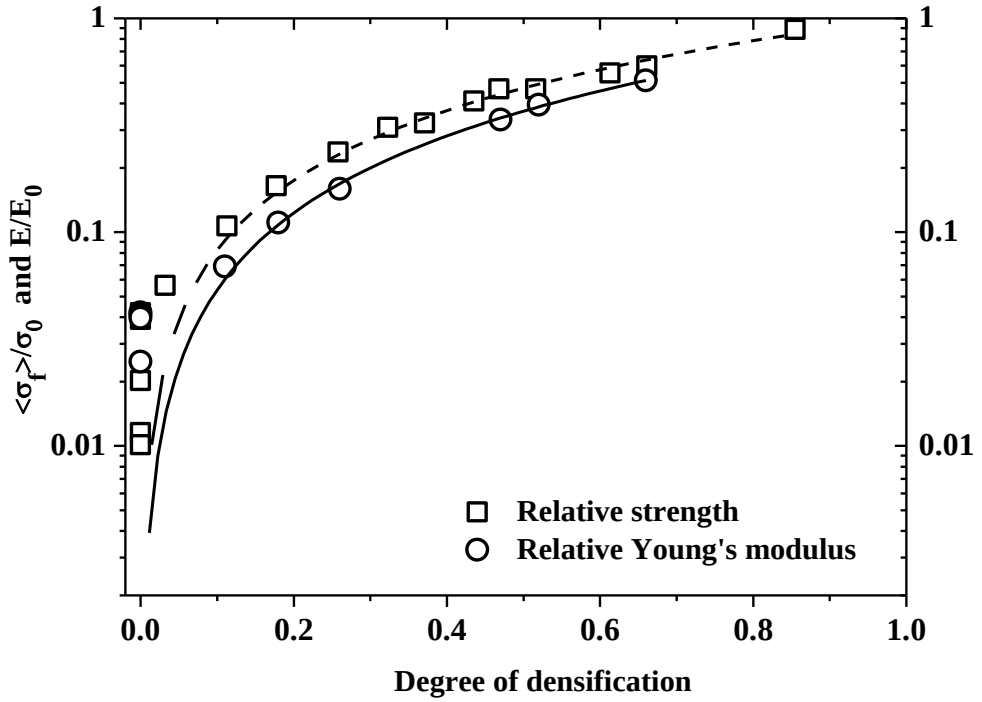

Figure 5.6. The relative average fracture strength, $\langle\sigma_f\rangle/\sigma_0$, and relative Young's modulus, $\langle E\rangle/E_0$, of HA [this study] as a function of degree of densification, ϕ, showing a very similar trend in the relative strength and Young's modulus versus ϕ. The dashed curve represents a least-squares fit of $\langle\sigma_f\rangle/\sigma_0$ to equation (4), and the solid curve represents a least-squares fit of $\langle E\rangle/E_0$ to equation (10).

As was discussed in Part I and by German [German 1994] and Barsoum [Barsoum 1997], during sintering of ceramic [Barsoum 1997] or metal [German 1994] powder compacts, there is a geometrically similar evolution of pore morphology through initial, intermediate and final stages. This near universality of powder-particle-size independent, geometrically-similar pore shape evolution for sintered powder compacts [Barsoum 1997, German 1994, Part I) likely contributes to the ability of any single mathematical form being able to describe the porosity dependence of $<E>/E_0$ versus ϕ and $<\sigma_f>/\sigma_0$ versus ϕ for the range of materials considered here.

In addition, the fracture testing (Table 5.2) in each study was performed on as-sintered, non-polished specimens, though the testing techniques were different in the four studies (ring-on-ring for HA [this study], four-point bend for alumina [Nanjangud 1995] and three-point bend for YSZ [Deng 2002] and silicon nitride [Yang 2003]). Also, for the Young's modulus data, the E measurements were by dynamic techniques (Table 5.4b) with the exception of the Ti study [Oh 2003] where E was measured by quasistatic compression testing. For a given material, E values determined by quasistatic techniques are often roughly 10 percent lower than measurements made by dynamic techniques.

In terms of the physical interpretation of the results of this study, it is helpful to consider the "boundary values" for equations (4) and (10). Consider equation (4), which is

$$\frac{<\sigma_f>}{\sigma_0} = A_\sigma\left(1-\frac{P}{P_G}\right)^n = A_\sigma(\phi)^n$$

When $P \rightarrow$ zero ($\phi \rightarrow$ one) $<\sigma_f>/\sigma_0$ approaches A_σ regardless of the value of the exponent n.

When P → zero, the specimen strength approaches the strength at zero porosity ($\sigma_f \rightarrow \sigma_0$), which means $A_\sigma \rightarrow 1$. When P approaches P_G (ϕ approaches zero), then $<\sigma_f>/\sigma_0 \rightarrow$ zero independently of the numerical values of A_σ or n. For Figure 5.4, the $<\sigma_f>/\sigma_0$ data does (i) approach 0 as ϕ approaches 0 and (ii) approach 1 as ϕ approaches 1. Similarly, for equation (10)

$$\frac{<E>}{E_0} = A_E\left(1-\frac{P}{P_G}\right)^q = A_E(\phi)^q$$

note that for P → 0 (that is, $\phi \rightarrow 1$), then $<E>/E_0 \rightarrow A_E$ for all values of exponent q. Since E → E_0 at P → 0, then A_E also → 1. In addition, if P → P_G, then $<E>/E_0 \rightarrow 0$ regardless of the numerical values of A_E and q. As was the case for the $<\sigma_f>/\sigma_0$ data and equation (4), the $<E>/E_0$ data does approach the asymptotic values expected from equation (10) for $\phi \rightarrow 0$ and $\phi \rightarrow 1$ (Figure 5.5).

Note that the numerical values of A_σ given in Table 5.1 for each of the materials (HA [this study], alumina [Nanjangud 1995], YSZ [Deng 2002] and Si_3N_4 [Yang 2003]) are relatively close to unity, except for alumina where $A_\sigma = 1.14 \pm 0.02$. Physically, for theoretically dense materials $\phi \rightarrow 1$ and $<\sigma_f>/\sigma_0$ approaches A_σ. Thus an A_σ value other than unity may indicate that the value of σ_0 (determined here by extrapolation of the $<\sigma_f>$ versus ϕ plot, see footnotes for Table 5.1) may be greater or smaller than the "true" value of σ_0 for the material. In practice, σ_0 can be problematic to determine since in addition to the included porosity, the actual values of σ_0 depends on the flaw population present in a given specimen [Case 2002, Case in press].

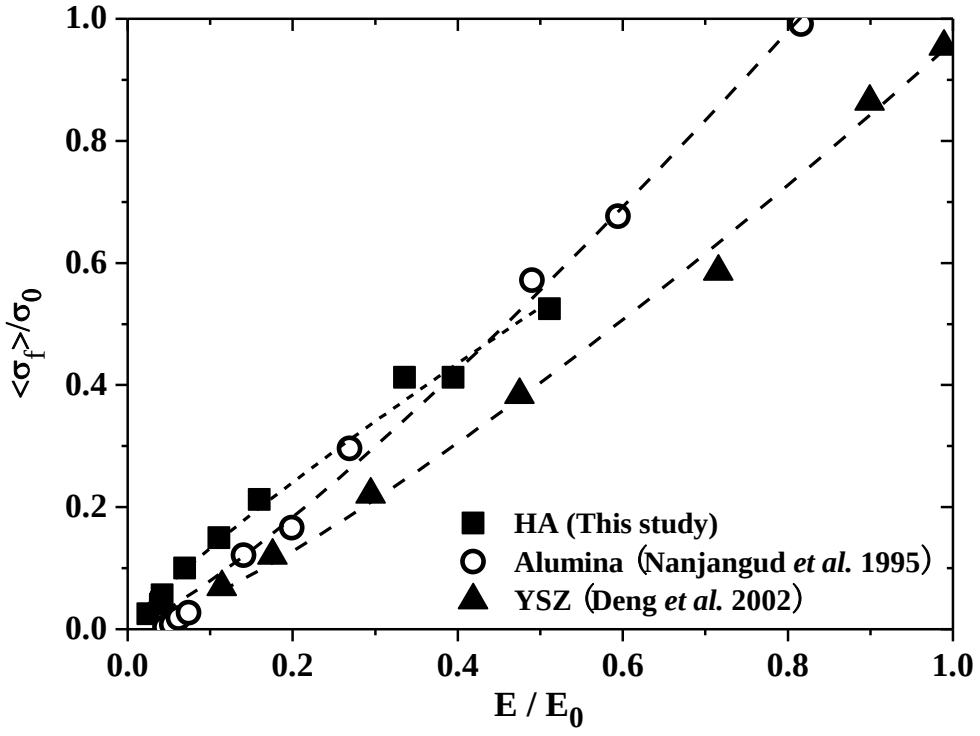

Figure 5.7. Normalized fracture strength $\langle\sigma_f\rangle/\sigma_0$ versus normalized Young's modulus, $\langle E\rangle/E_0$, for HA [this study], alumina [Nanjangud 1995] and YSZ [Deng 2002]. Each dashed line represents a least-squares fit to equation (12).

Also, for equation (10), the A_E values (Table 5.3) are close to, but in most cases, smaller than unity. Values of E_0 are less problematic than σ_0 values to determine, since for polycrystalline materials E_0 can be estimated from the aggregate average of single crystal Young's modulus data from the literature (footnotes for Table 5.3). It is not clear why the A_E values in Table 5.3 are not closer to unity.

For equations (4) and (10), the predictions that $<\sigma_f>/\sigma_0$ and $<E>/E_0$ go to zero for $P \rightarrow P_G$, is somewhat ambiguous [Barsoum 1997, Flatt 2004, Hornbaker 1997, Libowitzky 1999]. For green compacts (for which $P = P_G$ by definition) both the strength and the elastic moduli are dominated by mechanisms that are independent of the diffusional processes [Barsoum 1997, German 1994] that lead to the formation of solid contacts between particles.

4.5 Relationship between Young's modulus and fracture strength for partially sintered powder compacts

Since the relative fracture strength and relative Young's modulus for HA [this study] show very similar trends when plotted on the same normalized property versus degree of densification plot (Figure 5.6), it is natural to inquire about the direct relationship between fracture strength and relative Young's modulus. Combining equations (4) and (10) yields

$$\frac{<\sigma_f>}{\sigma_0} = A_\sigma \left(\frac{<E>}{E_0 A_E} \right)^{\frac{n}{q}} = A \left(\frac{<E>}{E_0} \right)^r \qquad (12)$$

where $A = A_\sigma / (A_E)^r$ and $r = n/q$. A least-squares fit of the $<\sigma_f>/\sigma_0$ versus the $<E>/E_0$ data to equation (12) gives $r = 0.86 \pm 0.05$ for the HA [this study], $r = 1.20 \pm 0.05$ for alumina [Nanjangud 1995] and $r = 1.25 \pm 0.06$ for YSZ [Deng 2002], with coefficients of

determination, R^2, of 0.990, 0.995 and 0.996, respectively (Figure 5.7). Thus, equation (12) describes the porosity dependence of $<\sigma_f>/\sigma_0$ versus the $<E>/E_0$ very well over the range of porosities included in the data (Table 5.5) for HA [this study], alumina [Nanjangud 1995] and YSZ [Deng 2002].

From an empirical point of view, the exponent *r* in equation (12) should be (and in fact is) close to unity since *n* and *q* are both close to unity. In addition, the factor A in equation (12) is a proportionality constant between fracture strength and Young's modulus. When considering the physical meaning of this proportionality, it must be emphasized that the data (Figure 5.7) represents partially sintered powder compacts over a range of volume fraction porosity P. In addition to being functions of porosity, both E and σ_f are functions of the damage state, including microcracking, where microcracks can be introduced into a specimen by various mechanisms such as thermal expansion anisotropy [Case 1981, Case 2002], thermal expansion mismatch [Cleveland 1978], phase transitions [Case 1984]. Also, the functional forms for E and σ_f have differing dependencies on crack size [Case 2002, Case in press, Rice 1998]. For brittle materials E is a function of the third moment of crack radius and σ_f depends on the largest flaw [Case 2002, Case in press], thus if microcracks or other damage were introduced into the partially sintered bodies, it is extremely likely that equation (12) would no longer hold. Nevertheless, equation (12) does describe extremely well the $<\sigma_f>/\sigma_0$ versus the $<E>/E_0$ data for the three brittle ceramics (HA, alumina and YSZ) depicted in Figure 5.7.

4.6. Relationship from literature for fracture toughness and porosity

For the partially sintered alumina specimens, Flinn [Flinn 2000] found the fracture toughness, K_C can be expressed as

$$\frac{K_{c-tip}}{K_{c-tip0}} = \left(1 - \frac{P}{P_1}\right)^j \tag{13}$$

where $K_{c\text{-}tip}$ = crack tip fracture toughness, $K_{c\text{-}tip0}$ = crack tip fracture toughness for a theoretically dense material, and exponent j is an empirically determined constant. Equation (13) and equations (4) and (10) have a similar functional form.

Using a least-squares fitting technique, Flinn [Flinn 2000] found j = 1.15 for their alumina powders, where the exponent j is similar in magnitude to the exponent n in equation (4) and q in equation (10) (Tables 5.1 and 5.3). For Flinn, the volume fraction porosity P_1, in equation (13) is not P_G. Instead Flinn [Flinn 2000] made P_1 in equation (13) an adjustable parameter, obtaining a P_1 value of 0.45 via a least-squares fit of their alumina data.

Flinn [Flinn 2000] also found a linear relationship between E and $K_{c\text{-}tip}$ that is analogous to the nearly linear E versus fracture strength behavior described in equation (12) in this study. However, an important difference between this study and the study by Flinn is that Flinn used pore formers to create bimodal pore size distributions. For specimens that are densified from powder compacts containing particles that are approximately equiaxed, the pore size distribution tends to be unimodal [Rice 1998]. To generate bimodal pore size distribution, researchers often use pore formers, for example: (1) fugitive phases in the form of solid particles that burn out during firing [Yuan 2008] or (2) liquid additives such as hydrogen peroxide volatilize during firing [Ren 2005]. In this study the green HA compacts

were sintered without pore formers (Tables 5.2 and 5.4a), however the HA powders in this study are rod shaped with an aspect ratio of ~ 3, thus the details of the pore size distribution likely depends on the degree of alignment of the powder particles. Nevertheless the Flinn data follows trends similar to those observed in this study. Thus, a comparison of this study with Flinn's study [Flinn 2000] implies that the relationships presented here for the ϕ dependence of $<\sigma_f>/\sigma_0$ (equation 4) and $<E>/E_0$ (equation 10) for materials with unimodal pore size distributions may also apply to materials with bimodal pore size distributions, but further study is needed to explore that topic.

5. Summary and Conclusions

In this study, the fracture strength and Young's modulus were measured for 540 polycrystalline HA specimens. In Part I of this study, the Weibull modulus, m, versus P behavior was examined for the same HA specimens as well as a combined data set with more than 1560 oxides and non-oxides, showing a 3-region, "U" – shaped trend. The Weibull modulus, m, is an important measure of the scatter in fracture strength (mechanical reliability). Also the fracture strength values themselves and the Young's modulus are important where, for example, the analysis of stress and strain by analytical or numerical means requires knowledge of the Young's modulus. Thus, the mechanical behaviors discussed in both Parts I and II are crucial to the design of brittle components.

Equation (4) was applied to describe the ϕ dependence of the normalized fracture strength data for polycrystalline HA [this study], alumina [Nanjangud 1995], 3 mol% yttria stabilized zirconia (YSZ) [Deng 2002] and silicon nitride [Yang 2003] (Figure 5.4). Also, this

study uses equation (10) to fit the Young's modulus versus ϕ data for alumina [Nanjangud 1995, Hardy and Green 1995, Ren 2009], HA [Ren 2009, this study], titanium [Oh 2003] and YSZ [Deng 2002] (Figures 5.5).

Equations (4) and (10) are similar power law functions of ϕ with the exponents ≈ 1 in both cases (Tables 5.1 and 5.3). Also both equations (4) and (10) are excellent descriptors of the ϕ dependence of Young's modulus and fracture strength (Figures 5.4, 5.5 and 5.6) respectively over the entire range of ϕ for specimens of approximately green density ($\phi = 0$) to specimens that are nearly theoretically dense ($\phi = 1$).While earlier researchers [Hardy and Green 1995, Nanjangud 1995] demonstrated a similar equation could be applied to alumina, this study shows that the results apply to many partially sintered brittle materials.

In addition, the similarity of equations that describe the ϕ dependence of $<\sigma_f>$ (equation (4)) and <E> (equation (10)), leads to a nearly linear relationship between $<\sigma_f>/\sigma_0$ and $<E>/E_0$ (equation (12) and Figure 5.7) for HA from this study, alumina [Nanjangud 1995] and yttria (3 mol%) - stabilized zirconia (YSZ) [Deng 2002].

6.0 Acknowledgements

The authors acknowledge the financial support of the National Science Foundation, Division of Materials Research Grant DMR-0706449. In addition, the authors acknowledge the use of the Electron Microscopy facilities at the Center for Advanced Microscopy, Michigan State University. The purchase of the Resonant Ultrasound Spectroscopy apparatus and the laser scattering apparatus equipment used in this study was funded by the Defense University Research Instrumentation Program (DURIP) Grant No.

N00014-07-1-0735.

APPENDIX

APPENDIX

DIFFERING TRENDS FOR THE MEAN FRACTURE STRENGTH AND WEIBULL MODULUS

In previous chapter, the Weibull modulus versus P for a large collection of brittle materials followed a three-region, U-shaped function of the volume fraction porosity, P, which begs the question "Since two of the parameters that characterize the fracture of brittle materials are fracture strength, σ_f, and Weibull modulus, m, then do σ_f and m, follow the same trends as a function of P?" If we examine the fracture strength, σ_f versus P and m versus P behaviors for six studies taken from the literature that include five different brittle materials, namely studies of TiO_2 by Kishimoto [Kishimoto1991], Al_2O_3 by Nanjangud [Nanjangud 1995], niobia-doped ZrO_2 and tantala-doped ZrO_2 by Pissenberger [Pissenberger and Gritzner 1995] and three studies of HA (one study each by Lopes [Lopes 1999], Ruys [Ruys 1995] and Villora [Villora 2004]), the m versus P trend is notably different than the fracture strength versus P behavior for each study. The σ_f versus P data tends to decrease monotonically with increasing P, however, for the m versus P data, there are no apparent trends in part because there are relatively few data points for m versus P in each study [Kishimoto1991, Lopes 1999, Nanjangud 1995, Pissenberger and Gritzner 1995, Ruys1995, Villora2004].

The difference between the physical nature of m and the fracture strength in terms of the characterization of brittle materials is further highlighted in a study by Sharpe [Sharpe 2008]

in which single crystal SiC micro-specimens were fractured in tension. For SiC specimens with circular or elliptical holes, the average tensile fracture strength was quite high, ranging from 0.71 to 1.36 GPa depending on the geometry of the holes. On the other hand, the values of Weibull modulus for the SiC specimens were modest (between 3.7 and 5.9). Thus, high fracture strength does not necessarily correspond to a high Weibull modulus.

However, in contrast to the SiC specimens in Sharpe's study [Sharpe 2008], the HA specimens in this study tested in the green (unfired) state had a very low average fracture strength at 0.6 MPa but a surprisingly high Weibull modulus of 21.2. Again, average fracture strength and Weibull modulus are often not correlated but characterize different physical properties, such that m measures the spread in the strength values and the mean strength indicates the "center" of the strength distribution.

REFERENCES

REFERENCES

[ASTM 2003] ASTM C1499-05, Standard Test Method for Monotonic Equibiaxial Flexural Strength of Advanced Ceramics at Ambient Temperature, 2003.

[Barsoum 1997] Barsoum, M.W., 1997. Fundamentals of ceramics, McGraw-Hill Co., Inc., New York.

[Carniglia 1972] Carniglia, S.C., 1972. Working model for porosity effects on the uniaxial strength of ceramics. J. Am. Ceram. Soc. 55, 610 - 618.

[Case 1981] Case, E. D., Smyth, J. R., Hunter, O., 1981. Microcracking in large-grain Al_2O_3. Mater. Sci. Eng. 51, 175 - 179.

[Case 2002] Case, E.D., 2002. The Saturation of Thermomechanical Fatigue in Brittle Materials, WIT Press, Southampton, UK.

[Case in press] Case, E. D., Thermo-mechanical properties of thermoelectric materials, Chapter 16 in CRC Handbook: Thermoelectrics and its Energy Harvesting: Modules, Systems and Applications, CRC Press, Boca Raton, FL, in press.

[Case 1985] Case E. D. and Glinka, C., 1984. Characterization of Microcracks in $YCrO_3$ Using Small Angle Neutron Scattering and Elasticity Measurements, J.Mater. Sci. 19 2962 - 2968.

[Cleveland 1978] Cleveland, J.J., Bradt, R.C., 1978. Grain size/microcracking relations for pseudobrookite oxides. J. Am. Ceram. Soc. 61, 478 - 481.

[Deng 2002] Deng, Z-Y., Yang, J-F., Beppu, Y., Ando, M., Ohji, T., 2002. Effect of agglomeration on mechanical properties of porous zirconia fabricated by partial sintering, J. Am. Ceram. Soc. 85, 1961 – 1965.

[Duckworth 1953] Duckworth, W., 1953. Discussion of Ryshkewitch paper by Winston Duckworth. J. Am. Ceram. Soc. 36, 68.

[Fisher 1964] Fisher, E.S., Renken, C.J., 1964. Single-crystal elastic moduli and the hcp → bcc transformation in Ti, Zr, and Hf. Phys. Rev. 135A, 482 – 494.

[Flatt 2004] Flatt, R.J., 2004. Dispersion forces in cement suspensions. Cement and Concrete Res. 34, 399 - 408.

[Flinn 2000] Flinn, B. D., Bordia, R. K., Zimmermann, A., Rodel, J., 2000. Evolution of defect size and strength of porous alumina during sintering. J. Eur. Ceram. Soc. 20, 2561 - 2568.

[Fung 2009] Fung, W. W. S., Kwan, A. K. H., Wong, H. H. C., 2009. Wet packing of crushed rock fine aggregate. Mater. Struct. 42, 631 - 643.

[German 1984] German, R.M., 1984. Powder Metallurgy Science, Metal Powder Industries Federation, New Jersey.

[German 1994] German, R.M., 1994. Powder Metallurgy Science, Metal Powder Industries Federation, New Jersey.

[German 1996] German, R.M., 1996. Sintering Theory and Practice, John Wiley & Sons, Inc., New York.

[Hardy 1995] Hardy, D., Green, D.J., 1995. Mechanical properties of a partially sintered alumina, J. Eur. Ceram. Soc. 15, 769-715.

[Hornbaker 1997] Hornbaker, D. J., Albert, R., Albert, I., Barabasi, A. L., Schiffer, P., 1997. What keeps sandcastles standing? Nature 387, 765.

[Ingel 1988] Ingel, R.P., Lewis III, D., 1988. Elastic anisotropy in zirconia single crystals. J. Am. Ceram. Soc. 71, 265 - 271.

[Kingery 1976] Kingery, W.D., 1976. Introduction to Ceramics, John Wiley & Sons, Inc., New York.

[Kishimoto 1991] Kishimoto, A., Koumoto, K., Yanagida, H., Nameki, M., 1991. Microstructure Dependence of Mechanical and Dielectric Strengths .1. Porosity. Eng. Fract. Mech. 40, 927-930.

[Lam 1994] Lam, D.C.C., Lange, F.F., Evans, A.G., 1994. Mechanical properties of partially dense alumina produced from powder compacts. J. Am. Cer. Soc. 77, 2113 –2117.

[Landolt 1979] Landolt, H., Bornstein, R., 1979. Elektrische, Piezoelektrische, Pyroelektrische, Piezooptische, Elektrooptische Konstanten und Nichtlineare Dielektrische Suszeptibilitaten, Zahlenwerte und Funktionen aus Naturwissenschaften und Technik, Gruppe III, Bd. 11. Springer-Verlag, Berlin.

[Libowitzky 1999] Libowitzky, E., 1999. Correlation of O-H Stretching Frequencies and O-H---O Hydrogen Bond Lengths in Minerals. Monatsh. Chem. 130, p.1047 - 1059.

[Lopes 1999] Lopes, M.A., Monteiro, F.J., Santos, J.D., 1999. Glass-reinforced hydroxyapatite composites: Secondary phase proportions and densification effects on biaxial bending strength. J. Biomed. Mater. Res. 48, 734-740.

[Manning 1972] Manning, W.R., Hunter O., Calderwood, J.W., Stacy, D.W., 1972. Thermal Expansion of Nb_2O_5. J. Am. Ceram. Soc. 55, 342 - 347.

[Martin 1973] Martin, H.C., and Carey, G.F., 1973. Introduction to Finite Element Analysis.

McGraw-Hill, New York.

[Millard 1959] Millard, D.J.Br., 1959. Relationship between strength and porosity for coal compacts. J. Appl. Phys. 10, 287 - 290.

[Mitarai 2006] Mitarai, N., Nori, R., 2006. Wet granular materials. Adv. Phys. 55, 1 - 45.

[Nanjangud 1995] Nanjangud, S.C., Brezny, R., Green, D.J., 1995. Strength and Young's Modulus Behavior of a Partially Sintered Porous Alumina. J. Am. Ceram. Soc. 78, 266-268.

[Nye 1957] Nye, J. F., 1957. Physical Properties of Crystals: Their Representation by Tensors and Matrices, Oxford University Press.

[Oh 2003] Oh, I-H., Nomura, N., Masahashi, N., Hanada, S., 2003. Mechanical properties of porous titanium compacts prepared by powder sintering. Scripta Mater. 49, 1197 - 1202.

[Phani 1987] Phani, K. K., Niyogi, S. K., 1987. Young's modulus of porous brittle solids, J. Mater. Sci. 22, 257-263.

[Pissenberger 1995] Pissenberger, A., Gritzner, G., 1995. Preparation and Properties of Niobia-Doped and Tantala-Doped Orthorhombic Zirconia. J. Mater. Sci. Lett. 14, 1580-1582.

[Quintanilla 2006] Quintanilla, M. A. S., Valverde, J. M., Castellanos, A., 2006. Adhesion force between fine particles with controlled surface properties. AICHE J. 52, 1715 - 1728.

[Ren 2005] Ren, F., Smith, I.O., Baumann, M. J., Case, E. D., 2005. Three-dimensional microstructural characterization of porous hydroxyapatite using confocal laser scanning microscopy. Int. J. Appl. Ceram. Technol. 2, 200 –211.

[Ren 2006] Ren, F., Case, E. D., Timm, E. J., Jacobs, M. D., Schock, H. J., 2006. Weibull analysis of the biaxial fracture strength of a cast p-type LAST-T thermoelectric material. Phil. Mag. Lett. 86, 673 - 682.

[Ren 2008] Ren, F., Case, E. D., Sootsman, J.R., Kanatzidis, M.G., Kong, H., Uher, C., Lara-Curzio, E., Trejo, R.M., 2008. The high-temperature elastic moduli of polycrystalline PbTe measured by resonant ultrasound spectroscopy. Acta Mater. 56, 5954 - 5963.

[Ren 2009] Ren, F., Case, E. D., Morrison, A., Tafesse, M., Baumann, M. J., 2009. Resonant ultrasound spectroscopy measurement of Young's modulus, shear modulus and Poisson's ratio as a function of porosity for alumina and hydroxyapatite. Philos. Mag. 89, 1163 - 1182.

[Rice 1998] Rice, R.W., 1998. Porosity of Ceramics, Marcel Dekker, Inc., New York.

[Rice 2000] Rice, R.W., 2000. Mechanical properties of ceramics and composites: grain and particle effects, Marcel Dekker, New York.

[Ruys 1995] Ruys, A.J., Wei, M., Sorrell, C.C., Dickson, M.R., Brandwood, A., Milthorpe,

B.K., 1995. Sintering Effects on the Strength of Hydroxyapatite. Biomaterials 16, 409-415.

[Ryshkewitch 1953] Ryshkewitch, E., 1953. Compression strength of porous sintered alumina and zirconia, J. Am. Ceram. Soc. 36, 65–68.

[Schiller 1958] Schiller, K.K., 1958. Porosity and strength of brittle solids (with particular reference to gypsum), mechanical properties of non-metallic brittle materials, Intersciemce Pub. Inc., New York.

[Sharpe 2008] Sharpe, W. N. Jr., Beheim, G. M., Evans, L. J., Nemeth, N. N., Jadaan, O. M., 2008. Fracture strength of single-crystal silicon carbide microspecimens at 24°C and 1000°C. J. Microelectromech. S. 17, 244 - 254.

[Spriggs 1961] Spriggs, R.M., 1961. Expression for effect of porosity on elastic modulus of polycrystalline refractory materials, particularly aluminum oxide. J. Am. Ceram. Soc. 44, 628 - 629.

[Stelte 2011] Stelte, W., Holm, J. K., Sanadi, A. R., Barsberg, S., Ahrenfeldt, J., Henriksen, U.B., 2011. A study of bonding and failure mechanisms in fuel pellets from different biomass resources. Biomass Bioenerg. 35, 910 - 918.

[Villora 2004] Villora, J.M., Callejas, P., Barba, M.F., Baudin, C., 2004. Statistical analysis of the fracture behaviour of porous ceramic Raschig rings. J. Eur. Ceram. Soc. 24, 589-594.

[Wachtman 1960] Wachtman, J.B., Tefft, W.E., Lam, D.G., Stinchfield, R.P., 1960. Elastic constants of synthetic single crystal corundum at room temperature. J. Res. Nat. Bur. Stand. 64A, 213 – 228.

[Wachtman 2009] Wachtman, J.B., Cannon, W.R., Matthewson, M.J., 2009. Mechanical Properties of Ceramics, Second Edition, John Wiley & Sons, Inc..

[Yang 2003] Yang, J-F., Deng, Z-Y., Ohji, T., 2003. Fabrication and characterisation of porous silicon nitride ceramics using Yb_2O_3 as sintering additive. J. Eur. Ceram. Soc. 23, 371-378.

[Yang 2007] Yang, R.Y., Zou, R.P., Dong, K.J., An, X.Z., Yu, A., 2007. Simulation of the packing of cohesive particles. Comput. Phys. Commun. 177, 206 – 209.

[Yu 2003] Yu, A. B., Feng, C. L., Zou, R. P., Yang, R. Y., 2003. On the relationship between porosity and interparticle forces. Powder Technol. 130, 70 - 76.

[Yuan 2008] Yuan, C., Vandeperre, L.J., Stearn, R.J., Clegg, W.J., 2008. The effect of porosity in thermal shock. J Mater. Sci. 43, 4099 – 4106.

CHAPTER 6

THE EFFECT OF INDENTATION-INDUCED MICROCRACKS ON THE ELASTIC MODULUS OF HYDROXYAPATITE

X. Fan, E. D. Case and M. J. Baumann
Department of Chemical Engineering and Materials Science, Michigan State University, East Lansing, MI, 48824

Published in: J Materials Science, 47:6333-6345, 2012.

Abstract

The presence of microcracks in materials affects a wide range of mechanical properties including elastic modulus, Poisson's ratio, fracture strength and fracture toughness. The microcrack-induced reductions of the Young's modulus, E, and Poisson's ratio, υ, are functions of the size, geometry and number density of microcracks. In this study, an array of Vickers indentation microcracks was placed on the surfaces of two hydroxyapatite (HA) specimens with totals of 391 and 513 indentations per specimen. This study tests the validity of theoretical studies of microcrack-damage-induced changes in E and υ, where the changes are expressed either by (i) the volumetric crack number density, N and (ii) the crack damage parameter, ε. All elasticity measurements were done via resonant ultrasound spectroscopy. For both the HA specimens included in the study and alumina specimens indented in an earlier study [Kim 1993], E and υ decreased approximately linearly with increasing microcrack damage. The slopes of the E and υ versus N and ε are also computed and compared to the available theoretical models.

1. Introduction

Applications of hydroxyapatite (HA, $Ca_{10}(PO_4)_6(OH)_2$), both in dense and porous forms, include filters [Misra 2005, da Silva 2006], catalytic supports [Opre 2005, Jamwal 2008, Rakap 2011] and dielectric coatings [Silva 2003, Silva 2005]. In addition, HA is used in many types of sensors, including those for toxic metal ions [El Mhammedi 2009], CO gas [Mahabole 2005], proteins [Ohtsuki 2010] and humidity [Owada 1989]. HA is also widely studied as a candidate for engineered hard tissue (bone and teeth) due to its chemical similarity to natural bone mineral and its excellent biocompatibility [Hench 1991, Burg 2000, Karageorgiou 2005].

The Young's modulus, E, and Poisson's ratio, υ, are two fundamental mechanical properties of materials. For example, for bodies with complex geometries, analytical methods to calculate stress and strain often become mathematically unwieldy, thus numerical techniques such as finite element techniques are needed [Martin 1973]. The construction of the stiffness matrix for finite element calculations and simulations requires Young's and Poisson's ratio data [Martin 1973].

Brittle materials including HA often incur microcrack damage and in general microcracks affect a wide range of mechanical properties including Young's modulus [Smith 1995, Perera 2010, Chotard 2008, Patapy 2009, Yousef 2005], Poisson's ratio [Case 1984, Wang 2009], fracture strength [Rokhlin 1993, Diaz 2008], hardness [Perera 2010] and fracture toughness [Evans 1986, Kratschmer 2011, Hubner 1977, Meschke 1997]. Other physical properties such as electrical conductivity [Ota 1986, Hilpert 2004], thermal

diffusivity [Hasselman 1993, Deroo 2010], thermal expansion [Chotard 2008] and dielectric constant [Kimura 1990, Morito 2005] are also functions of the microcrack damage state.

In particular, the median and radial microcracks induced by Vickers indentation (Figures 6.1a and 6.1b) are widely used to model the flaws produced in manufacturing processes such as grinding, cutting and polishing [Rice 2002]. Cracks induced by Vickers indentation are also used as model cracks for thermal shock studies [Lee 2002, Collin 2002], crack healing studies [Wilson 1997a, Wilson 1999, Wilson 1997b, Kese 2006], R-curve evaluation [Braun 1992], residual stress studies [Salomonson 1996] and in the design of dental crowns [Kim 2006].

In addition to the experimental studies linking microcracks with physical properties, a number of theoretical studies have explored the changes in properties due to microcracking. In particular, theoretical work on the dependence of Young's modulus on microcrack damage includes research by Budiansky and O'Connell [Budiansky 1976], Salganik [Salganik 1974], Hoenig [Hoenig 1979] and Laws and Brockenbrough [Laws 1987]. In each of these studies [Budiansky 1976, Salganik 1974, Hoenig 1979, Laws 1987], the effect of microcrack damage is described by a linear function of Young's modulus on the crack parameter, ε, and crack orientation function f, such that

$$E = E_0 (1 - f\varepsilon) \qquad (1)$$

where E_0 is the Young's modulus of non-microcracked specimen. For circular microcracks of uniform radius c, the crack damage parameter ε, is defined as $\varepsilon = N c^3$, where N is the volumetric crack number density.

(a)

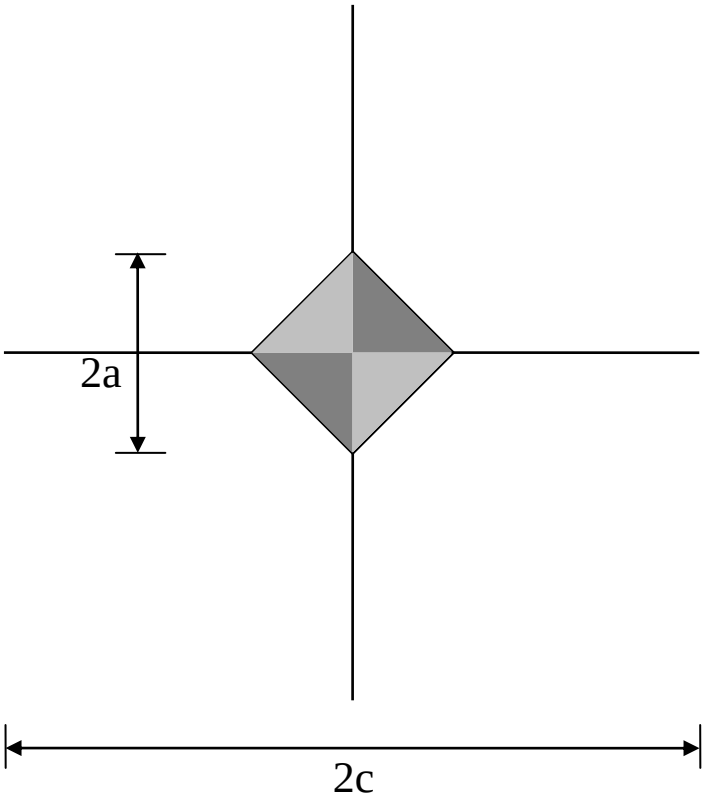

(b)

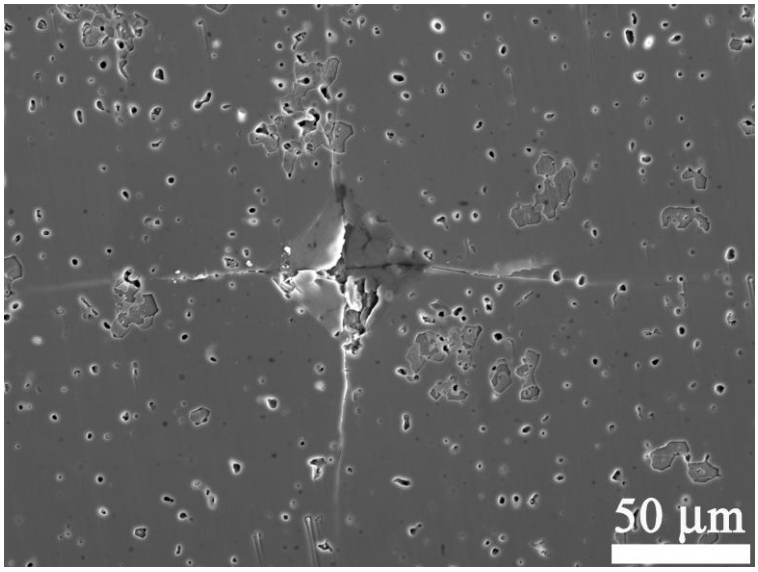

Figure 6.1. Schematic (a) and SEM micrograph (b) of a Vickers indentation system, including the indentation impression and radial cracks originating from the surface corners of the indentation impression.

For most experimental studies of microcrack-damaged materials, the N and c are not measured directly. Instead, if microcracking mechanisms such as thermal expansion anisotropy, thermal expansion mismatch or Martensitic-type crystallographic phase changes are present, then the microcracking damage state is inferred from changes in physical properties.

In addition to changes in elastic moduli, changes in electrical conductivity due to microcracking were explored by Hoenig [Hoenig 1979] such that for crack damage parameter, ε

$$\frac{\sigma}{\sigma_0} = 1 - g\varepsilon \tag{2}$$

where σ is the electrical conductivity of a cracked body and σ_0 is the electrical conductivity of a non-cracked body. For randomly oriented microcracks, $g = g_{\text{random}} = 8/9$. For an array of aligned cracks, $g = g_{\text{aligned}} = 8/3$. Similarly, for thermal conductivity, k, Hoenig obtained

$$\frac{k}{k_0} = 1 - g\varepsilon \tag{3}$$

where k is the thermal conductivity of a cracked body and k_0 is the thermal conductivity of a non-cracked body and ε is the crack damage parameter. The orientation parameter g takes on exactly the same numerical values as for electrical conductivity in the randomly oriented and aligned cases. Thus for a fixed value of the crack damage parameter, the microcracking induced changes are three times greater for the aligned case compared to the randomly oriented case for both electrical conductivity and thermal conductivity.

An expression by Hasselman [Hasselman 1979] for the relative change in thermal

conductivity due to randomly oriented microcracks, namely $k/k_0 = (1+8\varepsilon/9)^{-1}$, is nearly identical to Hoenig's expression [Hoenig 1979] for small values of crack density since by power series expansion, $(1 + x)^{-1} \approx 1- x$ for small values of x.

The Poisson's ratio change with respect to the volume crack number density was studied by Walsh [Walsh 1965], and is rewritten here as

$$\frac{\Delta\upsilon}{\upsilon_0} = S_\upsilon \cdot N \qquad (4)$$

where $\Delta\upsilon$ is the Poisson's ratio change, υ_0 is the Poisson's ratio of unindented specimen, N is the volumetric number density of microcracks, and S_υ is the product of a crack orientation and a crack geometry parameter. For 3-dimensional, randomly oriented cracks, Walsh [Walsh 1965] found a S_υ value of $4\pi c^3/3$ for randomly oriented microcracks.

As discussed above, in order to test the various microcracking-property change theories [Budiansky 1976, Salganik 1974, Hoenig 1979, Laws 1987, Hasselman 1979, Walsh 1965], knowledge of both the crack size, c, and crack number density, N, are needed. However, for a specimen with a 3-dimensional microcrack distribution, the N and c values obtained from surface measurements on the specimen are not representative of the 3-dimensional microcracks throughout the specimen bulk. This is in part because the specimen surface is subjected to biaxial stress while the bulk is typically under a triaxial stress state. Therefore a representative number and size of microcracks will not necessarily intercept the specimen surface [Case 1984]. A second factor that makes it difficult to determine N and/or c from surface measurement alone is that post-processing procedures, such as polishing and cutting,

may induce surface microcracks that are not related to internal microcracking mechanisms such as thermal expansion anisotropy or phase changes [Case 1984]. Thus, the surface crack population likely includes surface microcracks created by specimen processing.

In order to calculate the crack damage parameter ε (equation (1)) and determine the validity of equation (1), the values of N and c need to be determined. There are at least two possible solutions: (1) induce surface cracks by indentation (for example) so that N and c can be measured directly [Kim 1993, Kim 1993b, Case 1993], or (2) use a scattering technique such as small angle neutron scattering (SANS) in which penetrating radiation (neutrons) scatter from volumetrically distributed microcracks [Case 1984].

In this study, an array of microcracks was placed on the polished surfaces of two HA specimens using Vickers indentation in order to control the number density, size and location of the surface microcracks. The process of adding Vickers indentation cracks to the specimens was periodically interrupted in order to measure the Young's modulus, E, and Poisson's ratio, υ, via Resonant Ultrasound Spectroscopy (RUS). A total of 391 indentations were made on the first specimen and a total of 513 indentations were made on the second specimen.

In the literature, there are very few studies in which changes in elasticity are directly measured for an array of microcracks where both the size and the number of microcracks are known. In this study, the observed changes in Young's modulus and Poisson's ratio were compared to the theoretical predictions from the literature, as discussed in the next section of this paper. In addition, we also compare our HA Young's modulus results to a similar study

performed using Vickers indentation generated microcracking in commercial alumina specimens [Kim 1993, Kim 1993b, Case 1993]. Thus, in this study, we consider the effect of microcrack damage on two very widely used brittle materials: (1) HA which has many biomedical, filter and sensor applications (as discussed above), and (2) alumina which is used in a great variety of applications requiring high temperature, chemical stability and resistance to erosion [Dorre 1984]. In addition, as will be discussed in Section 3.2, alumina and HA have very different mechanical properties including the elastic moduli, hardness and fracture toughness.

2. Experimental Procedure

For each of the three HA specimens included in this study, approximately 2.5 grams of biomedical grade commercial HA powder (Taihei Chemical Industrials Co., Osaka, Japan) were uniaxially pressed to form disk-shaped compacts at 33 MPa and then sintered in air at 1360^{o}C for 4 hours with a heating/cooling rate of ~ 10^{o}C/minute. For each of the three HA specimens included in this study, the as-sintered disc diameter was 23.4 mm with a thickness of approximately 1.9 mm.

The three sintered HA specimens were then polished using 600 grit SiC abrasive paper followed by polishing with diamond paste down to a grit size of 0.5 μm. Two specimens (labeled as HA-391 and HA-513) were used to study the Vickers indentation damage-induced changes in Young's modulus and Poisson's ratio. A third specimen (labeled as HA-GS), (processed from the same powder batch with nominally identical processing parameters as HA-391 and HA-513) was thermally etched to determine grain size.

After polishing, each of the two disk-shaped HA specimens used for indentation was cut into a bar using a commercial milling machine (Michigan State University Physics Shop), yielding one specimen with dimensions of 13.4 mm x 10.3 mm x 1.6 mm (HA-391) and one specimen with dimensions of 15.8 mm x 12.2 mm x 1.8 mm (HA-513). Specimen HA-GS was not sectioned following polishing, but instead remained in the disk form.

Microcracks were induced by Vickers indentation (Buehler, Lake Bluff, Illinois, US) using a load of 9.8 N, a load time of 5 seconds and a loading rate of 70 μm/s. Indentations were placed across the surface in a grid pattern with 0.5 mm spacing between indentation centers. A 23 x 17 grid pattern was placed on specimen HA-391, and a 27 x 19 grid pattern was placed on specimen HA-513. The diagonal length of the indentation impression, $2a$, and the radial crack length, $2c$, for each specimen were measured for the first row of indentations (23 indents for HA-391 and 27 indents for HA-513) using the optical microscope mounted on the Vickers indenter.

The microstructure of each of the three HA specimens was examined using scanning electron microscopy (SEM, JEOL 6400V, JEOL Corp. Japan). A roughly 20 nm thick gold coating (EMSSCOPE SC500, Ashford, Kent, Great Britain) was sputtered on each specimen before SEM examination. SEM was conducted using a 15 mm working distance and a 15 kV accelerating voltage.

The specimen used for grain size evaluation (HA-GS) was thermally etched by annealing the as-densified specimen in air at 1300^{o}C for 2 hours. The mean grain size was evaluated via a linear intercept method using at least 200 intercepts [Case 1981]. For the

indented specimens, micrographs of the indentation impression and radial crack system were obtained.

The Young's modulus and Poisson's ratio of specimens HA-391 and HA-513 were measured via RUS [Migliori 1997] using commercial equipment (RUSpec, Quasar International, Albuquerque, NM, USA). RUS is a non-destructive technique widely used in the last decade to measure the elastic moduli of solid materials [Ren 2009, Schmidt 2010, Ni 2010, Zhang 2010, Gladden 2010, Ni 2009, Zhang 2007]. During the RUS measurements, the specimen was placed on a three-transducer configuration. One of the three transducers generates a mechanical vibration (a frequency range of 5 to 250 kHz in this case) and the other two transducers detect the specimen's mechanical resonance modes (Figure 6.2). The Young's modulus, and Poisson's ratio were calculated from the resonance frequencies and the mass, shape and the dimensions of the HA specimens using a commercial software package (RPModel, Quasar International, Albuquerque, NM, US). For both HA-391 and HA-513, the Young's modulus, E_0, and Poisson's ratio, υ_0 were measured prior to indentation (where the subscript "0" denotes the values of Young's modulus and Poisson's ratio without Vickers-indentation induced microcrack damage). Then seventeen rows of indentations with 23 indentations in each row were made in HA-391, E and υ were measured by RUS after completing the first row of 23 indentations. Subsequent E and υ measurements for specimen HA-391 were made after the 3^{rd}, 5^{th}, 7^{th}, 9^{th}, 11^{th}, 13^{th}, 15^{th} and 17^{th} rows of indentations were completed. For specimen HA-513, nineteen rows of indentations with 27 indentations in each row were placed on the specimen, then E and υ were measured by RUS after each

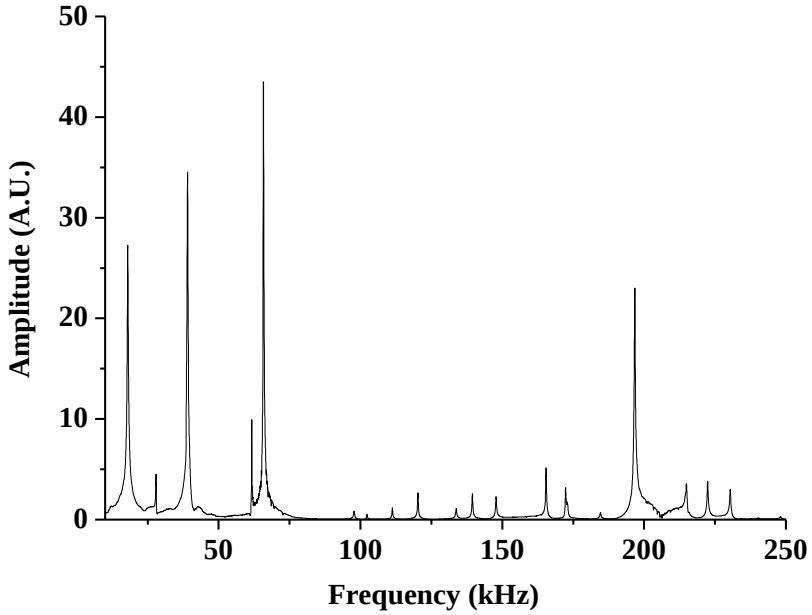

Figure 6.2. RUS spectra obtained for a polished, unindented HA specimen bar sintered at 1360^{o}C for 4 h. A.U. stands for arbitrary units.

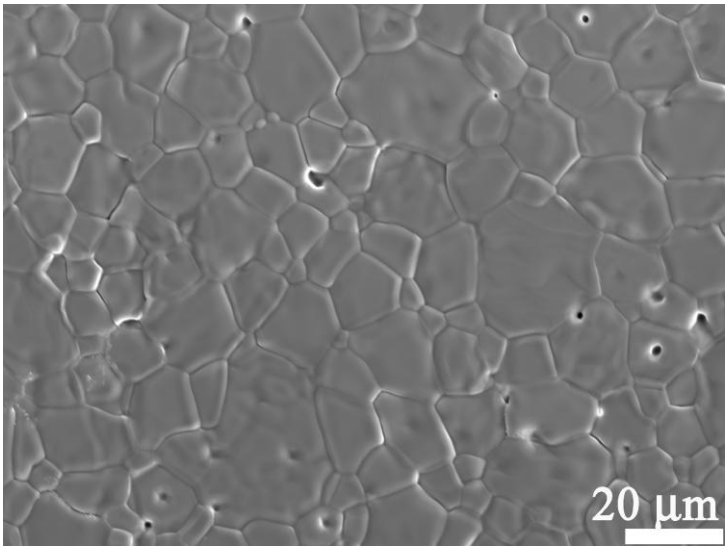

Figure 6.3. SEM micrographs of polished and thermally etched surface for specimen HA-GS in this study.

row of indentations was completed (that is, following every 27 indentations).

In addition to the elasticity measurements, the hardness and fracture toughness of the HA specimens were measured in this study in order to compare the detailed mechanical properties of our HA specimens (HA-391 and HA-513) to HA data from the literature.

Both the hardness, H, and fracture toughness, K_C, evaluations of the HA specimens were calculated for the first 20 indentations on each of the two indented HA specimens in order to compare the H and K_C values from this study to H and K_C data in the literature for HA specimens without extensive microcrack damage.

The hardness, H, of the HA specimens, was calculated from the relationship [Wachtman 2009]

$$H = \frac{1.8544P}{(2a)^2} \tag{5}$$

where P is the applied load and $2a$ is the diagonal length of the indentation impression. Also, the fracture toughness of the HA specimens was estimated via the Vickers indentation method using equation (6) [Wachtman 2009]

$$K_C = \varsigma\left(\frac{E}{H}\right)^{1/2}\frac{F}{c^{3/2}} \tag{6}$$

where E is the Young's modulus of the HA specimens, which was determined by RUS in this study, H is the hardness of the specimens calculated using equation (5). F is the applied load and c is half of the radial crack length. The calibration constant ζ was set to 0.016, according to Anstis [Ansis 1981].

3. Results and Discussion

3.1 Microstructure

The volume fraction porosity, *P*, for the sintered HA specimens was approximately 0.06 as determined from the measured mass and volume of the specimen. SEM examination revealed quasi-spherical pores, approximately 1 to 3 microns in diameter located at triple points, grain boundaries and within the grains (Figure 6.3). The grains were approximately equiaxed with a mean grain size of 8.6 μm, as determined from the linear intercept method (Figure 6.3).

The indentation impression diagonal length 2*a* and the radial crack length 2*c* were measured for the first 20 indentations on each specimen (Figure 6.1b). For specimen HA-391 the mean indentation diagonal length, <2*a*> was 66.2 ± 4.6 μm the mean radial crack length, <2*c*> was 253.8 ± 17.0 μm. For HA-513, <2*a*> was 64.2 ± 1.9 μm and <2*c*> was 252.2 ± 31.0 μm.

3.2 Rationale for comparing this study's HA indentation results with indentation results for alumina from the literature

In this study, we chose to compare our HA data to the alumina data by Case and Kim [Kim 1993, Case 1993, Kim 1993b]. The reason for this important comparison is that alumina and HA are both widely used brittle materials although their mechanical properties are quite different. For the commercial alumina specimens used by Case and Kim [Kim 1993], the hardness, *H*, Young's modulus, *E*, and toughness, K_C, for undamaged specimens were 12.9 GPa, 320 to 340 GPa and 3.1 MPa•$m^{1/2}$, respectively. For the HA samples in this study, we measured *H* ~4.2 GPa, *E* ~100 GPa and K_C ~0.5 MPa•$m^{1/2}$. In addition to the

differences in material properties, the indentation load and the number density of microcracks in alumina (49 N to 196 N) [Kim 1993] and HA (9.8 N) were different. Thus, the test of theories for the microcrack-induced changes in Young's modulus [Budiansky 1976, Salganik 1974, Hoenig 1979, Laws 1987] and Poisson's ratio [Walsh 1965] becomes more rigorous if we compare the theories' predictions with experimental results from two materials with dissimilar mechanical properties, indented using dissimilar loads.

3.3 Pre-indentation values of Young's modulus and Poisson's ratio

In order to assure that the HA specimens in this study have mechanical properties consistent with typical HA specimens in the literature, we compared our HA specimens to HA specimens in the literature in terms of the Young's modulus and Poisson's ratio (this section) and hardness, fracture toughness (Section 3.4).

In this study, the Young's modulus determined by RUS for unindented HA-391 and HA-513 were 103.5 ± 0.3 GPa and 104.1 ± 0.3 GPa**.** In order to make comparisons among specimens with differing volume fraction porosities P, we can use the empirical porosity dependence of Young's modulus as given by [Ren 2009, Spriggs 1961]

$$E = E_D \exp(-b_E P) \quad (7)$$

where E is the Young's modulus at a volume fraction porosity P, E_D is the value of E for theoretically dense materials ($P = 0$) and b_E is a material-dependent constant that describes the rate of decrease of E with increasing P. Using equation (7) and the values E_D =128 GPa and b_E = 3.5 obtained by Ren [Ren 2009] for a combined data set including HA specimens from studies by Ren [Ren 2009], Liu [Liu 1998], Arita [Arita 1995] and He [He 2008], as

well as the aggregate Young's modulus [Landolt 1979], the estimated Young's modulus for the HA specimens included in this study (P = 0.06) is 103.7 GPa. Thus, the measured Young's modulus for unindented HA specimens in this study is consistent with the modulus value of 103.7 GPa reported in the literature [Ren 2009].

The Poisson's ratio for unindented HA-391 and HA- 513 were 0.268 ± 0.003 and 0.265 ± 0.003, respectively. The Poisson's ratio of HA (P = 0.06) measured by Ren [Ren 2009] was approximately 0.27, which is also in agreement with the data from this study.

3.4 Comparing initial values of hardness and fracture toughness to literature values for HA

We also wish to compare the Vickers hardness, H, and the fracture toughness, K_C, from this study to those found in the literature. The H values of specimens HA-391 and HA-513 (P = 0.06 for both specimens) were 4.15 ± 0.45 GPa and 4.41 ± 0.21 GPa, respectively. In the literature, we used studies by Hoepfner [Hoepfner 2004] and Dey [Dey 2011] who measured the porosity-dependent hardness of polycrystalline HA for comparison. Hoepfner [Hoepfner 2004] measured H for cold die pressed and sintered HA with porosities of 0.02 to 0.31. Dey [Dey 2011] measured the hardness using nanoindentation on porous microplasma-sprayed HA coatings with porosities from 0.05 to 0.16. Thus the range of porosity in Hoepfner's study [Hoepfner 2004] and Dey's study [Dey 2011] brackets the P value measured for specimens in this study.

Both Hoepfner [Hoepfner 2004] and Dey [Dey 2011] did a least-squares fit of their H versus P results to the following relationship

$$H = H_D \exp(-b_H P) \quad (8)$$

where H_D is the value for theoretically dense materials ($P = 0$) and b_H is a material-dependent constant. A least-squares fit by Dey *et al.* of their H versus P data [Dey 2011] to equation (8) yielded values of $H_D = 5.92$ and $b_H = 5.9$. Hoepfner and Case's least-squares fit of their *H* versus *P* data to equation (8) [Hoepfner 2004] gave least-squares parameters of $H_D = 6.00$ and $b_H = 6.03$.

From equation (8), for $P = 0.06$ (which corresponds to the *P* values of our indented specimens), using Hoepfner's [Hoepfner 2004] least-squares fit parameters gives $H = 4.18$ GPa. Using Dey's [Dey 2011] parameters gives $H = 4.16$ GPa. In addition, Hoepfner [Hoepfner 2004] obtained an *H* value of 4.15 ± 0.25 GPa from 7 to 10 indentations made on the HA specimen at $P = 0.06$ with a mean grain size of 5.9 μm. In this study, the porosity of the HA specimens was 0.06 with a mean grain size of 8.6 μm. Thus the microstructure of the HA specimens and mean *H* values measured by Vickers indentation (4.15 ± 0.45 GPa and 4.41 ± 0.21 GPa for this study's specimens) agree very well with the results by Hoepfner [Hoepfner 2004]. Also, Dey's microplasma-sprayed HA coatings had *P* ranging from 0.05 to 0.16, however, the grain size was not specified but instead only an average splat size of 63 ± 21μm [Dey 2011]. Nevertheless, the hardness values of Dey's specimens and HA specimens in this study agreed quite well.

The measured fracture toughness of specimens HA-391 and HA-513 was 0.55 ± 0.03 MPa•$m^{1/2}$ and 0.54 ± 0.05 MPa•$m^{1/2}$, respectively, which agrees well with the fracture toughness values reported by both Wang [Wang 2009] and Dey [Dey 2011]. Wang measured

toughness of bulk HA specimens with P = 0.01 and grain size of 0.73 μm using the Vickers indentation method, yielding a toughness value of 0.61 ± 0.04 MPa•$m^{1/2}$. With nanoindentation loads of 100 mN, 300 mN, 500 mN, 700 mN and 1000 mN, Dey [Dey 2011] measured the fracture toughness of the same porous microplasma-sprayed HA coatings that were used for Dey's hardness measurements. As the applied indentation load increased, the fracture toughness decreased slightly from ~0.59 ± 0.02 MPa•$m^{1/2}$ to 0.50 ± 0.06 MPa•$m^{1/2}$ [Dey 2011].

Thus, the experimentally determined mechanical properties of hardness, fracture toughness, Young's modulus and Poisson's ratio of the HA specimens included in this study agree well with the corresponding experimental values for HA from the literature [Ren 2009, Hoepfner 2004, Dey 2011, Wang 2009].

3.5 Microcracking - elasticity relationship

3.5.1 Models for microcracking-Young's modulus relationship for aligned surface limited cracks

In a series of studies [Kim 1993, Case 1993, Kim 1993b], Case *et al.* used arrays of Vickers indentation-induced microcracks to show that microcracks decrease the effective Young's modulus of materials, and experimental data were acquired to test the microcrack-modulus relationships based on theory developed by Budiansky [Budiansky 1976], Salganik [Salganik 1974], Hoenig [Hoenig 1979] and Laws [Laws 1987]. However, in Kim and Case's studies [Kim 1993, Case 1993, Kim 1993b], experiments were conducted on aligned and surface-limited cracks in contrast to the 3-dimensional, randomly distributed

cracks assumed in theoretical work [Budiansky 1976, Salganik 1974, Hoenig 1979, Laws 1987].

Using Vickers indentation to induce surface microcracks on polycrystalline alumina allowed the direct measurement of the crack length, *c*, and the crack number density, *N*, [Kim 1993, Case 1993, Kim 1993b] and provided the opportunity for the first direct test of the microcracking-modulus theories [Budiansky 1976, Salganik 1974, Hoenig 1979, Laws 1987]. However, by studying the microcracks induced by Vickers indentation on the specimen surface, Kim and Case [Kim 1993, Case 1993, Kim 1993b] modified the microcracking-modulus theories so to apply them to surface-limited microcracks.

The effect of surface-limited microcracks on the overall Young's modulus change was evaluated using a rule of mixtures (ROM) model [Case 1993] and a dynamic beam vibration (DBV) model [Case 1993]. The details of these models are discussed in Appendix A.

The magnitude of the modulus decrement in both models [Case 1993] is a function of the size, geometry and number density of microcracks, such that

$$\frac{\Delta E}{E_0} = S_N \cdot N \qquad (9)$$

where ΔE is the modulus change, E_0 is the modulus of unindented specimen (no microcrack damage), N is the volumetric number density of microcracks, and S_N is the product of a crack orientation and a crack geometry parameter [Kim 1993b].

In this study, the crack geometries (Appendix A) used to evaluate the effect of Vickers indentation induced microcracks on the Young's modulus include the unmodified/modified

(a)

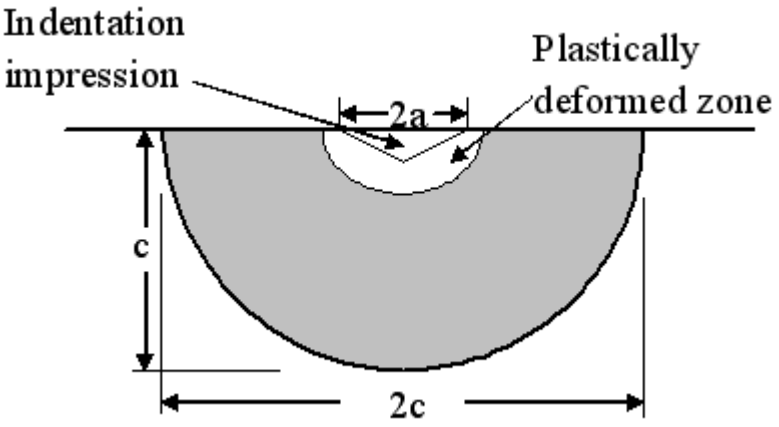

(b)

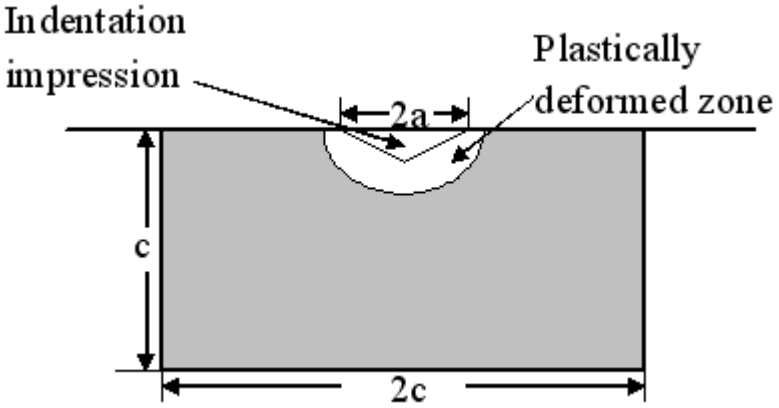

Figure 6.4. Side view of the indentation-crack systems for (a) a modified half ellipse crack geometry [Kim 1993b] and (b) a modified slit crack geometry [Kim 1993b].

half ellipse [Kim 1993b] (Figure 6.4a) and the unmodified/modified slit [Kim 1993b] (Figure 6.4b). In contrast to the unmodified geometries [Kim 1993b], for the modified geometries [Kim 1993b], the surface area of the deformation zone was subtracted and the perimeter of the deformation zone was added, as was discussed by Kim and Case [Kim 1993b]. Calculation of S_N for both ROM and DBV models that include a number of specific crack geometries [Kim 1993b] are given in Appendix A.

Case and Kim [Kim 1993, Case 1993, Kim 1993b] did not report changes in Poisson's ratio as a function of microcrack damage. However, in this study we compared the measurements of Poisson's ratio as a function of N to Walsh's equation (equation (4)) [Walsh 1965]. Although the expression by Walsh was derived for randomly oriented cracks, equation (4) still is consistent with this study's observed linear decrease in Poisson's ratio with microcracking damage (Figure 6.6, Section 3.5.3). Thus, we only analyzed the changes in Poisson's ratio as a function of N in this study since no expression for changes in ε for aligned cracks in the available literature.

3.5.2 Young's modulus – microcracking relationship for HA: experimental results and model predictions

In this study, a total number of 391 and 513 Vickers indentations were placed onto two HA bars, respectively, so that the number density, size and spatial location of the induced surface-limited microcracks was well controlled. For HA-391, as the number of indentations increased from zero to 391, the Young's modulus decreased, from 103.5 GPa for unindented specimen to 101.4 GPa. For HA-513, E decreased from 104.1 GPa to 102.4 GPa. The

Table 6.1. The experimental values of S_N for HA319 and HA513 indented at 9.8 N in this study and Al_2O_3 (single and double sides indented at 196 N) [Kim 1993] compared to the S_N values predicted by each model [Kim 1993]. All S_N values are in unit mm^3.

Experiment/models	**HA319**	**HA513**	**Al_2O_3 (double)**
Experiment	1.05×10^{-2}	1.16×10^{-2}	1.773×10^{-2}
DBV modified half ellipse	0.99×10^{-2}	1.13×10^{-2}	1.465×10^{-2}
DBV modified slit	1.27×10^{-2}	1.17×10^{-2}	1.906×10^{-2}
DBV unmodified half ellipse	1.40×10^{-2}	1.31×10^{-2}	2.304×10^{-2}
DBV unmodified slit	1.67×10^{-2}	1.56×10^{-2}	2.855×10^{-2}
ROM modified half ellipse	0.39×10^{-2}	0.43×10^{-2}	0.815×10^{-2}
ROM modified slit	0.49×10^{-2}	0.45×10^{-2}	1.06×10^{-2}
ROM unmodified half ellipse	0.54×10^{-2}	0.50×10^{-2}	1.283×10^{-2}
ROM unmodified slit	0.65×10^{-2}	0.60×10^{-2}	1.590×10^{-2}

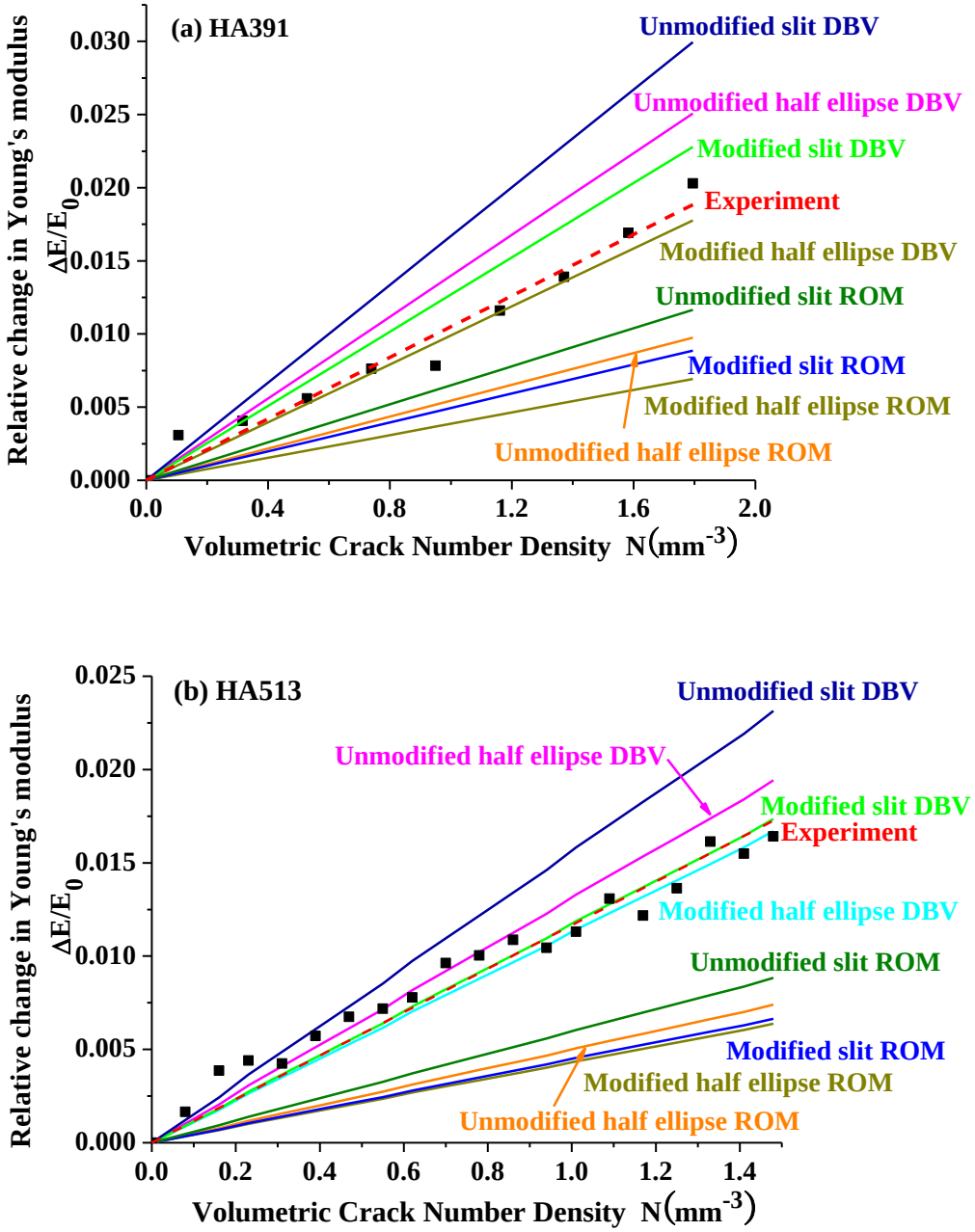

Figure 6.5. Relative Young's modulus change as a function of volumetric crack number density for (a) HA-391 and (b) HA-513. Each solid line represents the prediction given by each model with particular crack geometry [Kim 1993b]. The dashed line represents a least-squares fit to equation (9) for the HA data.

effective Young's modulus decrement, $\Delta E/E_{0,}$ was plotted as a function of number density of microcracks, N (Figures 6.5a and 6.5b). The load and the crack orientation of Vickers indentation were fixed, so S_N in equation (9) was also fixed since S_N is the product of a crack orientation and a crack geometry parameter. As expected from equation (9), $\Delta E/E_0$ was a linear function of N (Figures 6.5a and 6.5b), with $S_N = 0.0105$ mm^3 (Table 6.1) and the coefficient of determination $R^2 = 0.968$ for HA-391. For HA-513, $S_N = 0.0116$ mm^3 (Table 6.1) and $R^2 = 0.951$. Each solid line in Figures 6.5a and 6.5b represents the prediction given by each model with particular crack geometry. Since each parameter in each model is known, each solid line is plotted using a fixed S_N value (not from least-squares fitting).

Among all the combinations between models and crack geometries [Kim 1993b], the best correlations with experimental data for specimen HA-391were the DBV model with modified slit crack geometry ($S_N = 0.0127$ mm^3, Table 6.1) and the DBV model with modified half ellipse crack geometry ($S_N = 0.0099$ mm^3, Table 6.1, Figure 6.5a).

Also, as was the case for specimen HA-391, the experimental data for specimen HA-513 correlated best with the DBV models with the modified slit ($S_N = 0.0117$ mm^3, Table 6.1) and the modified half ellipse ($S_N = 0.0113$ mm^3, Table 6.1) crack geometries (Figure 6.5b).

The Young's modulus versus microcrack number density data in this study was bracketed by the predictions for the modified slit and half ellipse crack geometries for the DBV models (Figures 6.5a and 6.5b), implying that the microcrack geometry in this study was possibly a slit shape with truncated round corners.

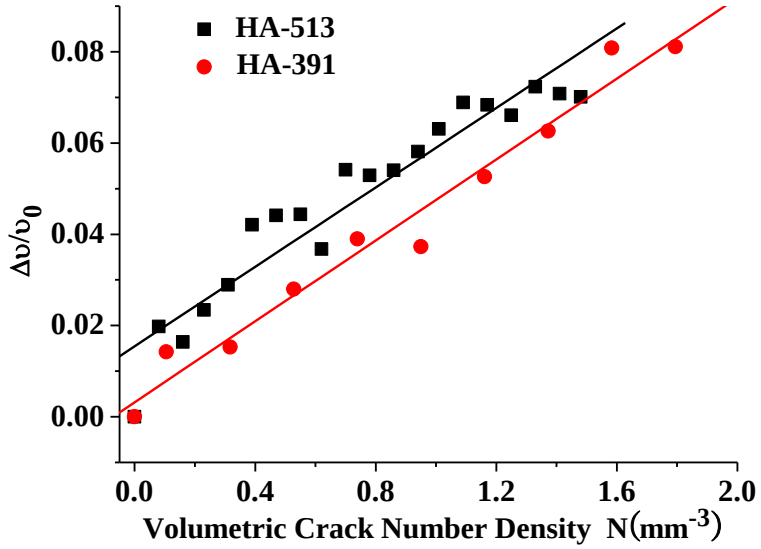

Figure 6.6. Relative Poisson's ratio change vs. volumetric crack number density for HA-391 and HA-513. The dashed line represents a least-squares fit to equation (4) for the HA data.

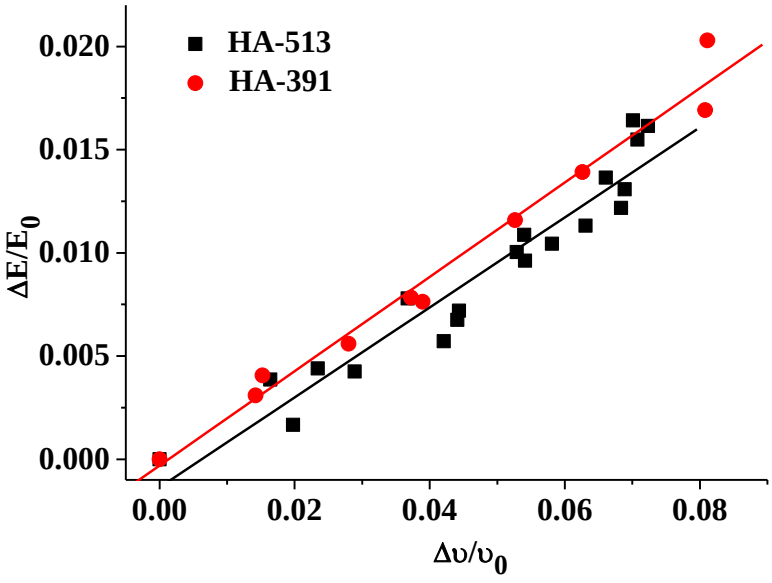

Figure 6.7. Relative Young's modulus change vs. relative Poisson's ratio change for HA-391 and HA-513. The dashed lines represent least-squares fits to equation (10) respectively.

In this study, the Young's modulus was measured in a dynamic ultrasound resonance method, so it is reasonable that the DBV models [Kim 1993b] agreed better with the experimental data compared to the ROM models [Kim 1993b], since DBV models [Case 1993] are based on the dynamic beam vibration equation and the ROM represent a static mixing approximation.

Besides being a function of microcrack damage, E is also a function of porosity [Ren 2009, Ni 2009, Rice 1998, Jang 2005] and composition [Diaz 2008, Ren 2007, Krstic 2008]. However in this study, both the composition and the porosity of the specimens are fixed. Also, E is generally considered to be independent of grain size [Rice 1998, Ren 2009b], except for grain sizes smaller than about 100 nm [Zhou 2008], which is not the case for the materials included in this study and from the literature.

3.5.3 Poisson's ratio– microcracking relationship for HA

The Poisson's ratio values for the unindented HA-391 and HA- 513 were 0.268 ± 0.003 and 0.265 ± 0.003, respectively. After the introduction of 391 and 513 indentations per specimen, the Poisson's ratio for HA-391 and HA- 513 dropped to 0.245 ± 0.006 and 0.246 ± 0.008, respectively.

The effective Poisson's ratio decrement, $\Delta\upsilon/\upsilon_{0,}$ for both HA specimens were plotted as a function of N (Figure 6.6), similar to the $\Delta E/E_0$ versus N plots discussed in earlier (Figures 6.5a and 6.5b). As was predicted by Walsh [Walsh 1965] (equation (4)), a linear relationship between Poisson's ratio and crack number density was observed for the HA specimens in this

study, with coefficients of determination given by $R^2 = 0.972$ for HA-391 and $R^2 = 0.908$ for HA-513. The least-squares fit of $\Delta\upsilon/\upsilon_0$ for aligned cracks to equation (4) gave the slope S_υ = 0.044 mm^3 for HA-391 and S_υ = 0.044 mm^3 for HA-513. Using $S_\upsilon = 4\pi c^3/3$ (as proposed by Walsh [Walsh 1965] for randomly oriented cracks) the calculated value of S_υ in equation (4) is 0.009 mm^3.

3.5.4 Relative change in Young's modulus as a function of the relative change in the Poisson's ratio

In Case's paper [Case 1984], the four microcracking – elasticity models considered in this study [Budiansky 1976, Salganik 1974, Hasselman 1979, Walsh 1965] were expressed in terms of E and υ. Walsh [Walsh 1965] proposed a linear relationship between $\Delta E/E_0$ and $\Delta\upsilon/\upsilon_0$. The other three studies [Budiansky 1976, Salganik 1974, Hasselman 1979] predicted a nearly linear $\Delta E/E_0$ versus $\Delta\upsilon/\upsilon_0$ behavior.

Also, the relative Young's modulus change (equation (9)) and the relative Poisson's ratio change (equation (4)) for the HA specimens demonstrated similar linear trends when plotted as a function of volume crack number density, N (Figures 6.7). Thus, combining equations (4) and (9) gives

$$\frac{\Delta E}{E_0} = \frac{S_N}{S_\upsilon}\ \frac{\Delta\upsilon}{\upsilon_0} \qquad (10)$$

which supports Walsh's [Walsh 1965] statement that $\Delta E/E_0$ changes linearly with $\Delta\upsilon/\upsilon_0$.

The linear relationship between $\Delta E/E_0$ and $\Delta\upsilon/\upsilon_0$ proposed by Walsh [Walsh 1965] had a value of slope $S_N/S_\upsilon = 1$ (equation (10)). The nearly linear $\Delta E/E_0$ versus $\Delta\upsilon/\upsilon_0$ behavior proposed by the other three studies [Budiansky 1976, Salganik 1974, Hasselman 1979] had

S_N/S_υ (equation (10)) close to 1, especially for low $\Delta\upsilon/\upsilon_0$.

The nearly linear relationship between $\Delta E/E_0$ and $\Delta\upsilon/\upsilon_0$ is shown for specimens HA-391 and HA-513 with R^2 of 0.979 and 0.924, respectively, as predicted by the literature [Budiansky 1976, Salganik 1974, Hasselman 1979, Walsh 1965]. The least-squares fit of $\Delta E/E_0$ versus $\Delta\upsilon/\upsilon_0$ to equation (10) yielded slopes S_N/S_υ of 0.23 and 0.22 for HA-391 and HA-513, respectively (Figure 6.7).

In order to compare to slopes of $\Delta E/E_0$ versus $\Delta\upsilon/\upsilon_0$ for randomly oriented microcracks induced by thermal expansion anisotropy or phase transformation, Case [Case 1984] examined five sets of experimental data from the literature. The slopes of $\Delta E/E_0$ versus $\Delta\upsilon/\upsilon_0$ for the data presented by Case [Case 1984] were extracted using the software Datathief (B. Tummers, DataThief III. 2006, http://datathief.org). The slopes are 0.46 ± 0.38 for HfO_2 [Dole 1978], 0.15 ± 0.42 for Gd_2O_3 [Case 1981], 1.53 ± 0.23 for Nb_2O_5 [Manning 1973], 0.19 ± 0.13 for Eu_2O_3 [Suchomel 1976] and 1.26 ± 0.21 for $YMg_xCr_{1-x}O_3$ [Case 1984]. The large uncertainty is likely due to the large scatter in the Poisson's ratio measurements. Thus, while the data presented in the Case study [Case 1984] from several researchers [Case 1984, Dole 1978, Case 1981, Manning 1973, Suchomel 1976] represents specimens with randomly oriented cracks, the scattered in the slope values from 0.15 to 1.53 precludes a clear comparison with the predicted slope for $\Delta E/E_0$ versus $\Delta\upsilon/\upsilon_0$.

3.6 Comparison of Young's modulus – microcracking results for HA (this study) and alumina [Kim 1993]

In the study by Case and Kim [Kim 1993], a 46 x 7 grid pattern of Vickers indentations

were placed on single surface or both surfaces of polycrystalline alumina bars (~ 69 x 12 x 1mm) using loads of 49, 98 and 196 N. The Young's modulus was measured using the dynamic sonic resonance technique [Kim 1993]. The mean crack lengths ranged from 227.6 ± 20.3 micron (49N), 370.1 ± 35.1 micron (98N) to 664.8 ± 31.9 micron (196N). The effective Young's modulus versus the microcrack number density of the indented alumina specimen showed a linear relationship as stated in equation (9).

HA and alumina are quite different in mechanical properties including hardness, Young's modulus and fracture toughness (Section 3.2). Also, the load used for indentation and number density of microcracks in alumina [Kim 1993] and HA are different (The range of loads used for Vickers indentation were 49 N to 196 N for alumina [Kim 1993, Kim 1993b, Case 1993] and 9.8 N for the HA in this study). However, the Young's modulus - microcrack relationship for both alumina and HA showed the same linear trend of decreasing Young's modulus with increasing crack number density with different S_N (equation (9), $S_N = 1.05 \times 10^{-2}$ mm^3 for HA-391, $S_N = 1.16 \times 10^{-2}$ mm^3 for HA-513, $S_N = 1.61 \times 10^{-2}$ mm^3 for alumina indented on single side and $S_N = 1.77 \times 10^{-2}$ mm^3 for alumina indented on both sides [Kim 1993] (Table 6.1)). The difference in slopes for the relative modulus change versus N is a function of load and also due to the large difference in toughness for the two materials (Section 3.2). The alumina results [Kim 1993, Kim 1993b, Case 1993] and the HA results (this study) lead to the question "how do we compare the alumina and HA results since the physical properties are much different for the two materials?" We will address this question by plotting all of the

alumina data and the HA data together on a single plot of $\Delta E/E_0$ versus ε (Figures 6.8a and 6.8b), such that

$$\frac{\Delta E}{E_0} = S_E \cdot \varepsilon \qquad (11)$$

Information on calculation of ε and theoretical prediction of the slopes, S_p for different crack geometries is given in Appendix B.

For each HA specimen, the predicted slopes, S_p, of the Young's modulus change, $\Delta E/E_0$, versus crack damage parameter, ε, by both the DBV models with modified half ellipse and modified slit crack geometries, are similar to the S_E values obtained by a least-squares fit of $\Delta E/E_0$versus ε (Tables 6.2 and 6.3). The slopes S_E (Figures 6.8a and 6.8b) obtained from the least-squares fit are within 10% of the predicted values of slopes, S_p (Tables 6.2 and 6.3). For alumina specimens with microcracks induced by a 49 N Vickers indentation load [Kim 1993], the values of S_E in equation (11) are quite close to the predicted values, S_p using DBV models with modified half ellipse crack geometry (Table 6.2); while for DBV models with modified slit crack geometry, S_E are within 20% of S_p (Table 6.3). Thus, both the DBV models with modified half ellipse and modified slit crack geometries predict reasonably well the Young's modulus change as a function of microcrack damage state, with DBV models with modified half ellipse crack geometry being a better model in this case.

3.7 The role of r in the modulus change as a function of microcrack damage

For alumina specimens indented using loads of 98 N and 196 N [Kim 1993], the slopes, S_p calculated from both the DBV models with modified half ellipse and modified slit crack

Table 6.2. For DBV model with modified half ellipse crack geometry, ratio of the depths of the microcracked layer over the unmicrocracked layer, *r*, the number of points fitted, *NP*, the least-squares fit values of slope, S_E and the R^2 value for the fit, the least-squares fit values of slope through the zero point, S_{E0} and the R^2 value for the fit, and the theoretically predicted value of slope, S_P.

Specimens	*r*	*NP*	S_E	R^2	S_{E0}	R^2	S_P
HA - 391	0.086	10	1.15 ± 0.07	0.97	1.18 ± 0.04	0.97	1.005
HA - 513	0.075	20	1.03 ± 0.04	0.98	1.17 ± 0.03	0.95	0.905
Al_2O_3 49N both sides	0.13	7	1.27 ± 0.12	0.96	1.14 ± 0.07	0.95	1.372
Al_2O_3 49N single side	0.13	8	1.49 ± 0.10	0.97	1.62 ± 0.06	0.96	1.372
Al_2O_3 98N both sides	0.23	8	0.87 ± 0.04	0.99	0.85 ± 0.02	0.99	1.905
Al_2O_3 98N single side	0.23	5	0.89 ± 0.04	0.99	0.88 ± 0.02	0.99	1.905
Al_2O_3 196N both sides	0.47	10	1.41 ± 0.05	0.99	1.43 ± 0.03	0.99	2.426
Al_2O_3 196N single side	0.47	6	1.38 ± 0.02	0.99	1.39 ± 0.01	0.99	2.426

Table 6.3. For DBV model with modified slit crack geometry, ratio of the depths of the microcracked layer over the unmicrocracked layer, *r*, the number of points fitted, *NP*, the least-squares fit values of slope, S_E and the R^2 value for the fit, the least-squares fit values of slope through the zero point, S_{E0} and the R^2 value for the fit, and the theoretically predicted value of slope, S_P.

Specimens	*r*	*NP*	S_E	R^2	S_{E0}	R^2	S_P
HA - 391	0.086	10	0.84 ± 0.05	0.97	0.86 ± 0.03	0.97	0.924
HA - 513	0.075	20	0.75 ± 0.03	0.98	0.86 ± 0.02	0.95	0.832
Al_2O_3 49N both sides	0.13	7	0.90 ± 0.08	0.96	0.81 ± 0.05	0.95	1.266
Al_2O_3 49N single side	0.13	8	1.05 ± 0.07	0.97	1.14 ± 0.04	0.96	1.266
Al_2O_3 98N both sides	0.23	8	0.62 ± 0.03	0.99	0.61 ± 0.02	0.99	1.758
Al_2O_3 98N single side	0.23	5	0.64 ± 0.03	0.99	0.63 ± 0.01	0.99	1.758
Al_2O_3 196N both sides	0.47	10	1.03 ± 0.04	0.99	1.04 ± 0.02	0.99	2.239
Al_2O_3 196N single side	0.47	6	1.01 ± 0.01	0.99	1.02 ± 0.01	0.99	2.239

geometries are almost twice the slope values, S_E obtained from the least-squares fit of the experimental data, respectively (Tables 6.2 and 6.3).

The mismatch between the models and the experimental data may be due to the limited thickness of the alumina specimens. For example, in developing a Vickers indentation technique for direct measurement of fracture toughness for bar-shaped specimens of brittle materials, Anstis *et al.* [Anstis 1981] noted that "to avoid interactions with the lower free surface, the crack dimensions were not allowed to exceed one-tenth of the thickness". In this study and in the work by Kim and Case [Kim 1993, Case 1993, Kim 1993b], the ratio of crack depth to specimen thickness was expressed in terms of *r*, where *r* = depth of the microcracked layer/depth of the unmicrocracked layer $L/(t\text{-}L)$.

If we express the Anstis criteria in terms of *r*, then *r* is less than 0.11. In Tables 6.2 and 6.3, for indented HA specimens HA-391 and HA-513, also for the Case and Kim's data, the experimental value of *r* very nearly satisfies the Anstis criteria [Anstis 1981] for indentation cracks made with Vickers indentations loads of 49 N (Tables 6.2 and 6.3, Figures 6.9a and 6.9b). For alumina specimens indented under loads of 98 N and 196 N [Kim 1993], the *r* values are 0.23 and 0.47, respectively. Thus, the values of *r* for the of 98 N and 196 N indentations in alumina [Kim 1993] represent relative crack depth/specimen thickness ratios that are far higher than the upper bound of 0.11 suggested by Anstis [Anstis 1981] and therefore the stress fields indentation crack lengths are likely significantly perturbed by proximity of the free specimen surface to the penetrating indentation crack.

4. Conclusions

For Young's modulus and Poisson's ratio changes due to surface-limited microcrack damage in HA (as a function of the volumetric crack number density, N), this study confirms the theoretical work by Case and Kim and Walsh. Based on the $\Delta E/E_0$ versus N results presented in this study, we recommend that the Case and Kim's DBV model with modified half ellipse crack geometry be used for analyzing the relative change in Young's modulus as a function of N since this model provides the best fit to the experimental data. In addition, this study allows one to predict the changes in normalized Young's modulus versus normalized Poisson's ratio.

In terms of the Young's modulus change as a function of crack damage parameter, ε, the experimental work on HA included this study and the Case and Kim's alumina work from the literature demonstrates the linear $\Delta E/E_0$ versus ε trend predicted from earlier theoretical work by Laws and Brockenbough and Budiansky and O'Connell, as modified for surface-limited damage by the Case and Kim model. Since alumina and HA have quite different mechanical properties and were indented using considerably different loads, this result supports the conclusion that the $\Delta E/E_0$ versus ε trend may apply to a wide variety of brittle materials and loading conditions.

5. Acknowledgements

The authors acknowledge the financial support of the National Science Foundation, Division of Materials Research Grant DMR-0706449.

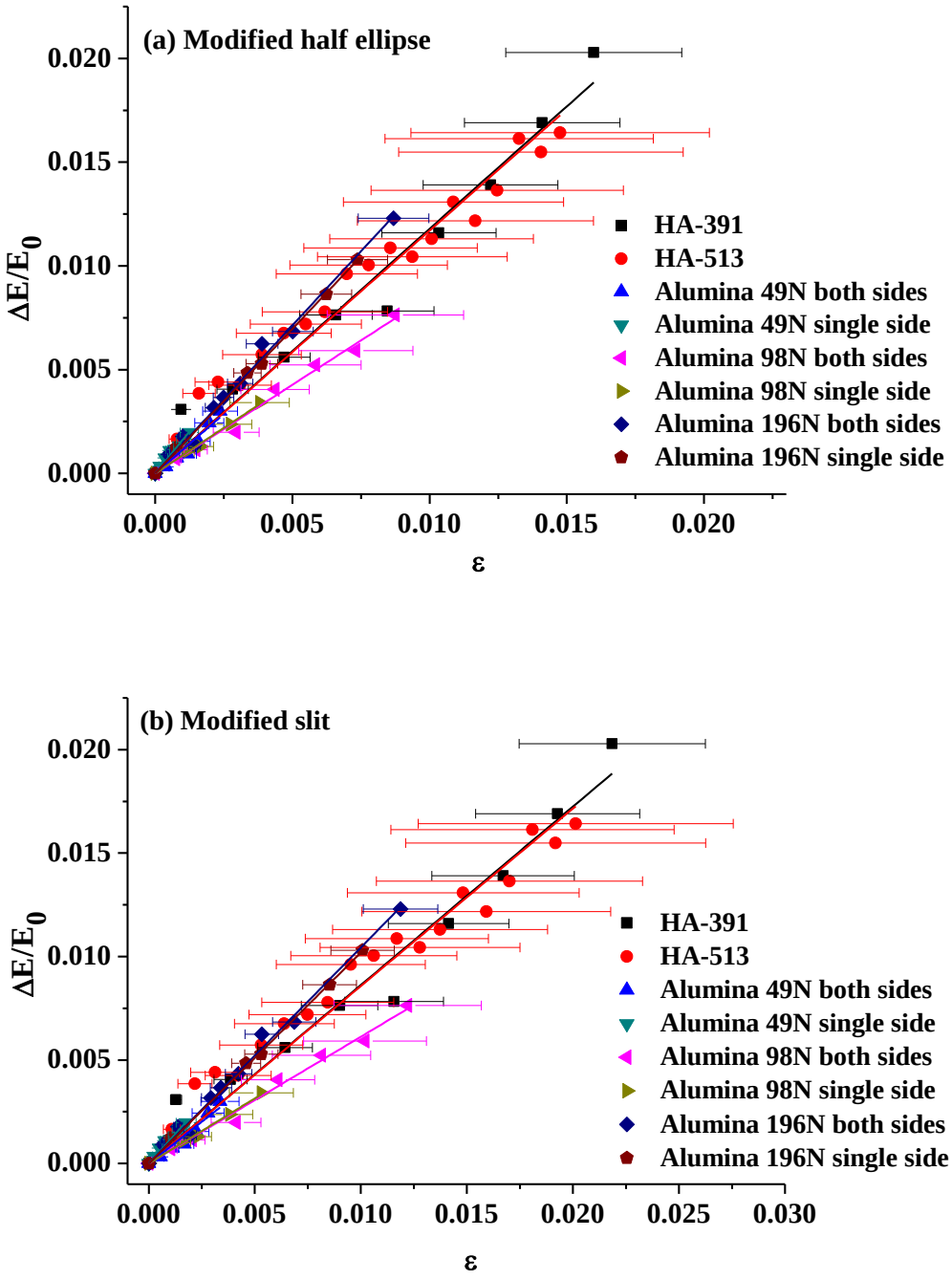

Figure 6.8. Relative Young's modulus change vs. the microcrack damage parameter for HA-391, HA-513 and alumina specimens from Kim [1993] using (a) DBV model with modified half ellipse crack geometry and (b) DBV model with modified slit crack geometry.

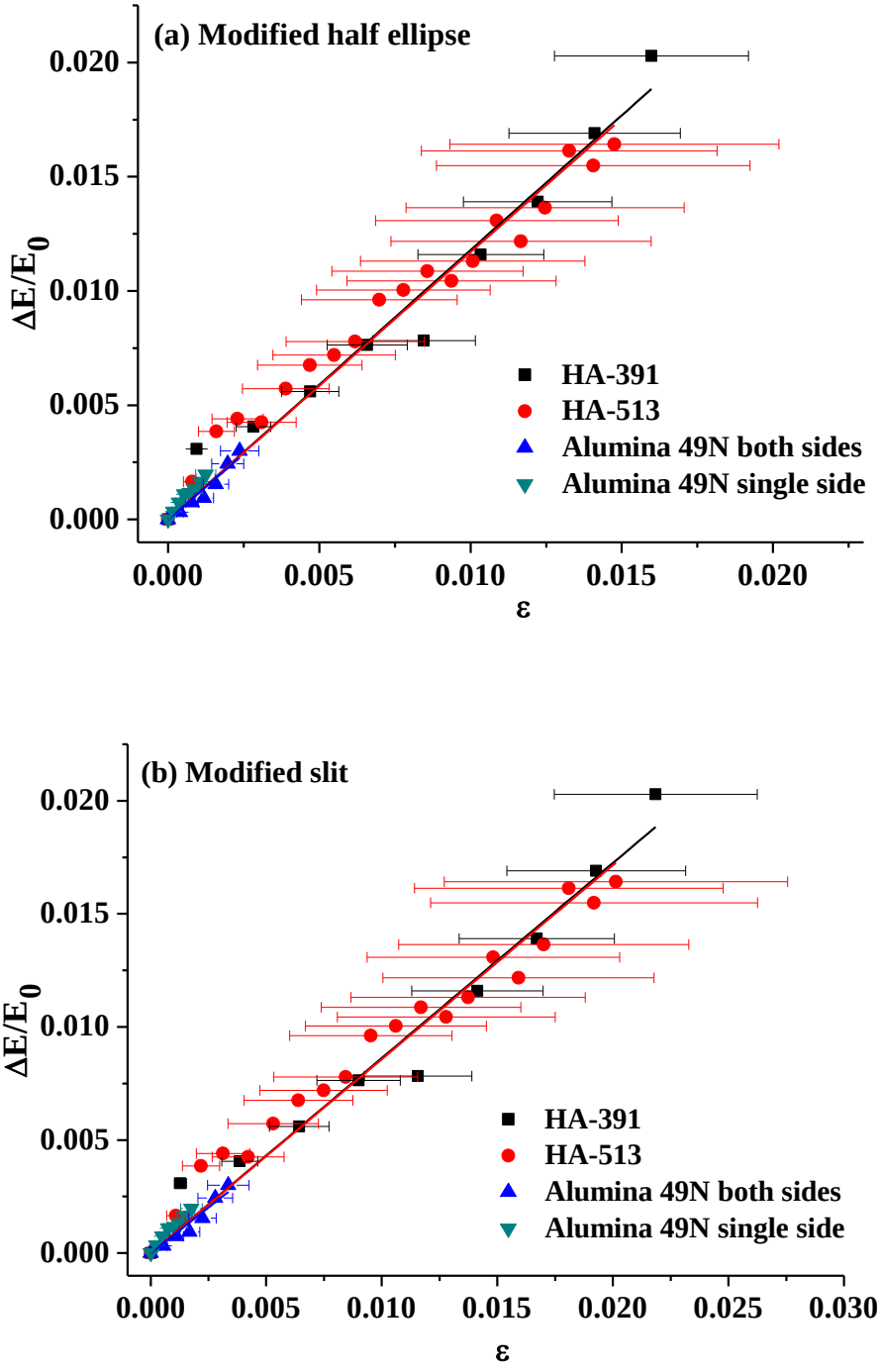

Figure 6.9. Relative Young's modulus change vs. microcrack damage parameter for HA-391, HA-513 and alumina specimen indented under a 49 N load from Kim [1993] using (a) DBV model with modified half ellipse geometry and (b) DBV model with modified slit geometry.

APPENDICES

APPENDIX A

EQUATIONS TO CALCULATE S_N (THE PRODUCT OF A CRACK ORIENTATION AND A CRACK GEOMETRY PARAMETER IN EQUATION (9)), FOR EACH MODULUS/MICROCRACK MODEL WITH A PARTICULAR CRACK GEOMETRY EMPLOYED IN THIS STUDY

In the ROM model [Case 1983], the overall modulus was taken as the sum modulus of the undamaged layer and the damaged layer. The strain in the undamaged layer was set equal to the strain in the damaged layer. In the DBV model [Case 1983], the Bernoulli – Euler beam equation was applied with the boundary conditions that both the bending moments and shear force were zero at the beam ends.

In the ROM model [Case 1983], S_N (equation (9)) was calculated using equation (A1)

$$S_N = f \cdot \frac{2 < A^2 >}{\pi < P >} \tag{A1}$$

In the DBV model [Case 1983], S_N was expressed as equation (A2)

$$S_N = \frac{r^2 + 3}{(r+1)^2} \cdot f \cdot \frac{2 < A^2 >}{\pi < P >} \tag{A2}$$

In both equations (A1) and (A2), f is the microcrack orientation parameter, $<A^2>$ is the mean of the square of the crack surface area and $<P>$ is the mean crack perimeter. In equation (A2), r is the ratio between the half the crack length and the specimen thickness [Case 1983].

Equations to calculate S_N for different crack geometries in the ROM model are summarized in equation (A3) – (A6).

ROM model with unmodified slit crack geometry

$$S_N = \frac{\pi^2(1-u_0{}^2)}{2}\frac{2(2c^2)^2}{4\pi c} \tag{A3}$$

ROM model with modified slit crack geometry

$$S_N = \frac{\pi^2(1-u_0{}^2)}{2}\frac{2(2c^2-\pi a^2/2)^2}{\pi(4c+\pi a)} \tag{A4}$$

ROM model with unmodified half ellipse crack geometry

$$S_N = \frac{16(1-u_0{}^2)}{3}\frac{2(\pi c^2/2)^2}{\pi^2 c} \tag{A5}$$

ROM model with modified half ellipse crack geometry

$$S_N = \frac{16(1-u_0{}^2)}{3}\frac{2(\pi c^2/2-\pi a^2/2)^2}{\pi(\pi c+\pi a)} \tag{A6}$$

The value of S_N for DBV model is calculated via multiplying each corresponding S_N value for ROM model by $\frac{r^2+3}{(r+1)^2}$, where r is the ratio between the half the crack length and the specimen thickness.

APPENDIX B

EQUATIONS USED TO PREDICT THE SLOPES, S_P, OF THE $\Delta E/E_0$ VERSUS ε PLOTS FOR HA SPECIMENS IN THIS STUDY AND ALUMINA [Kim 1993]

The relative change in Young's modulus, $\Delta E/E_0$ in DBV model (from equations (11) and (28) in Case's paper [Case 1983]) is given by

$$\Delta E/E_0 = \frac{r^2+3}{(r+1)^2}\,\frac{r}{r+1}\; f\,G\,N_l \tag{B1}$$

where f is the microcrack orientation parameter, for aligned microcracks in penny, half penny, ellipse and half ellipse crack shapes (from Table II in Kim and Case's paper [Kim 1993b]), f is defined as

$$f = 16(1 - \upsilon_0^{\,2})/3 \tag{B2}$$

for aligned slit crack shapes (from Table II in Kim and Case's paper [Kim 1993b])

$$f = \pi^2 (1 - \upsilon_0^{\,2})/2 \tag{B3}$$

G is the geometry parameter (from equation (4) in Kim and Case's paper [Kim 1993b])

$$G = \frac{2 < A^2 >}{\pi < P >} \tag{B4}$$

For DBV model with modified half ellipse crack geometry (from Table II in Kim and Case's paper [Kim 1993b])

$$G = \frac{(a+c)(c-a)^2}{2} \tag{B5}$$

For the DBV model with a modified slit crack geometry (from Table II in Kim and Case

[Kim 1993b])

$$G = \frac{2(4c^4 - 2\pi a^2 c^2 + \pi^2 a^4/4)}{4\pi c + \pi^2 a} \quad \text{(B6)}$$

N_l is the microcrack number density in the microcracked surface layer

N_l = the number of microcracks/(specimen length x specimen width x depth of the microcrack damaged layer)

r = depth of the microcracked layer/depth of the unmicrocracked layer

In the plot of $\Delta E/E_0$ versus ε for HA specimens in this study and alumina specimens [Kim 1993], ε is defined as GN_l. The theoretically predicted slope, S_p of $\Delta E/E_0$ versus ε is expressed as

$$S_p = \frac{r^2 + 3}{(r+1)^2} \frac{r}{r+1} f \quad \text{(B7)}$$

REFERENCES

REFERENCES

[Anstis 1981] Anstis GR, Chantikul P, Lawn BR, Marshall DB (1981) J. Am. Ceram. Soc. 64:533-538.

[Arita 1995] Arita IH,. Castano VM, Wilkinson DS (1995) J. Mater. Sci. Mater. Med. 6:19-23.

[Braun 1992] Braun LM, Bennison SJ, Lawn BR (1992) J. Am. Ceram. Soc. 75:3049 – 3057.

[Budiansky 1976] Budiansky B, O'Connell RJ (1976) Int. J. Solids Struct. 12:81 - 97.

[Burg 2000] Burg KJL, Porter S, Kellam JF (2000) Biomaterials 21:2347 - 2359.

[Case 1981] Case ED, Smyth JR, Monthei V (1981) J. Am. Ceram. Soc. 64:C24 – C25.

[Case 1984] Case ED (1984) J. Mater. Sci. 19:3702-3712.

[Case 1984b] Case ED, Glinka C (1984) J. Mat. Sci. 19:2962-2968.

[Case 1991] Case ED, Smyth JR, Hunter O Jr (1981) J. Nuclear Mater. 102:135-142.

[Case 1993] Case ED, Kim Y (1993) J. Mater. Sci. 38:1885 - 1900.

[Chotard 2008] Chotard T, Soro J, Lemercier H, Huger M, Gault C (2008) J. Eur. Ceram. Soc. 28:2129–2135.

[Collin 2002] Collin M, Rowcliffe D (2002) J. Eur. Ceram. Soc. 22:435 – 445.

[da Silva 2006] da Silva OG, da Silva EC, da Fonseca MG, Arakaki LNH, Airoldi C (2006) J. Colloid. Interf. Sci. 302:485 – 491.

[Deroo 2010] Deroo F, Kim JY (2010) J. Acoust. Soc. Am. 127:3315 - 3318.

[Dey 2011] Dey A, Mukhopadhyay AK (2011) Int. J. Appl. Ceram. Technol. 8:572–590.

[Diaz 2008] Diaz LA, Torrecillas R, Simonin F, Fantozzi G (2008) J. Eur. Ceram. Soc. 28:2853 – 2858.

[Dole 1978] Dole SL, Hunter O Jr, Calderwood FW, Bray DJ (1978) J. Amer. Ceram. Soc. 61:486-490.

[Dorre 1984] Dorre E, Hubner H (1984) Alumina : processing, properties, and applications. Springer-Verlag, Berlin.

[El Mhammedi 2009] El Mhammedi MA, Achak M, Najih R, Bakasse M, Chtaini A (2009) Mater. Chem. Phys. 115:567 - 571.

[Evans 1986] Evans AG, Fu Y (1986) In: Evans AG (ed) Ceramic Containing Systems, Noyes Press, Park Ridge, NJ.

[Gladden 2010] Gladden JR, Li G, Adebisi R, Firdosy S, Caillat T, Ravi V (2010) Phys. Rev. B 82:045209.

[Hasselman 1979] Hasselman DPH, Singh JP (1979) Am. Cer. Soc. Bul. 58:856-860.

[Hasselman 1993] Hasselman DPH (1993) J. Amer. Ceram. Soc. 76:2180 - 2184.

[He 2008] He LH, Standard OC, Huanga TTY, Latella BA, Swain MV (2008) Acta Biomater. 4:577-586.

[Hench 1991] Hench LL (1991) J. Am. Ceram. Soc. 74:1487 - 1510.

[Hilpert 2004] Hilpert T, Ivers-Tiffee E (2004) Solid State Ionics 175:471 – 476.

[Hoenig 1979] Hoenig A (1979) Int. J. Solids Struct. 15:137 – 154.

[Hoepfner 2004] Hoepfner TP, Case ED (2004) Mater. Lett. 58:489 – 492.

[Hubner 1977] Hubner H, Jillek W (1977) J. Mat. Sci. 12:117 - 125.

[Jamwal 2008] Jamwal N, Gupta M, Paul S (2008) Green Chem. 10:999 – 1003.

[Jang 2005] Jang BK, Matsubara H (2005) Mater. Lett. 59:3462 – 3466.

[Karageorgiou 2005] Karageorgiou V, Kaplan D (2005) Biomaterials 26:5474–5491.

[Kese 2006] Kese KO, Li ZC, Bergman B (2006) J. Eur. Ceram. Soc. 26:1013 – 1022.

[Kim 1993] Kim Y, Case ED (1993) J. Mater. Sci. 38:1901 - 1909.

[Kim 1993b] Kim Y, Case ED, Gaynor S (1993) J. Mater. Sci. 38:1910 - 1918.

[Kim 2006] Kim JW, Bhowmick S, Hermann I, Lawn BR (2006) J. Biomed. Mater. Res. B 79:58 – 65.

[Kimura 1990] Kimura T, Miyamoto S, Yamaguchi T (1990) J. Am. Ceram. Soc. 73:127 - 130.

[Kratschmer 2011] Kratschmer T, Aneziris CG (2011) Int. J. Appl. Ceram. Technol. 8:398 –

410.

[Krstic 2008] Krstic Z, Krstic VD (2008) J. Eur. Ceram. Soc. 28:1723–1730.

[Landolt 1979] Landolt H, Bornstein R (1979) Elektrische, Piezoelektrische, Pyroelektrische, Piezooptische, Elektrooptische Konstanten und Nichtlineare Dielektrische Suszeptibilitaten, Zahlenwerte und Funktionen aus Naturwissenschaften und Technik, Gruppe III, Bd. 11. Springer-Verlag, Berlin.

[Laws 1987] Laws N, Brockenbrough JR (1987) Int. J. Solids Struct. 23:1247 – 1268.

[Lee 2002] Lee SK, Moretti JD, Readey MJ (2002) J. Am. Ceram. Soc. 85:279 – 281.

[Liu 1998] Liu DM (1998) Ceram. Int. 24:441-446.

[Mahabole 2005] Mahabole MP, Aiyer RC, Ramakrishna CV, Sreedhar B, Khairnar RS (2005) B. Mater. Sci. 28:535 - 545.

[Manning 1973] Manning WR, Hunter O Jr (1973) J. Amer. Ceram. Soc. 56:602-603.

[Martin 1973] Martin HC, Carey GF (1973) Introduction to Finite Element Analysis. McGraw-Hill, New York.

[Meschke 1997] Meschke F, Kolleck A, Schneider GA (1997) J. Eur. Ceram. Soc. 17:1143 - 1149.

[Migliori 1997] Migliori A, Sarrao JL (1997) Resonant ultrasound spectroscopy applications to physics, materials measurements and nondestructive evaluation, Wiley-Interscience, Hoboken, NJ, USA.

[Misra 2005] Misra V, Pandey SD (2005) Bull. Environ. Contam. Toxicol. 74:725 – 731.

[Morito 2005] Morito K, Suzuki T (2005) J. Appl. Phys. 97:104 - 107.

[Ni 2009] Ni JE, Ren F, Case ED, Timm EJ (2009) Mater. Chem. Phys. 118:459 – 466.

[Ni 2010] Ni JE, Case ED, Khabir KN, Stewart RC, Wu CI, Hogan TP, Timm EJ, Girard SN, Kanatzidis MG (2010) Mater. Sci. Eng. B 170:58–66.

[Ohtsuki 2010] Ohtsuki C, Ichikawa Y, Shibata H, Kawachi G, Torimoto T, Ogata S (2010) J. Mater. Sci. Mater. Med. 21:1225 - 1232.

[Opre 2005] Opre Z, Grunwaldt JD, Maciejewski M, Ferri D, Mallat T, Baiker A (2005) J. Catal. 230:406 - 419.

[Ota 1986] Ota T, Yamai I, Takahashi J (1986) Adv. Ceram. Mat. 1:371- 377.

[Owada 1989] Owada H, Yamashita K, Umegaki T, Kanazawa T, Nagai M (1989) Solid State Ionics 35:401 - 404.

[Patapy 2009] Patapy C, Gault C, Huger M, Chotard T (2009) J. Eur. Ceram. Soc. 29: 3355–3362.

[Perera 2010] Perera FH, Martinez-Vazquez FJ, Miranda P, Ortiz AL, Pajares A (2010) Ceram. Int. 36:1929 – 1935.

[Rakap 2011] Rakap M, Ozkar S (2011) Int. J. Hydrogen Energ. 36:7019 - 7027.

[Ren 2007] Ren F, Case ED, Timm EJ, Schock HJ (2007) Philos. Mag. 87:4907–4934.

[Ren 2009] Ren F, Case ED, Morrison A, Tafesse M, Baumann MJ (2009) Philos. Mag. 89:1163–1182.

[Ren 2009b] Ren F, Case ED, Ni JE, Timm EJ, Lara-Curzio E, Trejo RM, Lin CH, Kanatzidis MG (2009) Philos. Mag. 89:143-167. [1998] Rice RW (1998) Porosity of Ceramics, Marcel Dekker, Inc., New York.

[Rice 2002] Rice RW (2002) J. Eur. Ceram. Soc. 22:1411 – 1424.

[Rokhlin 1993] Rokhlin SI, Chu YC, Hefetz M (1993) Ceram. Eng. Sci. Proc. 14:454 - 462.

[Salganik 1974] Salganik RL (1974) Mech. Solids 8:135 – 143.

[Salomonson 1996] Salomonson J, Zeng K, Rowcliffe D (1996) Acta Mater. 44:543 – 546.

[Schmidt 2010] Schmidt RD, Ni JE, Case ED, Sakamoto JS, Kleinow DC, Wing BL, Stewart RC, Timm EJ (2010) J. Alloy. Comp. 504:303–309.

[Silva 2003] Silva CC, Almeida AFL, De Oliveira RS, Pinheiro AG, Goes JC, Sombra ASB (2003) J. Mater. Sci. 38:3713 - 3720.

[Silva 2005] Silva CC, Rocha HHB, Freire FNA, Santos MRP, Saboia KDA, Goes JC, Sombra ASB (2005) Mater. Chem. Phys. 92:260 - 268.

[Smith 1995] Smith DT, Wei L (1995) J. Am. Ceram. Soc. 78:1301-1304.

[Spriggs 1961] Spriggs RM (1961) J. Am. Ceram. Soc. 44:628 - 629.

[Suchomel 1976] Suchomel RR, Hunter O Jr (1976) J. Amer. Ceram. Soc. 59:149-152.

[Wachtman 2009] Wachtman JB., Cannon WR, Matthewson MJ (2009) Mechanical Properties of Ceramics, Second Edition, John Wiley & Sons, Inc., New York.

[Walsh 1965] Walsh JB (1965) J. Geophys. Res. 70:5249-5257.

[Wang 2009] Wang J, Shaw LL (2009) Biomaterials 30:6565–6572.

[Wang 2009b] Wang Q, Ji SC (2009) J. Geophys. Res-Earth, 114:B09202.

[Wilson 1997] Wilson BA, Case ED (1997) J. Mat. Sci. 32:3163 – 3175.

[Wilson 1997b] Wilson BA, Lee KY, Case ED (1997) Mater. Res. Bull. 32:1607 – 1616.

[Wilson 1999] Wilson BA, Case ED (1999) J. Mat. Sci. 34:247 – 250.

[Yousef 2005] Yousef SG, Rodel J, Fuller Jr. ER, Zimmermann A, El-Dasher BS (2005) J. Am. Ceram. Soc. 88:2809–2816.

[Zhang 2007] Zhang Z, Keppens V, Senkov ON, Miracle DB (2007) Mater. Sci. Eng. A 471:151–154.

[Zhang 2010] Zhang L, Rogl G, Grytsiv A, Puchegger S, Koppensteiner J, Spieckermann F, Kabelka H, Reinecker M, Rogl P, Schranz W, Zehetbauer M, Carpenter MA (2010) Mater. Sci. Eng. B 170:26–31.

[Zhou 2008] Zhou J, Li Z, Zhu R, Li Y, Zhang Z (2008) J. Mater. Process. Technol. 197:325-336.

CHAPTER 7

WEIBULL MODULUS AND FRACTURE STRENGTH OF HIGHLY POROUS HYDROXYAPATITE

X. Fan[1], E. D. Case[1], I. Gheorghita[2] and M. J. Baumann[1]

[1]Department of Chemical Engineering and Materials Science, Michigan State University, East Lansing, MI, 48824

[2]Dr. Phillips High School, Orlando, FL 32819

Published in: J Mechanical Behavior of Biomedical Materials, 20:283-295, 2013.

Abstract

Porous hydroxyapatite (HA) is used in a variety of applications including biomedical materials such as engineered bone materials and microbe filters. Despite the utility of the Weibull modulus, m, as a gauge of the mechanical reliability of brittle solids, there have been very few studies of m for porous HA. A recent study of porous HA that included the current authors (Fan, X., Case, E. D., Ren, F., Shu, Y., Baumann, M. J., 2012. J. Mech. Behav. Biomed. 8, 21-36) showed increases in m for porosity, P, approaching P_G, the porosity of the green (unfired) specimen. In this paper, eighteen groups of highly porous HA specimens (12 groups fabricated in this study and 6 groups from Fan 2012 Part I) were analyzed with P values from 0.59 to 0.62, where $P_G = 0.62$. The partially sintered HA specimens were fractured in biaxial flexure using a ring-on-ring test fixture. The fracture strength decreased monotonically with decreasing sintering temperature, T_{sinter}, from 4.8 MPa for specimens

sintered at 1025^{o}C to 0.66 MPa for specimens sintered at 350^{o}C. However, the Weibull modulus remained surprisingly high, ranging from 6.6 to 15.5. In comparison, for HA specimens with intermediate values of P, from about 0.1 to 0.55, the Weibull modulus tended to be lower (ranging from about 4 to 11) than the highly porous specimens included in this study.

1. Introduction

Porous hydroxyapatite (HA, $Ca_{10}(PO_4)_6(OH)_2$) is widely studied and used as a candidate material for hard tissue replacement due to its similarity to the natural minerals found in bones and teeth [Hench 1991]. HA can directly bond to bone, showing excellent biocompatibility and osteoconductivity [Hench 1991]. To allow for bone in-growth and circulation of body fluid and nutrients [Baumann 2007], the porosity of the artificial bone scaffold is made to be equivalent to the natural cancellous bone, which has a relative porosity of 0.3 to 0.9 [Wagoner Johnson and Herschler 2011].

In addition to its use as tissue engineering materials, porous HA is used in other biomedical applications. For example, porous HA with a bimodal porosity having $0.22 < P < 0.5$ has been studied as a filter to separate microorganisms from water and gas [Yang 2007a, 2007b]. Also, studies of porous bulk HA scaffolds used for sensor applications show that changes in the localized surface plasmon resonance of embedded silver nanoparticles are proportional to the concentration of absorbed protein [Ohtsuki 2010].

Additional health-related applications of HA include three dimensional HA structures consisting of spherical macropores that capture cadmium and lead from waste water

[Srinivasan 2006]. In use as a CO sensor, the electrical conductivity of porous HA pellets change with the adsorption level of flowing CO gas, enabling the monitoring of CO in the environment [Mahabole 2005].

Porous brittle materials other than HA are also applied as both biomedical and non-biomedical materials. For example, Zhou [2011] used nanoporous silica to deliver an anticancer drug to cells *in vitro*. Layered porous alumina (with $0.35 < P < 0.6$) is used in gas separation and dehydration applications [Sommer and Melin 2005]. NiO/YSZ ceramics with $0.15 < P < 0.5$ are being studied as anodes in solid oxide fuel cells [Liu 2011].

In addition to current and potential applications involving partially densified ceramic powder compacts, there are a number of uses for extremely porous cellular materials with porosities up to 0.9 or greater [Gibson 2010]. Porous HA scaffolds with $P \sim 0.89$ that were functionalized with poly(lactic-co-glycolic acid) (PLGA) microspheres have been studied as (i) *in vivo* and *in vitro* drug delivery platforms, and (ii) enhanced bone regeneration surfaces [Son 2011]. Alumina and mullite substrates with P from 0.75 to 0.9 have been used to support transition metal catalysts [Twigg and Richardson 2007].

This broad range of medical and non-medical applications for porous brittle materials and for hydroxyapatite in particular means that it is critical to determine how the physical properties of these materials, including the mechanical properties, are affected by porosity. For example, many researchers have studied the porosity dependence of the elastic moduli of brittle materials including alumina [Hardy and Green 1995, Nanjangud 1995, Ren 2009], partially stabilized zirconia [Deng 2002], and hydroxyapatite [Fan 2012 Part II, Ren 2009].

Also, the fracture strength of porous brittle materials has been studied extensively, including porous HA specimens under compressive, flexural and tensile loading for relative porosities from roughly 0.03 to 0.85 [Akao 1981, He 2008, Le Huec 1995, Pramanik 2007, Yao 2005].

In terms of the mechanical properties of brittle materials, the Weibull modulus, m, is very important, where m may be defined in terms of the two-parameter Weibull distribution

$$\ln\ln\left(\frac{1}{1-\Lambda_f}\right) = m\ln\sigma_f - m\ln\sigma_c \qquad (1)$$

In equation (1), Λ_f is the cumulative probability of failure and m is the Weibull shape parameter, or the Weibull modulus. Also, σ_f is the fracture strength and σ_C is the Weibull scale parameter, known as the characteristic strength [Wachtman 2009]. The Weibull modulus, m, is a measure of mechanical reliability, for example, a high Weibull modulus (say, $m > 20$) indicates a very narrow flaw size population and hence a narrow range of fracture strengths. Conversely, a low Weibull modulus (for example, $m < 2$) means that the spread in flaw size and strength is very wide. The relationship between the Weibull modulus and distribution of fracture strengths for a given group of specimens is discussed in more detail in Appendix A, where it is important to note that for a nominally identical group of specimens, the Weibull modulus (a single value per group) characterizes the spread in fracture strength.

In this study (Sections 2.1 and 2.2) and our previous study [Fan 2012 Part I], we varied the sintering temperature while keeping the processing and testing parameters fixed in order to study the effect of microstructural evolution of the powder compact (porosity and the initial necking between adjacent grains). The vast majority of the literature on the Weibull

modulus of brittle materials is limited to relatively dense specimens ($P > 0.1$), however the recent study by Fan [Fan 2012 Part I] did measure the Weibull modulus for HA specimens with $0.08 \leqslant P \leqslant 0.62$ (where $P = 0.62$ corresponds to the porosity of the HA powder compacts in this study). One of the findings of the Fan study [Fan 2012 Part I] and a key motivation for this study was that m increased for $P > 0.55$, a result which has not been reported for any brittle material, perhaps in part because there also have been so few Weibull modulus studies for $P > 0.55$.

In addition to microstructure (porosity and interparticle necking), the Weibull modulus may be affected by powder processing techniques [Villora 2004], strength testing techniques [Cordell 2009], loading rate [Andrews 2010], grain size and shape [Kim 1995] and surface finish [Nakamura 2010]. However, in this study and our previous study [Fan 2012 Part I], we varied the sintering temperature to achieve microstructural differences while keeping constant the specimen preparation and testing parameters (Sections 2.1 and 2.2) in order to study the Weibull modulus behaviour in the porosity regime for $P > 0.55$. In particular, we concentrated on the P range between $P = 0.59$ and 0.62, which is also called the initial sintering stage, as will be discussed next. Also, in Section 3.2 we will review, discuss and compare Weibull modulus values from the literature, this study and from our previous study [Fan 2012 Part I].

In both our recent Weibull study [Fan 2012 Part I] and the current study, the evolution of microstructure during sintering is of central importance. As powder compacts are heated, their microstructure evolves via (i) an initial, (ii) an intermediate and then (iii) a final

sintering stage. The initial sintering stage extends from the unfired powder compacts to partially sintered specimens with shrinkage of roughly 3% to 10 % [Coble 1961, German 1996, Barsoum 1997]. Thus the initial sintering stage corresponds to the porosity range of interest (approximately $0.59 \leqslant P \leqslant 0.62$) in this study. The initial sintering stage includes two subdomains: first necks grow between adjacent powder particles without specimen densification and then interparticle neck growth continues with densification [Coble 1961, German 1996, Barsoum 1997]. During the first part of the initial sintering stage, although densification does not occur, the elastic moduli and fracture strength increase as the neck size between adjacent particles increases [Fan 2012 Part II]. By the intermediate stage, the porosity has evolved into tubular pores along the grain edges and in the final sintering stage the pores are quasi-spherical and located at grain boundaries or triple points [German 1996, Barsoum 1997].

Given the results of our earlier study [Fan 2012 Part I], in order to further explore the Weibull modulus behaviour of HA specimens in the initial sintering stage, we first examine the Weibull modulus for 18 different groups of specimens (12 groups fabricated in this study and 6 groups from Fan 2012 Part I) of highly porous HA specimens with P from 0.59 to 0.62 (Table 7.1a). Note that each group of specimens was processed at a different sintering temperature (Table 7.1a), where each group yields a single value of Weibull modulus, since the Weibull modulus is a measure of the scatter in the fracture strength for that group (Appendix A). We will also compare the Weibull modulus behaviour for HA specimens with $0.59 < P < 0.62$ with (i) trends in Weibull modulus for HA for $0.08 \leqslant P \leqslant 0.62$ and a

number of additional materials ($0 < P \leqslant 0.62$, Table 7.1b). In addition, we consider the fracture strength as a function of sintering temperature for HA specimens with $0.59 < P < 0.62$ (Table 7.1b).

2. Experimental Procedure

2.1 Specimen preparation

For this study and the previous Weibull modulus study [Fan 2012 Part I], each HA specimen was made from ~2.5 grams of the same lot of biomedical grade commercial HA powders (HAP-200, Lot # is 10040501) with a vendor-specified purity of Cl $\leqslant$ 20ppm; S $\leqslant$ 50ppm; Heavy metals $\leqslant$ 5ppm; As $\leqslant$ 1ppm; Fe $\leqslant$ 10ppm; Mg$\leqslant$ 50ppm; Mn $\leqslant$ 20ppm (Taihei Chemical Industrials Co., Osaka, Japan). Also, for this study and the earlier study [Fan 2012 Part I], each specimen was fabricated from HA powder discs compacted uniaxially in a cylindrical steel die using a hydraulic press (Carver Inc, Wabash, IN) at 33 MPa for 1 minute. All specimens fabricated in this study and the previous study [Fan 2012 Part I] were sintered in air for in an electrical resistance furnace (CM Inc. Bloomfield, NJ) with a heating/cooling rate of 10^{o}C/min.

Each group of specimens in this study (Table 7.1a and Table 7.1b) and the previous study [Fan 2012 Part I] was sintered at a different temperature. The differences in processing between this study and the previous study [Fan 2012 Part I] were that in this study the sintering was performed at temperatures between 350^{o}C and 1025^{o}C, producing specimens with $0.59 \leqslant P \leqslant 0.62$ (Table 7.1a) while in the previous study, the sintering temperatures ranged from 550^{o}C to 1360^{o}C yielding specimens with $0.08 \leqslant P \leqslant 0.62$.

Table 7.1a. Sintering temperature, T, and time, specimen thickness, t, and diameter, D, volume fraction porosity, P, the number of valid specimens, N, the mean fracture strength $<\sigma_f>$, the characteristic strength, σ_c, and the Weibull modulus m. Each specimen was hard die pressed at 33 MPa and then sintered in air in an electrical resistance furnace.

T (^{o}C)	Time (mins)	t (mm)	D (mm)	P	N	$<\sigma_f>$ (MPa)	σ_c (MPa)	m
350	120	2.41	32.15	0.62	18	0.66 ± 0.11	0.71	6.6 ± 0.4
400	120	2.42	32.15	0.62	16	0.78 ± 0.07	0.82	11.7 ± 0.9
450	120	2.44	32.15	0.62	15	0.95 ± 0.10	1.0	10.8 ± 0.5
500	120	2.44	32.15	0.62	16	1.0 ± 0.1	1.1	14.8 ± 1.9
550*	120	2.47	32.14	0.62	22	1.3 ± 0.1	1.3	10.6 ± 0.8
600*	120	2.48	32.15	0.62	21	1.4 ± 0.1	1.4	12.7 ± 1.1
650	120	2.49	32.20	0.62	17	1.6 ± 0.2	1.6	11.5 ± 0.7
700*	120	2.50	32.17	0.62	19	2.0 ± 0.2	2.1	10.4 ± 0.8
725	120	2.46	32.19	0.62	20	2.6 ± 0.2	2.7	14.7 ± 0.3
750	120	2.44	32.21	0.62	19	2.9 ± 0.4	3.1	9.4 ± 0.5
775	120	2.51	32.18	0.62	17	2.9 ± 0.3	3.1	11.9 ± 0.7
800*	120	2.49	32.16	0.62	19	3.3 ± 0.3	3.4	12.2 ± 0.8
850	120	2.44	32.13	0.62	22	3.5 ± 0.3	3.7	13.7 ± 0.4
900*	120	2.47	32.00	0.62	21	3.5 ± 0.3	3.6	15.5 ± 0.4
950	120	2.40	31.74	0.60	19	3.6 ± 0.4	3.7	10.9 ± 0.9
975	120	2.41	31.58	0.60	16	3.9 ± 0.4	4.1	10.9 ± 0.5
1000*	120	2.42	32.16	0.60	21	4.5 ± 0.5	4.8	10.1 ± 0.7
1025	120	2.42	30.91	0.59	16	4.9 ± 0.6	5.1	11.9 ± 0.8

* Specimens were from our previous Weibull study [Fan 2012 Part I]

Thus, using the same processing techniques (the same cold pressing pressure and time, the same sintering furnace and heating/cooling rate) allow us to directly compare the results between this study and the our previous study [Fan 2012 Part I]. Also, within each group of HA specimens, the porosity of sintered specimens was quite uniform with a standard deviation in volume fraction porosity, P, of less than 0.005 for the specimens within the group.

The porosity of the sintered specimens was calculated from the specimen mass along with average specimen diameter and thickness, assuming a theoretical density (a density corresponding to P = 0) of 3.156 g/cm^3 for HA [CRC 2009].

2.2 Mechanical testing and Weibull analysis

In a Weibull modulus study, the specimens should be fractured using a standard test technique such as the four-point bend test or a biaxial flexure text [Wachtman 2009, ASTM 2003]. In this study the biaxial flexure test (BFT) was used to fracture the partially sintered HA specimens. The BFT technique has been employed for fracture studies of a wide variety of biomedical materials including bone cement [Boyd 2008], dental ceramics [Addison 2012, Yoshimura 2012, Gonzaga 2011] and hydroxyapatite [Meganck 2005, Fan 2012 Part II Fan 2012 Part II]. As noted by Addison [2012], Wachtman [2009] and others, an advantage of BFT technique is a reduced sensitivity to specimen edge flaws which may be introduced during the cutting or processing of a specimen. Additional details of the BFT technique are given in Appendix B.

In this study and the previous study [Fan 2012 Part I], the as-sintered HA specimens

were tested using identical procedures. Each HA specimen was fractured in biaxial flexural testing, with the loading axis perpendicular to the circular face of the disk shaped specimens, on a universal testing machine (Model 4206, Instron, Norwood, MA) via a ring-on-ring configuration ([ASTM 2003], Appendix B). The crosshead speed was 1 mm/min.

The fracture strength, σ_f, was calculated using the following equation [ASTM 2003]

$$\sigma_f = \frac{3F}{2\pi h^2}\left[(1-\nu)\frac{D_S^2 - D_L^2}{2D^2} + (1+\nu)\ln\left(\frac{D_S}{D_L}\right)\right] \quad (2)$$

where F is the load at failure, h and D are the thickness and the diameter of the test specimen; D_S and D_L are the diameters of the supporting ring and the loading ring (Appendix B). In this study, D_S = 20 mm and D_L = 10 mm. A Poisson's ratio, ν, of 0.27 [Ren 2009] was used.

The remnants of the fractured specimens were examined to determine whether or not each of the fractured specimens represented a valid ring-on-ring (ROR) test. The definitions of valid and invalid ROR tests are discussed in Appendix B. Only the data for validly fractured specimens were used in the analysis of Weibull modulus and fracture strength.

2.3 Microstructural examination

SEM on fractured surfaces of two HA specimens sintered at 350^{o}C and 1025^{o}C. For the two HA examined by SEM, a 21 nm thick gold coating was sputtered on the examined surfaces using a gold sputter (EMSSCOPE SC500, Ashford, Kent, UK) prior to SEM examination. An accelerating voltage of 15 kV and a working distance of 15 mm were used.

2.4 Statistical analysis

A one-way ANOVA analysis was used to compare Weibull modulus values as a

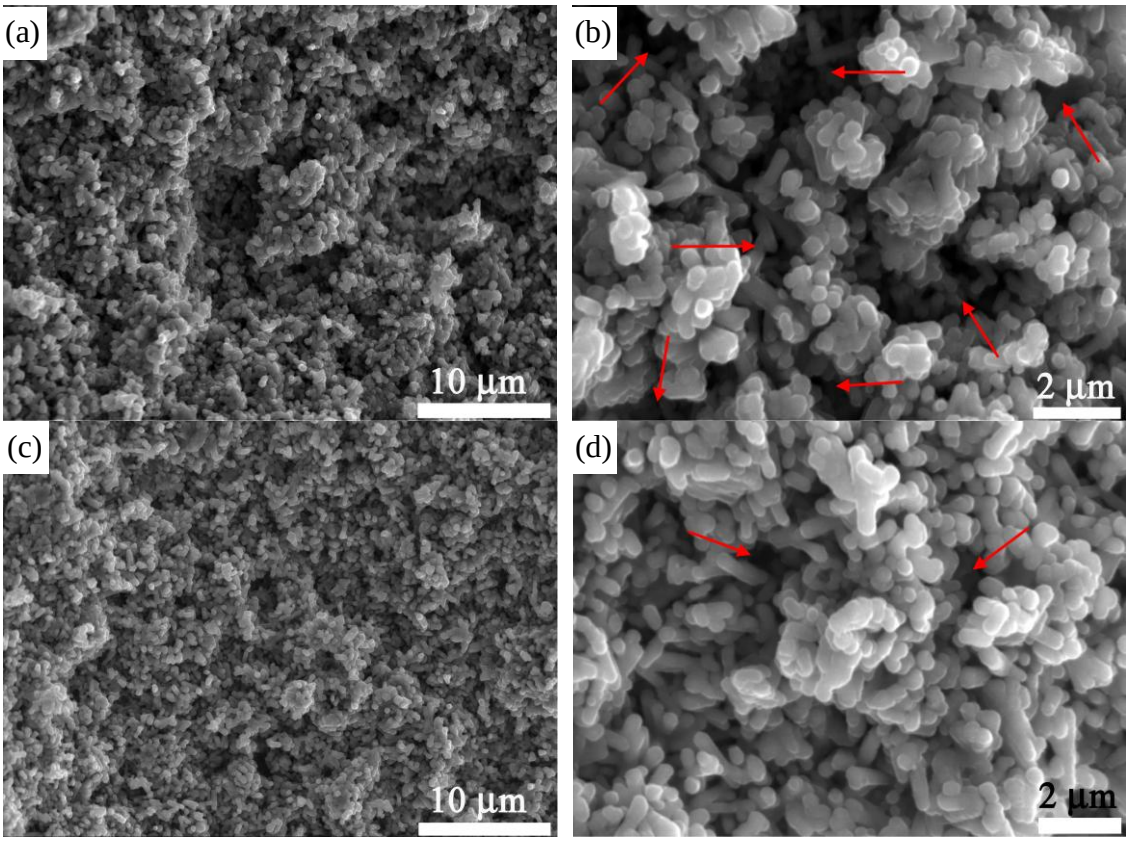

Figure 7.1. SEM micrographs of partially densified HA specimens sintered at 350^{o}C (a) at low magnification, (b) at higher magnification and HA specimens sintered at 1025^{o}C at (c) low magnification and (d) higher magnification. Note that 350^{o}C is the minimum sintering temperature in this study and 1025^{o}C is the maximum sintering temperature in this study.

function of porosity for HA specimens fabricated in this study along with data from our earlier study [Fan 2012 Part I].

3. Results and Discussion

3.1 Microstructural and phase analyses

3.1.1 SEM analysis of initial powders and the sintered specimens

SEM showed the initial HA powders consisted of irregularly-shaped agglomerates composed of rod-shaped particles approximately 0.8 μm in length with an aspect ratio of ~ 3 (Figure 7.2 in Fan 2012 Part I]. The rod-like geometry of the agglomerates in the initial powder particles is consistent with the high green porosity, P_G of 0.62 [German 1994]. In contrast, the green density is about 0.4 to 0.5 for powder compacts composed of nearly equiaxed powder particles [German 1994]. For this study, micrographs of fractured surfaces showed a morphology that is typical of the initial sintering stage [German 1994, Barsoum 1997], with (i) the start of necking between adjacent powders and (ii) the presence of an open network of pores (Figure 7.1a –7.1d). The arrows in Figure 7.1b indicate the connected pore channels with diameter of ~2 μm is observed wandering through the entire microstructure. Micrographs of the specimen sintered at 1025^{o}C (Figure 7.1c and 7.1d) showed a more uniform distribution of pores, where in Figure 7.1d the arrows indicate isolated pores with diameters of ~ 1 μm. The uniformity of pore distribution after sintering at 1025^{o}C may be due to the rearrangement of powder particles during initial sintering stage [Henrich 2007].

3.1.2 Evolution of relative density versus sintering temperature for the HA specimens in the initial and intermediate sintering stages

Table 7.1b. Summary of the types of analysis done in this study along with the number of specimen groups, number of individual specimens and the associated figures in this study.

Analysis done	Material	Number of groups	Number of specimens in total and with valid fractures	Corresponding figures
Relative density, RD	HA	23 (12 from this study and 11 from Fan 2012 Part I)	552 in total (288 from this study and 264 from Fan 2012 Part I)	7.2
Weibull modulus (high P analyzed in this study)	HA	18 (12 from this study and 6 from Fan 2012 Part I)	432 in total (288 from this study and 144 from Fan 2012 Part I) 334 with valid fractures (211 from this study and 123 from Fan 2012 Part I)	7.3 (Weibull probability plots), 7.5 (Weibull vs. porosity), 7.6 (Weibull modulus versus T_{sinter})
Weibull modulus (HA fabricated in this study and from Fan 2012 Part I)	HA	35 (12 from this study and 13 from Fan 2012 Part I)	828 in total (288 from this study and 540 from Fan 2012 Part I); 652 with valid fractures (211 from this study and 441 from Fan 2012 Part I)	7.4a
Weibull modulus (combined)	HA, alumina titania, mullite, LAST-T, silicon nitride silicon	96	More than 1771 valid fractures	7.4b
Fracture strength	HA	18 (12 from this study and 6 from Fan 2012 Part I)	432 in total (288 from this study and 144 from Fan 2012 Part I); 334 with valid fractures (211 from this study and 123 from Fan 2012 Part I)	7.7

In general, for sintered ceramic powder compacts, the relative density versus sintering temperature may be represented in terms of a sigmoidal relationship (Ewsuk and Ellerby 2006, Ouyang 2012**],** as given by equation (3) such that

$$RD = RD_f - \frac{RD_i - RD_f}{1 + \exp\left(\frac{T - T_{const1}}{T_{const2}}\right)} \quad (3)$$

where RD_f is the final relative density, RD_i is the initial relative density. The temperatures T_{const1} and T_{const2} are two constants defining the inflection points on the sigmoidal curve, both with units of ^oC.

In examining the Weibull moduli of porous HA specimens in this study, we employed the HA specimens fabricated in this study along with specimens from our previous study [Fan 2012 Part I]. Although, as discussed in Sections 2.1 and 2.2, the specimens in the two studies were fabricated and tested using the same procedures, it is worthwhile to determine whether or not the densification behavior for the HA specimens fabricated in this study and in the previous study [Fan 2012 Part I] follow the expected sigmoidal behavior (equation 3). For the RD versus sintering temperature evaluation (Figure 7.2), we expanded the scope of our examination of the HA specimens to include a total of 23 specimen groups, of which 12 groups consisted of HA specimens fabricated in this study (Table 7.1b, Figure 7.2) along and 11 groups were specimens from a previous study ([Fan 2012 Part I], Table 7.1b, Figure 7.2). The 12 specimen groups fabricated in this study were each sintered for 2 hours. The 11 porosity groups selected from the Fan 2012 study were sintered for 2 hours except for one group that was sintered for 110 minutes [Fan 2012 Part I]. The remaining groups from Fan

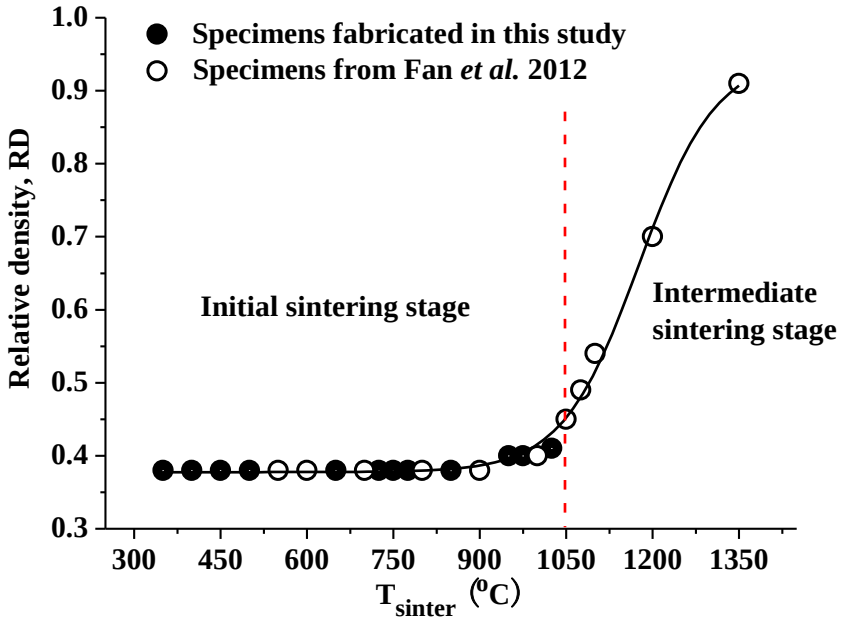

Figure 7.2. Relative density, RD, as a function of sintering temperature for HA specimens in this study and a previous study [Fan 2012 Parts I and II] (Table 7.1b).

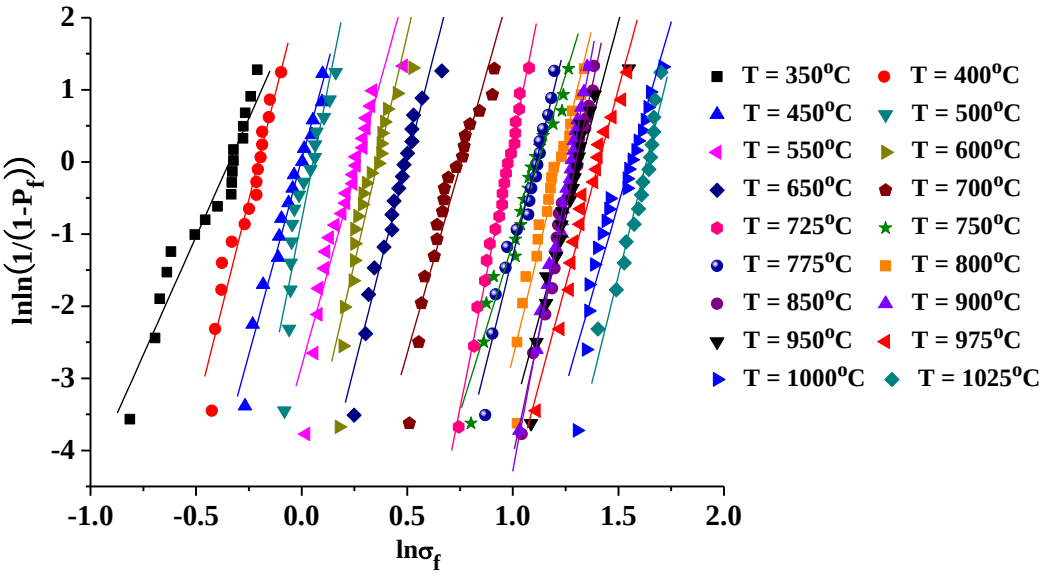

Figure 7.3. Weibull plots for the 18 groups of specimens analyzed in this study (Table 7.1b).

2012 study were not included in the RD analysis in this study because their sintering times differed significantly from 2 hours [Fan 2012 Part I].

A least-squares fit of these 23 porosity groups (Table 7.1b and Figure 7.2) shows that equation (3) describes the relative density versus sintering temperature extremely well with the fitting parameters $RD_f = 0.95 \pm 0.02$, $RD_i = 0.38 \pm 0.003$, $T_{const1} = 1176 \pm 7^oC$, $T_{const2} = 67 \pm 4\ ^oC$, and a coefficient of determination, $R^2 = 0.995$ (Figure 7.2). Thus, as expected, it is confirmed that the sintering behavior for the combined data set (Table 7.1b) is consistent with equation 3 (Figure 7.2) which in turn supports the use of the combined data from this study and the previous study (Table 7.1b) in considering the trends in Weibull modulus as a function of microstructural evolution.

3.1.3 X-ray diffraction results

X-ray diffraction (XRD) results from our earlier study [Fan 2012 Part I] using the same powders and sintering procedures as in this study did not show the presence of secondary phases either for the initial powders (prior to sintering) or the bulk specimens sintered at 1100°C, 1200°C and 1360°C. Thus, we assume that the HA specimens included in this study sintered from 350°C to 1025°C should also be single phase.

3.2 Weibull modulus and fracture strength for HA specimens

A two-parameter Weibull analysis (equation (1)) was used to analyze the fracture data for each of the validly fractured specimens in each group (Figure 7.3, Table 7.1b). A total of 432 specimens yielded 334 valid fractures (Table 7.1b). Except for the data set with $T_{sinter} = 350^oC$, the Weibull probability plots for the specimens fabricated in this study (Figure 7.3)

were relatively linear, indicating that likely one type flaw dominated the fracture process which was also the case for the Weibull data in our paper [Fan 2012 Part I].

Figures 7.4a and 7.4b show the Weibull modulus as a function of porosity for HA data included in this study, HA data from our previous study (Figure 7.4a), and a combined data set including the HA data along with Weibull modulus data from the literature for a number of other brittle materials [Fan 2012 Part I]. Figure 7.4b shows a Weibull modulus trend pointed out in our earlier paper [Fan 2012 Part I], namely that of a U-shaped distribution as a function of porosity. We shall first discuss Figure 7.4a, then Figure 7.4b and then discuss details concerning the three porosity regions (Regions I, II and III, Figure 7.4b).

Figure 7.4a includes the (i) Weibull moduli in the range from HA specimens $0.59 < P < 0.62$ for specimens fabricated in this study (filled circles in Figure 7.4a) along with the entire set of HA data from a previous study [Fan 2012 Part I]. A one-way ANOVA analysis with $p < 0.0005$ showed that the m values in Region III ($P > 0.55$) were significantly higher than those in Region II ($0.1 < P < 0.55$). Thus, the additional data provided by this study (Figure 7.4a) bolsters our earlier observation [Fan 2012 Part I] that Weibull modulus values for the partially sintered HA ($0.59 < P < 0.62$) tends to be higher than that for Region II ($0.1 < P < 0.55$).

In addition, Figure 7.4b compares Weibull moduli from this study and our previous study of HA [Fan 2012 Part I] to Weibull modulus data from a variety of brittle materials in addition to HA. Included in Figure 7.4b are valid fracture data (Appendix B) from 1560 specimens (441 HA specimens from Fan 2012 Part I, 372 HA specimens from the

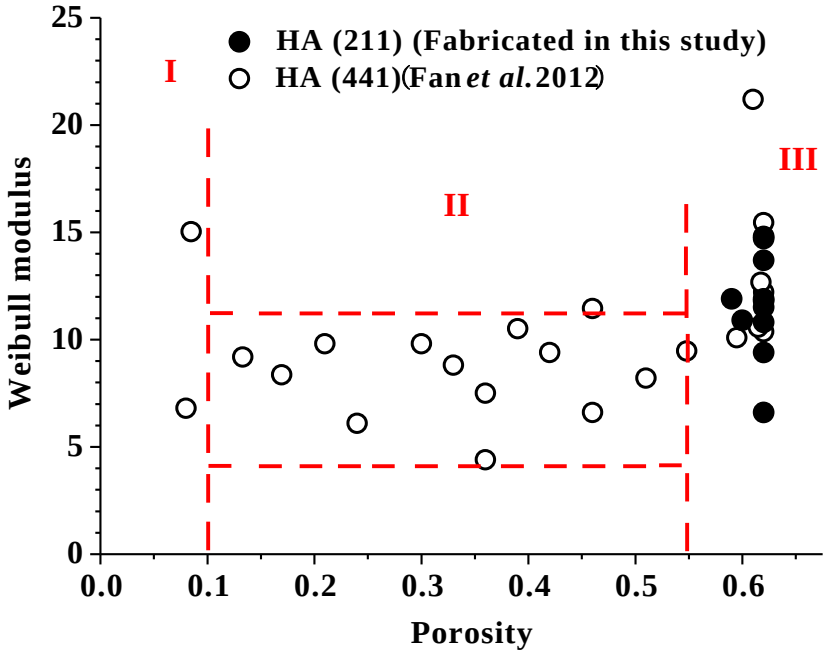

Figure 7.4a. The Weibull modulus versus porosity for HA specimens fabricated in this study along with HA specimens from our previous study ([Fan 2012 Part I], Table 7.1b);

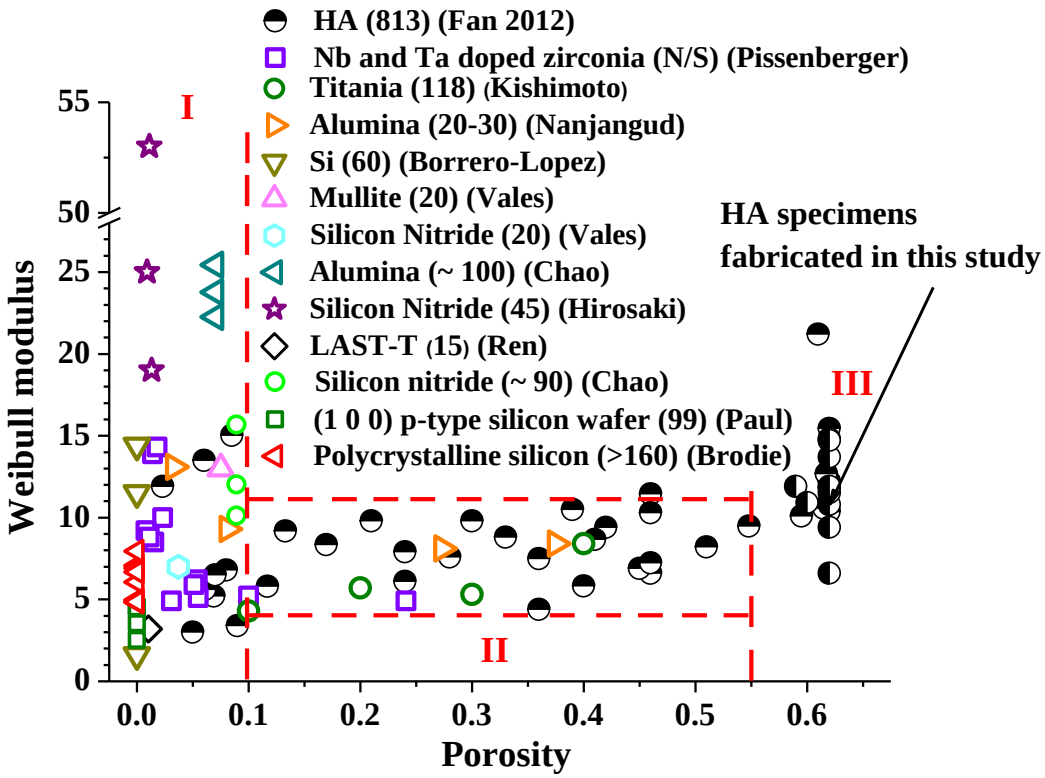

Figure 7.4b. The Weibull modulus versus porosity for (a) HA specimens fabricated in this study along with HA specimens from our previous study ([Fan 2012 Part I], Table 7.1b); (b) the combined data set of the HA data shown in Figure 7.4a and Weibull modulus data from literature data for other brittle materials [Fan 2012 Part I].

literature and data for more than 747 specimens for seven brittle materials other than HA.

Recall that each Weibull modulus value in the literature represents roughly 15 to 20 or more fractured specimens (Appendix A), such that from the literature Figure 7.4b includes a total number of m values for the specimens include 37 m values for HA from Fan [2012 Part I], 12 m values for zirconia, 7 m values for titania, 4 m values for alumina, 15 m values for silicon, one m value for mullite, 7 m values for silicon nitride, one m value for LAST-T thermoelectrics.

When the additional HA data from the current study is combined with the previous study [Fan 2012 Part I], then Figure 7.4b represents the fracture of a total of 1771 brittle specimens, including the 652 HA specimens from this study and the previous Weibull study [Fan 2012 Part I]. For the combined data set (Figure 7.4b, Table 7.1b), the Weibull modulus data shows a three region, U-shaped trend over the entire porosity range including the data from the previous Weibull study [Fan 2012 Part I] and the data from this study for $0.59 < P < 0.62$.

In terms of the nature of the three regions in Figures 7.4a and 7.4b, it is important to note that the particular values of P used to delimit each region, $P_{boundary}$, are empirical and were determined solely from an examination of the m versus P behavior. For example, in Region I ($P \leqslant 0.1$), the Weibull moduli showed a wide range of values with $2 < m < 53$ (Figure 7.4b). The spread in m values is due to the various processing and testing techniques as well as the surface defects caused during processing. The value of $P_{boundary} = 0.1$ marks

an apparent change in the distribution of m values as a function of P, so $P_{boundary} = 0.1$ is assigned as a boundary between Regions I and II (Figures 7.4a and 7.4b).

For other powder compacts, with values of P_G that are different than the HA powders in this study and in our previous Weibull study [Fan 2012 Part I], the $P_{boundary}$ values may be somewhat different than shown in Figure 7.4b. It may be preferable to plot m versus the degree of densification, ϕ, where $\phi = (1 - P/P_G)$ rather than m versus P (Figures 7.4a and 7.4b) in order to account for differences in P_G among powder compacts. However, P_G is not stated in the Weibull modulus literature for either (i) HA work performed by research groups other than the current authors and [Fan 2012 Part I] or for (ii) m data for materials other than HA. Thus, re-plotting Figure 7.4b in terms of m versus ϕ must await additional research on the Weibull modulus of porous brittle materials.

Region II ($0.1 < P \leqslant 0.55$) displays a behavior not reported in the literature prior to our earlier paper [Fan 2012 Part I], namely a band of m values, with $4 < m < 11$ (Figures 7.4a and 7.4b). The narrow range of m values in Region II results from the near universal evolution of pore morphology during the intermediate of sintering stage of sintering powder compacts, where the specimen porosity dominates the flaw population and diminishes the influence of differing processing and testing techniques.

For Region III ($P > 0.55$) (Figures 7.4a and 7.4b), the relatively high m values for the HA specimens may stem from the relatively open, interconnected pore structure. We expect that materials other than HA sintered from powder compacts may exhibit a similar behaviour in Region III, due to the very similar evolution of interparticle necking and pore modification

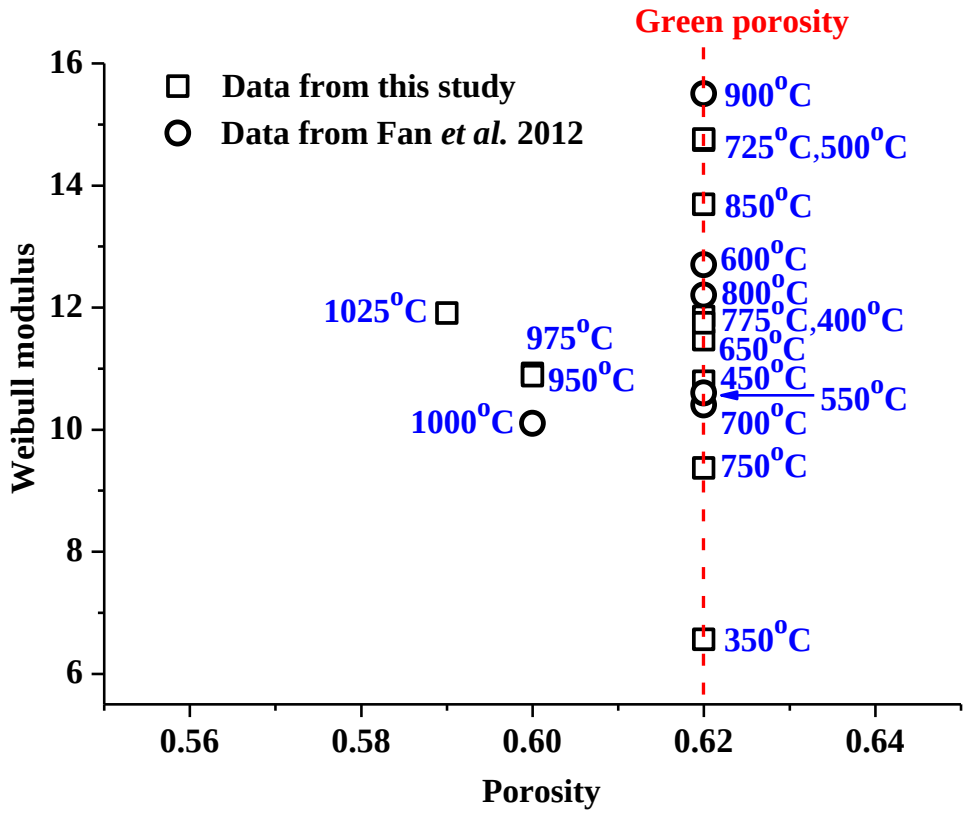

Figure 7.5. Weibull modulus, m, as a function of porosity for the HA specimens analysed in this study (Table 7.1b). Each data point in this plot represents the valid fracture of roughly 15 to 20 individual specimens.

Table 7.2. For the HA specimens included in this study, the fitting parameters for least-squares fit of the mean fracture strength, $<\sigma_f>$, versus the sintering temperature, T_{sinter}, to equations (6), (7) and (8).

Equation number	a_i (MPa)	b_i	c_i	R^2
5	-0.282 ± 0.759	0.001 ± 0.002 [a]	3.69e-6 ± 1.62e-6 [c]	0.964
6	-1.93 ± 0.26	0.0062 ± 0.0004 [a]	N.A.	0.951
7	0.363 ± 0.059	0.0025 ± 0.0002 [b]	N.A.	0.945

[a] Units of b_1 (equation (6)) and b_2 (equation (7)) are MPa/^oC

[b] Units of b_3 (equation (8)) are $^oC^{-1}$; [c] Units of c_1 are MPa/$(^oC)^2$

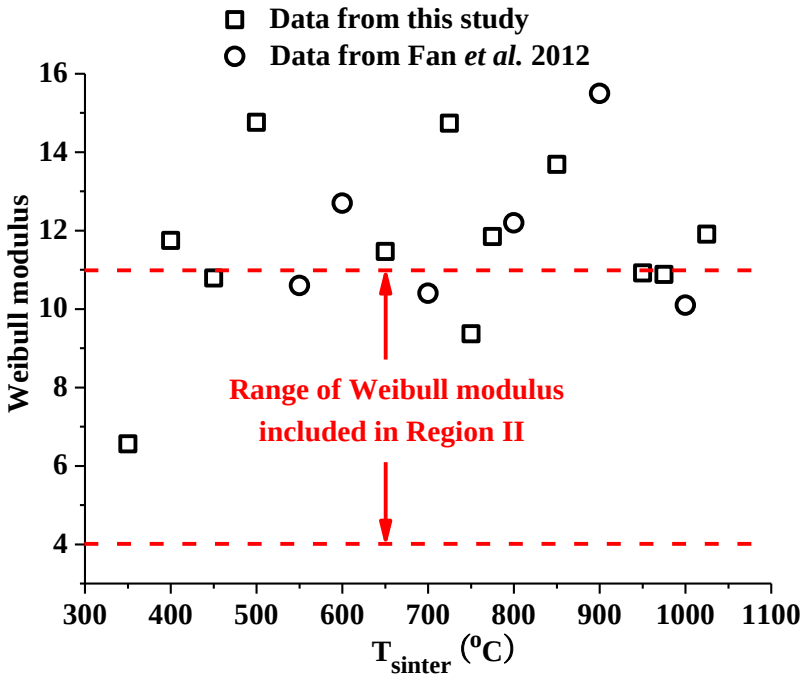

Figure 7.6. Weibull modulus, m, as a function of sintering temperature, T_{sinter}, for the HA specimens analysed in this study (Table 7.1b).

observed during the initial sintering stage for wide range of metal and ceramic materials [German 1996, Barsoum 1997]. Thus, this study confirms the apparent trend that the Weibull modulus tends to be surprisingly high for P > 0.55 (Figures 7.4a, 7.5, Table 7.1b), as was also observed in the study by Fan 2012 Part I. It should be noted that except for this study and the earlier study by Fan [2012] Part I, only two Weibull modulus values were available in the literature for P > 0.47 for any brittle material [Villora 2004]. In particular, those two literature m data values at P = 0.55 and 0.65 were obtained from diametral compression testing on composite HA specimens that included diatoms and industrial sludge [Villora 2004].

In addition to m as a function of P, we also consider m as a function of the sintering temperature, T_{sinter} (Figure 7.6). A band of m values from roughly 9 to 15 (except one m value at ~7) from this study displays considerable scatter as a function of T_{sinter} (Figure 7.6, Table 7.1b), although the m values are consistently high. Since for sintering between 350^{o}C and 900 ^{o}C, there is no densification, Figure 7.6 shows a spread in the m values from 7 to 15 at fixed value of P = 0.62, which corresponds to the porosity of the green powder compacts. Changes in the Weibull modulus for specimens sintered in the temperature interval between 350^{o}C and 900^{o}C is likely related to an increase in the relative interparticle neck size increased with increasing T_{sinter}, as will be discussed further in the following section on fracture strength.

3.3 Fracture strength for HA specimens

Since the Weibull moduli of the highly porous (P > 0.55) HA specimens in both this study and the Fan 2012 Part I study show behavior that has not been reported previously, it is of interest to also consider the behavior of the mean fracture strength for these specimens. However, first we shall very briefly review the highlights of fracture strength versus P relationships for brittle materials in order to put the behavior of our materials into context.

A widely used empirical strength-porosity relationship [Ryshkewitch 1953, Duckworth 1953] describes the decrease in modulus with increasing P such that

$$\sigma_f = \sigma_0 \exp(-bP) \tag{4}$$

where σ_0 is the strength for the theoretically dense material, P is the volume fraction porosity and b is a unitless, material-dependent constant measuring the rate of decrease in σ_f with increasing P. As reviewed by Rice [1998], equation (4) generally describes well the strength-porosity behaviour for brittle materials up to a critical porosity, P_C, but for $P > P_C$, the fracture strength may decrease more rapidly than equation (4) predicts [Rice 1998].

Equation (5), a modified Phani equation [Phani and Niyogi 1987], has been used by Fan [2012 Part II] as an alternative to equation (4). Using equation (5), the relative fracture strength, $<\sigma_f>/ \sigma_0$, can be described as a function of the degree of densification over the entire range of P from P near zero to P near P_G, such that

$$\frac{<\sigma_f>}{\sigma_o} = A_\sigma\left(1-\frac{P}{P_G}\right)^n = A_\sigma(\phi)^n \tag{5}$$

where $<\sigma_f>$ is the average fracture strength of a group of porous ceramics with a fixed value of P, P_G is the porosity of the green (unfired) powder compact, $\phi = (1 - P/P_G)$ is defined as

the degree of densification, A_σ and n are dimensionless constants.

In our previous papers [Fan 2012 Part I and Part II], the porosity dependence of the fracture strengths of partially sintered HA specimens was described well by equation (5). This study deals with fracture of highly porous HA specimens, namely from 0.59 to 0.62, so that the sintering process is limited to the initial sintering stage in which interparticle necks develop. Moreover, in this study, for sintering temperatures between 350^{o}C and 900^{o}C, there is no densification. Since the specimens do not densify, the porosity is fixed at $P = P_G$ (where $P_G = 0.62$ in this study). Thus, although equations (4) and (5) are extremely useful in describing strength-porosity relationships when the entire data set includes only specimens with $P < P_G$, equations (4) and (5) are of very limited utility in describing the changes in strength that are observed with changes in sintering temperature over the sintering range from 350^{o}C and 900^{o}C where the porosity is fixed at $P = P_G$.

However, if we consider the mean fracture strength $<\sigma_f>$ versus the sintering temperature, T_{sinter}, there is a monotonic decrease in $<\sigma_f>$ with decreasing T_{sinter} (Figure 7.7, Table 7.1b). The $<\sigma_f>$ versus T_{sinter} trends were examined via a least-squares fit of the data to each of three empirical functions given by equations (6) through (8)

$$<\sigma_f> = a_1 + b_1 T_{sinter} + c_1 (T_{sinter})^2 \quad (6)$$

$$<\sigma_f> = a_2 + b_2 T_{sinter} \quad (7)$$

$$<\sigma_f> = a_3 \exp(b_3 T_{sinter}) \quad (8)$$

where the numerical values and physical units of each of the empirical fitting parameters a_1,

b_1, c_1, a_2, b_2, a_3, and b_3 are given in Table 7.2 along with the coefficient of determination, R^2 for the least squares fit of the data to each equation (Figure 7.7). Based on the R^2 values given in Table 7.2, the quadratic empirical relationship (equation (6)) best describes the $<\sigma_f>$ versus T_{sinter} behavior observed in this study, although the quadratic relationship (equation (6)) is only marginally better than the linear relationship (equation (7)).

In addition to the porosity and sintering temperature, it is important to consider whether other factors might affect the measured $<\sigma_f>$ values. For example, since the strength of brittle materials can be affected by factors such as grain size [Barsoum 1997, Ren 2006, Wachtman 2009] and microcracking [Hoepfner and Case 2004, Rokhlin 1993, Sridhar 1994, Tomczyk 2012], we shall briefly consider the role that the grain size and microcracking might play in the measured state of the $<\sigma_f>$ values. In general, during final sintering stage ($P < 0.05$) the grain size, G, typically increases dramatically, P is relatively constant, and fracture strength $\approx G^{-0.5}$ [Barsoum 1997]. However, during the initial sintering stage, from the measured grain size-density trajectory for the HA specimens in the Fan 2012 Part I (which are identical to the powders used in the current study), the grain size ranged from about 0.5 micron to 1.5 microns for HA with P from about 0.62 to 0.2. Furthermore, in the range of P included in this study (0.59 to 0.62), the grain size was essentially fixed at approximately 0.5 microns [Fan 2012 Part I] and thus the functional dependence of strength upon G is likely not a significant consideration in this study.

HA typically occurs in the hexagonal form [Case 2005], which along with all non-cubic crystalline materials, making HA susceptible to microcracking due to thermal expansion

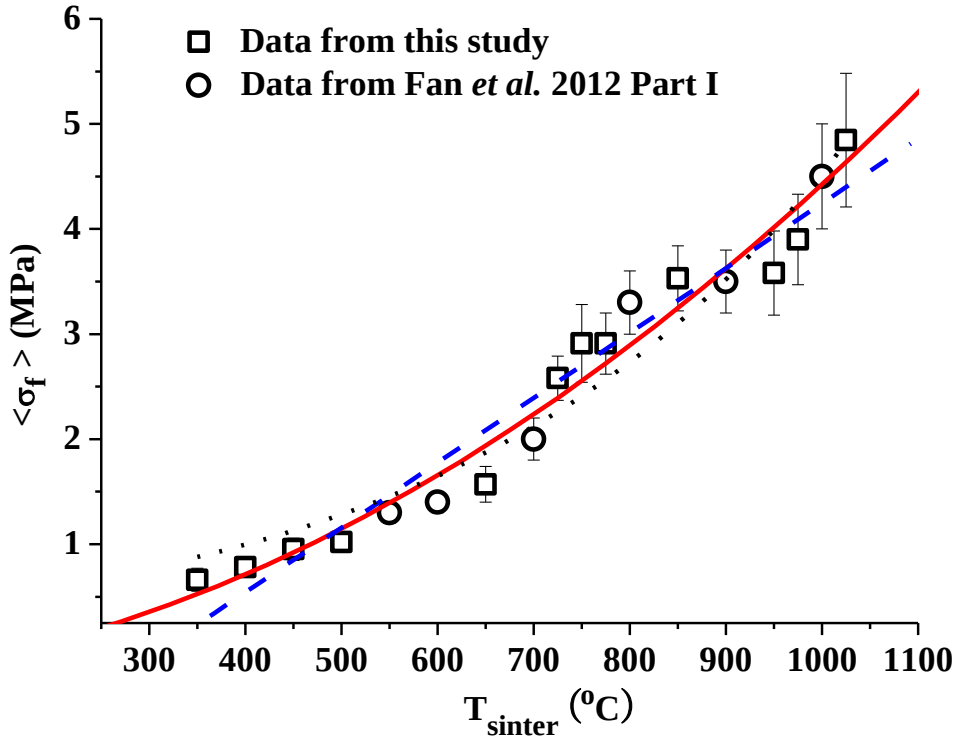

Figure 7.7. The mean fracture strength, $<\sigma_f>$, as a function of sintering temperature for the HA specimens analysed in this study (Table 7.1b), where the solid curve represents a least-squares fit of the data to equation (6), the dashed line represents a least-squares fit of the data to equation (7) and the dotted curve represents a least-squares fit of the data to equation (8).

anisotropy (TEA). TEA-induced microcracking for grain sizes larger than a material-dependent critical grain size, G_C, can occur upon cooling from an elevated temperature due to the unequal thermal expansion along the crystallographic axes in a polycrystal [Hoepfner and Case 2004, Sridhar 1994, Tomczyk 2012].

SEM observations by Case [2005] indicate microcracking due to TEA does occur in polycrystalline HA with $P \approx 0.02$ and a mean grain size of 7.9 ± 1.5 microns, although the same study did not observe microcracking in the non-cubic materials tricalcium phosphate (TCP) and biphasic calcium phosphate (BCP, a two- phase polycrystalline material containing both HA and TCP). In the Case study [2005], the grain sizes for the TCP and BCP were 2.9 ± 0.6 microns and 1.3 microns respectively, with $P > 0.37$ for both TCP and BCP [Case 2005]. In interpreting the microcracking results from the Case study [2005], it is important to consider that (i) $P > 0.2$ to 0.3 can strongly suppress microcracking in brittle materials [Manning 1972] and (ii) for $G < G_C$ microcracking does not occur. Given the very high P values and small grain sizes (about 0.5 micron) of the HA specimens in this study, it is unlikely that microcracking plays a significant role.

Thus, grain size and TEA-induced microcracking should have a limited role in determining the $<\sigma_f>$ versus T_{sinter} behavior of the HA specimens in this study. Likewise, given that 14 of the 18 groups of specimens in this study have a fixed porosity of $P = P_G$, the results of $<\sigma_f>$ are not a strong function of porosity. Thus, the monotonic decrease in the $<\sigma_f>$ versus T_{sinter} is likely due to the development of interparticle necking of adjacent grains (Figure 7.7).

4. Summary and Conclusions

Since the Weibull modulus is a measure of the spread or scatter in fracture strength, the Weibull modulus is extremely important as a gauge of mechanical reliability (Appendix A). Nevertheless, Weibull modulus data for highly porous materials is extremely limited in the open literature. This study explored the porosity dependence of the Weibull modulus and fracture strength of a total of 432 HA specimens that were sintered from 350^{o}C to 1025^{o}C for 2 hours resulting in a range of volume fraction porosity from 0.59 to 0.62, indicating only limited densification occurred (since the porosity of the unfired powder compacts, P_G, was 0.62). The specimens were then fractured via biaxial flexural testing on a ring-on-ring test fixture.

A key result of this study is that the Weibull modulus ranged from 6.6 to 15.5 for these highly porous, partially sintered HA specimens ($0.59 < P < 0.62$), which represents surprisingly small scatter in strength for such specimens. However, in contrast to the Weibull modulus behavior, the mean fracture strength drops monotonically as the sintering temperature decreases (Figure 7.7), indicating that the extent of interparticle necking decreases as T_{sinter} decreases. Considering the Weibull modulus and fracture strength data together, we conclude that as T_{sinter} decreases, the interparticle neck dimensions decrease as we would expect from the evolution of necking during sintering while the open, interconnected porosity leads to a relatively narrow flaw size distribution and thus a correspondingly high Weibull modulus.

This study and our earlier Weibull modulus study [Fan 2012 Part I] constitute the first

systematic work on the Weibull modulus of high porous brittle materials. In particular, this study confirms that for HA, the Weibull modulus remains high for partially sintered specimens with P at or near the green density, P_G (Region III in Figures 7.4a and 7.4b).

It is likely the Weibull modulus versus porosity behavior in Region III (P near or equal to P_G) for other brittle materials will be similar to that observed in this study for HA. This prospect is supported by the fact that in Region II ($0.1 < P \leqslant 0.55$, Figure 7.4b) the band of 32 m versus P values includes data from four different materials, namely alumina (three m values), zirconia (two m values), titania (three m values) and HA (24 m values). Thus if the behavior in Region II (Figure 7.4b) is similar for various brittle materials, that similarity may carry over to Region III also. However, except for this study and the Fan 2012 Part I paper, the current lack of Weibull modulus data in the literature for brittle materials with P > roughly 0.2 makes wide-ranging comparisons difficult to make.

As discussed in the Introduction, many of the current uses of highly porous materials are for porosity ranges between 0.2 and 0.5. However, from the results of study, we may conclude that knowing the Weibull modulus for these materials in the initial sintering stage may stimulate the development of both biomedical and non-biomedical applications of sensors, catalyst supports and filters. Despite their low strength, the mechanical reliability (low scatter in strength values) indicated by the surprisingly high Weibull modulus of the materials may indicate to designers that new, practical applications are possible.

The extremely diverse range of biomedical and non-biomedical applications and potential uses for HA and other highly porous brittle materials makes these findings on

Weibull modulus very interesting, due to the direct connection between Weibull modulus and mechanical reliability. Future work should explore the porosity dependence of the Weibull modulus for highly porous specimens of biomaterials other than HA as well as additional brittle materials.

5. Acknowledgements

The authors acknowledge the financial support of the National Science Foundation, Division of Materials Research Grant DMR-0706449. The authors would like to thank Jennifer Ni (graduate student, Chemical Engineering and Materials Science Department, Michigan State University) for her help in taking the SEM images. The authors also thank the Michigan State University High School Honors Science/Mathematics/Engineering Program (HSHSP) for support received by I. Gheorghita during this research.

APPENDICES

APPENDIX A

WEIBULL ANALYSIS

Weibull analysis has been widely used in to characterize the scatter in a measured property, such as fracture strength [Meganck 2005, Ren 2006, Wachtman 2009, Morrison 2012]. Thus, the Weibull modulus is directly linked to material reliability, since the less scatter in a property such as strength, the more reliable a component is.

Typically Weibull analysis is performed on a group of specimens that are nominally identical. In this study and in our earlier study [Fan 2012 Part I], a group of specimens consisted of 24 specimens that were fabricated and tested in the same way (Sections 2.1 and 2.2), except that the sintering time and temperature differed among the groups which resulted in specimens with differing stages of microstructural development [German 1996, Barsoum 1997].

As an example of the application of Weibull analysis to a particular group of fractured specimens, let us consider the group of HA specimens from this study which was sintered at 725^{o}C with 20 valid fractures (Table 7.1a). Figure 7.A1 is a Weibull probability plot, where the Weibull modulus, m, is the slope of the least-squares fit of $\ln\ln(1/(1-\Lambda_f))$ versus $\ln\sigma_f$ (Figure 7.A1, equation 1). The characteristic strength, σ_C, (Table 7.1a) can be calculated from the least-squares fit at $\ln\ln(1/(1-\Lambda_f)) = 0$. At characteristic strength, σ_C, the value of Λ_f is 0.63, which means 63% of specimens will fail at or below σ_C.

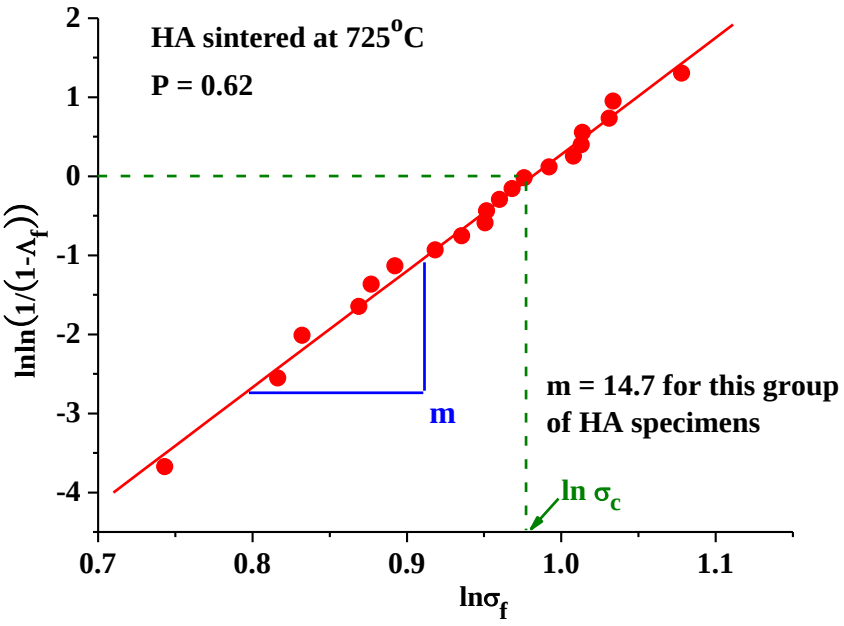

Figure 7.A1. The Weibull plot of a group of HA specimens sintered in this study at 725°C (Table 7.1a). The slope of the plot, m, is the Weibull modulus, which is a measure of the scatter in fracture strength values for this group of specimens.

It is important to comment on the nature of both the Weibull modulus and the characteristic strength. If the fracture strength was exactly the same for each specimen of a given group then the plotted line in Figure 7.A1 would be vertical and the Weibull would be infinite. Conversely, a Weibull modulus value approaching zero would correspond to an infinite scatter among the strength values of the group of specimens.

In addition, the characteristic strength is akin to the median strength, where for the median strength, 50% of the fractures would fall below the median. Often the median and the mean of a distribution are similar but the difference between the median and the mean depends on the details of the distribution. Likewise, the characteristic strength and the mean strength are typically similar but not equal.

APPENDIX B

BIAXIAL FLEXURE TESTING

Biaxial flexure is used widely for fracture testing of biomedical and non-biomedical materials. In biaxial flexure testing, typically a disc specimen is placed on a support ring (Figure 7.B1a) which the load applied by either a sphere (referred to as “ball on ring testing”, [Wachtman 2009]) or by a loading ring (termed “ring on ring testing”, ASTM C1499 2003).

In this study, ring on ring testing was used (Figures 7.B1a and Figure 7.B1b).

In a valid ring-on-ring test (ASTM C1499 2003), the cracks initiate on the specimen surface between the support ring and loading ring (Figure 7.B2). A common type of invalid fracture test is one in which the specimen fails via a diametral crack, indicating that failure initiated from the specimen edge (Figure 7.B2). Only the data for validly fractured specimens were included in the Weibull modulus and fracture strength studies.

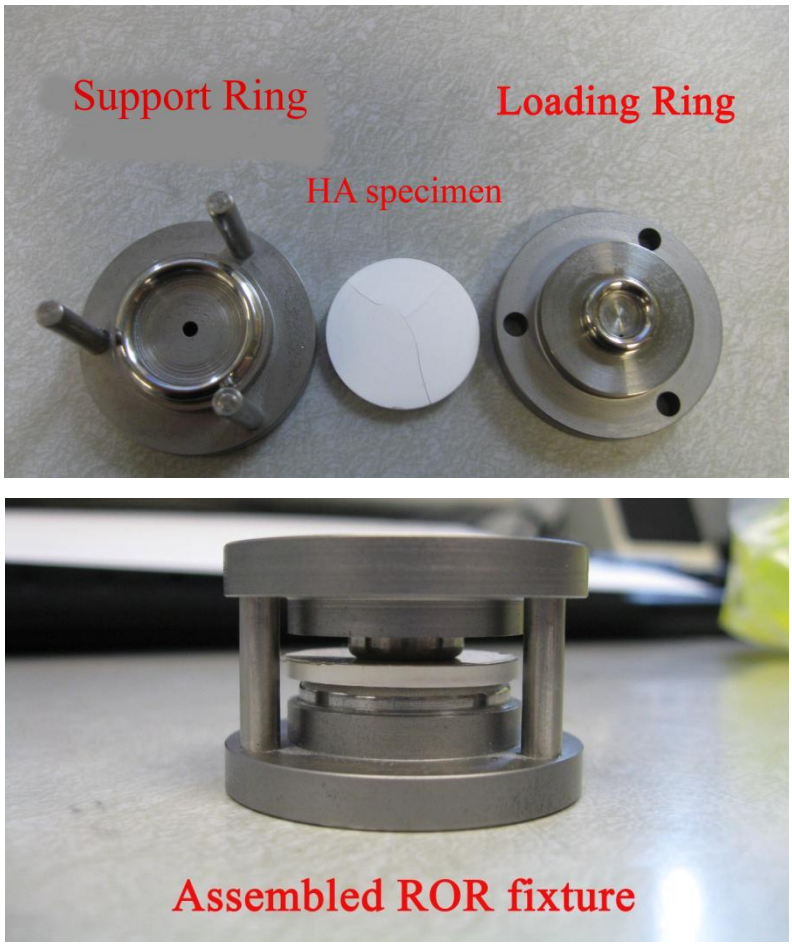

Figure 7.B1. Digital image of (a) the ring-on-ring fixture showing the specimen support ring and loading ring used in the biaxial flexure testing in this study; (b) the assembled ring-on-ring fixture used in the biaxial flexure testing in this study.

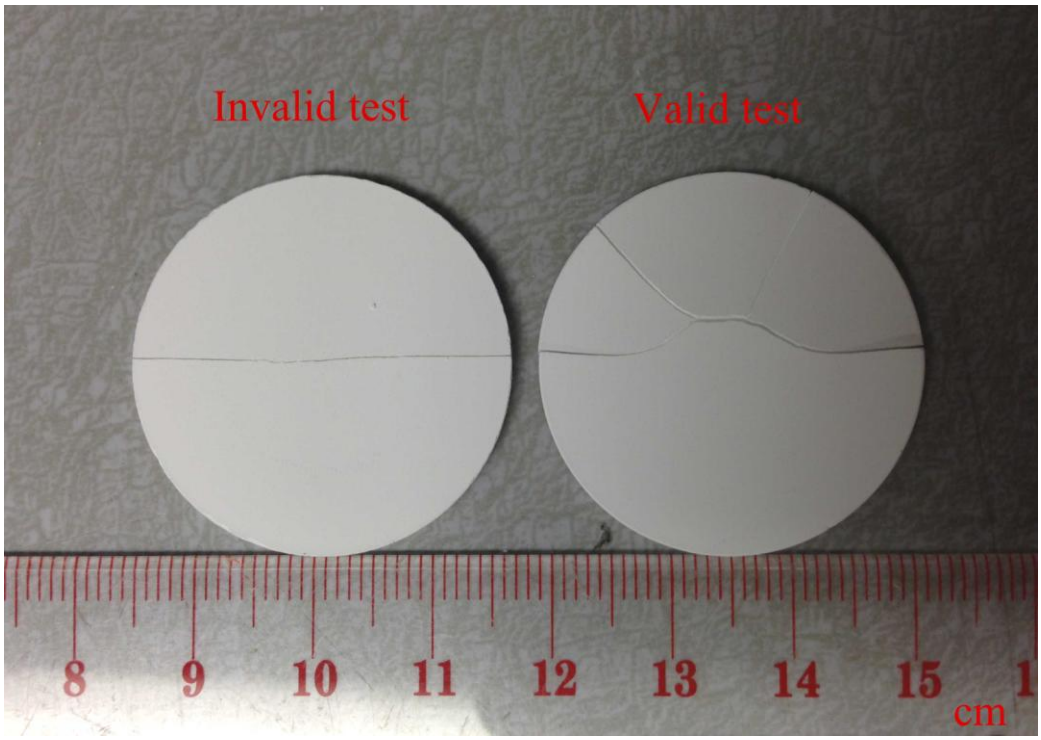

Figure 7.B2. Digital image of examples of valid and invalid fractures of HA specimens included in this study. The crack patterns for the valid test specimens are discussed in the ASTM standard for ring-on-ring testing (ASTM C1499 2003).

REFERENCES

REFERENCES

[Addison 2012] Addison, O. Cao X., Sunnar P., Fleming G. J. P., 2012, Machining variability impacts on the strength of a ‘chair-side’ CAD–CAM ceramic, Dental Materials, 28, 880–887.

[Akao 1981] Akao, M., Aoki, H., Kato, K., 1981. Mechanical-properties of sintered hydroxyapatite for prosthetic applications. J. Mater. Sci. 16, 809–812.

[ASTM 2008] ASTM C1161 - 02c(2008)e1, 2008, Standard Test Method for Flexural Strength of Advanced Ceramics at Ambient Temperature, ASTM, West Conshohocken, PA.

[ASTM 2003] ASTM C1499-05, 2003, Standard Test Method for Monotonic Equibiaxial Flexural Strength of Advanced Ceramics at Ambient Temperature, ASTM, West Conshohocken, PA.

[Barsoum 1997] Barsoum, M. W., 1997. Fundamentals of Ceramics, The McGraw – Hill Companies, Inc., New York.

[Baumann 2007] Baumann, M.J., Case, E.D., Smith, I.O., 2007. Pores needed for biological function could paradoxically boost fracture energy in bioceramic bone tissue scaffolds, in Developments in Porous, Biological and Geopolymer Ceramics, Ceramic Engineering and Science Proceedings, Volume 28, Issue 9, M. Brito, E. D. Case and W. M. Kriven, Editors, Wiley InterScience, New York, pp 197 – 207.

[Borrero-Lopez 2009] Borrero-Lopez, O., Vodenitcharova, T., Hoffman, M., Leo, A. J., 2009. Fracture strength of polycrystalline silicon wafers for the photovoltaic industry. J. Am. Ceram. Soc. 92, 2713 - 2717.

[Boyd 2008] Boyd D., Towler M. R, Wren A., Clarkin O. M., 2008, Comparison of an experimental bone cement with surgical SimplexP, Spineplex and Cortoss. J Mater Sci: Mater Med 19, 1745–1752.

[Brodie 2003] Brodie, R.C., Bahr, D.F., 2003. Fracture of polycrystalline silicon. Mater. Sci. Eng. A 351, 166 - 173.

[Case 2005] Case, E.D., Smith, I.O., Baumann, M.J., 2005. Microcracking and porosity in calcium phosphates and the implications for bone tissue engineering, Mater. Sci. Eng. A 390, 246–254.

[Chao 1991] Chao, L.Y., Shetty, D. K., Leo, J., 1991. Reliability analysis of structural ceramics subjected to biaxial flexure. J. Am. Ceram. Soc. 74, 333 - 344.

[Coble 1961] Coble, R. L., 1961, Sintering crystalline solids I. intermediate and final state diffusion models. J. Appl. Phys. 32, 787 – 792.

[Cordell 2009] Cordell, J.M., Vogl, M.L., Johnson, A.J.W., 2009. The influence of micropore size on the mechanical properties of bulk hydroxyapatite and hydroxyapatite scaffolds. J. Mech. Behav. Biomed. 2, 560-570.

[CRC 2009] CRC Handbook of Chemistry and Physics, 90th ed., CRC press, four-55, 2009.

[Deng 2002] Deng, Z-Y., Yang, J-F., Beppu, Y., Ando, M., Ohji, T., 2002. Effect of agglomeration on mechanical properties of porous zirconia fabricated by partial sintering, J. Am. Ceram. Soc. 85, 1961 – 1965.

[Duckworth 1953] Duckworth, W., 1953. Discussion of Ryshkewitch paper by Winston Duckworth. J. Am. Ceram. Soc. 36, 68.

[Ewsuk 2006] Ewsuk, K. G., Ellerby, D. T., 2006. Analysis of nanocrystalline and microcrystalline ZnO sintering using master sintering curves. J. Am. Ceram. Soc. 89, 2003–2009.

[Fan 2012 Part I] Fan, X., Case, E. D., Ren, F., Shu, Y., Baumann, M. J., 2012. Part I: Porosity dependence of the Weibull modulus for hydroxyapatite and other brittle materials. J. Mech. Behav. Biomed. 8, 21-36.

[Fan 2012 Part II] Fan, X., Case, E. D., Ren, F., Shu, Y., Baumann, M. J., 2012. Part II: Fracture strength and elastic modulus as a function of porosity for hydroxyapatite and other brittle materials. J. Mech. Behav. Biomed. 8, 99-110.

[German 1994] German, R.M., 1994. Powder Metallurgy Science, Metal Powder Industries Federation, New Jersey.

[German 1996] German, R. M., 1996. Sintering Theory and Practice, John Wiley & Sons, Inc., New York.

[Gibson 2010] Gibson, L. J., Ashby, M. F., Harley, B. A., 2010. Cellular materials in nature and medicine. Cambridge University Press, Cambridge, UK.

[Gonzaga 2011] Gonzaga C. C., Cesar P. F., Miranda W. G. Jr., Yoshimura H. N., 2011, Slow crack growth and reliability of dental ceramics, Dental Materials, 27, 394–406

[Hardy 1995] Hardy, D., Green, D.J., 1995. Mechanical properties of a partially sintered alumina, J. Eur. Ceram. Soc. 15, 769-715.

[He 2008] He, L., Standard, O., Huang, T., Latella, B., Swain, M., 2008. Mechanical behaviour of porous hydroxyapatite. Acta Biomater 4, 577–586.

[Hench 1991] Hench, L.L., 1991. Bioceramics - from concept to clinic. J. Am. Ceram. Soc. 74, 1487 – 1510.

[Henrich 2007] Henrich, B., Wonisch, A., Kraft, T., Moseler, M., Riedel, H., 2007. Simulations of the influence of rearrangement during sintering. Acta Materialia 55, 753–762.

[Hirosaki 1993] Hirosaki, N., Akimune, Y., 1993. Effect of Grain Growth of p-Silicon Nitride on Strength, Weibull Modulus, and Fracture Toughness. J. Am. Ceram. Soc. 76, 1892 - 1894.

[Hoepfner 2004] Hoepfner, T. P., Case, E. D, 2004. An estimate of the critical grain size for microcracks induced hydroxyapatite by thermal expansion anisotropy, Mater. Lett. 58, 489 -492.

[Kim 1995] Kim, Y.M., Mitomo M., Hirosaki, N., 1995. R-curve behaviour and microstructure of sintered silicon nitride. . J. Mater. Sci. 30, 5178 - 5184.

[Kishimoto 1991] Kishimoto, A., Koumoto, K., Yanagida, H., Nameki, M., 1991. Microstructure Dependence of Mechanical and Dielectric Strengths .1. Porosity. Eng. Fract. Mech. 40, 927-930.

[Le Huec 1995] Le Huec, J., Schaeverbeke, T., Clement, D., Faber, J., Le Rebeller, A., 1995, Influence of porosity on the mechanical resistance of hydroxyapatite ceramics under compressive stress. Biomaterials 16, 113–118.

[Liu 2011] Liu, L., Loh, N. H., Tay, B.Y., Tor, S. B., Yin, H. Q., Qu, X. H., 2011. Investigation of final-stage sintering of various microsize structures prepared by micro powder injection molding. Appl. Phys. A 103, 1145–1151.

[Lopes 1999] Lopes, M.A., Monteiro, F.J., Santos, J.D., 1999. Glass-reinforced hydroxyapatite composites: Secondary phase proportions and densification effects on biaxial bending strength. J. Biomed. Mater. Res. 48, 734-740.

[Mahabole 2005] Mahabole, M.P., Aiyer, R.C., Ramakrishna, C.V., Sreedhar, B., Khairnar, R.S., 2005. Synthesis, characterization and gas sensing property of hydroxyapatite ceramic, Mater. Sci. B 28, 535-545.

[Manning 1972] Manning, W. R., Hunter O. Jr., Calderwood, J.W. Stacy, D. W. Thermal expansion of Nb_2O_5 1972, J. Am. Ceram. Soc. 55, 342–347.

[Meganck 2005] Meganck, J.A., Baumann, M.J., Case, E.D., McCabe, L.R., Allar, J.N., 2005. Biaxial flexure testing of calcium phosphate bioceramics for use in tissue engineering. J. Biomed. Mater. Res. A 72. 115-126.

[Morrison 2012] Morrison, A.Q, Case, E.D., Ren F., Baumann A.J., Hendricks T.J., Cauchy C., Barnard, J. 2012, Elastic Modulus and Biaxial Fracture Strength of Thermally Fatigued Hot Pressed LAST Materials, Materials Chemistry and Physics, 134: 973-987.

[Murray 1995] Murray, M.G.S., Wang, J., Ponton, C.B., Marquis, P.M., 1995. An Improvement in Processing of Hydroxyapatite Ceramics. J. Mater. Sci. 30, 3061-3074.

[Nakamura 2010] Nakamura, Y., Hojo S., Sato, H., 2010. The effect of surface roughness on the Weibull distribution of porcelain strength. Dent. Mater. J. 29, 30 - 34.

[Nanjangud 1995] Nanjangud, S.C., Brezny, R., Green, D.J., 1995. Strength and Young's Modulus Behavior of a Partially Sintered Porous Alumina. J. Am. Ceram. Soc. 78, 266-268.

[Ohtsuki 2010] Ohtsuki, C., Ichikawa, Y., Shibata, H., Kawachi, G., Torimoto, T., Ogata, S., 2010. Sensing of protein adsorption deposited. J. Mater. Sci. Mater. Med. 2, 1225–1232.

[Ouyang 2012] Ouyang, C.X., Zhu, S.G., Ma, J., Qu, H.X., 2012. Master sintering curve of nanocomposite WC-MgO powder compacts. J. Alloy. Compd. 518, 27–31.

[Paul 2006] Paul, I., Majeed, B., Razeeb, K. M., Barton, J., 2006. Statistical fracture modeling of silicon with varying thickness. Acta Mater. 54, 3991 - 4000.

[Phani 1987] Phani, K. K., Niyogi, S. K., 1987. Young's modulus of porous brittle solids, J. Mater. Sci. 22, 257-263.

[Pissenberger 1995] Pissenberger, A., Gritzner, G., 1995. Preparation and Properties of Niobia-Doped and Tantala-Doped Orthorhombic Zirconia. J. Mater. Sci. Lett. 14, 1580-1582.

[Pramanik 2007] Pramanik, S., Agarwal, A. K., Rai, K., Garg, A., 2007. Development of high strength hydroxyapatite by solid-state-sintering process. Ceram. Int. 33, 419–426.

[Ren 2006] Ren, F., Case, E.D., Timm, E.J., Jacobs, M.D., Schock, H.J., 2006. Weibull analysis of the biaxial fracture strength of a cast p-type LAST-T thermoelectric material. Phil. Mag. Lett. 86, 673–682.

[Ren 2009] Ren, F., Case, E.D., Morrison, A., Tafesse, M., Baumann, M.J., 2009. Phil. Mag. 89, 1163-1182.

[Rice 1998] Rice, R.W., 1998. Porosity of Ceramics, Marcel Dekker, Inc., New York.

[Rokhlin 1993] Rokhlin, S.I., Chu, Y.C. Hefetz, M., 1993. Ultrasonic evaluation of microcrack thermal shock damage, Ceram. Eng. Sci. Proc. 14, 454- 462.

[Ruys 1995] Ruys, A.J., Wei, M., Sorrell, C.C., Dickson, M.R., Brandwood, A., Milthorpe, B.K., 1995. Sintering Effects on the Strength of Hydroxyapatite. Biomaterials 16, 409-415.

[Ryshkewitch 1953] Ryshkewitch, E., 1953. Compression strength of porous sintered alumina and zirconia. J. Am. Ceram. Soc. 36, 65–68.

[Sommer 2005] Sommer, S., Melin, T., 2005. Performance evaluation of microporous inorganic membranes in the dehydration of industrial solvents. Chem. Eng. Process 44, 1138-1156.

[Son 2011] Son, J. S., Appleford, M., Ong, J. L., Wenke, J.C., Kim, J. M., Choi, S. W., Oh, D. S., 2011. J. Control. Release 153, 133–140.

[Sridhar 1994] Sridhar, N., Yang,W., Srolovitz, D., Fuller,J.E., 1994. Microstructural mechanics model of anisotropic-thermal expansion-induced microcracking. J. Am. Ceram. Soc. 77, 1123–1138.

[Srinivasan 2006] Srinivasan, M., Ferraris, C., White, T., 2006. Cadmium and lead ion capture with three dimensionally ordered macroporous hydroxyapatite. Environ. Sci. Technol. 40, 7054-7059.

[Tomczyk 2012] Tomczyk, M., Senos, A.M. Vilarinho, P.M., Reaney I.M., 2012. Origin of microcracking in YMnO3 ceramics, Scripta Mater. 66, 288–291.

[Twigg 2007] Twigg, M.V., Richardson, J.T., 2007. Fundamentals and applications of structured ceramic foam catalysts. Ind. Eng. Chem. Res. 46, 4166-4177.

[Vales 1999] Vales, F., Rezakhanlou, R., Olagnon, C., 1999. Determination of the fracture mechanical parameters. J. Mat. Sci. 34, 4081 - 4088.

[Villora 2004] Villora, J.M., Callejas, P., Barba, M.F., Baudin, C., 2004. Statistical analysis of the fracture behaviour of porous ceramic Raschig rings. J. Eur. Ceram. Soc. 24, 589-594.

[Wachtman 2009] Wachtman, J. B., Cannon, W. R., Matthewson, M. J., 2009. Mechanical Properties of Ceramics, 2nd ed., Wiley Interscience, New York.

[Wagoner Johnson 2011] Wagoner Johnson, A. J., Herschler, B. A., 2011. Acta Biomater. 7, 16–30.

[Yang 2007a] Yang, L., Ning, X. S., Xiao, Q. F., Chen, K. X., Zhou, H. P., 2007. Development and characterization. J. Biomed. Mater. Res. B 81B, 50 - 56.

[Yang 2007b] Yang, L., Ning, X. S., Chen, K. X., Zhou, H. P., 2007. Preparation and properties of hydroxyapatite filters for microbial filtration. Ceram. Int. 33, 483 - 489.

[Yao 2005] Yao, X., Tan, S., Jiang, D., 2005. Improving the properties of porous hydroxyapatite ceramics by fabricating methods. J. Mater. Sci. 40, 4939–4942.

[Yoshimura 2012] Yoshimura H. N., Gonzaga C. C., Cesar P. F., Miranda W. G. Jr., 2012, Relationship between elastic and mechanical properties, Ceram. Int. 38, 4715–4722.

[Yu 2010] Yu, F., Wang, H. Yang, J., Gao, J., 2010. Effects of organic additives on microstructure of porous Si_3N_4 ceramics. Bull. Mater. Sci., 33, 285–291.

[Zhou 2011] Zhou, L., Wang, W., Wei, S. H., Feng, Y. Y., Zhou, J. H., Liu, J. H., Shen, J., 2011. Encapsulation of hydrophobic anticancer drug. J Porous Mater. 18, 517–522.

CHAPTER 8

ROOM TEMPERATURE ELASTIC PROPERTIES OF GADOLINIA-DOPED CERIA AS A FUNCTION OF POROSITY

X. Fan, E. D. Case, Qing Yang and Jason D. Nicholas
Department of Chemical Engineering and Materials Science, Michigan State University, East Lansing, MI, 48824

Accepted by: Ceramics International

Abstract

Gadolinia doped ceria (GDC) is commonly used in chemical reactors, gas sensors, gas separation membranes, and solid oxide fuel cells (SOFCs). In the present study, the room temperature elastic properties of GDC10 ($Ce_{0.9}Gd_{0.1}O_{1.95}$) were measured as a wide function of porosity for the first time. GDC10 specimens with volume fraction porosities ranging from 0.07 to 0.60 were produced by hard die pressing and sintering GDC10 powders in air at temperatures ranging from 825 ^{o}C to 1475^{o}C. The room temperature Young's modulus, shear modulus, bulk modulus, Poisson's ratio were measured using resonant ultrasound spectroscopy. The elastic moduli decreased exponentially with increasing porosity.

1. Introduction

Dense gadolinia doped ceria (GDC) is commonly used as a membrane and/or diffusion blocking material in oxygen sensors, oxygen separators, and Solid Oxide Fuel Cells (SOFCs)

[Steele 2001, Fergus 2006, Bouwmeester 1997]. In contrast, porous GDC is commonly used as an anode catalyst [Sauvet 2001, Trovarelli 1996], an anode mixed ionic electronic conductor (MIEC) [Goodenough 2007], an oxygen storage material [Trovarelli 1996], a mechanical support [Liu 2002], and/or a composite cathode oxygen ion conductor [Murray 2001] within these same devices. In fact, nano-composite cathodes (NCC's) of porous GDC surface-decorated with nano-sized MIEC catalyst particles have received much attention in the literature due to their high electrochemical performance [Nicholas 2010, Nicholas 2012, Shah 2009, Shah 2008, Samson 2011] and electrochemical/microstructural durability [Samson 2012] at intermediate (500-700^{o}C) temperatures. Like conventional SOFCs, SOFCs utilizing NCC's [Jiang 2006, Vohs 2009] must be designed so that coefficient of thermal expansion (CTE) mismatch between the cell layers (electrolyte, cathode, current collector, etc.) do not lead to fracture [Sun 2009, Lin 2007, Montross 2002]. Unfortunately, the porous GDC elastic properties needed to model load transfer into the MIEC-GDC NCC layer are not available in the literature (to a first order approximation, the mechanical response of a NCC is determined solely by that of the porous, structurally-supporting, ionic-conducting scaffold).

In fact, the mechanical property literature for SOFC materials has been almost entirely limited to materials with relatively low porosity. For example, hardness and fracture toughness have been measured for samaria-doped ceria [Shemilt 1997] and gadolina-doped ceria [Fu 2010, Morales 2010] but only for specimens with $P < 0.08$. In terms of the fracture

strength, σ_f, of GDC10 in particular, the values available in the literature also include only low porosity specimens, with σ_f values from 200 to 300 MPa ($P < 0.08$) [Ishida 2005] and from 150 to 175 MPa ($P < 0.04$) [Reddy 2005]. While no creep data for GDC10 is available in the literature, Ikuma *et al*. studied the creep of undoped ceria with $0.01 < P < 0.08$ [Ikuma 1997]. Two recent reviews of the mechanical properties of SOFC materials by Nakajo *et al*. [Nakajo 2012a, Nakajo 2012b] included creep data on SOFC materials other than GDC, but no creep data on GDC. Routbort *et al* [Routbort 1997] studied GDC creep above 1200^{o}C, but only for samples with $P > 0.08$. In addition, Nakajo *et al* [Nakajo 2012a] noted that creep data was extremely sparse for any porous SOFC material but suggested that finite element models that deal with the deformation of struts can perhaps be "adequate for preliminary studies, because of the actual uncertainties on the creep behaviour of SOFC materials". Lastly, as will be discussed in detail in Section, 3.2, the available literature data on elastic modulus and Poisson's ratio of GDC10 includes only low porosity specimens. Therefore, the present paper focuses on the room temperature elastic moduli and Poisson's ratio of GDC10 over a wide range of porosity ($0.07 \leq P \leq 0.60$).

2. Experimental Methods

2.1 Specimen preparation

All GDC10 specimens were prepared from a single batch of 99.9% pure, 30.7 m^2/g (~27 nm primary particle size) Anan Kasei $Ce_{0.9}Gd_{0.1}O_{1.95}$ (GDC10) powder obtained from Rhodia, Inc. (Cranbury, NJ). Light scattering measurements performed by the vendor yielded

a 240 nm d_{50} (i.e. the diameter of particle agglomerates in the 50^{th} volumetric percentile) particle size. This value was consistent with previous transmission electron microscopy, x-ray diffraction, and light scattering measurements on a separate lot of 30-35 m^2/g Rhodia GDC10 powder [Nicholas 2007] which showed ~30 nm equiaxed primary particles grains agglomerated into lenticular masses 75 nm wide and 600 nm long. Vendor analysis on this previous lot of GDC10 powder showed it to have less than 10 ppm SiO_2 [Nicholas 2007]. All powder processing in the present study was done in the absence of Pyrex® glassware and other potential sources of Si contamination.

Cylindrical specimens 2.7 ± 0.3g in weight were prepared for mechanical testing by cold pressing the GDC10 nano-powders to 27.3 MPa in a three quarter inch stainless steel die. These specimens were fired in air with a 4^oC/min heating rate and held for 5 hours at various temperatures in order to produce specimens of varying porosities.

2.2 Elastic modulus measurements

The resonant ultrasound spectroscopy (RUS) technique [Migliori 1993, Migliori 2005] was used to measure the elastic moduli of as-sintered GDC10 specimens which were fired to 825, 850, 875, 900, 950, 975, 1000, 1050, 1100, 1200, 1450, or 1475^oC and therefore had sintered porosities of 60, 55, 48, 45, 38, 33, 27, 23, 15, 18, 8 and 6%, respectively. RUS is a non-destructive technique that has been used to measure the elastic moduli for a number of different oxides including hydroxyapatite [Fan 2012], alumina [Ren 2009] and lithium lanthanum zirconia oxide [Ni 2012] as well as non-oxide ceramics [Seiner 2012], thermoelectrics [Morrison 2012, Schmidt 2012], metals [Hurley 2010, Kaplan 2009] and

composites [Gorsse 2003, Vdovychenko 2006].

The RUS equipment (RUSpec, Quasar International, Albuquerque, NM) used in the present study consists of a computer controlled transceiver and a tripod arrangement of PZT (lead zirconate titanate) transducers that includes a single driver transducer and two pick-up transducers. Each specimen was placed on the tripod transducer stage where the driver transducer excited the mechanical vibrations in the specimen and the other two transducers detected the acoustic response of the specimen. The frequency of the driver transducer was swept from 10 kHz to 500 kHz in 29999 steps. The resonant vibrational frequencies of the specimen were sensed and recorded (Figure 8.1). Using the frequencies of the resonant peaks (Figure 8.1) along with the specimen mass and dimensions, the elastic moduli of the disc-shaped specimens were calculated using a commercial software package (CylModel, Quasar International, Albuquerque, NM).

2.3 Microstructural examination procedures

An Auriga Dual Column focused ion beam-scanning electron microscope (FIB-SEM) (Carl Zeiss Microscopy, LLC, Thornwood, NY) with a nominal x-y resolution of 1 nm was used to perform microstructural examinations on four fractured surfaces and one thermally etched polished surface. The thermally etched specimen was prepared by polishing down specimen#5 (P = 0.077) to a final grit of 1 μm and holding the specimen in air for 2 hours at 1350^{o}C (1350^{o}C is 100^{o}C lower than the 1450^{o}C sintering temperature used to produce this specimen). In order to suppress electrostatic charging during SEM analysis, a 15 nm thick gold coating was sputtered onto all specimens surfaces prior to the SEM examination. The

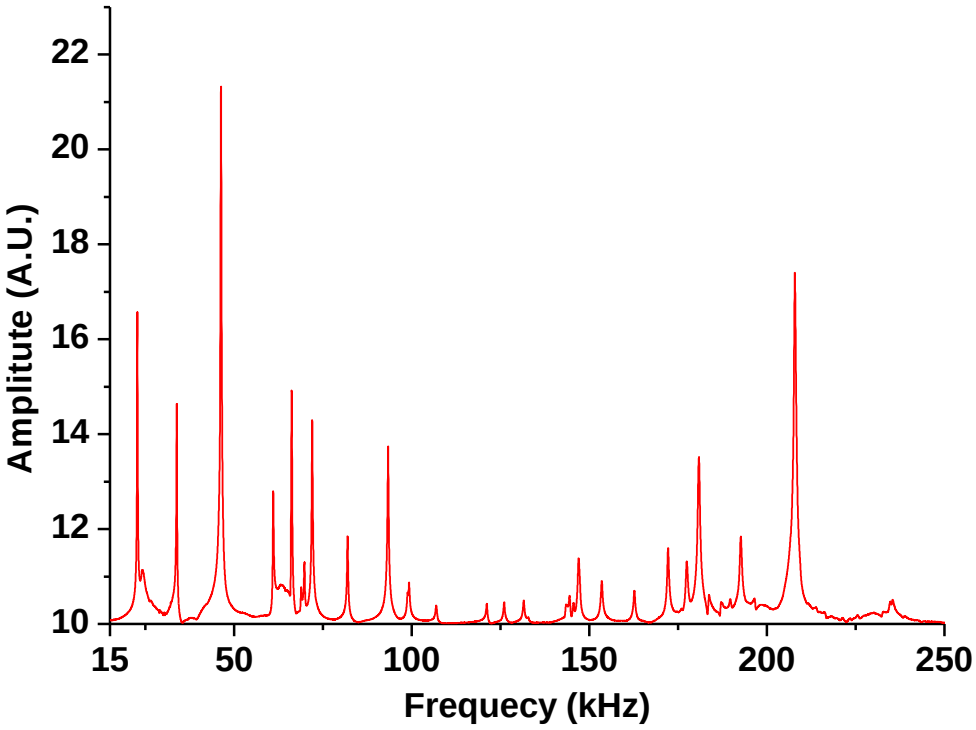

Figure 8.1. A portion of the RUS spectrum obtained for GDC10 specimen with P = 0.52 in the present study (A.U. stands for arbitrary units).

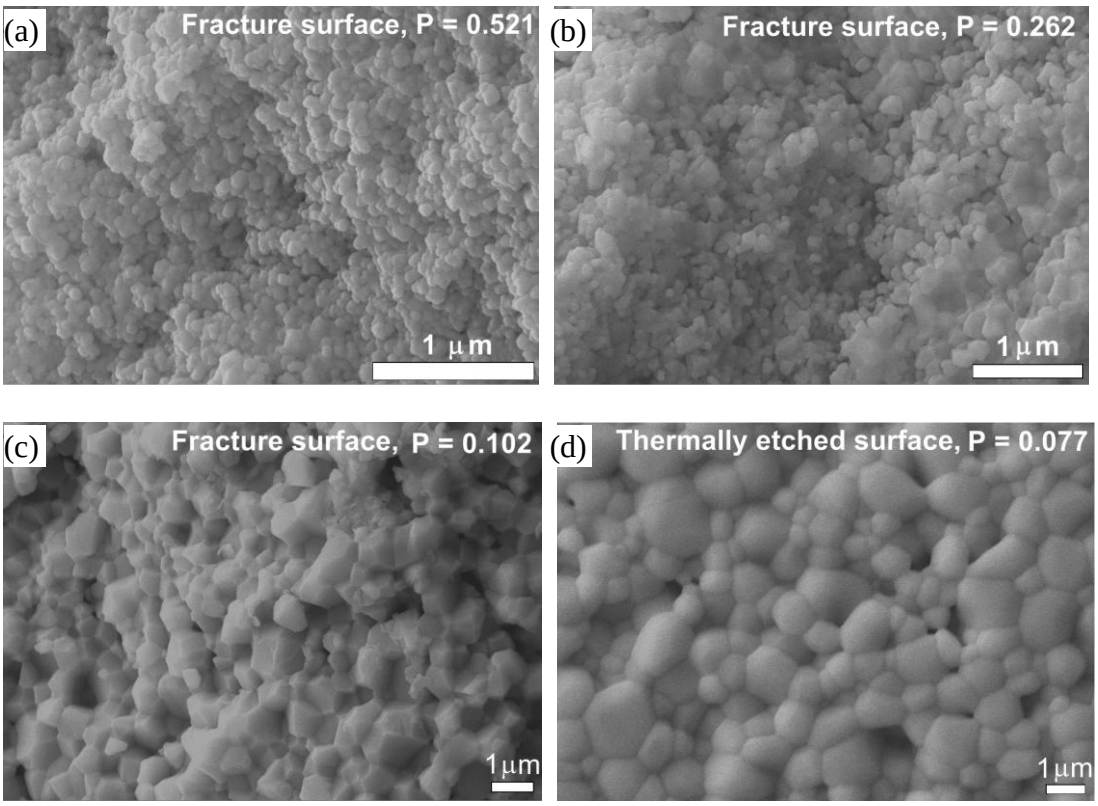

Figure 8.2. SEM micrographs of (a) fracture surface for GDC10 specimen #39 (P = 0.521); (b) fracture surface for GDC10 specimen #11 (P = 0.262); (c) fracture surface for GDC10 specimen #3 (P = 0.102) and (d) thermally etched polished surface for GDC10 specimen #5 (P = 0.077).

mean grain size was evaluated from the SEM micrographs via the linear intercept technique using a total of 150 to 200 intercepts per micrograph with a stereographic projection factor of 1.5 [Underwood 1968].

3. Results and Discussion

3.1 Microstructural analysis

For the GDC10 specimens included in the present study, the evolution of the microstructure as a function of P is depicted in Figure 8.2. For P = 0.521(specimen #39, Figure 8.2a), clusters of agglomerates appear with aspect ratios of roughly 1.1 to 1.7 and agglomerate dimensions of ~ 350 nm x ~200 nm to ~150 nm x ~ 100 nm. For P = 0.262 (specimen #11, Figure 8.2b), relatively dense islands of grains with tubular pores along the grain boundaries are separated by relatively porous regions. For P = 0.102 (specimen #3, Figure 8.2c) and P = 0.177 (specimen #14, micrograph not shown), the fracture mode is predominately intergranular. These more dense microstructures are more uniform, with pores ranging from several to hundreds of nanometers across located at triple points. For P = 0.077 (specimen #5, Figure 8.2d), this thermally etched specimen shows equiaxed grains and isolated pores of up to hundreds of nanometers across located at triple points or grain boundaries.

A grain-size density trajectory for the GDC10 specimens in the present study is typical of that observed for a variety of oxide ceramics [Fan 2012b, Berry 1986], namely there is limited grain growth from green density up to relative density, RD, of roughly 0.8 to 0.85 (corresponding to a volume fraction porosity of ~ 0.2 – 0.15). For RD > 0.8, the grain size of

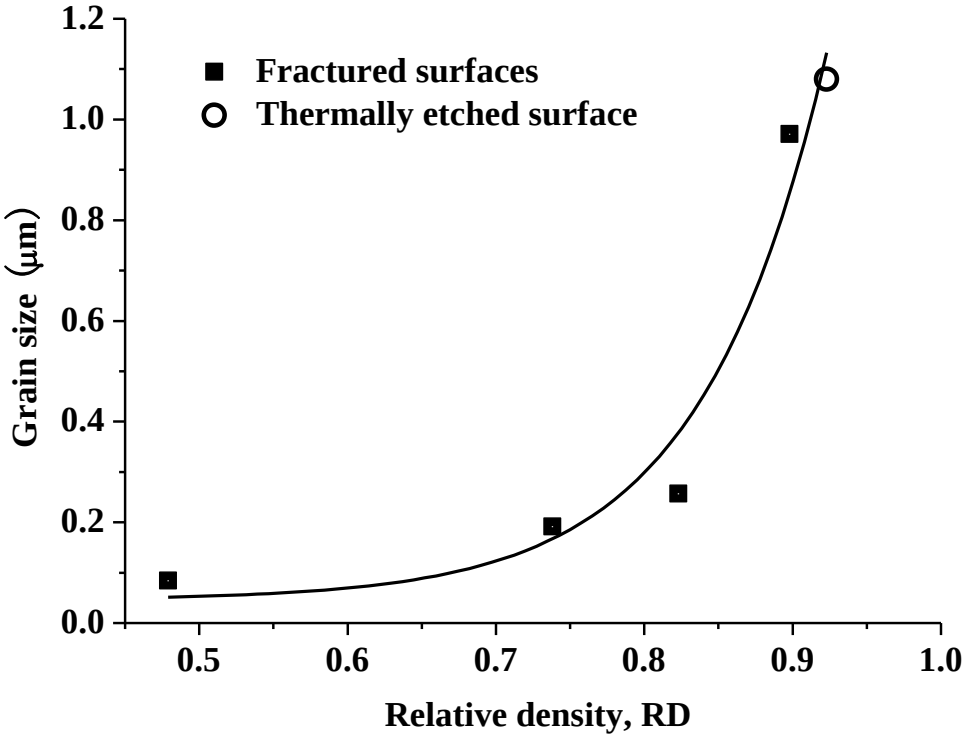

Figure 8.3. Grain size-density trajectory for the GDC10 specimens in the present study. The solid curves represents the least-squares fit of the grain size versus density data to equation (1).

the GDC10 specimens increased rapidly from about 0.3 μm to 1.1 μm for RD = 0.93 (P = 0.07, Figures 8.2d and 8.3). This implies that approximately two thirds of the 21 GDC10 specimens included the present study had grain sizes from roughly 0.1 μm and 0.3 μm (Figure 8.3).

The grain-size density trajectory (Figure 8.3) for the GDC10 specimens was least-squares fit to the following empirical relationship

$$GS = A_1 \exp(RD/B_1) + GS_0 \quad (1)$$

where A_1 and B_1 define the shape of the exponential curve. A_1 has units of grain dimension, B_1 is dimensionless and GS_0 is the initial powder particle size. The least-squares fit of the grain size versus relative density data to equation (1) gives $A_1 = 0.00002$ μm, $B_1 = 0.085$ and $GS_0 = 0.046$ μm, with a coefficient of determination, $R^2 = 0.963$. Equation (1) describes the grain size-density trajectory very well for the GDC10 specimens included in the present study as well as a grain size-density trajectory from the literature for sintered hydroxyapatite [Fan 2012b]. Taken together, these results represent the first time detailed microstructural analyses of GDC10 grain size, pore shape, fracture mode, and porosity have been reported along with elastic property measurements.

3.2 Elastic modulus as a function of porosity

Several studies in the literature report on the elastic moduli of relatively dense bulk GDC10 specimens [Selcuk 1997, Amezawa 2011, Kushi 2009, Wang 2007]. Among these studies [Selcuk 1997, Amezawa 2011, Kushi 2009, Wang 2007], only Selcuk and Atkinson [Selcuk 1997] report the Young's modulus as a function of volume fraction porosity, P. Using

Table 8.1. Comparison of specimen fabrication techniques, elastic modulus measurement techniques and porosity ranges for the present study, Selcuk and Atkinson [Selcuk 1997], Amezawa *et al.* [Amezawa 2011], Kushi *et al.* [Kushi 2009] and Wang *et al.* [Wang 2007].

References	**Specimen fabrication technique**	**Elastic modulus measurement technique**	**Relative porosity range**
The present study	Hard die pressed at 27.3 MPa, sintered from 825 ^{o}C to 1450 ^{o}C for 5 h	Resonant ultrasound spectroscopy	0.066 – 0.595
Selcuk and Atkinson [Selcuk 1997]	Circular disk cut from extruded green tape, binder burn out at 400^{o}C, densified at 1500^{o}C for 1 h	Impulse excitation technique	0.02 – 0.05
Amezawa *et al.* [Amezawa 2011]	Powder prepared by co-precipitation, hydrostatically pressed at 150 MPa, sintered at 1550^{o}C for 5 h	Sonic resonance measurement. Room temperature, one specimen under 0.01% O_2, one under 99.15% H_2 and 0.85% H_2O	0.035 and 0.033
Kushi *et al.* [Kushi 2009]	Powder prepared by co-precipitation, hydrostatically pressed at 150 MPa, sintered at 1550^{o}C	Sonic resonance measurement. Room temperature under pure Argon	0.051
Wang *et al.* [Wang 2007]	Powder mixed with 3 wt % PVB, uniaxially pressed then CIPed at 250 MPa. Held at 400^{o}C for 1 h and sintered at 1550^{o}C for 20 h	Nanoindentation, with assumed Poisson's ratio of 0.3	< 0.02

the impulse excitation technique (IET), Selcuk and Atkinson [Selcuk 1997] measured the Young's modulus, E, shear modulus, G, and Poisson's ratio, ν, for 26 disc-shaped polycrystalline GDC10 specimens over a very limited P range, namely $0.02 < P < 0.05$ (Table 8.1). (The number of specimens was not directly stated by Selcuk and Atkinson [Selcuk 1997] but here 26 data points have been extracted from Selcuk and Atkinson's plots). The Amezawa *et al.* [Amezawa 2011] and Kushi *et al.* [Kushi 2009] GDC10 elasticity measurements were performed using the sonic resonance technique in a low pO_2 atmosphere (Table 8.1). As will be discussed later in this section, heating in a low pO_2 atmosphere can induce atomic scale defects which can in turn decrease the elastic modulus [Wang 2007, Wachtel 2011]. Wang *et al.*'s E data [Wang 2007] was obtained by nano-indentation on a > 98% dense GDC10 specimen cooled from 800°C and various pO_2 levels (Table 8.1).

In the present study, the RUS technique was employed to measure the E, G, ν and the bulk modulus, B, for 21 disk-shaped, as-sintered GDC10 specimens with P values ranging from 0.07 to 0.60, where the porosity of the green (unfired) powder compacts, P_G, was 0.62. The porosity dependence of E, G and B, was assumed to have the same functional forms (equations (2) – (5)) employed by Selcuk and Atkinson [Selcuk 1997], namely

$$M = M_0 \exp(-b_M P) \quad (2)$$

$$M = M_0 (1 - b_M P) \quad (3)$$

$$M = M_0 \left[1 + \frac{b_M P}{1 - (b_M + 1)P}\right] \quad (4)$$

$$M = M_0 (1-P)^2 (1 + b_M P) \quad (5)$$

Table 8.2. Fitting parameters, E_0 and R^2, for the least-squares fit of Young's modulus data for the present study, Selcuk and Atkinson [Selcuk 1997], and the combined data set [the present study, Selcuk 1997, Amezawa 2011, Kushi 2009, Wang 2007] to equations (2) – (5).

Ref.	E_0 from equation (2) (GPa)	E_0 from equation (3) (GPa)	E_0 from equation (4) (GPa)	E_0 from equation (5) (GPa)	R^2 from equation (2)	R^2 from equation (3)	R^2 from equation (4)	R^2 from equation (5)
The present study	235.2	161.3	292.0	175.7	0.989	0.931	0.969	0.963
Selcuk and Atkinson [Selcuk 1997]	217.8 [a]	218.1 [a]	217.0 [a]	218.5 [a]	0.886 [a]	0.886 [a]	0.885 [a]	0.885 [a]
Combined data set [the present study, Selcuk 1997, Amezawa 2011, Kushi 2009, Wang 2007]	226.7	200.3	239.8	206.4	0.992	0.942	0.987	0.986

[a] E_0 and R^2 values are taken from Selcuk and Atkinson [Selcuk 1997].

where M represents the elastic moduli (E, G, or B in this case), M_0 is the elastic moduli at P = 0 and b_M is a unitless, material-dependent constant that measures the rate of decrease in M with increasing P. For P → zero, equations (2), (4) and (5) are approximated well by the linear relationship given by equation (3). Equation (2) is an empirical relationship widely used to describe the elastic modulus change as a function of porosity [Rice 1998]. Equation (4) is modified from equation (2) to treat materials with dilute distribution of spherical pores [Hasselman 1962]. Equation (5) is based on the theoretical composite sphere model, where spherical pores were treated as a second phase randomly distributed in the matrix material [Ramakrishnan 1993].

Equations (2) – (5) were used to fit the Young's modulus for GDC10 specimens in the present study. Among equations (2) – (5), the exponential relationship (equation (2)) best described the E versus P data. Since equations (3) - (5) are best suited to low porosity, P, and the exponential relationship (equation (2)) is approximated by the linear form (equation (3)), it is not surprising that equations (2) – (5) fit the Selcuk and Atkinson elasticity data (for which $0.02 < P < 0.5$) about equally well (Table 8.2). For equations (2) through (5), Table 8.2 compares the least-squares fitting parameters and R^2 for (i) the data from the present study, (ii) the Selcuk and Atkinson data [Selcuk 1997] and (iii) the combined data set (the present study, and references [Selcuk 1997, Amezawa 2011, Kushi 2009, Wang 2007]). When E data from the present study and the combined data set are least-squares fit to equations (2) to (5), then based on the R^2 values in Table 8.2, equation (2) provides the best description of the P

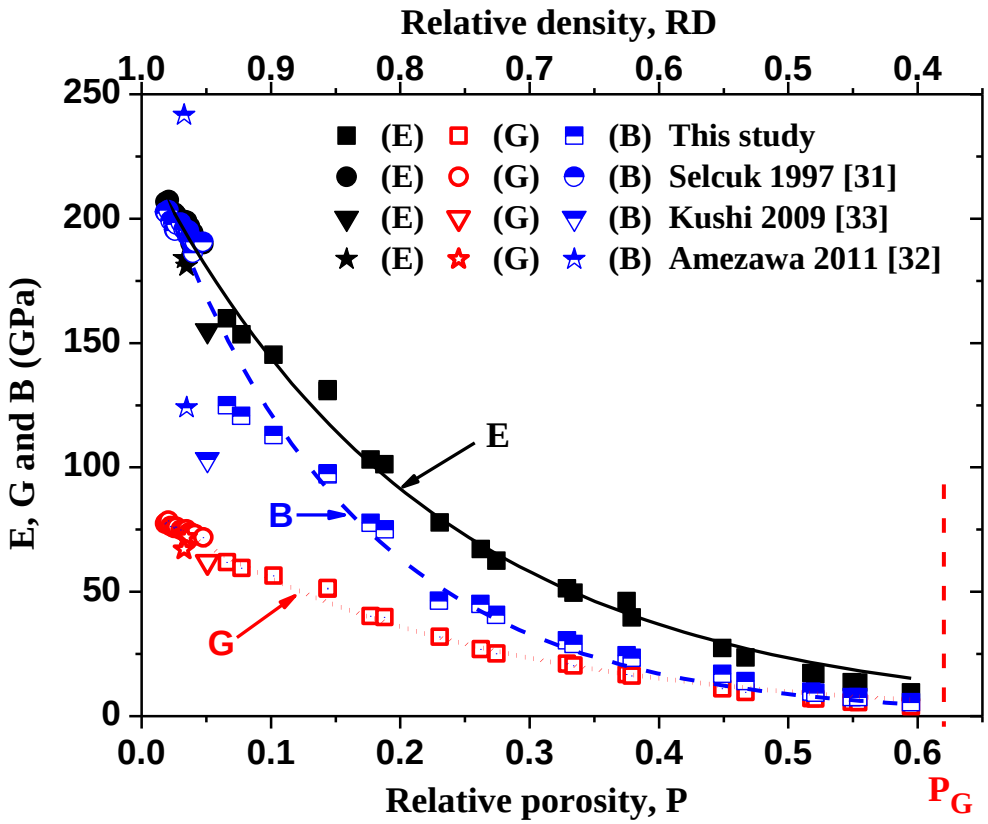

Figure 8.4. Young's modulus, shear modulus and bulk modulus versus porosity for GDC10 specimens from the combined data set (the present study, Selcuk and Atkinson [Selcuk 1997], Amezawa *et al.* [Amezawa 2011], and Kushi *et al.* [Kushi 2009]). The solid, dashed and dotted curves represent the least-squares fit to equation (2) for the E-P, B-P and G-P data, respectively.

dependence of the Young's, shear and bulk moduli (Table 8.2). Also, the values of E_0 predicted by equations (3) and (5) are lower than all of the 26 points in the Selcuk and Atkinson study (Figure 8.4), thus, the E_0 values from equations (3) and (5) are not physically reasonable. Also, the E_0 value of 292 GPa predicted by equation (4) seems unreasonably high (Figure 8.4). In contrast, the E_0 value predicted by equation (2) fits well the E versus P trend (Figure 8.4).

The E_0 and R^2 values provided by Selcuk [Selcuk 1997] were similar for each equation (equations (2) – (5)). However, the R^2 values were lower than the present study or the combined data set (the present study, and references [Selcuk 1997, Amezawa 2011, Kushi 2009, Wang 2007]) The lower R^2 values for the Selcuk and Atkinson study [Selcuk 1997] may be related to the small porosity range (0.02 to 0.05) in that study, thus a small error in the measured porosity, P, can lead to a large relative error in the (E, P) data values.

Equation (2) was also used to fit the E, G and B values for the combined data set (with data from the present study, and references [Selcuk 1997, Amezawa 2011, Kushi 2009, Wang 2007]) (Figure 8.4). Although Selcuk and Atkinson [Selcuk 1997], Amezawa *et al.* [Amezawa 2011] and Kushi *et al.* [Kushi 2009] did not report B values in their studies, for isotropic polycrystalline specimens, B can be calculated from the E and G data supplied by Selcuk and Atkinson [Selcuk 1997], Amezawa *et al.* [Amezawa 2011] and Kushi *et al.* [Kushi 2009] using equation (6), which allowed E, G, and B to be plotted for the combined data set (Figure 8.4).

Table 8.3. The number of data points, ND, parameters from least-squares fit to equation (2), E_0, b_E, G_0, b_G, B_0, b_B, and coefficient of determination, $R^2(E)$, $R^2(G)$ and $R^2(B)$. E_0, G_0 and B_0 are intercepts of the least-squares fits with the y axis, respectively.

Reference	**ND**	**E_0 (GPa)**	**b_E**	**$R^2(E)$**	**G_0 (GPa)**	**b_G**	**$R^2(G)$**	**B_0 (GPa)**	**b_B**	**$R^2(B)$**	**Relative porosity range**
The present study	21	235.2	4.7	0.989	88.4	4.5	0.987	190.7	5.4	0.986	0.07–0.60
Selcuk and Atkinson [Selcuk 1997]	26	217.8	2.9	0.886	82.2	3.0	0.871	211.1	2.5	0.788	0.02–0.05
Combined data set [the present study, Selcuk 1997, Amezawa 2011, Kushi 2009]	50	226.7	4.5	0.992	85.0	4.3	0.993	233.7	6.5	0.950	0.02–0.60

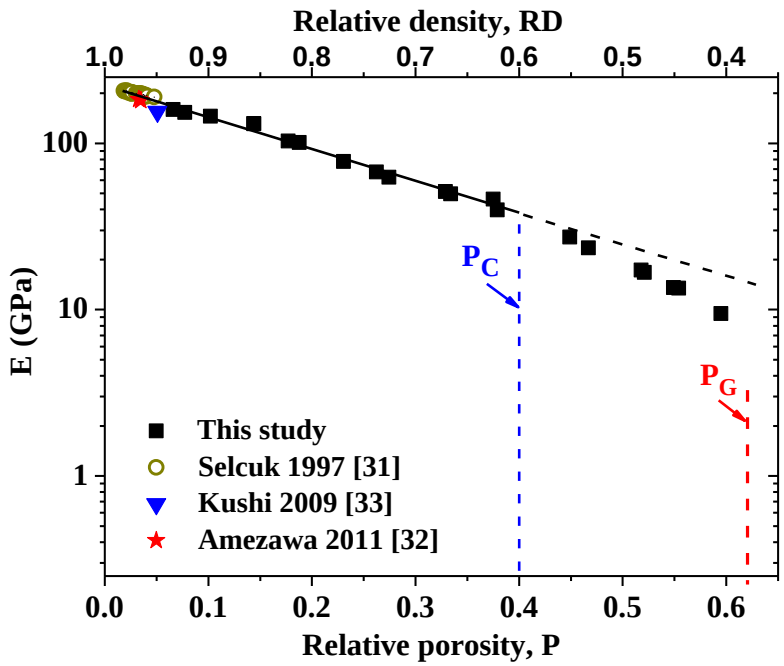

Figure 8.5. Semi-log plot of the Young's modulus versus porosity for GDC10 specimens from the combined data set (the present study, Selcuk and Atkinson [Selcuk 1997], Amezawa *et al.* [Amezawa 2011], and Kushi *et al.* [Kushi 2009]).The solid line represents the least-squares fit of E-P data with P up to P_C ~0.4 to equation (2), and the dashed line is the extrapolation of the solid line to higher porosity values.

$$B = \frac{EG}{3(3G - E)} \quad (6)$$

The least-squares fit parameters obtained for the 50 pairs of modulus-porosity data points for E, G and B from the combined dataset (the present study, and references [Selcuk 1997, Amezawa 2011, Kushi 2009])) to equation (2) are E_0 = 226.7 ± 4.4 GPa, b_E = 4.5 ± 0.2; G_0 = 85.0 ± 0.7 GPa, b_G = 4.3 ±0.1; B_0 = 233.7 ± 6.6 GPa, b_B = 6.5 ± 0.5. The coefficients of determination, R^2, were 0.992, 0.993 and 0.950 for E, G and B, respectively (Table 8.3). E_0, G_0 and B_0 (the extrapolations of the E, G and B data to P = 0) obtained from the least-squares fit are useful in that they can be compared directly to the aggregated average moduli from single crystal data [Simmons 1971] or the theoretical elastic moduli values calculated from the density functional theory [Kanchana 2006] or the statistical moment method [Van Hung 2011]**.**

Except for the Young's modulus measured by nano-indentation [Wang 2007], the moduli obtained from the three different experimental techniques: RUS (the present study), sonic resonance [Amezawa 2011, Kushi 2009] and IET [Selcuk 1997] agree extremely well, even accounting for a possible shift in modulus due to low pO_2 for GDC10 from the Amezawa *et al.* [Amezawa 2011] and Kushi *et al.* [Kushi 2009] studies. In general, a low pO_2 induces atomic scale defects (mainly oxygen vacancies) which in turn lower the observed elastic moduli in GDC10 specimens [Amezawa 2011, Kushi 2009, Hashida 2009] and 7wt-% yttria stabilized zirconia [Huang 2008].

Wang *et al.* [Wang 2007] computed the E value from their nano-indentation data using

Table 8.4. The values of b_E obtained from a least-squares fit of the Young's modulus, E, versus porosity, P, data to the equation (2) for the GDC10 specimens included in this study and several oxides from the literature. The number of data points, ND, included in the least-squares fit and the relative porosity range of the data is also specified.

Ref.	Material	b_E value	E range (GPa)	E measurement method	Processing technique	Relative porosity range	ND
The present study	$Ce_{0.9}Gd_{0.1}O_{1.95}$	4.7 ± 0.2	9.5 – 158.3	Resonant ultrasound spectroscopy	Cold pressed at 27.3 MPa, sintered 825°C to 1450°C for 5h	0.066 – 0.595	21
Ren *et al.*	$Ca_{10}(PO_4)_6(OH)_2$	3.4 ± 0.2	12 - 107	Resonant ultrasound spectroscopy	Cold pressed at 33 MPa, 1125°C to 1360°C for 1 to 6 h	0.05 – 0.51	15
	Al_2O_3	3.4 ± 0.1	105 - 340	Resonant ultrasound spectroscopy	Uniaxially cold pressed at 23 MPa, 1200°C to 1475°C for 1 to 4 h	0.06 – 0.39	9
Luo and Stevens	3Y-TZP	3.69	50 - 220	Ultrasonic velocity method	Single action die pressed followed by CIP. Sintered at 1150–1450°C	0 – 0.38	12
Oduleye *et al.*	(Bi-Pb)SrCaCuO	2.77	30 - 75	Bending test	Extruded. Sintered at 810°C - 855°C	0.2 – 0.53	17
Petrak *et al.* [	CoO	4.51	103 - 159	Resonant sphere technique	Pressed, sintered at 1400°C in Ar. Also hot pressed at 1300°C	0.09 – 0.20	8
	$Co_{0.5}Mg_{0.5}O$	4.36	137 - 206	Resonant sphere technique	Pressed, sintered at 1650°C - 1700°C in air	0.05 – 0.15	8
	$CoAl_2O_4$	5.39	124 - 234	Resonant sphere technique	Pressed, sintered at 1650°C - 1700°C in air	0.03 – 0.15	10

the Oliver –Pharr equation [Oliver 1992], such that

$$\frac{1}{E_r} = \frac{(1-\upsilon^2_{indenter})}{E_{indenter}} + \frac{(1-\upsilon^2_{sample})}{E_{sample}} \quad (7)$$

where E_r is the reduced modulus, which is functions of both the modulus of the indenter and the specimen. $\upsilon_{indenter}$ and υ_{sample} are the Poisson's ratios of the diamond indenter and the specimen, respectively. $E_{indenter}$ and E_{sample} are the elastic modulus of the diamond indenter and the specimen, respectively. Assuming $\upsilon_{indenter} = 0.07$, $E_{indenter} = 1140$ GPa for the diamond indenter and $\upsilon_{sample} = 0.3$, the E value for 98% dense GDC10 [Wang 2007] is 254.6 GPa. Several research groups have noted differences between the elastic moduli obtained via nano-indentation and the elastic moduli measured by dynamic methods such as RUS, sonic resonance and IET. For example, in a study by Radovic *et al.* [Radovic 2004] that compared E measurements by the nano-indentation and RUS techniques, the E values measured by nano-indentation were 10% higher than E measured by RUS. Similarly, for skutterudite thermoelectric materials, Schmidt *et al.* [Schmidt 2010] reported that E measured via nano-indentation was 8% higher than E measured by RUS.

While equation (2) fits the elastic modulus versus P data relatively well, it has been observed empirically that the fit at higher porosity (say, $P > 0.30$ or 0.40) is not as good as the fit at lower P values [Rice 1998]. For example, equation (2) describes well the elastic modulus versus porosity change in ceramics for the porosity range $0 < P < P_C$, where P_C is a critical porosity value [Rice 1998]. For $P > P_C$, the elastic moduli decrease faster with increasing P than predicted by equation (2). According to Rice [Rice 1998], the value of P_C

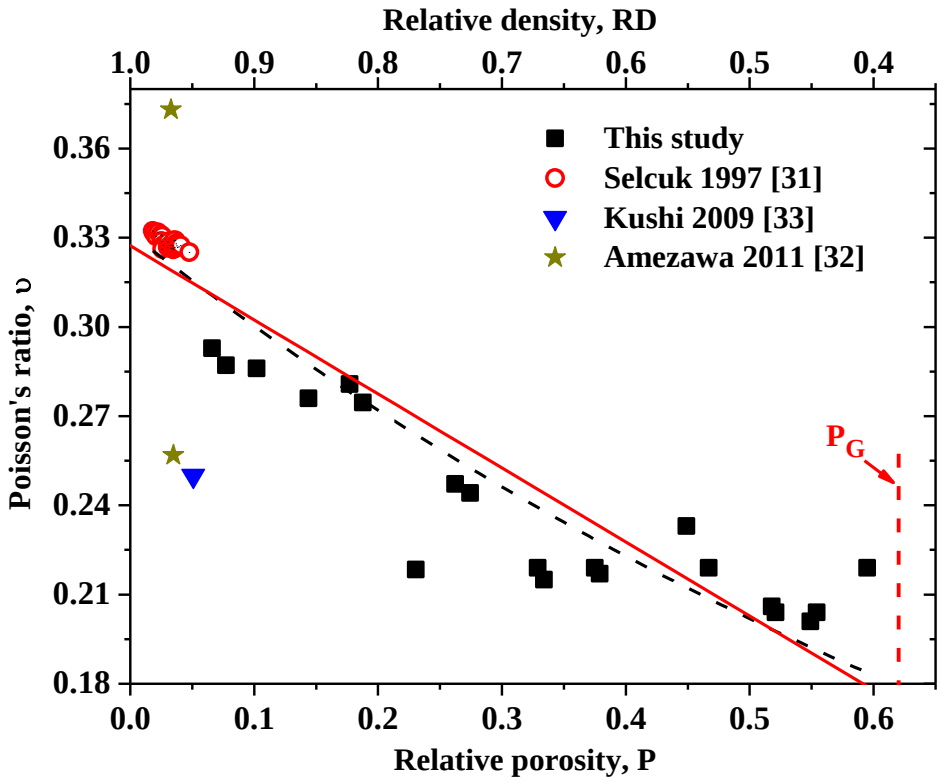

Figure 8.6. Poisson's ratio for GDC10 specimens for the combined data set (the present study, Selcuk and Atkinson [Selcuk 1997], Amezawa *et al.* [Amezawa 2011], and Kushi *et al.* [Kushi 2009]). The solid curves represents the least-squares fit of the υ-P data to equation (3) and the dashed curves represents the least-squares fit of the υ-P data to equation (2).

depends on the pore size and spatial distribution of pores, as well as the state of agglomeration of the powders, size of initial powders, powder packing parameters and fabrication techniques. However, neither Rice [Rice 1998] nor others in the literature give particular functional relationships for the dependence of P_c on such microstructural or processing parameters.

Based on empirical observations, for uniaxially hard die pressed and sintered powders, $P_c \sim 0.5$ for alumina [Hardy 1995] and $P_c \sim 0.5$ for hydroxyapatite [Ren 2009].

For the GDC10 data in the present study, a semi-log plot of E versus P for the combined data set [the present study, Selcuk 1997, Amezawa 2011, Kushi 2009] (Figure 8.5) shows that in a semi-logarithmic plot, the fit to equation (2) is excellent for $0 < P < 0.4$, however, beginning at approximately P = ~ 0.45, E begins to deviate from the behavior predicted by equation (2) such that the Young's modulus drops off faster than the least squares fit to equation (2). Thus, this behavior is consistent with that described by Rice [1998] for the drop-off in E for $P > P_c$. It is important to note that this disagreement is not the result of a difference in oxygen nonstoichiometry (and hence different lattice parameters and elastic properties [Wang 2007]) for samples with different porosities/grain sizes. Powder x-ray diffraction (XRD) analyses of specimen #5 (with a grain size of 1.1 μm) and the raw GDC powder (with a grain size of ~27 nm) yielded XRD peak positions that were identical within the 0.2^{o} resolution of the XRD; resulting in a lattice parameter of 5.418 ±0.011A for both samples. The reduced GDC mechanical property study of Wang *et al.* [Wang 2007] indicates that the small oxygen vacancy concentration differences indicated by such small lattice

Table 8.5. From the literature for the Young's modulus for partially sintered powder compacts including the GDC10 specimens in this study, three oxides and titanium metal, the values of E_{PNG}/E_0, where E_{PNG} is the Young's modulus at $P \sim P_G$ and E_0 is the Young's modulus at $P = 0$. E_{PNG}/E_0 is similar for each material, where E_{PNG}/E_0 is independent of the choice of E versus P model. The degree of densification, ϕ, is also given.

Ref.	Material	P	E (GPa)	E_{PNG}/E_0	E measurement method	Processing technique	ϕ	Green porosity
The present study	GDC10	0.595	9.5	0.04	Resonant ultrasound spectroscopy	Hard die pressed at 27.3 MPa, sintered at 825^{o}C for 5 h	0.04	0.62
Fan *et al.*	HA	0.55	8.3	0.07	Resonant ultrasound spectroscopy	Uniaxially cold pressed at 33 MPa, sintered at 550^{o}C for 2 h	0.11	0.62
Hardy *et al.*	Al_2O_3	0.45	36	0.09	Ultrasonic velocity technique	Uniaxially pressed at 45 MPa, sintered at 800^{o}C for 2h	0.01	0.46
Nanjangud *et al.*	Al_2O_3	0.415	20	0.05	Ultrasonic velocity technique	Extruded, sintered at 800^{o}C for 2 h	0.01	0.42
Deng *et al.*	YSZ	0.51	21	0.09	Pulse-echo method	Single - ended pressing at 75 MPa, sintered at 1100^{o}C for 30 min	0.09	0.56
Oh *et al.*	Ti	0.356	9	0.08	Compression test	Pressed at 70 MPa for 0.6 ks, sintered at 1573 K for 7.2 ks	0.01	0.36

parameter differences would not cause observable elastic modulus changes.

3.3 Poisson's ratio as a function of P

The porosity dependence of Poisson's ratio, ν, is more complicated than that for E, G and B. In the literature, ν is relatively insensitive to P for alumina [Phani 2008] and LAST (Lead–antimony–silver–tellurium) [Ni 2009]. However, based on empirical observations Boccaccini [Boccaccini 1994] suggested that the changes in ν as a function of P is related to ν_0, the values of Poisson's ratio at P = 0 for a given material. For literature from fifteen different ceramics, including both oxides and non-oxides, for $\nu_0 > 0.25$, ν tended to decrease as P increased and for $\nu_0 < 0.25$, ν tended to increase as P increased [Boccaccini 1994].

For the GDC10 specimens in the present study, Poisson's ratio decreased with increasing porosity (Figure 8.6). For P = 0.07, ν is approximately 0.29 and for 0.5 < P < 0.6, ν dropped to approximately 0.21. Thus, the ν versus P behavior for GDC10 specimens is broadly consistent with the trends identified by Boccaccini [Boccaccini 1994]. Also, although Amezawa [Amezawa 2011] and Kushi [Kushi 2009] did not report the ν values, the value of ν can be computed from Amezawa *et al.*'s and Kushi *et al.*'s E

and G data via [Wachtman 2009]

$$\nu = E/2G - 1 \qquad (8)$$

For the combined data (with data from the present study, and references [Amezawa 2011, Kushi 2009, Selcuk 1997]), a least-squares fit of Poisson's ratio versus P using both equation (3) (linear) and equation (2) (exponential) yielded $\nu_0 = 0.33$, with coefficients of

determination, R^2, of 0.819 and 0.844, respectively. Although the fit to equations (2) and (3) is relatively poor, this is likely due in part to the inherent scatter in the ν versus P data.

3.4 Elastic modulus-porosity for other materials in the literature

The literature also shows that porosity dependence of the Young's modulus-porosity, for example, can be described by equation (2) for a number of oxides such as Al_2O_3 [Rem 2009], $Ca_{10}(PO_4)_6(OH)_2$ [Ren 2009], 3Y-TZP [Luo 1999], (Bi-Pb)SrCaCuO [Oduleye 1998], CoO [Petrak 1975], $Co_{0.5}Mg_{0.5}O$ [Petrak 1975] and $CoAl_2O_4$ [Petrak 1975] (Table 8.4). In addition, b_E values from the literature for the seven oxides listed in Table 8.4 bracket the b_E of 4.7 for GDC10 in the present study, namely the b_E ranges from 5.39 for $CoAl_2O_4$ [Petrak 1975] to 2.77 for (Bi-Pb)SrCaCuO [Oduleye 1998].

For the GDC10 specimens in the present study, the Young's modulus dropped from ~ 160 GPa to ~ 10 GPa as P increased from 0.07 to 0.60. This dramatic drop in elastic modulus with increasing P also is consistent with the literature for a wide range of materials including the oxides ($Ca_{10}(PO_4)_6(OH)_2$ [Fan 2012], Al_2O_3 [Hardy 1995, Nanjangud 1995], YSZ [Deng 2002] and metal Ti [Oh 2003] (Table 8.5). The degree of densification, ϕ, ($\phi = 1 - P/P_G$) was included in Table 8.5 to facilitate direct comparison among studies with differing values of the green porosity, P_G (the present study, [Fan 2012a, Fan 2012b, Hardy 1995, Nanjangud 1995, Deng 2002, Oh 2003]). If we consider E_{PNG}, the Young's modulus at $P \sim P_G$ and normalize E_{PNG} by E_0, then E_{PNG}/E_0 is roughly 0.04 to 0.09 for a number of materials, including GDC10 in the present study, as well as ($Ca_{10}(PO_4)_6(OH)_2$

[Fan 2012], Al_2O_3 [Hardy 1995, Nanjangud 1995], YSZ [Deng 2002] and metal Ti [Oh 2003] (Table 8.5).

4. Summary and Conclusions

Twenty-one $Ce_{0.9}Gd_{0.1}O_{1.95}$ (GDC10) specimens were hard-die pressed and partially sintered in air at temperatures from 825°C to 1475°C for 5 hours to produce specimens with volume fraction porosities, P, from 0.07 to 0.60. Room temperature Young's, E, shear, G. and bulk, B, moduli were measured as a function of P using resonant ultrasound spectroscopy. The least-squares fit of E, G. and B to equations (2) through (5) showed that the exponential equation (equation (2)) best described the observed porosity dependence. The values of E_0, G_0 and B_0, obtained by extrapolating E, G and B to zero porosity are useful since E_0, G_0 and B_0 can be compared to (1) aggregated average moduli from single crystal data or (2) elastic moduli calculated from density functional theory.

The decrease in elastic moduli with increasing P was very dramatic, with the E, G and B values at P = 0.60 being only on the order of roughly 5 % of the E_0, G_0 and B_0 values, respectively. As summarized in Table 8.5, for specimens with very high porosity levels, similar drastic decreases in elastic moduli for specimens have been observed for a number of other oxide materials in addition to GDC10.

In solid oxide fuel cell applications, porous GDC structure will undergo thermal and mechanical stresses arising from manufacturing, external loading and differences in thermal expansion coefficients between cell layers. The knowledge of elastic moduli of GDC is essential to model the response of the SOFCs to internal or external stresses and to design

more reliable SOFCs with longer service life. Thus, it is of great importance to know the elastic moduli at different porosity levels since without using the appropriate moduli in analytical and numerical models, the predicted stresses and strains will exhibit very large errors.

5. Acknowledgements

This work was supported, in part, through a Michigan State University Faculty Startup Package.

REFERENCES

REFERENCES

[Amezawa 2011] K. Amezawa, T. Kushi, K. Sato, A. Unemoto, S.-i. Hashimoto, T. Kawada, Elastic Moduli of Ce0.9Gd0.1O2-d at High Temperatures under Controlled Atmospheres, Solid State Ionics 198 (1) (2011) 32-38.

[Berry 1986] K.A. Berry, M.P. Harmer, Effect of MgO Solute on Microstructure Development in Al2O3, J. Am Cer. Soc. 69 (2) (1986) 143-149.

[Boccaccini 1994] A.R. Boccaccini, Effective Elastic Moduli of Porous Ceramic Materials-Comment, J. Am Cer. Soc. 77 (10) (1994) 2779-2781.

[Bouwmeester 1997] H.J.M. Bouwmeester, A.J. Burggraff, Dense Ceramic Membranes for Oxygen Separation, in: P.J. Gellings, H.J.M. Bouwmeester (Eds.) The CRC Handbook of Solid State Electrochemistry, CRC Press, New York, 1997, pp. 481-554.

[Deng 2002] Z.Y. Deng, J.F. Yang, Y. Beppu, M. Ando, T. Ohji, Effect of Agglomeration on Mechanical Properties, J. Am Cer. Soc. 85 (8) (2002) 1961-1965.

[Duncan 2007] K.L. Duncan, Y.L. Wang, S.R. Bishop, F. Ebrahimi, E.D. Wachsman, The Role of Point Defects in the Physical Properties, J. Appl. Phys. 101 (4) (2007).

[Fan 2012] X. Fan, E.D. Case, F. Ren, Y. Shu, M.J. Baumann, Part II: Fracture Strength and Elastic Modulus as a Function of Porosity for Hydroxyapatite and other Brittle Materials, J. Mech. Behav. Biomed. 8 (2012) 99-110.

[Fan 2012] X. Fan, E.D. Case, F. Ren, Y. Shu, M.J. Baumann, Part I: Porosity Dependence of the Weibull Modulus for Hydroxyapatite and other Brittle Materials, J. Mech. Behav. Biomed. 8 (2012) 21-36.

[Fergus 2006] J.W. Fergus, Electrolytes for Solid Oxide Fuel Cells, J. Power Sources 162 (2006) 30-40.

[Fu 2010] Y.P. Fu, S.H. Chen, J.J. Huang, Preparation and Characterization of Ce0.8M0.2O2-d (M = Y, Gd, Sm, Nd, La) Solid Electrolyte Materials for Solid Oxide Fuel Cells, Int. J. Hydrogen Energy 35 (2) (2010) 745-752.

[Goodenough 2007] J.B. Goodenough, Y.-H. Huang, Alternative Anode Materials for Solid Oxide Fuel Cells, J. Power Sources 173 (1) (2007) 1-10.

[Gorsse 2003] S. Gorsse, D.B. Miracle, Mechanical Properties of Ti-6Al-4V/TiB Composites with Randomly Oriented and Aligned TiB Reinforcements, Acta Mater. 51 (9) (2003) 2427-2442.

[Hardy 1995] D. Hardy, D.J. Green, Mechanical Properties of Partially Sintered Alumina, J. Eur. Ceram. Soc. 15 (8) (1995) 769-775.

[Hashida 2009] T. Hashida, K. Sato, Y. Takeyama, T. Kawada, J. Mizusaki, Deformation and Fracture Characteristics of Zirconia and Ceria-Based Electrolytes for SOFCs under Reducing Atmospheres Electrochem. Soc. Trans. 25 (2) (2009) 1565-1575.

[Hasselman 1962] D.P.H. Hasselman, On the Porosity Dependence of the Elastic Moduli of Polycrystalline Refractory Materials, J. Am Cer. Soc. 45 (9) (1962) 452-453.

[Huang 2008] X. Huang, Q. Yang, Effects of Co-doping on Elastic Modulus for Zirconia Based Ternary Ceramic Materials, Mater. Sci. Tech. 24 (6) (2008) 751-755.

[Hurley 2010] D.H. Hurley, S.J. Reese, S.K. Park, Z. Utegulov, J.R. Kennedy, K.L. Telschow, In Situ Laser-Based Resonant Ultrasound Measurements of Microstructure Mediated Mechanical Property Evolution, J. Appl. Phys. 107 (6) (2010).

[Ikuma 1997] Y. Ikuma, T. Uchida, High Temperature Creep of Stoichiometric Polycrystalline CeO2 at Low Stresses, J. Mat. Sci. Lett. 16 (20) (1997) 1637-1639.

[Ishida 2005] T. Ishida, F. Iguchi, K. Sato, T. Hashida, H. Yugami, Fracture Properties of (CeO2)1-x(RO1.5)x (R=Y, Gd, and Sm; x=0.02-0.20) Ceramics, Solid State Ionics 176 (31-34) (2005) 2417-2421.

[Jiang 2006] S.P. Jiang, A Review of Wet Impregnation - An Alternative Method for the Fabrication of High Performance and Nano-structured Electrodes of Solid Oxide Fuel Cells, Mat. Sci. Eng. A-Struct. 418 (1-2) (2006) 199-210.

[Kanchana 2006] V. Kanchana, G. Vaitheeswaran, A. Svane, A. Delin, First-Principles Study of Elastic Properties, J. Phys.- Condens. Mat. 18 (42) (2006) 9615-9624.

[Kaplan 2009] G. Kaplan, T.W. Darling, K.R. McCall, Resonant Ultrasound Spectroscopy and Homogeneity in Polycrystals, Ultrasonics 49 (1) (2009) 139-142.

[Kushi 2009] T. Kushi, K. Sato, A. Unemoto, K. Amezawa, T. Kawada, Investigation of High Tempearture Elastic Modulus and Internal Friction of SOFC Electrolytes Using Resonance Method, Electrochem. Soc. Trans. 25 (2) (2009) 1673-1677.

[Lin 2007] C.K. Lin, T.T. Chen, Y.P. Chyou, L.K. Chiang, Thermal Stress Analysis of a Planar SOFC Stack, J. Power Sources 164 (1) (2007) 238-251.

[Luo 1999] J. Luo, R. Stevens, Porosity Dependence of Elastic Moduli and Hardness of 3Y-TZP Ceramics, Ceram. Int. 25 (3) (1999) 281-286.

[Madsen 2002] J. Liu, B.D. Madsen, Z. Ji, S.A. Barnett, A Fuel-Flexible Ceramic-Based Anode for Solid Oxide Fuel Cells, Electrochem. Solid-State Lett. 5 (6) (2002) A122-A124.

[Migliori 1993] A. Migliori, J.L. Sarrao, W.M. Visscher, T.M. Bell, M. Lei, Z. Fisk, R.G. Leisure, Resonant Ultrasound Spectroscopic Techniques for Measurement of the Elastic Moduli of Solids, Physica B 183 (1-2) (1993) 1-24.

[Migliori 2005] A. Migliori, J.D. Maynard, Implementation of a Modern Resonant Ultrasound Spectroscopy System for the Measurement of the Elastic Moduli of Small Solid Specimens, Rev. Sci. Instrum. 76 (12) (2005).

[Montross 2002] C.S. Montross, H. Yokokawa, M. Dokiya, Thermal Stresses in Solid Oxide Fuel Cells Due to Thermal Expansion Differences, Brit. Ceram. Trans. 101 (3) (2002) 85-93.

[Morales 2010] M. Morales, J.J. Roa, X.G. Capdevila, M. Segarra, S. Pinol, Mechanical Properties at the Nanometer Scale of GDC and YSZ used as Electrolytes for Solid Oxide Fuel Cells, Acta Mater. 58 (7) (2010) 2504-2509.

[Morrison 2012] A.Q. Morrison, E.D. Case, F. Ren, A.J. Baumann, D.C. Kleinow, J.E. Ni, T.P. Hogan, J. D'Angelo, N.A. Matchanov, T.J. Hendricks, N.K. Karri, C. Cauchy, J. Barnard, M.G. Kanatzidis, Elastic Modulus, Biaxial Fracture Strength, Electrical and Thermal Transport Properties of Thermally Fatigued Hot Pressed LAST and LASTT Thermoelectric Materials, Mater. Chem. Phys. 134 (2-3) (2012) 973-987.

[Murray 2001] E.P. Murray, S.A. Barnett, (La,Sr)MnO3--(Ce,Gd)O(2-x) Composite Cathodes for Solid Oxide Fuel Cells, Solid State Ionics 143 (2001) 265-273.

[Nakajo 2012] A. Nakajo, J. Kuebler, A. Faes, U.F. Vogt, H.J. Schindler, L.-K. Chiang, S. Modena, J. Van herle, T. Hocker, Compilation of Mechanical Properties for the Structural Analysis of Solid Oxide Fuel Cell Stacks. Constitutive Materials of Anode-Supported Cells, Ceram. Int. 38 (5) (2012) 3907-3927.

[Nakajo 2012b] A. Nakajo, F. Mueller, J. Brouwer, J. Van Herle, D. Favrat, Mechanical Reliability and Durability of SOFC Stacks. Part II: Modelling of Mechanical Failures during

Ageing and Cycling, Int. J. Hydrogen Energy 37 (11) (2012) 9269-9286.

[Nanjangud 1995] S.C. Nanjangud, R. Brezny, D.J. Green, Strength and Youngs Modulus Behavior of a Partially Sintered Porous Alumina, J. Am. Cer. Soc. 78 (1) (1995) 266-268.

[Ni 2009] J.E. Ni, F. Ren, E.D. Case, E.J. Timm, Porosity Dependence of Elastic Moduli in LAST Thermoelectric Materials, Mater. Chem. Phys. 118 (2-3) (2009) 459-466.

[Ni 2012] J.E. Ni, E.D. Case, J.S. Sakamoto, J.B. Wolfenstein, Room Temperature Elastic Moduli of Hot-Pressed LLZO Cubic Garnet, J. Mat. Sci. 47 (2012) 7978–7985.

[Nicholas 2007] J.D. Nicholas, L.C. DeJonghe, Prediction and Evaluation of Sintering Aids for Cerium Gadolinium Oxide, Solid State Ionics 178 (19-20) (2007) 1187-1194.

[Nicholas 2010] J.D. Nicholas, S.A. Barnett, Measurements and Modeling of SOFC Cathodes, J. Electrochem Soc. 157 (2010) B536-B541.

[Nicholas 2012] J.D. Nicholas, L. Wang, A.V. Call, S.A. Barnett, Use of the Simple Infiltration Microstructure Polarization Loss Estimation (SIMPLE) Model to Predict the Measured Polarization Resistance of Infiltrated Nano-Composite Solid Oxide Fuel Cell Cathodes, Phys. Chem. Chem. Phys. 14 (2012) 15379-15392.

[Oduleye 1998] O.O. Oduleye, S.J. Penn, N.M. Alford, The Mechanical Properties of (Bi-Pb)SrCaCuO, Supercond. Sci. Tech. 11 (9) (1998) 858-865.

[Oh 2003] I.H. Oh, N. Nomura, N. Masahashi, S. Hanada, Mechanical Properties of Porous Titanium Compacts Prepared by Powder Sintering, Scripta Mater. 49 (12) (2003) 1197-1202.

[Oliver 1992] W.C. Oliver, G.M. Pharr, An Improved Technique for Determining Hardness and Elastic Modulus Using Load and Displacement Sensing Indentation Experiments, J. Mat. Res. 7 (6) (1992) 1564-1583.

[Petrak 1975] D.R. Petrak, D.T. Rankin, R. Ruh, R.D. Sisson, Effect of Porosity on Elastic Moduli of CoO, CoO-MgO Solid Solutions, J. Am Cer. Soc. 58 (1-2) (1975) 78-79.

[Phani 2008] K.K. Phani, A Novel Method of Predicting Ultrasonic and Elastic Properties of Isotropic Ceramic Materials after Sintering from the Properties of Partially Sintered or Green Compacts, J. Am Cer. Soc. 91 (1) (2008) 215-222.

[Radovic 2004] M. Radovic, E. Lara-Curzio, L. Riester, Comparison of Different Experimental Techniques for Determination of Elastic Properties of Solids, Mat. Sci. Eng.

A-Struct. 368 (1-2) (2004) 56-70.

[Ramakrishnan 1993] N. Ramakrishnan, V.S. Arunachalam, Effective Elastic Moduli of Porous Ceramic Materials, J. Am Cer. Soc. 76 (11) (1993) 2745-2752.

[Reddy 2005] K.R. Reddy, K. Karan, Sinterability, Mechanical, Microstructural, and Electrical Properties of Gadolinium-doped Ceria Electrolyte for Low-Temperature Solid Oxide Fuel Cells, J. Electroceram. 15 (1) (2005) 45-56.

[Ren 2009] F. Ren, E.D. Case, A. Morrison, M. Tafesse, M.J. Baumann, Young's Modulus, Shear Modulus and Poisson's Ratio as a Function of Porosity for Alumina and Hydroxyapatite, Phil. Mag. 89 (14) (2009) 1163-1182.

[Rice 1998] R.W. Rice, Porosity of Ceramics, Marcel Dekker, New York, 1998.

[Routbort 1997] J.L. Routbort, K.C. Goretta, A.R. de Arellano-López, J. Wolfenstine, Creep of Ce0.9Gd0.1O1.95, Scripta Materialia 38 (2) (1997) 315-320.

[Samson 2011] A. Samson, M. Sogaard, R. Knibbe, N. Bonanos, High Performance Cathodes for Solid Oxide Fuel Cells Prepared by Infiltration of La0.6Sr0.4CoO3-d into Gd-Doped Ceria, J. Electrochem. Soc. 158 (6) (2011) B650-B659.

[Samson 2012] A.J. Samson, P. Hjalmarsson, M. Søgaard, J. Hjelm, N. Bonanos, Highly Durable Anode Supported Solid Oxide Fuel Cell with an Infiltrated Cathode, J. Power Sources 216 (0) (2012) 124-130.

[Sauvet 2001] A.L. Sauvet, J. Fouletier, Catalytic Properties of New Anode Materials for Solid Oxide Fuel Cells Operated under Methane at Intermediary Temperature, J. Power Sources 101 (2001) 259-266.

[Schmidt 2010] R.D. Schmidt, J.E. Ni, E.D. Case, J.S. Sakamoto, D.C. Kleinow, B.L. Wing, R.C. Stewart, E.J. Timm, Room Temperature Young's Modulus, Shear Modulus, and Poisson's Ratio of Skutterudite Materials, J. Alloys Compd. 504 (2) (2010) 303-309.

[Schmidt 2012] R.D. Schmidt, E.D. Case, J. Giles, III, J.E. Ni, T.P. Hogan, Room-Temperature Mechanical Properties and Slow Crack Growth Behavior of Mg2Si Thermoelectric Materials, J. Electron. Mater. 41 (6) (2012) 1210-1216.

[Seiner 2012] H. Seiner, P. Sedlak, L. Bodnarova, A. Kruisova, M. Landa, A. de Pablos, M. Belmonte, Sensitivity of the Resonant Ultrasound Spectroscopy to Weak Gradients of Elastic Properties, J. Acoust. Soc. Am. 131 (5) (2012) 3775-3785.

[Selcuk 1997] A. Selcuk, A. Atkinson, Elastic Properties of Ceramic Oxides Used in Solid Oxide Fuel Cells, J. Eur. Ceram. Soc. 17 (1997) 1523-1532.

[Shah 2009] M. Shah, J.D. Nicholas, S.A. Barnett, Prediction of Infiltrated Solid Oxide Fuel Cell Cathode Polarization Resistance, Electrochem. Commun. 11 (2009) 2-5.

[Shah 2009] M. Shah, S.A. Barnett, Solid Oxide Fuel Cell Cathodes by Infiltration of Gd-Doped Ceria, Solid State Ionics 179 (2008) 2059–2064.

[Shemilt 1997] J.E. Shemilt, H.M. Williams, M.J. Edirsinghe, J.R.G. Evans, B. Ralph, Fracture Toughness of Doped-Ceria Ceramics, Scripta Mater. 36 (1997) 929-934.

[Simmons 1971] G. Simmons, H. Wang, Single Crystal Elastic Constants and Calculated Aggregate Properties: A Handbook, MIT Press, Cambridge, MA, 1971.

[Steele 2001] B.C.H. Steele, A. Heinzel, Materials for Fuel-Cell Technologies, Nature 414 (2001) 345-352.

[Sun 2009] B. Sun, R.A. Rudkin, A. Atkinson, Effect of Thermal Cycling on Residual Stress and Curvature of Anode-Supported SOFCs, Fuel Cells 9 (6) (2009) 805-813.

[Trovarelli 1996] A. Trovarelli, Catalytic Properties of Ceria, Catal. Rev.-Sci. Eng. 38 (1996) 439-509.

[Underwood 1968] E.E. Underwood, A.R. Colcord, R.C. Waugh, Quantitative Relationships for Random Microstructures, Ceramic Microstructures, John Wiley & Sons, New York, 1968

[Van Hung 2011] V. Van Hung, L.T. Mai Thanh, Study of Elastic Properties of CeO2 by Statistical Moment Method, Physica B 406 (21) (2011) 4014-4018.

[Vohs 2009] J.M. Vohs, R.J. Gorte, High-Performance SOFC Cathodes Prepared by Infiltration, Adv. Mater. 21 (9) (2009) 943-956.

[Wachtel 2011] E. Wachtel, I. Lubomirsky, The Elastic Modulus of Pure and Doped Ceria, Scripta Mater. 65 (2) (2011) 112-117.

[Wachtman 2009] J.B. Wachtman, W.R. Cannon, M.J. Matthewson, Mechanical Properties of Ceramics, John Wiley & Sons, New York, 2009.

[Wang 2007] Y. Wang, K. Duncan, E.D. Wachsman, F. Ebrahimi, The Effect of Oxygen Vacancy on the Elastic Modulus of Fluorite, Solid State Ionics 178 (1-2) (2007) 53-58.

CHAPTER 9

ROOM TEMPERATURE HARDNESS OF GADOLINIA-DOPED CERIA AS A FUNCTION OF POROSITY

X. Fan, E. D. Case, Qing Yang and Jason D. Nicholas
Department of Chemical Engineering and Materials Science, Michigan State University, East Lansing, MI, 48824

Submitted to: J Materials Science.

Abstract

Porous gadolina doped ceria ($Ce_{0.9}Gd_{0.1}O_{1.95}$, GDC10) is commonly used as a functional electrode support in solid oxide fuel cells, gas sensors, and gas separators. In addition, dense GDC10 is commonly used as a solid oxide fuel cell electrolyte. Although porosity affects a wide range of electrical, thermal and mechanical properties of solids, this study focuses on (i) the Vickers indentation hardness, H, as a function of volume fraction porosity, P, ranging from 0.08 to 0.60 and (ii) the load dependence of H for Vickers indentation loads of 0.98 N to 9.8 N. For the thirteen GDC10 included in this study, the decrease in H with increasing P is approximated by the empirical relationship $H = H_0\exp(-b_H P)$, where $H_0 = 5.844$ GPa and $b_H = 6.68$. In addition, H was independent of the applied indentation load.

1. Introduction

Porous ceramics have a wide range of uses, including as filters [Yang 2007a, Yang 2007b, Khattab 2012], sensors [Dawicke 1986, Kale 2009, Mahabole 2005], catalytic supports [Twigg 2007], drug delivery platforms [Son 2011], engineered bone tissue growth scaffolds [Baumann 2007, Ren 2005], and solid oxide fuel cell (SOFC) electrodes [Nicholas 2010, Nicholas 2012, Vohs 2009, Yang 2012, Sarikaya 2012, Liang 2012]. However, the porosity that enables the various sensor and electrode functions also affects a broad range of physical properties, including electrical conductivity [Geis 2002, Shimizi 2009, Sulistyo 2010], dielectric constant [Geis 2002, Sulistyo 2010, Hoepfner 2002, Case 2006, Yang 2010], dielectric breakdown strength [Geis 2002, Ewais 2011], thermal conductivity [Hu 2010], thermal diffusivity [Luo 1997], fracture strength [Fan 2012, Nanjangud 1995, He 2008, Pramanik 2007, Yao 2005, Hu 2010], Weibull modulus [Fan 2012b, Fan 2013], fracture surface energy [Case 1981, Vandeperre 2004], Young's modulus [Ren 2009, Boccaccini 1994, Selcuk 197], shear modulus [Ni 2010, Ni 2009, Schmidt 2010], and hardness [Hoepfner 2003, Li 2012].

In particular, hardness, H, is related to a material's wear resistance [Zeng 2005, Krakhmalev 2006] and machinability [Kamboj 2003, Wang 2002], which are two essential factors for fabrication and mechanical stability in application. In addition, for dense, fine grained materials, a material's compressive strength is roughly H/3 [Rice 2002]. As is the case with many material properties, microstructure can affect hardness. Although the quantity, size, and distribution of inclusions [Canakci 2011] and/or precipitates [Liao 2011] are the most commonly discussed microstructural features affecting hardness, porosity is also a critical microstructural feature because it exponentially lowers H.

This study focuses on the hardness of gadolina doped ceria ($Ce_{0.9}Gd_{0.1}O_{1.95}$, GDC10) as a function of (i) porosity and (ii) the applied Vickers indentation load. “Dense” gadolinia doped ceria (GDC), i.e. that with a volume fraction porosity, P, typically ranging from 0 to 0.08, is commonly used as an intermediate temperature (500-700^{o}C) SOFC electrolyte [Minh 1995]. Porous GDC is commonly used as a anode catalyst [Sauvet 2001, Trovarelli 1996], mixed ionic electronic conductor (MIEC) [Goodenough 2007], oxygen storage material [Trovarelli 1996], and mechanical support [Liu 2002] in SOFC anodes, gas sensors, and gas separation membranes [Gellings2007, Chen 2011, Muthukkumaran 2008]. In addition, porous GDC is also used as an ionic conductor and electro-catalyst support in high-performance, low-temperature SOFC nano-composite cathodes [Nicholas 2012, Nicholas 2010]. The P of GDC in these electrode applications typically ranges from 0.2 to 0.55, with the lower limit set by the need for an interpenetrating gas network and the upper limit set by the mechanical strength of the component and the need to prevent ionic current focusing [Nicholas 2009].

In this study, measurements of the hardness, H, for 13 partially sintered GDC10 specimens were performed by Vickers indentation. The resulting H decreased roughly exponentially as a function of increasing porosity over the volume fraction porosity, P, range from 0.08 to 0.60 where P = 0.60 corresponds to the green state porosity for the specimens in this study. For fixed values of P, H was approximately independent of Vickers indentation load over the range from 0.98 N to 9.8 N.

2. Experimental procedure

2.1 Specimen preparation

Each of the thirteen specimens in this study was included in a previous study of the elastic modulus of GDC10 [Fan 2013]. In both this study and the Fan *et al.* study [Fan 2013], approximately 2.7 grams of 99.9% pure $Ce_{0.9}Gd_{0.1}O_{1.95}$ (GDC10) nano-powders (Rhodia, Inc. Cranbury, NJ) with ~27 nm mean particle size were uniaxially cold pressed at 27.3 MPa in a 19 mm diameter steel die. The specimens were then fired in air for 5 hours in an electrical resistance furnace at temperatures from 825^{o}C to 1450^{o}C to produce disc-shaped specimens with volume fraction porosities, P, ranging from 0.08 and 0.60. The porosity was calculated from the specimen mass (measured with an electronic balance) and specimen dimensions (measured by digital calipers). Although Fan *et al.* [Fan 2013] measured the elastic moduli for the specimens in the as-sintered state, prior to the hardness testing, each specimen was polished via an automatic polishing machine (Leco Vari/Pol VP-50, Leco Corporation, St. Joseph, MI) using a series of diamond pastes with grit sizes ranging from 90 μm to 1μm.

2.2 Microstructural examination procedure

An Auriga Dual Column focused ion beam-scanning electron microscope (FIB-SEM, Carl Zeiss Microscopy, LLC, Thornwood, NY) was used to examine the polished and fractured surfaces of selected GDC10 specimens. An accelerating voltage of 15 kV and a working distance of 5 mm were used. The average grain size was calculated using linear intercept technique with a stereographic projection factor of 1.5 [Underwood 1969]. Prior to SEM examination, a gold coating approximately 15 nm thick was sputtered on the specimen surfaces to enhance their electrical conductivity.

X-ray diffraction on the sintered specimens and the as-received GDC10 powders was performed using a Rigaku MiniFlex II diffractometer with Cu K_{α} radiation using a 2θ range of 20^{o} to 80^{o}, a scan rate of 0.5^{o} min^{-1} and a 0.05^{o} step size.

2.3 Hardness measurements

Using a Vickers indenter (Shimazdu HMV 2000, Kyoto, Japan), ten indentations were placed on each GDC10 specimen. For every specimen except for the specimens with P = 0.55 and P = 0.60, the indentations were performed using a 4.9 N load and a 10 second loading time. However, at a load of 4.9 N, the indentation impressions for the most porous specimens (P = 0.55 and P = 0.60), were greater than 350 μm across so that their images filled the field of view of the optical microscope mounted on the indenter. For specimens with P = 0.55 and P = 0.60, the Vickers indentation loads therefore were reduced to 2.94 N and 0.98 N, respectively, which reduced the dimensions of the indentation impressions sufficiently to allow them to be measured. The hardness measurements performed by the Vickers indenter were calibrated using a HV 790 steel standard calibration block (Yamamoto Scientific Tools Lab Co. LTD, Chiba, Japan). For each load used in this study (0.98 N, 2.94 N, 4.9 N and 9.8 N), the calibration factors, ζ, were determined from the average hardness value obtained from ten indentations of the calibration block using a loading time of 10 seconds. For the entire range of loads included in this study, the calibration factor, ζ ranged from 0.95 to 0.97.

The hardness values, H, for the GDC specimens were calculated from the average of 10 indentations per specimen using the following equation [Lawn 2012]

$$H = \zeta \frac{1.8544F}{(2a)^2} \quad (1)$$

where the dimensionless constant, ζ, is the calibration factor obtained from the indentation of the calibration block, F is the applied indentation load and a is half of the diagonal length of the indentation impression.

(a)

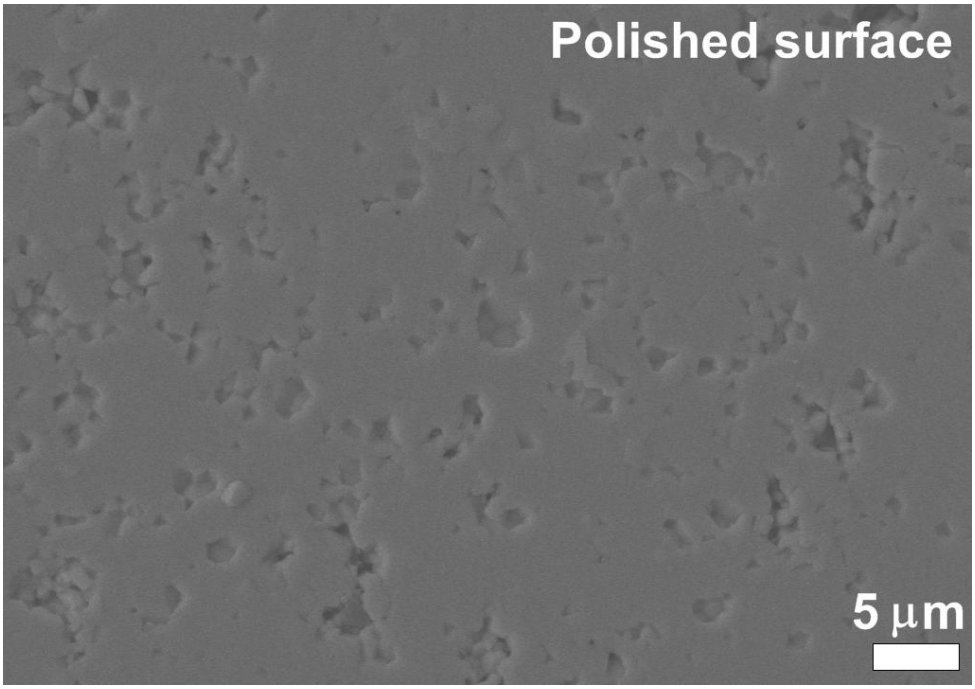

(b)

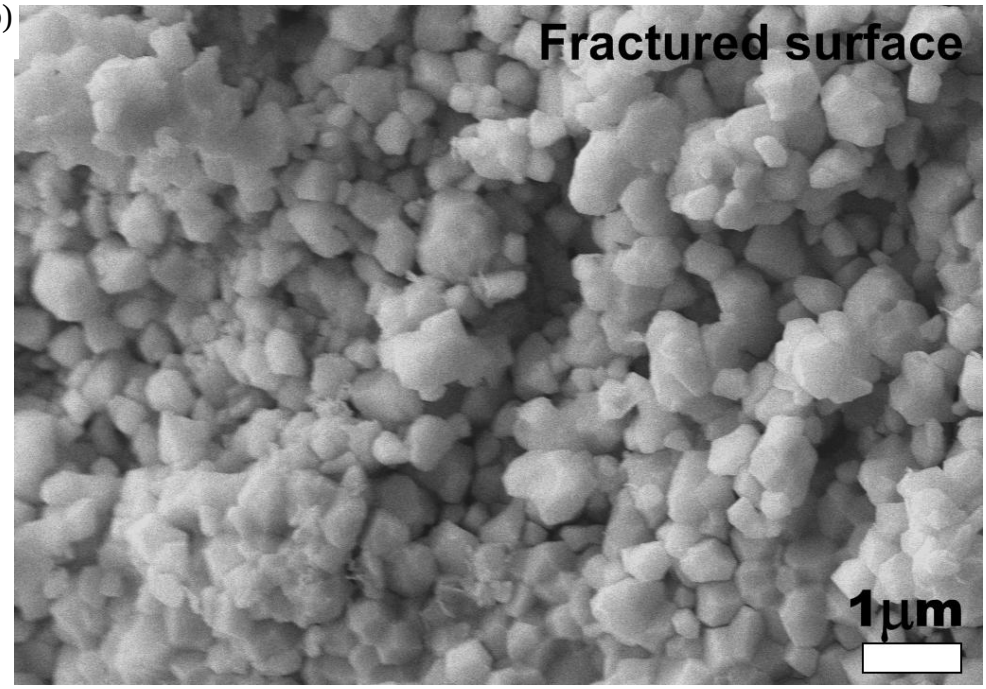

Figure 9.1. SEM micrographs of (a) polished surface for the GDC10 specimen with P = 0.08, (b) fractured surface for the GDC10 specimen with P = 0.10.

In addition, the load dependence of H was studied using three of the GDC10 specimens, namely with P = 0.08, P = 0.23 and P = 0.38. Each of the three specimens were indented at four values of load (0.98 N, 2.94 N, 4.9 N and 9.8 N), again with ten indentations per load value on each specimen.

3. Results and Discussion

3.1 Microstructural and phase analysis

SEM micrographs of the polished surface for the specimen with P = 0.08 (Figure 9.1a) showed irregularly-shaped pores ranging from roughly 1μm to 3 μm across, with occasional pore clusters. The fractured surface for the specimen with P = 0.10 (Figure 9.1b) displayed equiaxed grains and a predominately intergranular fracture mode with pores also in 1 to 3 μm range. No microcracks or macrocracks were observed on either the polished surfaces (Figure 9.1a) or on the fractured surfaces (Figure 9.1b) of the specimens.

In a recent elasticity study, Fan et al. [Fan 2013] found that the grain size-density trajectory for the GDC10 specimens included in the present study followed the trend typical of a sintered ceramic compact [Berry 1986, Barsoum 1997]. In particular, as P decreased from about 0.6 to 0.2 during sintering, there was a relatively small increase in grain size from about 0.1 μm to 0.3 μm. As further densification occurred, the grain growth accelerated, reaching a maximum grain size in this study of 1.1 μm for the minimum porosity of P = 0.08.

All peaks in the XRD analysis (Figure 9.2) corresponded to GDC10, which is consistent with the 99.9% purity of the starting powders (Section 2.1).

3.2 Hardness as a function of porosity

The H versus P behavior for brittle materials is often described by the empirical exponential relationship (equation 2) [Rice 1998]

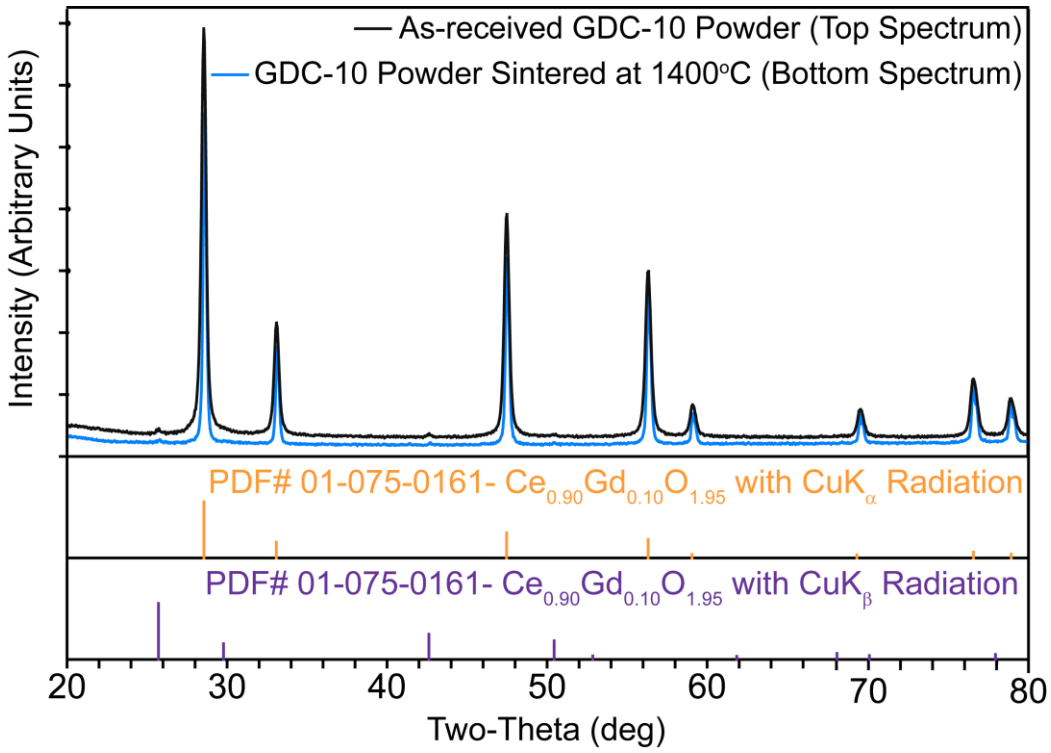

Figure 9.2. XRD patterns of the as-received GDC10 powder and GDC10 specimen sintered at 1400°C (P = 0.10).

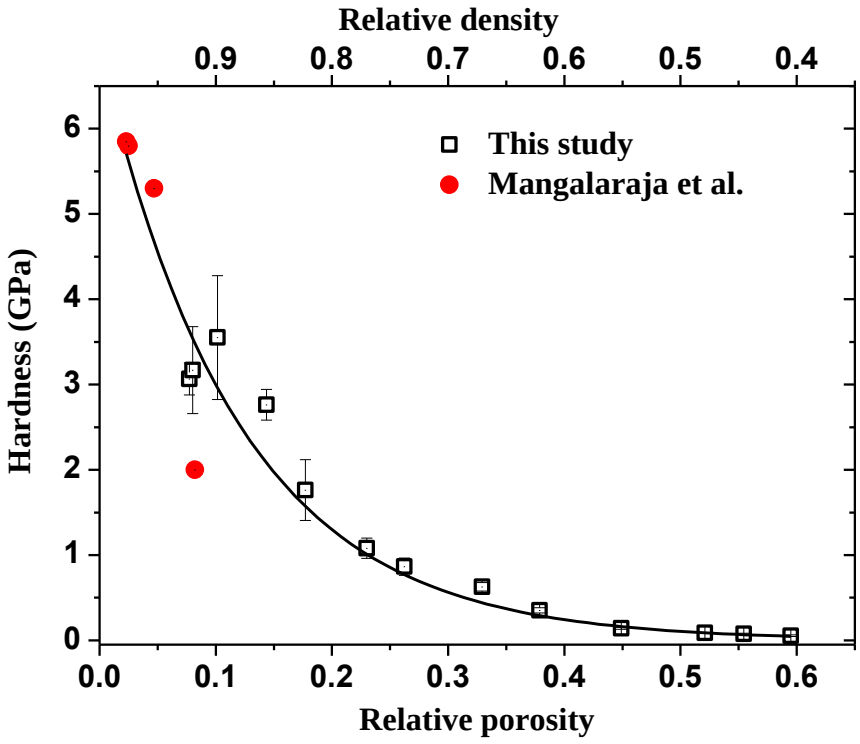

Figure 9.3. Hardness versus porosity for a combined GDC10 data set (this study and Mangalaraja *et al*. [Mangalaraja 2009]), where the curve represents a least-squares fit to equation 2. Note that in this study the indentation load was 4.9 N for all the specimens except two with the highest porosities and in Mangalaraja's study [Mangalaraja 2009] the indentation load was 5 N. For P > 0.2, the error bars on the H data for this study are smaller than the symbol size.

$$H = H_0 \exp(-b_H P) \quad (2)$$

where H_0 is the hardness value at P = 0, b_H is a dimensionless, material-dependent constant that is related to the rate of H change as a function of P. A least-squares fit of the H versus P for the thirteen GDC10 specimens in this study (Figure 9.3) to the equation (2) yielded H_0 = 5.84 ± 0.57 GPa, b_H = 6.68 ± 0.77 with a coefficient of determination, R^2, of 0.955.

In this study, the maximum P value is P = 0.60, which is nearly equal to the unfired (green) porosity of P_G = 0.62 for the GDC10 specimens. However, few studies in the literature include values of H for brittle materials for P greater than 0.35. An exception is a Vickers indentation study of the porosity dependence of H for Ti doped Al_2O_3- Cr_2O_3 solid solutions by Cho [69] with 0.05 < P < 0.45, however in Cho's study both the composition (Ti addition and the Al_2O_3/Cr_2O_3 ratio) and P varied simultaneously. Also, Ramadass [Ramadass 1983] studied the Vickers hardness of Y_2O_3 partially stabilized zirconia for 0 < P < 0.45, but once again both P and the specimen chemistry changed in tandem (with the Y_2O_3 additions ranging from 0 to 7.5 mol%). Unfortunately, neither the Cho [Cho 1990] nor the Ramadass [Ramadass 1983] studies included a sufficient number of specimens to clearly separate the compositional effects from the P dependence of H. Thus, the current study is one of very few in the literature to study the porosity dependence of H over a large range of P (0.08 < P < 0.60).

In addition, studies of the porosity dependence of H for GDC10 are also very limited even for a restricted P range. For example, Mangalaraja [Mangalaraja 2009] fabricated GDC10 specimens using a nitrate-fuel combustion method with four different organic fuels:

urea, citric acid, glycine and poly ethylene glycol. However, the Mangalaraja study included a very limited porosity range, with P ranging only from about 0.02 to 0.08 [Mangalaraja 2009]. Both the indentation load (4.9 N [Mangalaraja 2009] and 5.0 N [this study]) and the grain size range (0.4 to 1.0 μm [Mangalaraja 2009] and 0.1 to 1.0 μm [this study]) were comparable between the two studies.

This similarity between the indentation load and grain size of the two H studies of GDC10 [Mangalaraja 2009 and this study] motivated the least-squares fit to equation (2) of the 13 H values from this study along with four hardness values from Mangalaraja's study [Mangalaraja 2009] which yielded the fitting parameters $H_0 = 6.92 \pm 0.50$ GPa, $b_H = 8.37 \pm 1.01$ and $R^2 = 0.940$.

Despite the relatively high value of the coefficient of determination for the H versus P data included in this study (Figure 9.3), Rice [Rice 1998] has shown that for a critical porosity P_C (which is typically on the order of 0.3 to 0.4), H versus P data often deviates from the exponential relationship for $P > P_c$. A semi-log plot of the hardness data of thirteen GDC10 specimens in this study (Figure 9.4) shows that H decreases more rapidly than predicted in equation 2 for $P > 0.4$. A similar behavior was observed for the Young's modulus versus P behavior for GDC10 [Fan 2013] where P_c was approximately 0.45 and as reviewed by Fan et al [Fan 2013] this behavior is commonly observed in for the Young's modulus, E, versus P data for highly porous ceramics. Furthermore, the departure from the empirical exponential relationship (equation 2) for H as a function of P is also commonly observed for highly porous ceramics [Rice 2000]. It should be emphasized, however, that equation 2 (as well as the exponential E versus P relationship) is an empirical equation and

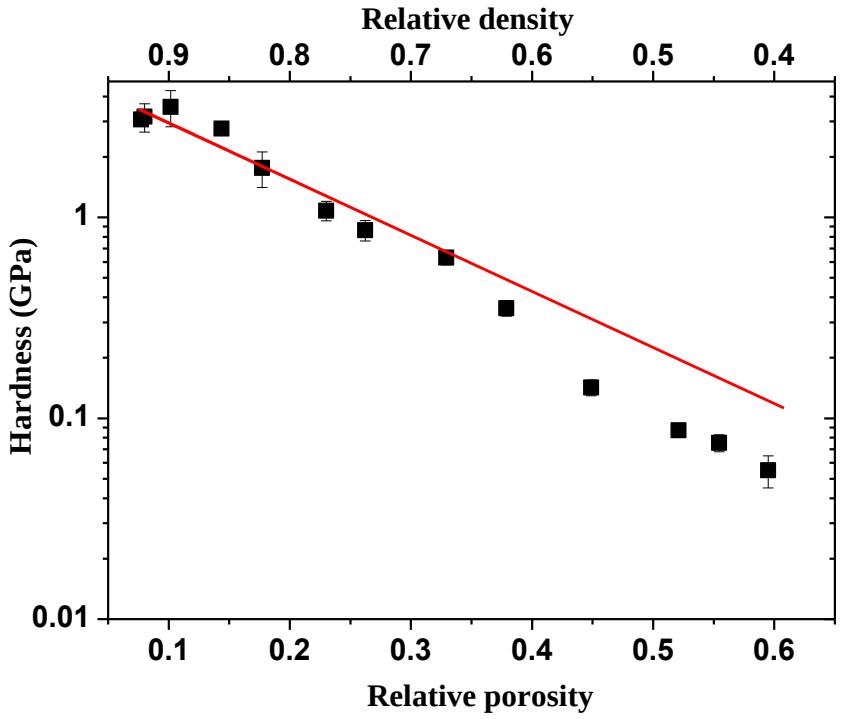

Figure 9.4. Semi-logarithmic plot of the hardness versus porosity for GDC10 specimens in this study. The solid line represents a least-squares fit of data to equation (2) for the P range of $0.08 < P < 0.4$.

this H versus P behavior may only indicate that the exponential relationship is inadequate to describe the nature of H for high values of P.

In this study, the diagonal length of the Vickers indentation impression, 2a, ranged from 50.3 μm for the specimen with P = 0.10 to 341.5 μm for the specimen with P = 0.52. The typical pore sizes obtained from the SEM micrographs were from 0.3 μm to 3 μm so that the ratio of indentation impression size to the pore size falls between roughly 15 and 100. In addition, for the GDC10 specimens in this study, 2a was >> the mean grain sizes, which ranged from about 0.1 to 1.0 μm. Thus, 2a is large compared to the specimens' microstructural features (pores and grains) so that the H values reported in this study should represent bulk values.

The hardness versus porosity relationship for GDC10 from this study and other oxides from the literature including $Ca_{10}(PO_4)_6(OH)_2$ [Hoepfner 2003], 3Y-TZP [Luo 1999], $Pb_{0.74}Ca_{0.26}[(Co_{0.5}W_{0.5})_{0.05}Ti_{0.95}]O_3$ + 1% MnO [Ricote 1994] is described relatively well by the exponential relationship (equation 2, Table 9.1). The values of b_H for GDC10 from this study and the combined data set [this study, Mangalaraja 2009] are 6.68 and 8.37, respectively, which are higher than the b_H values for the literature data for the three oxides, namely b_H = 6.03 for $Ca_{10}(PO_4)_6(OH)_2$ [Hoepfner 2003], b_H = 5.04 for 3Y-TZP [Luo 1999], and b_H = 3.08 for $Pb_{0.74}Ca_{0.26}[(Co_{0.5}W_{0.5})_{0.05}Ti_{0.95}]O_3$ + 1% MnO [Ricote 1994] (Table 9.1).

3.3 Hardness as a function of load

For a variety of materials, the value of H has been observed to be a function of the applied indentation load [Nix 1998, Sangwal 2000, Bull 1989, Pharr 2010]. When H is a

Table 9.1. For the GDC10 specimens included in this study and porosity-hardness data for several oxides from the literature, the values of b_H obtained from a least-squares fit of the hardness, H, versus porosity, P, data to equation 2 ($H = H_0 \exp(-b_H P)$). The number of data points, ND, included in the least-squares fit and the relative porosity range of the data is also specified.

Ref.	Material	b_H	H range (GPa)	H meas. method	Processing technique	Relative porosity range	ND
This study	$Ce_{0.9}Gd_{0.1}O_{1.95}$ (GDC10)	6.68 ± 0.77	0.05 to 3.55	Vickers, load = 4.9 N	Hard die pressed at 27.3 MPa, sintered from 825°C to 1450°C for 5 h	0.08 – 0.60	13
Hoepfner and Case 2003	$Ca_{10}(PO_4)_6(OH)_2$	6.03	0.91 to 5.54	Vickers, load = 2.94, 4.9 and 9.81 N	Uniaxially cold pressed at 6.55 MPa, sintered from 1050 °C to 1400 °C	0.02 – 0.31	42
Luo and Stevens 1999	3Y-TZP	5.04	~ 1.5 to ~ 11.8	Vickers	Single action die pressing followed by CIP. Sintered at 1150 – 1450°C	0 – 0.38	13
Ricote *et al.* 1994 [a]	$Pb_{0.74}Ca_{0.26}[(Co_{0.5}W_{0.5})_{0.05}Ti_{0.95}]O_3$ + 1% MnO	3.08	~ 2.0 to ~ 3.3	Vickers	Sintered. Sintering conditions not specified.	0.04 – 0.18	6

[a] Data taken from the paper by Datathief and replotted by the authors

function of load, the load dependence is typically discussed in terms of either an indentation size effect (ISE) [Nix 1998] or a reverse indentation size effect (RISE) [Sangwal 2000]. For ISE, the measured H decreases with increasing applied load, which has been observed for both ceramics [Bull 1989, Sangwal 2009] and metals [Pharr 2010]. ISE has been attributed to elastic recovery and working hardening during indentation or surface dislocation pinning in metals [Gong 1999]. For RISE [Sangwal 2000], the H values decrease with decreasing load, where stress relaxation during unloading [Sangwal 2000] has been proposed as a mechanism for RISE [Sangwal 2000].

In this study, three GDC10 specimens with P = 0.08, P = 0.23 and P = 0.38 were indented under a series of loads (0.98 N, 2.94 N, 4.9 N and 9.8 N), with 10 indentations performed at each load for each specimen. In this study, the hardness values for each specimen were relatively constant over the entire load range (Figure 9.5). The average hardness values (indicated by the horizontal lines in Figure 9.5) were 3.38 ± 0.47 GPa, 1.24 ± 0.15 GPa and 0.38 ± 0.04 GPa for specimens with porosities P = 0.08, P = 0.23 and P = 0.38, respectively. Thus, for the GDC10 specimens included in this study, no significant ISE or RISE is observed for the range of indentation loads included in this study.

A recent study $Ce_{1-X}Gd_XO_2$ (for x = 0 to 2) by Korobko *et al.* [Korobko 2012] reported an H value of about 6.8 GPa under a "slow" loading rate of 3 mNs^{-1} and 8.1 GPa with a "fast" loading rate of 15 mNs^{-1}. However the differences in the specimens and experimental procedures between the Korobko *et al.* [Korobko 2012] study and the current study makes comparison of the H data very difficult. For example, Korobko *et al.* [Korobko 2012] used a nanoindenter with a Berkovich indenter with a triangular-based indenter tip at a fixed load of

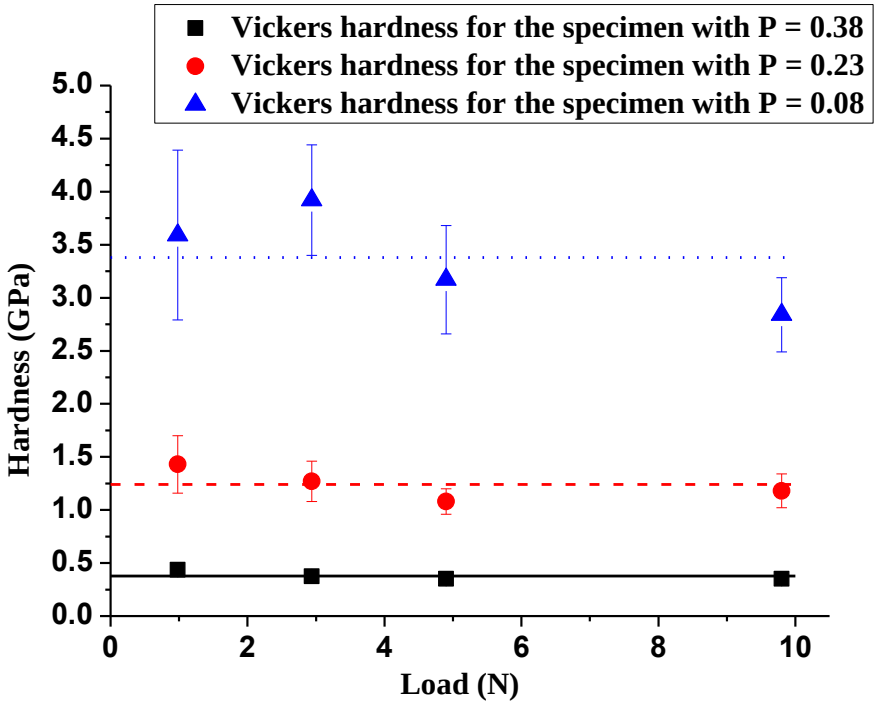

Figure 9.5. The hardness versus applied indentation load for three selected GDC10 specimens in this study. The horizontal lines represent the average of the H values as a function of load, namely the solid line for P = 0.38, the dashed line for P= 0.23 and the dotted line for P = 0.08.

0.15 N while this study employed a Vickers indenter with a square-based pyramidal indenter tip at loads of 0.98 to 9.8 N. Also, while the instrumented nanoindenter used by Korobko *et al.* [Korobko 2012] is capable of varying the load rate, the typical Vickers indenter such as the instrument used in this study does not have that capability. In addition, the Korobko *et al.* [Korobko 2012] stated that for the specimens in their study "grain size exceeded 1.5 μm for all samples" and that the "density of all pellets exceeded 95%". This uncertainity in the microstructural parameters makes comparison difficult, especially given the steep slope of the H versus P curve for P values less than roughly 0.1 (Figure 9.3 and equation 2). Also, it is widely observed for oxides and other brittle materials [Kolemen 2006, Ozturk 2013, Daguano 2012, Machaka 2011] that an ISE becomes significant at loads less than roughly 1 to 2 N, such that as the indentation load approaches the 0.15 N employed in the Korobko *et al.* [Korobko 2012] nanoindentation study, H typically increases dramatically. Thus, the differences in microstructure, the experimental apparatus, the experimental technique along with the possible ISE at the 0.15 N loads make it difficult to make a definitive comparison between the H values found in this study those reported by Korobko *et al.* [Korobko 2012].

Mangalaraja [Mangalaraja 2009] also investigated the H versus Vickers indentation load behavior for GDC10. For GDC10 specimens processed with citric acid and glycine (P ~ 0.02 in both cases), the measured H increased approximately linearly from about 5 GPa to approximately 9 GPa as the applied load increased from 1 N to 20 N [Mangalaraja 2009**].** However, except for an increase from about 4.6 GPa at 1 N load to roughly 5.3 GPa at 5 N load for GDC10 processed with urea, H was relatively independent of load over the range of 1 to 20 N for specimens processed with urea and poly ethylene glycol fuels. The difference in the load dependent behavior of H among the processing routes used by Mangalaraja

[Mangalaraja 2009] may be related at least in part to processing-related differences in specimen chemistry since the authors state that "the fuels released high carbonaceous residues during combustion". Thus, the amount of residual carbon in the specimens may differ. Also, the exothermic peak heights are roughly 50% higher for GDC10 specimens processed with citric acid and glycine than for GDC10 specimens processed with urea and poly ethylene glycol (Figure 9.3 in [Mangalaraja 2009]). Thus, although the authors [Mangalaraja 2009] did not discuss it, the differences in the exothermic reactions coincides with the differences in hardness-load dependence behavior, with marked RISE behavior for GDC10 specimens processed with citric acid and glycine and little or no RISE behavior for GDC10 specimens processed with urea and polyethylene glycol.

Studies that include both the load dependence and porosity dependence of H are sparse in the literature. One study by Milman [Milman 1999] measured the hardness versus load for silicon carbide specimens with P of 0, 0.05, 0.16 and 0.20 at loads of 1 N, 10 N and 50 N. For the four porosity groups, a load-dependent H was observed with H decreasing with increasing load more sharply at higher P than lower P. The hardness values at 50 N load decreased 18%, 20%, 60% and 70% compared to the H values obtained at 1 N load for specimens with P = 0, 0.05, 0.16 and 0.20, respectively. In this study, no significant load dependence of H was observed for GDC10 specimens with P = 0.08, 0.23 and 0.38, indicating that for the porosity range from 0.08 to 0.38, H for GDC10 is relatively constant over the load range.

3.4 Hardness versus grain size behavior

In this study, we did not measure H as a function of G, but we will discuss here the difficulties with H versus G behavior of ceramics in general and the grain size independence

of H observed for GDC in particular. A Hall-Petch type relationship between H and grain size, G, that is available in the literature is [Rice 2000]

$$H = H_0 + kG^{-1/2} \qquad (3)$$

where H_0 is considered as the H value in the single crystal limit and k is called the Petch parameter. While Hall-Petch type relationships are commonly observed for the strength of both metals and ceramics [Lawn 2012], for hardness Hall-Petch behavior is very common in metals [Lawn 2012] but the nature of the H versus GS behavior is uncertain for many ceramics [Rice 2000, Armstrong 2011]. In an extensive review of the G dependence of H in ceramics, Rice [Rice 2000] notes that Hall-Petch behavior is common for relatively soft ceramics such as alkaline halides, but there is a great deal of scatter in the H versus GS data scatter for most hard ceramics [Rice 2000, Armstrong 2011]. Furthermore, Rice notes [Rice 2000] that H_0 obtained from H versus G data is not always a good predictor for the H of single crystals. In addition, for some ceramics, such as ZrO_2 and $AlMg_2O_4$, H is independent of grain size [Rice 2000]. A further complication for using equation 3 is that minima in H versus G data are often observed for intermediate grain sizes (G on the order of several microns) and thus the Petch parameter k frequently takes on both negative and positive values (with unequal magnitudes) for a given set of data [Rice 2000, Armstrong 2011] whether it suggested that the observed minima may be related to surface or subsurface cracking near the indentation site. Nevertheless, there is not an alternative to equation 3 in the literature and thus in general the H versus G behavior for brittle materials is not clear from the standpoint of the available data or the available functional relationship (equation 3).

For gadolina-doped ceria materials in particular, Mangalaraja *et al.* [Mangalaraja 2009] noted that for each of the GDC10 specimens included in their study (which represents mean grain sizes from 0.4 to 1.0 μm and P ~ 0.02) "all the samples showed grain size independent hardness". For GDC20 ($Ce_{0.8}Gd_{0.2}O_{2-\delta}$) with a mean grain sizes of 0.5 μm to 9.5 μm and P from about 0.02 to 0.01, Zhang *et al.* [Zhang 2004] observed that H "increased slightly" as G increased from the smallest to largest grain size. Thus from the literature, and the dramatic decrease in H with increasing P observed in the present study (Figure 9.3), it appears that H for GDC is relatively independent of grain size for grains sizes between about 0.4 and 9.5 μm. However, a study beyond the scope of the present work aimed at understanding the full relationship between hardness, porosity, and grain size is needed before this can be concluded for certain.

4. Summary and Conclusions

This paper reports room temperature GDC10 hardness data over a wide range of porosities for the first time. Specifically, a total of 13 GDC10 specimens with volume fraction porosities, P, from 0.08 to 0.60 were cold pressed and partially sintered. Vickers hardness values were measured (i) as a function of P for a fixed load of 4.9 N (Figure 9.3) and (ii) as a function of indentation load from 0.98 to 9.8 N for fixed P values of 0.08, 0.23 and 0.38 (Figure 9.5).

The least-squares fit of the hardness data to the exponential H versus P relation (equation 2) described the hardness versus porosity data relatively well, yielding $H_0 = 5.84$ GPa, $b_H = 6.68$ and a R^2 of 0.955. However, for $P_c > 0.4$ in this case, the hardness decreased faster with increasing P than is predicted by the exponential relation given in equation 2

(Figure 9.4). In contrast to the Mangalaraja study [Mangalaraja 2009], over the range of loads and porosities included this study, no significant load dependence on the hardness was observed for the GDC10 specimens (Figure 9.5).

5. Acknowledgements

Authors Qing Yang and Jason D. Nicholas acknowledge support of Michigan State University Faculty Startup Package.

REFERENCES

REFERENCES

[Armstrong 2011] Armstrong RW (2011) Materials 4:1287

[Barsoum 1997] Barsoum MW (1997) Fundamentals of Ceramics, McGraw-Hill, New York

[Baumann 2007] Baumann MJ, Case ED, Smith IO (2007) In: Developments in Porous, Biological and Geopolymer Ceramics, Ceramic Engineering and Science Proceedings, Wiley InterScience, New York, pp 197-207

[Berry 1986] Berry KA, Harmer MP (1986) J Am Ceram Soc 69:143

[Boccaccini 1994] Boccaccini AR (1994) J Am Ceram Soc 77:2779

[Bull 1989] Bull SJ, Page TF, Yoffe EH (1989) Phil Mag Lett 59:281

[Canakci 2011] Canakci A (2011) J Mater Sci 46:2805

[Case 1981] Case ED, Smyth JR (1981) J Mater Sci 16:3215

[Case 2006] Case ED (2006) In: Lee S (ed) Encyclopedia of Chemical Processing (ECHP), Marcel Dekker Inc, New York, pp 1687-1697

[Chen 2011] Chen CY, Liu CL (2011) Ceram Int 37:2353

[Cho 1990] Cho SA, Arenas FJ, Ochoa J (1990) Ceram Int 16:301

[Daguano 2012] Daguano JKMF, Suzuki PA, Strecker K, Fernandes MHFV, Santos C (2012) Mater Sci Eng A533: 26

[Dawicke 1986] Dawicke JW, Blumenthal RN (1986) J Electrochem Soc 133:904

[Ewais 2011] Ewais EMM, Barg S, Grathwohl G, Garamoon AA, Morgan NN (2011) Int J Appl Ceram Tec 8:85

[Fan 2012] Fan X, Case ED, Ren F, Shu Y, Baumann MJ (2012) J Mech Behav Biomed Mater.8:99

[Fan 2012] Fan X, Case ED, Ren F, Shu Y, Baumann MJ (2012) J Mech Behav Biomed 8:21

[Fan 2013] Fan X, Case ED, Gheorghita I, Baumann MJ (2013) J Mech Behav Biomed. Mater., accepted, DOI, 10.1016/j.jmbbm.2013.01.031

[Fan 2013] Fan X., Case ED, Yang Q, Nicholas, JD (2013) Ceram. Int., accepted, DOI, 10.1016/j.ceramint.2013.02.022.

[Geis 2002] Geis S, Fricke J, Lobmann P (2002) J Eur Ceram Soc 22:1155

[Gellings 2007] Gellings PJ, Bouwmeester HJ (eds) (2007) The CRC Handbook of Solids State Electrochemistry, CRC Press, Boca Raton, FL

[Gong 1999] Gong J, Wu J, Guan Z (1999) J Eur Ceram Soc 19:2625

[Goodenough 2007] Goodenough JB, Huang YH (2007) J Power Sources 173:1

[He 2008] He L, Standard O, Huang T, Latella B, Swain M (2008) Acta Biomater 4:577

[Hoepfner 2002] Hoepfner TP, Case ED (2002) J Biomed Mater Res 60:643

[Hoepfner 2003] Hoepfner TP, Case ED (2003) Ceram Int 29:699

[Hu 2010] Hu LF, Wang CA (2010) Ceram Int 36:1697

[Hu 2010] Hu LF, Wang CA (2010) J Mater Sci 45:3242

[Kale 2009] Kale GM (2009) Adv Powder Technol 20:426

[Kamboj 2003] Kamboj RK, Dhara S, Bhargava P (2003) J Eur Ceram Soc 23:1005

[Khattab 2012] Khattab RM, Wahsh MMS, Khalil NM (2012) Ceram Int 38:4723

[Kolemen 2006] Kolemen U, Uzuna O, Yılmazlar M, Guclua N, Yanmazc E (2006) J Alloys Compd 415:300

[Korobko 2012] Korobko R, Chen C-T, Kim S., Cohen SR, Wachtel E., Yavo N, Lubomirsky, I, (2012) Scripta Materialia 66:155

[Krakhmalev 2006] Krakhmalev PV, Bergstrom J (2006) Wear 260:450

[Lawn 2012] Lawn BR, Cook RF (2012) J Mater Sci 47:1

[Li 2012] Li X, Zhang L, Yin X (2012) Mater Sci Eng A 549:43

[Liang2012] Liang B, Suzuki T, Hamamotoa K, Yamaguchia T, Sumi H, Fujishiro Y, Ingram BJ, Carter J (2012) J Power Sources 202:225

[Liao 2011] Liao Y, Baker I (2011) J Mater Sci 46:2009

[Liu 2002] Liu J, Madsen BD, Ji Z, Barnett SA (2002) Electrochem Solid State Lett 5:A122

[Luo 1997] Luo J, Stevens R, Taylor R (1997) J Am Ceram Soc 80:699

[Luo 1999] Luo J, Stevens R (1999) Ceram Int 25:281

[Machaka 2011] Machaka R, Derry TE, Sigalas I, Herrmann M (2011) Advances in Materials Science and Engineering, Article 539252

[Mahabole 2005] Mahabole MP, Aiyer RC, Ramakrishna CV, Sreedhar B, Khairnar RS (2005) Mater Sci B 28:535

[Mangalaraja 2009] Mangalaraja RV, Ananthakumar S, Uma K, Jimenez RM, Lopez M, Camurri CP (2009) Mater Sci Eng A 517:91

[Milman 1999] Milman YV, Chugunova SI, Goncharova IV, Chudoba T, Lojkowski W, Gooch W (1999) Int J Refract Met H 17:361

[Minh 1995] Minh NQ, Takahashi T (1995) Science and Technology of Ceramic Fuel Cells. Elsevier Science, New York, NY

[Muthukkumaran 2008] Muthukkumaran K, Kuppusami P, Kesavamoorthy R, Mathews T, Mohandas E, Raghunathan VS, Selladurai S (2008) Ionics 14:165

[Nanjangud 1995] Nanjangud SC, Brezny R, Green DJ (1995) J Am Ceram Soc 78:266

[Ni 2009] Ni JE, Ren F, Case ED, Timm EJ (2009) Mater Chem Phys 118:459

[Ni 2010] Ni JE, Case ED, Khabir KN, Wu CI, Hogan TP, Timm EJ, Girard S, Kanatzidis MG (2010) Mater Sci Eng B 170:58

[Nicholas 2009] Nicholas JD, Barnett SA (2009) J Electrochem Soc 156:B458

[Nicholas 2010] Nicholas JD, Barnett SA (2010) J Electrochem Soc 157:B536

[Nicholas 2012] Nicholas JD, Wang L, Call AV, Barnett SA (2012) Phys Chem Chem Phys 14:15379

[Nix 1998] Nix WD, Gao H (1998) J Mech Phys Solids 46:411

[Ozturk 2013] Ozturk O, Erdem M, Asikuzun E, Yildiz O, Yildirim G, Varilci A, Terzioglu C (2013) J Mater Sci: Mater Electron 24:230

[Pharr 2010] Pharr GM, Herbert EG, Gao Y (2010) Annu Rev Mater Res 40:271

[Pramanik 2007] Pramanik S, Agarwal AK, Rai K, Garg A (2007) Ceram Int 33:419

[Ramadass 1983] Ramadass N, Mohan SC, Reddy SR (1983) Mater Sci Eng 60:65

[Ren 2005] Ren F, Smith IO, Baumann MJ, Case ED (2005) Int J Appl Ceram Tec 2:200

[Ren 2009] Ren F, Case ED, Morrison A, Tafesse M, Baumann MJ (2009) Phil Mag 89:1163

[Rice 1998] Rice RW (1998) Porosity of Ceramics. Marcel Dekker, Inc., New York

[Rice 2000] Rice RW (2000) Mechanical Properties of Ceramics and Composites, Marcel Dekker, New York

[Ricote 1994] Ricote J, Pardo L, Jimenez B (1994) J Mater Sci 29:3248

[Sangwal 2000] Sangwal K (2000) Mater Chem Phys 63:145

[Sangwal 2009] Sangwal K (2009) Cryst Res Technol 44:1019

[Sarikaya 2012] Sarikaya A, Petrovsky V, Dogan F (2012) Int J Hydrogen Energy 37:11370

[Sauvet 2001] Sauvet AL, Fouletier J (2001) J Power Sources 101:259

[Schmidt 2010] Schmidt RD, Ni JE, Case ED, Sakamoto JS, Kleinow DC, Wing BL, Stewart RC, Timm EJ (2010) J Alloy Compd 504:303

[Selcuk 1997] Selcuk A, Atkinson A (1997) J Eur Ceram Soc 17:1523

[Shimizi 2009] Shimizi S, Yamaguchi T, Fujishiro Y, Awan M (2009) J Ceram Soc Japan 117:875

[Son 2011] Son JS, Appleford M, Ong JL, Wenke JC, Kim JM, Choi SW, Oh DS (2011) J Control Release 153:133

[Sulistyo 2010] Sulistyo J, Hata T, Kitagawa H, Bronsveld P, Fujisawa M, Hashimoto K, Imamura Y (2010) J Mater Sci 45:1107

[Trovarelli 1996] Trovarelli A (1996) Catal Rev Sci Eng 38:439

[Twigg 2007] Twigg MV, Richardson JT (2007) Ind Eng Chem Res 46:4166

[Underwood 1969] Underwood EE (1969) J Microsc 89:161

[Vandeperre 2004] Vandeperre LJ, Wang J, Clegg WJ (2004) Phil Mag 84:3689

[Vohs 2009] Vohs JM, Gorte RJ (2009) Adv Mater 21:943

[Wang 2002] Wang R, Pan W, Jiang M, Chen J, Luo Y (2002) Mater Sci Eng B90:261

[Yang 2007a] Yang L, Ning XS, Chen KX, Zhou HP (2007) Ceram Int 33:483

[Yang 2007b] Yang L, Ning XS, Xiao QF, Chen KX, Zhou HP (2007) J Biomed Mater Res B 81B:50

[Yang 2010] Yang A, Wang CA, Guo R, Huang Y, Nan CW (2010) Ceram Int 36:549

[Yang 2012] Yang YC, Chang TH, Wu YC, Wang SF (2012) Int J Hydrogen Energy 37:13746

[Yao 2005] Yao X, Tan S, Jiang D (2005) J Mater Sci 40:4939

[Zeng 2005] Zeng J, Sato Y, Ohkubo C, Hosoi T (2005) J Prosthet Dent 94:453

[Zhang 2004] Zhang TS, Ma J, Kong LB, King P, Kilner JA (2004) Solid State Ionics 167:191

CHAPTER 10

ROOM TEMPERATURE MECHANICAL PROPERTIES OF NATURAL MINERAL BASED THERMOELECTRICS

X. Fan[1], E. D. Case[1], X. Lu[2], D. T. Morelli[1,2]
[1] Department of Chemical Engineering and Materials Science, Michigan State University, East Lansing, MI, 48824
[2] Department of Physics & Astronomy, Michigan State University, East Lansing, MI, 48824

Submitted to: Journal of Materials Science

Abstract

Low-cost, highly efficient thermoelectric materials for waste heat recovery applications can be made by combining the naturally-occurring thermoelectric mineral tetrahedrite ($Cu_{10}Zn_2As_4S_{13}$) and the synthetic compound ($Cu_{12}Sb_4S_{13}$). To better utilize this material in waste harvesting applications, it is essential to characterize the material's mechanical properties including elastic modulus, hardness and fracture toughness. In this study, powders of $Cu_{10}Zn_2As_4S_{13}$ were mixed with varying amounts of $Cu_{12}Sb_4S_{13}$ and then densified by hot pressing. The room temperature mechanical properties were investigated as a function of (i) composition and (ii) ball milling time. Elastic moduli were measured using resonant ultrasound spectroscopy (RUS). Hardness and fracture toughness were determined by Vickers indentation technique.

1. Introduction

Because of their potential ability to convert heat to electricity, thermoelectric materials are under intense scrutiny by both experimental and theoretical researchers. Through a variety of new approaches, significant improvements in thermoelectric figure of merit have been achieved over the last decade. One example are the filled skutterudite compounds, first investigated in the mid-1990's [Morelli 1995, Sales 1996], that have recently been shown to exhibit dimensionless figure of merit exceeding 1.5 at 800 K [Shi 2011]; another example are hierarchically-structured PbTe –PbS solid solutions, that combine point defects, grain-boundaries, and precipitated second phases on the nanoscale to achieve ZT values in excess of two [Biswas 2012].

While these improved ZT values are exciting, some concerns remain regarding their implementation in commercial devices, mainly due to their use of low abundance elements such as rare earths and tellurium. For this reason, work continues to focus on the development of materials that not only can exhibit high thermoelectric performance, but also possess the potential to be synthesized economically on a large scale; examples include oxide-based and silicon-based thermoelectrics. As is typical of new high-performance materials in many applications, there is a trade-off between high figure of merit and cost, and one can make a good case that materials that do not necessarily exhibit the highest performance but that can be produced inexpensively will have wide-scale implementation in heat-recovery and power generation schemes. Another good example of such compounds, recently reported by Lu, *et al*., [Lu 2013a] are semiconductors based on tetrahedrite, $Cu_{12}Sb_4S_{13}$. They showed that compounds of composition $Cu_{12-x}(Fe,Zn)_xSb_4S_{13}$ can reach figure of merit close to unity at 700 K. Unlike typical semiconductor thermoelectrics, in

which the doping level needs to be fairly carefully controlled to optimize ZT, the figure of merit in these compounds is relatively insensitive to the amount of metal impurity x. Lu, *et al.* noted that the range of x spanned the range determining the composition of natural mineral tetrahedrites, and for this reason they further suggested that one might be able to use the natural mineral itself as a source thermoelectric material. In a subsequent very recent work, Lu and Morelli showed that tetrahedrite samples containing as much as 50 % natural mineral tetrahedrite did indeed possess similar values for ZT [Lu 2013b]. Since tetrahedrites are the most widespread sulfosalts on Earth, this presents the potential for an earth-abundant, inexpensive source of thermoelectric materials.

In addition to ZT and the transport properties, mechanical properties are crucial to the successful fabrication and application of thermoelectric generators. For example, waste heat recovery applications will impose a variety of thermal and mechanical stresses on thermoelectric materials originating from the heat up and cool down of the waste heat source.

The thermal stress, σ_T, can be induced by the thermal gradients or thermal transients [Kaliakin 2002, Martin 1973] during waste heat recovery. In order to simulate the thermal stress by either analytic or finite element method, the Young's modulus and Poisson's ratio are required [Kaliakin 2002, Zienkiewicz 2005], such that

$$\sigma_T = \frac{E(T)\alpha(T)\Delta T}{(1-\nu(T))}$$

where E(T) is the temperature-dependent Young's modulus, $\nu(T)$ is the temperature-dependent Poisson's ratio, $\alpha(T)$ is the temperature-dependent thermal expansion, and ΔT is the temperature difference.

However, the literature on the mechanical properties of thermoelectric materials is limited. In particular, for both naturally-occurring and synthetic tetrahedrite compositions such as $Cu_{10}Zn_2As_4S_{13}$, mechanical property data are entirely absent in the literature.

2. Experimental procedure

2.1 Specimen preparation

The natural thermoelectric mineral used in this study had the chemical composition $Cu_{9.7}Zn_{1.9}Fe_{0.4}As_4S_{13}$ (Stefano Fine Minerals, Ann Arbor, Michigan, USA). Two groups of specimens were processed, one group for a composition-property study and a second group for a milling time-property study. For the composition-property study, the synthetic thermoelectric (TE) material $Cu_{12}Sb_4S_{13}$ was first synthesized by direct solid state reaction of the elements Cu (99.99% purity), Sb (99.9999% purity), and S (99.999%) from Alfa-Aesar, which were loaded in stoichiometric ratios into quartz ampoules. The ampoules were then evacuated to $<10^{-5}$ Torr, sealed, loaded into a vertical furnace and heated at a ramp rate of 0.3 ºC min^{-1} to 650ºC, and then held at that temperature for 12 hours. The reacted powders were then cooled to room temperature at the rate of 0.4 ºC min^{-1}. The $Cu_{12}Sb_4S_{13}$ and the natural mineral powders were mixed by ball milling for 30 min in a SPEX Mixer/Mill using a stainless steel mill jar with stainless steel grinding media. In a glove box with flowing argon gas, the specimens were hot pressed at 723 K for 20 minutes at 70 MPa pressure using a 10 mm graphite die.

For the milling time-property study, the elemental Cu powders (10 micron mean particle size, 99.9% purity), Sb shot (99.999% purity) and S chunks (99.999% purity) from Alfa-Aesar were mixed in the stoichiometric ratio needed to form $Cu_{12}Sb_4S_{13}$ using a tungsten

carbide milling jar with tungsten carbide grinding media. The natural mineral powders of composition $Cu_{9.7}Zn_{1.9}Fe_{0.4}As_4S_{13}$ were added to the milling jar in a mass ratio of 1:1 with the elemental powders. The powders were then milled in the Spex mill for 30 minutes. The specimens were then densified by hot pressing, using the same time-temperature-pressure profile used to densify the specimens in the composition-property study.

2.2 Microstructural and phase characterization

The microstructure of the specimens included in this study was analyzed with a JEOL 7500F scanning electron microscope (SEM) using a working distance of 8mm and an accelerating voltage of 15 kV. Mean grain sizes were determined using linear intercept technique with a minimum of 150 intercepts per micrograph [Wurst 1972].

X-ray diffraction analysis was performed on each of the densified specimens using a Rigaku Miniflex II bench-top X-ray diffractometer (Cu K_α radiation). The XRD results were analyzed using a commercial software package (Jade).

2.3. Elasticity measurements

The Young's modulus, E, shear modulus, G, Poisson's ratio, ν, and bulk modulus, B, were measured via a non-destructive method, namely, the resonant ultrasound spectroscopy [Migliori 1997] (RUS, RUSpec, Quasar International, Albuquerque, NM, USA). The RUS apparatus excited, detected and recorded resonance modes of the specimens over a frequency range from 20 to 600 kHz. The elastic moduli were calculated from the resonant frequencies along with the mass, shape, and the dimensions of the specimens using a commercial software (RPModel package, Quasar International, Albuquerque, NM, USA). Additional details of the RUS measurement technique are available elsewhere [Ren 2008, Ren 2009, Schmidt 2013].

2.4 Hardness and fracture toughness measurements

Hardness, H, and fracture toughness, K_c, were evaluated using Vickers indentation. Prior to the indentation, specimens were polished with diamond paste with diamond grit sizes from 90 μm to 1 μm using an automatic polishing machine (Leco Vari/Pol VP-50, Leco Corporation, St. Joseph, MI).

For specimens NM II and 45% (Table 10.1), an indentation load, F, of 4.9 N and a load time of 5 s were used. For the other specimens in this study, spalling occurred near the indentation site so F was lowered to 2.94 N but the 5 s loading time was retained. Ten Vickers indentations (Shimazdu HMV 2000, Kyoto, Japan) were placed on each specimen.

Hardness was calculated using

$$H = \frac{1.8544F}{(2a)^2} \tag{1}$$

where 2*a* is the diagonal length of the indentation impression [Wachtman 2009]. Fracture toughness was calculated using equation (2)

$$K_c = \frac{\xi(E/H)^{0.5}F}{c^{1.5}} \tag{2}$$

where ξ is a dimensionless calibration constant equal to 0.016 [Anstis 1981], E is the Young's modulus measured by RUS, H is the hardness value and c is half of the radial crack length.

3. Results and discussion

3.1 Microstructural and phase characterization

In each of the specimens included in this study, the grains were approximately equiaxed, with quasi-spherical pores along the grain boundaries (Figure 10.1). From SEM micrographs

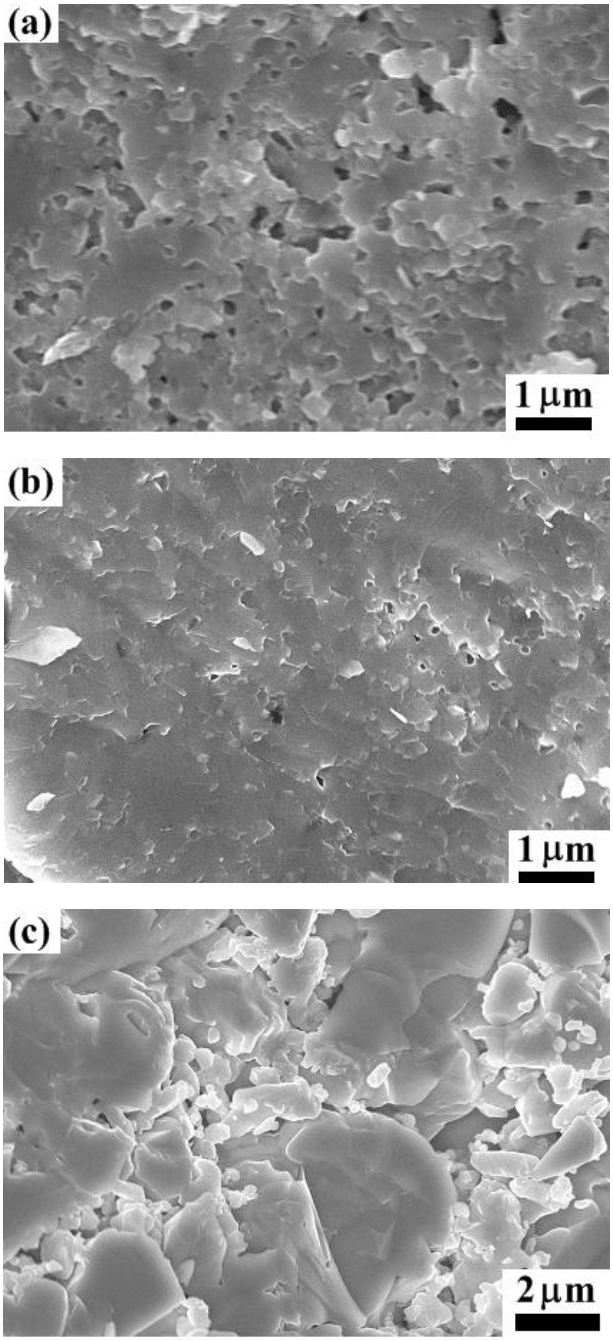

Figure 10.1. SEM micrographs of fracture surfaces of specimens included in both the composition and milling time studies. For the composition study, the microstructures are shown in figures (a) – (c) for the weight fraction of synthetic phase, x, where (a) x = 0, (b) x = 0.5, (c) x = 1. For the milling time study, the microstructures correspond to (d) 1 h milling time, (e) 9 h milling time.

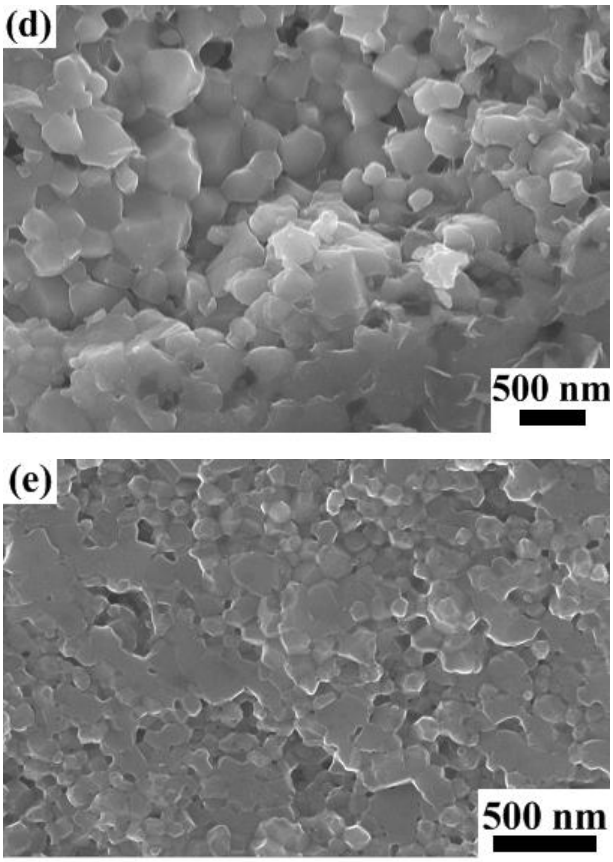

Figure 10.1 (cont'd). SEM micrographs of fracture surfaces of specimens included in both the composition and milling time studies. For the composition study, the microstructures are shown in figures (a) – (c) for the weight fraction of synthetic phase, x, where (a) x = 0, (b) x = 0.5, (c) x = 1. For the milling time study, the microstructures correspond to (d) 1 h milling time, (e) 9 h milling time.

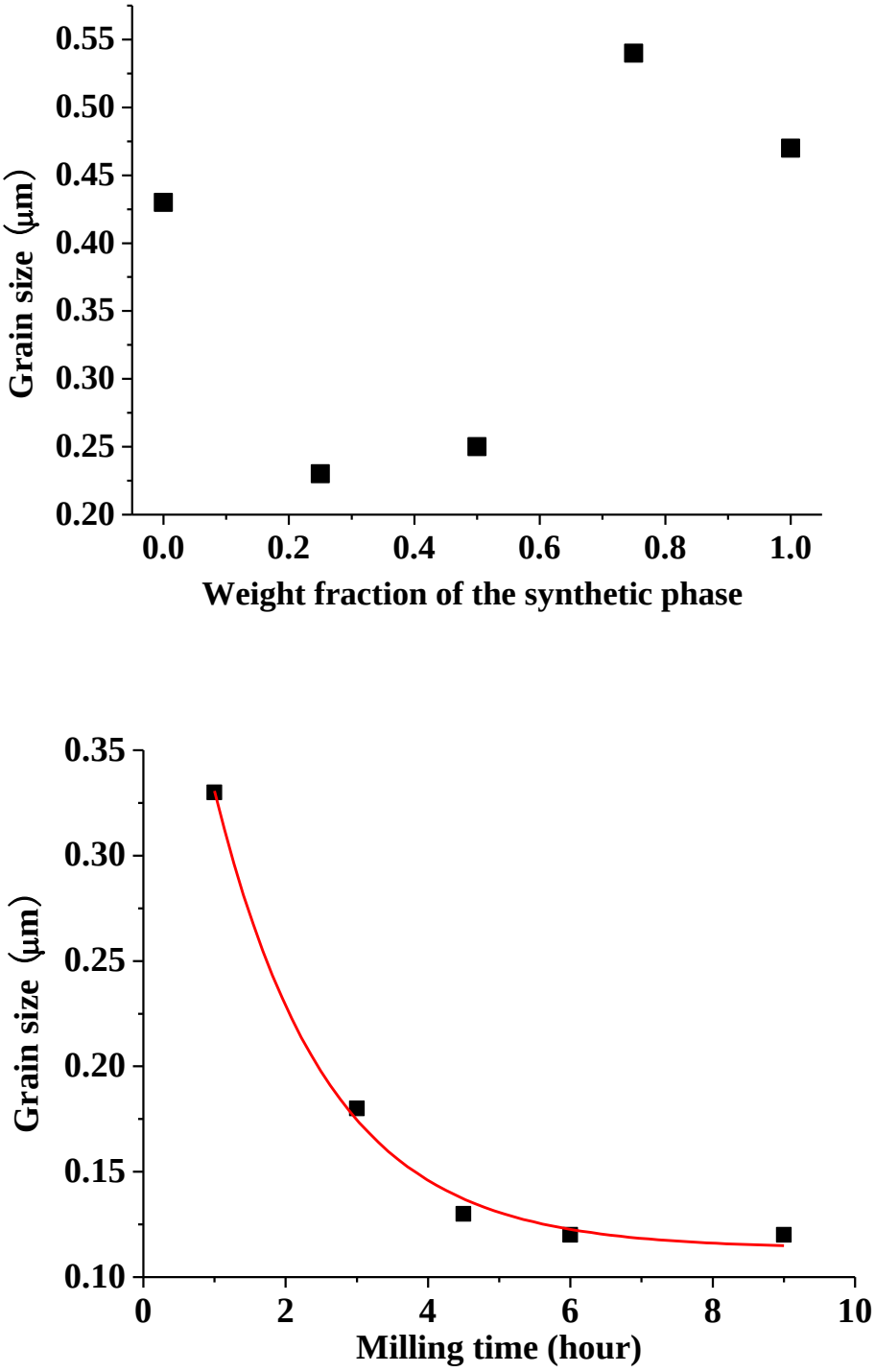

Figure 10.2. Grain size as a function of (a) the weight fraction of the synthetic phase; (b)the milling time.

of fracture surfaces, the mean grain sizes of the composition-property group of specimens range from about 0.23 to 0.54 microns (Figure 10.2a). For the milling time-properties study, the grain size decreased exponentially with milling time from about 0.33 μm for specimens fabricated from powders milled for one hour, reaching a steady-state mean grain size of approximately 0.12μm after 4 hours of milling (Figure 10.2b).

The fracture mode appears to be a function of both composition and milling time. For example, in terms of the weight fraction of synthetic phase, x, the fracture mode changes from mostly transgranular, to predominantly intergranular to mostly transgranular to a mixture of transgranular and intergranular for x = 0, 0.25, 0.5, 0.75 and 1.0. As a function of milling time, at 1 hour the fracture surfaces are intergranular, then mostly intergranular at 3 hours, a mixture of transgranular and intergranular at 4.5 hours, and then mostly intergranular at milling times of 6 and 9 hours. The fracture mode can be a function of several parameters, including grain size and inclusions, where one likely source of inclusions is the contamination from the milling process. For example, in a study on lead zirconate titanate (PZT) ceramics, the fracture mode was found to be predominantly intergranular at grain size of approximately 9.5 μm and entirely transgranular at the large grain size of about 18 μm [Kim 1990].

In addition, the XRD analysis did not detect the presence of minor phases in any of the specimens included in this study.

3.2 Elastic moduli, hardness and fracture toughness as a function of composition

For the solid state compositions that result from combinations of the synthetic TE material $Cu_{12}Sb_4S_{13}$ and the natural TE mineral $Cu_{9.7}Zn_{1.9}Fe_{0.4}As_4S_{13}$, the room temperature Young's modulus, E, shear modulus, G and bulk modulus, B (Table 10.1), the

Table 10.1. For the specimens, the number of RUS resonant peaks measured, N, the RMS error, the Young's modulus, E, shear modulus, G, Poisson's ratio, υ, bulk modulus, B, mass density, ρ.

Specimen Label	N	RMS Error	E (GPa)	G (GPa)	υ	B (GPa)	ρ (g/cc)
0 Syn-disk	35	0.40%	56.67 ± 0.12	21.97 ± 0.03	0.290± 0.002	44.9	4.30
0 Syn-bar [a]	19	0.58%	58.55 ± 0.41	22.98 ± 0.08	0.274± 0.008	43.2	4.26
0.45 Syn-bar	33	0.32%	59.98 ± 0.18	22.56 ± 0.05	0.329± 0.003	58.5	4.70
0.25 Syn-disk	25	0.44%	61.27 ± 0.12	23.23 ± 0.03	0.317± 0.002	56.3	4.48
0.50 Syn-disk	31	0.51%	55.45 ± 0.14	21.2 ± 0.04	0.308± 0.003	48.1	4.65
0.75 Syn-disk	13	0.63%	51.03 ± 0.14	19.08 ± 0.04	0.337± 0.003	52.2	4.72
1 Syn-disk	26	0.15%	33.54 ± 0.02	12.5 ± 0.06	0.342± 0.001	35.3	4.62
0.50 Syn-1h-disk	19	0.40%	50.85 ± 0.09	19.49 ± 0.03	0.304± 0.002	43.3	4.40
0.50 Syn-3h-disk	19	0.11%	55.99 ± 0.03	21.56 ± 0.01	0.298± 0.001	46.3	4.32
0.50 Syn-4.5h- disk	26	0.12%	52.92 ± 0.03	20.06 ± 0.008	0.319± 0.001	48.7	4.5
0.50 Syn-6h-bar	21	0.49%	55.23 ± 0.10	21.04 ± 0.02	0.312± 0.002	49.1	4.42
0.50 Syn-9h-disk	13	0.11%	55.01 ± 0.03	20.99 ± 0.008	0.310± 0.001	48.3	4.51

[a] The geometry of the bar is not ideal for RUS measurements since the opposing surfaces of the bar are not parallel.

hardness, H, (Table 10.1) and the Poisson's ratio, υ, are functions of composition (Figure 10.3). For the weight fraction of the synthetic phase $Cu_{12}Sb_4S_{13}$, x ($0 \leqslant x \leqslant 1$), the composition dependence of property, A (where A is E, G, B, H, or υ), can be described relatively well by the equation

$$A = A_0 + (A_1 - A_0)x + k\,x\,(1-x) \qquad (3)$$

where A_0 = the value of A at x = 0, A_1 = the value of A at x = 1, and k is a parameter (sometimes called the "bowing parameter") which has the same unit as A (Figure 10.3). When k = 0, equation (3) reduces to a rule of mixtures relationship. For E, G, and H, the coefficient of determination, R^2, is between 0.973 and 0.982, although for the B data, R^2 is only 0.801 and thus equation (3) did not fit the B data as well (Table 10.2). In addition, for Poisson's ratio, υ, $\upsilon_0 = 0.284$ +/- 0.008, $\upsilon_1 = 0.341$ +/- 0.011, k = 0.047 +/- 0.041, $R^2 = 0.851$ and $x_{\upsilon max} = 1.106$, where $x_{\upsilon max}$ is the x value when υ reaches the highest value on the least squares fitting curve.

For solid solution systems in the literature, equation (3) also describes the compositional dependence of E, G [Ravinder 2001, Ren 2007] and H [Schenk 1998, Ren 2008]. It should be noted that while E and G are measures of a material's resistance to elastic deformation, H is a measure of the resistance to plastic deformation. Thus, although the elastic moduli and H represent fundamentally different physical entities, when equation (3) is normalized by A_0, the changes in the normalized E, G, and H values are nearly identical (Figure 10.4).

Table 10.2. For the composition-property study, the results of the least-squares fit the elastic moduli, E, G, and B, and hardness, H, data to equation 3.

Property	A_0 (GPa)	A_1 (GPa)	K (GPa)	R^2	x_{Amax}
E	57.59 ± 1.25	34.16 ± 1.71	48.68 ± 6.41	0.975	0.233
G	22.44 ± 0.43	12.75 ±0.59	17.26 ± 2.20	0.982	0.259
B	44.46 ± 3.01	35.90 ± 4.11	60.20 ± 15.41	0.801	0.429
H	3.26 ± 0.12	1.81 ± 0.12	2.72 ±0.05	0.973	0.233

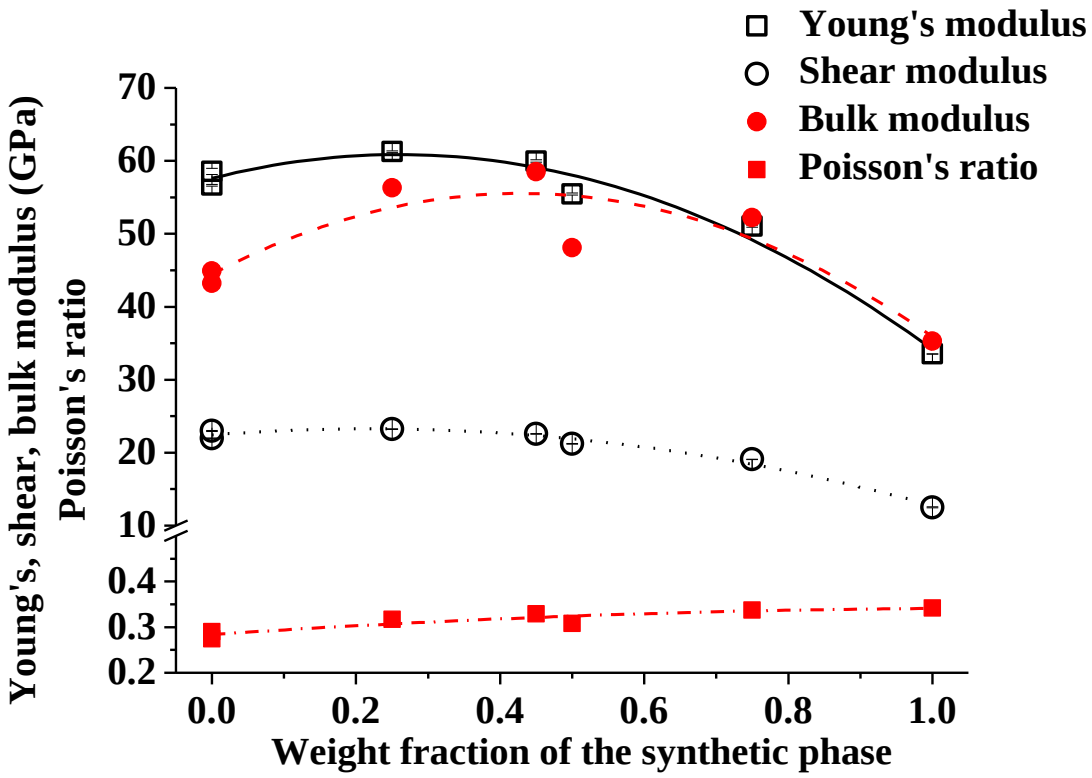

Figure 10.3. Young's, shear, bulk modulus and Poisson's ratio as a function of the weight fraction of the synthetic phase for the mineral TE materials in this study. The solid, dashed, dotted and dash-dotted curves represent respectively the least squares fit of equation (3) to the Young's modulus, shear modulus, bulk modulus and Poisson's ratio data.

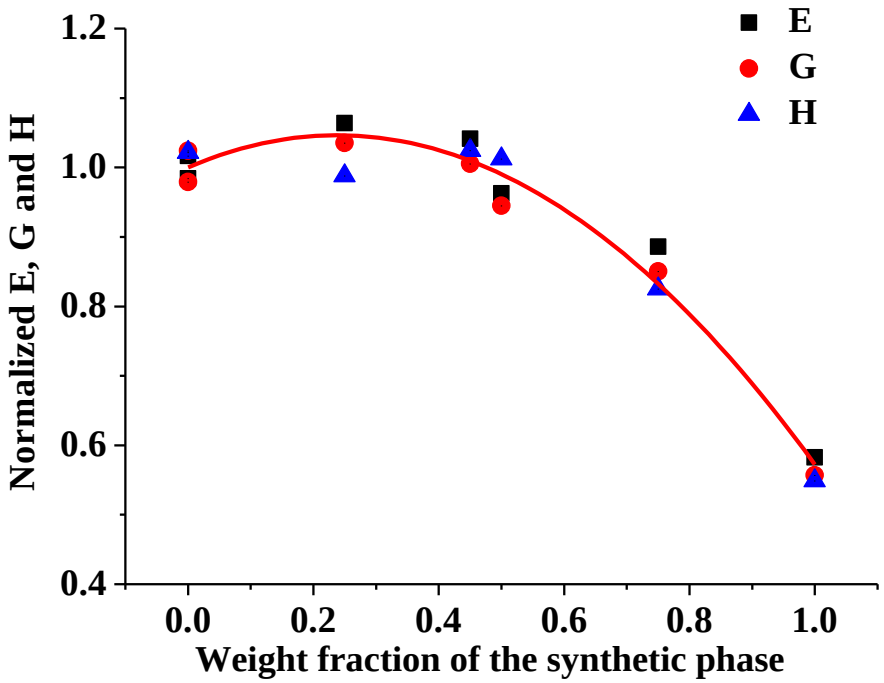

Figure 10.4. Normalized Young's, shear modulus and hardness as a function of the weight fraction of the synthetic phase (in each case, the data were normalized by dividing the each coefficient in equation (3) by A_0). The solid curve represents a least squares fit of all the normalized E, G and H data to equation (3).

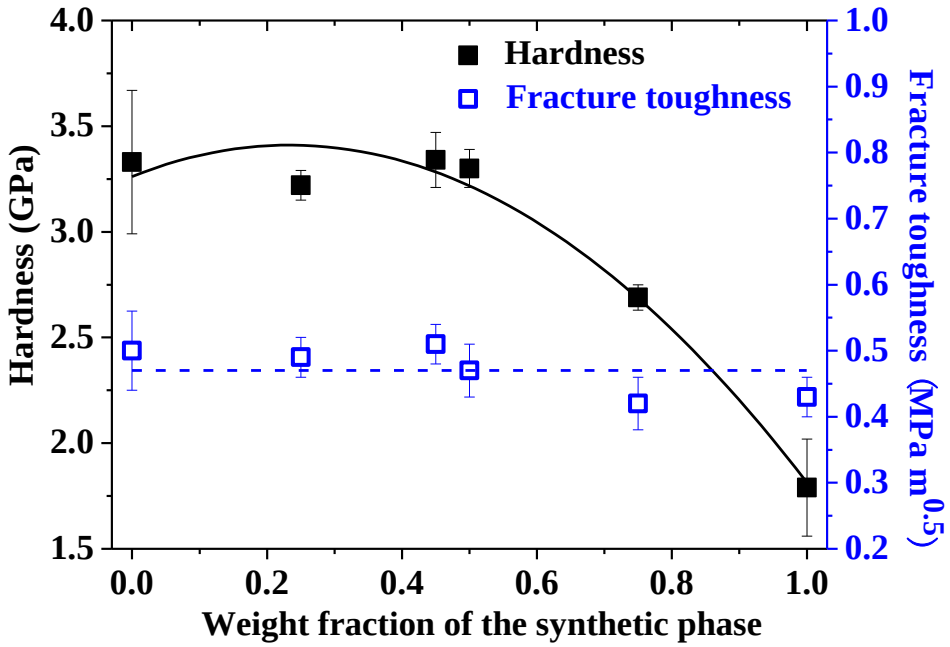

Figure 10.5. Hardness and fracture toughness as a function of the weight fraction of the synthetic phase for the mineral TE materials in this study. The solid curve represents a least squares fit of the hardness data to equation (3); the dashed line represents the mean value of K_c over the entire weight fraction of the synthetic phase.

The fracture toughness, K_C, was essentially independent of composition for the specimens included in this study, with an average K_C value of 0.47 ± 0.04 MPa•$m^{0.5}$ (Figure 10.5). A K_C value that is independent of composition for a solid solution system has been observed by Shibata [Shibata 1997]. For the Cr_2O_3-Al_2O_3 solid solution system, the H and K_C values were essentially constant ~23.5 GPa and ~4 MPa•$m^{0.5}$, respectively over a range of Al_2O_3 from 0 to 25 mol % [Shibata 1997]. However, the literature on K_C as a function of composition for solid solution systems is relatively limited. There are a number of papers on K_C versus composition for zirconia systems, however the extent of transformation toughening is a sensitive function of the Zr content [Fu 2009]. Also, a number of researchers studied solid solution matrices that include nano/micro scale inclusions such that it is difficult to separate the contributions to K_C from solid solution composition and the inclusions [Charitidis 2007].

The elastic moduli and Poisson's ratio reported in this study are global properties of the specimen since they are determined by RUS from the spectrum of mechanical resonances for the bulk specimen. However, the H and K_C values are determined via Vickers indentation measurements and thus it is important to consider whether H and K_C are "local" or "global" values. The hardness values are functions of the diagonal length of the Vickers pyramidal indentation impression, 2a, (equation 2), where average value of 2a in this study was 40 μm. In comparison, the grain sizes of every specimen included in this study were less than 1 μm. Thus, the hardness values represent an average over thousands of individual grains. Also, for the indentation measurements of K_C, the average crack length, c, ranged from about 45 to 65

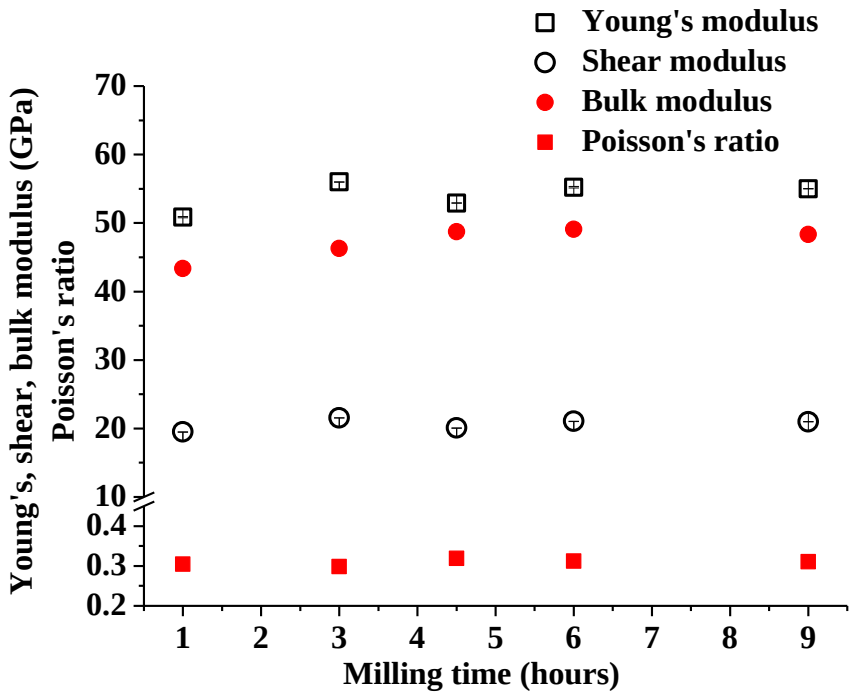

Figure 10.6. Young's, shear, bulk modulus and Poisson's ratio as a function of milling time.

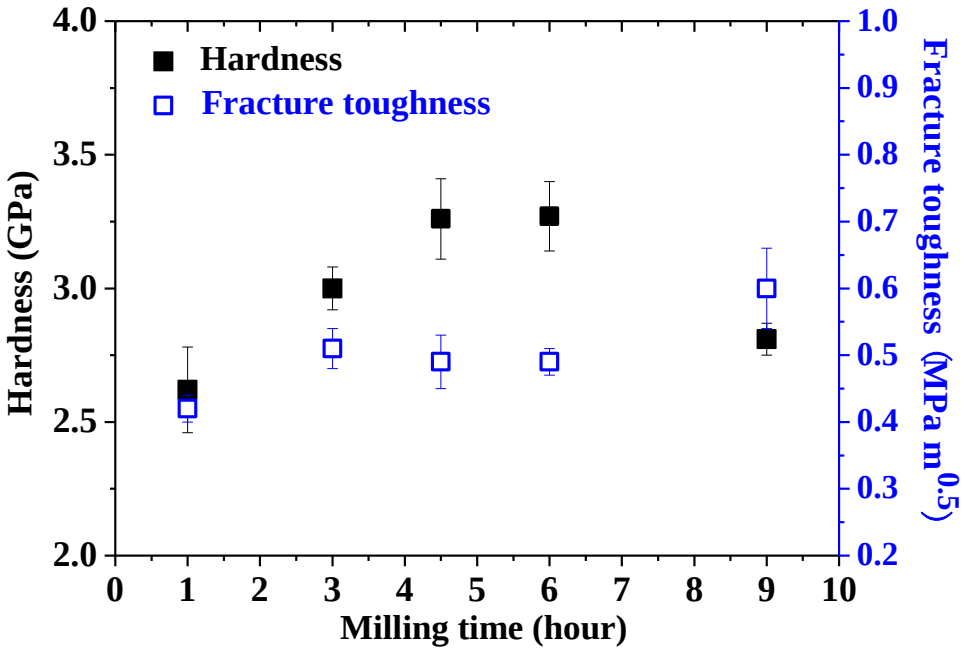

Figure 10.7. Hardness and fracture toughness as a function of milling time.

μm so that the fracture toughness measurements represent the interaction of the indentation-induced crack with more than a hundred grains. Thus, the H and K_C values determined should be relatively insensitive to localized fluctuations in microstructure.

3.3 Elastic moduli, hardness and fracture toughness as a function of milling time

During ball milling of brittle materials [Suryanarayana 2001, Hall 2009, Pilchak 2007], including thermoelectrics [Hall 2009, Pilchak 2007], the powder particle size initially decreases rapidly, reaching a steady state (grindability limit) typically within a few hours. The current study shows that ball milling for times longer than 4 hours does not result in a smaller as-sintered grain size for the solid solution formed by mixing then sintering the natural mineral and synthetic tetrahedrite powders. This result is significant since ball milling (using a variety of mill jar and milling media) can result in significant contamination that generally increases as the milling time increases [Singh 2009].

The Young's shear and bulk moduli along with Poisson's ratio were approximately constant as a function of milling time (Figure 10.6). In contrast, the hardness and fracture toughness values (Figure 10.7) apparently increase and then either go through a maximum or reach a plateau for milling times of 4 hours or more. However, the scatter in the H and K_C data make it difficult to clearly identify the H and K_C versus milling time trends.

4. Summary and conclusions

The composition dependencies of the Young's modulus, E, shear modulus, G (Figure 10.3) and hardness, H (Figure 10.5), are described well by equation 3, in agreement with the trends observed for the elastic moduli and hardness of a number of solid solution systems in the literature. When normalized by the A_0, value of the property in equation 3 for zero mass

fraction of the synthetic tedrahedrite, the changes in E, G and H are remarkably similar (Figure 10.4). However, the fracture toughness, K_C, is essentially independent of the composition over the entire solid solution range.

For the milling time-property study, the elastic moduli and Poisson's ratio are essentially independent of milling time. The scatter in the H and K_C make it difficult to discern a trend as a function of milling time (Figure 10.7).

5. Acknowledgements

The authors acknowledge the financial support of the Department of Energy, "Revolutionary Materials for Solid State Energy Conversion Center," an Energy Frontiers Research Center funded by the U.S. Department of Energy, Office of Science, Office of Basic energy Sciences under award number DE-SC0001054.

REFERENCES

REFERENCES

[Anstis 1981] Anstis GR, Chantikul P, Lawn BR, Marshall DB (1981) J Am Ceram Soc 64:533

[Biswas 2012] Biswas K, He J, Blum ID, Wu CI, Hogan TP, Seidman DN, Dravid VP, Kanatzidis MG (2012) Nature 489:414

[Charitidis 2007] Charitidis CA, Karakasidis TE, Kavouras P, Karakostas TH (2007) J Phys Condens Matter 19:266209

[Fu 2009] Fu YP, Hu SH, Liu BL (2009) Ceram Int 35:3005

[Hall 2009] Hall BD, Case ED. Ren F, Johnson J, Timm EJ (2009) Mater Chem Phys 113: 497

[Kaliakin 2002] Kaliakin VN (2002) In Introduction to Approximate Solution Techniques, Numerical Modeling, and Finite Element Methods, Marcel Dekker, New York

[Kim 1990] Kim SB, Kim DY (1990) J Am Ceram Soc 73:161

[Lu 2013a] Lu X, Morelli DT, Xia Y, Zhou F, Ozolins V, Chi H, Zhou X, Uher C (2013) Adv Energy Mater 3:342

[Lu 2013b] Lu X, Morelli DT (2013), Phys Chem Chem Phys 15:5762

[Martin 1973] Martin HC, Carey GF (1973) In Introduction to Finite Element Analysis, McGraw-Hill, New York

[Migliori 1997] Migliori A, Sarrao JL (1997) Wiley-Interscience, Hoboken

[Morelli 1995] Morelli DT, Meisner GP (1995) J Appl Phys **77**:3777

[Pilchak 2007] Pilchak AL, Ren F, Case ED, Timm EJ, Wu CI, Hogan TP, Schock HJ (2007) Philos Mag 87:4567

[Ravinder 2001] Ravinder D, Alivelumanga T (2001) Mater Lett 49:1

[Ren 2009] Ren F, Case ED, Ni JE, Timm EJ, Lara-Curzio E, Trejo RM, Lin CH, Kanatzidis MG (2009) Philos Mag 89:143

[Ren 2007] Ren F, Case ED, Timm EJ, Schock HJ (2007) Philos Mag 87:4907

[Ren 2008] Ren F, Case ED, Sootsman JR, Kanatzidis MG, Kong H, Uher C, Lara-Curzio E, Trejo RM (2008) Acta Mater 56:5954

[Ren 2008] Ren F, Case ED, Timm EJ, Schock HJ (2008) J Alloy Compd 455:340

[Sales 1996] Sales BC, Mandrus D, Williams RK (1996) Science 272:1325

[Schenk 1998] Schenk M, Le THD (1998) Semicond Sci Technol 13:335

[Schmidt 2013] Schmidt RD, Case ED, Lehr GJ, Morelli DT (2013) Intermetallics 35:15

[Shi 2011] Shi X, Yang J, Salvador JR, Chi M, Cho JY, Wang H, Bai S, Yang J, Zhang W, Chen L (2011) J Am Chem Soc 133:7837

[Shibata 1997] Shibata K, Yoshinaka M, Hirota K, Yamaguchi O (1997) Mater Res Bull 32:627

[Singh 2009] Singh S, Godkhindi MM, Krishnarao RV, Murty BS (2009) J Eur Ceram Soc 29:2069

[Suryanarayana 2001] Suryanarayana C (2001) Prog Mater Sci 46:1-184

[Wachtman 2009] Wachtman JB, Cannon WR, Matthewson MJ (2009) Mechanical Properties of Ceramics, second ed., John Wiley & Sons, Inc., New York

[Wurst 1972] Wurst JC, Nelson JA (1972) J Am Ceram Soc 55:109

[Zienkiewicz 2005] Zienkiewicz OC (2005) The finite element method for solid and structural mechanics, Elsevier Butterworth-Heinemann, Boston

CHAPTER 11

ROOM TEMPERATURE MECHANICAL PROPERTIES OF THERMOELECTRIC INTERMETALLIC MATERIAL ZrNiSn

X. Fan[1], L. G. GUERRERO[2], E. D. Case[1], H. Sun[1], D. T. Morelli[1]
[1]Department of Chemical Engineering and Materials Science, Michigan State University, East Lansing, MI, 48824
[2]Technical University of Madrid, Madrid, Spain, 28040

Abstract

The intermetallic half-Heusler compound ZrNiSn is of interest as a thermoelectric material for waste heat recovery applications. For this study, ten polycrystalline ZrNiSn specimens were prepared from arc melted ingots that were subsequently powder processed and then densified by pulsed electric current sintering. Using resonant ultrasound spectroscopy (RUS), the room temperature Young's modulus, shear modulus and Poisson's ratio were determined. Also, the room temperature hardness was measured by Vickers indentation. Using a range of sintering temperatures between 800^{o}C and 1025^{o}C, the volume fraction porosity, P, of the specimens was intentionally varied from 0.01 to 0.24. Both porosity dependence of the elastic moduli and the hardness can be described well by the empirical exponential relationship $A(P) = A_0\exp(-b_A P)$ where A is the porosity-dependent mechanical property, A_0 is the value of A at P = 0, and b_A is a measure of the rate of decrease in A with increasing P.

1. Introduction

Thermoelectric (TE) materials are capable of converting waste heat into electricity, and have attracted wide interest recently. Among the various types of the TE materials, the class of the intermetallic compounds known as the half-Heusler (HH) have received extensive attention [Zou 2013, Kong 2012, Populoh 2012, Fu 2013]. Half-Heusler compounds have high figure of merit (ZT near 1) at high temperatures [Yu 2009]. Half-Heusler compounds have chemical formula of XYZ, for example, MNiSn (M = Hf, Zr, Ti) – based HH have been widely studied as n-type TE materials [Populoh 2012, Shen 2001].

However, most studies of HH compounds have focused on the improvement of transport properties [Zou 2013, Kong 2012, Populoh 2012, Yu 2009], while the literature on mechanical property measurements of HH compounds are very limited [Verges 2011]. Nevertheless, designers need the elastic moduli of a material in order to model its stress and strain behavior under applied thermal and/or mechanical stresses. For example, the finite element analysis requires the Young's modulus and Poisson's ratio in order to construct the stiffness matrix [Martin 1973]. In addition, the elastic moduli can be used to monitor the level of microcrack damage in a brittle material [Fan 2012a]. Moreover, hardness is related to the machinabily [Kamboj 2003] and wear resistance [Krakhmalev 2006] of the material, which are directly related to the fabrication and stability of TE materials.

In general, porosity affects mechanical, electrical and thermal properties of materials. For example, both the thermal conductivity, κ and electrical conductivity, σ_e, of ceramics [Rice 1998], metals and semiconductors decrease with increasing porosity. In particular, for

thermoelectric materials such as CoSi [Kim 2002], $Ca_{2.76}Cu_{0.24}Co_4O_9$ [Kim 2013], Al-doped ZnO [Ohtaki 2011] and the intermetallic half-Heusler compound FeVSb [Fu 2013], the observed decreases in κ and σ_e with increasing P has been attributed to the scattering of phonons and charge carriers by pores [Ohtaki 2011, Fu 2013]. The efficiency of TE materials is characterized by a dimensionless figure of merit (ZT, $ZT = S^2\sigma_e T/\kappa$), where S is the Seebeck coefficient, σ_e is the electrical conductivity, T is the absolute temperature, and κ is the thermal conductivity. Both κ and σ_e decrease with increasing porosity in manners such that $\kappa = \kappa_0 \exp(-b\kappa P)$ and $\sigma_e = \sigma_{e0} \exp(-b\sigma_e P)$, where κ_0 and σ_{e0} are κ and σ_e at zero porosity, P, respectively, $b\kappa$ and $b\sigma_e$ are material-dependent constants. The values of $b\kappa$ and $b\sigma_e$ were empirically found to be in the range of 1.5 to 2.0 and 1.5 to 3.5, respectively [Case 2012]. Seebeck coefficient has been found enhanced by porosity [Kallel 2012, Lee 2010]. Thus, the ZT could be increased, remained constant, or decreased in the presence of porosity.

A wide range of mechanical properties are also porosity dependent, including fracture strength [Fan 2012b], fracture surface energy [Vandeperre 2004], elastic moduli [Fan 2012b] and hardness [Hoepfner 2003].

In this paper, the room temperature elastic moduli and hardness of half-Heusler compound ZrNiSn as a function of porosity were studied. It is of great importance to study porosity in thermoelectric materials for the following reasons: (i) porosity has the potential to increase ZT in TE materials; (ii) porosity may improve the thermal fatigue resistance in TE materials in analogy to thermal barrier coatings [Case 2012]; (iii) the obtained modulus-porosity relation allows the comparison of data with different porosity levels by

different researchers; (iv) the extrapolation value of the modulus-porosity relation allows the comparison of experimental data with porosity to theoretical calculations without porosity.

2. Experimental procedure

2.1 Specimen preparation

The starting materials for the ZnNiSn ingots were obtained from Alfa Aesar, namely Zr lump material (roughly 3-6mm in diameter, 99.8% pure, stock#36253), Ni slugs (6.35mm dia x 12.7mm length, 99.995%, purity, stock# 42330) and Sn shot (3mm diameter, 99.999% pure, stock# 11010). An arc melting furnace (Centorr, Model 5SA) was used to melt the elements in stoichiometric proportions to form the ZrNiSn phase on a copper hearth without water-cooling and under flowing argon gas.

After casting, the ingot surfaces with lightly sanded with 1200 grit sandpaper and were then cleaned for 5 minutes in a detergent bath in an ultrasonic cleaner. The specimens were then rinsed with DI water, cleaned in an ethanol bath and then rinsed with DI water.

The cleaned ingots were then crushed, ground, sieved and reground (CGSR) (Retsch RM200, Retsch GmbH, Haan, Germany) in a glovebox with flowing argon until all powders passed through a 53 μm sieve. The CGSR powder was then either (i) densified directly using pulsed electric current sintering (PECS) or (ii) dry milled prior to PECS densification via a planetary mill (PM100, Retsch, Newtown, PA) using a 250 cc alumina-lined milling jar and spherical alumina grinding media [Pilchak 2007].

2.2 Pulsed electric current sintering (PECS)

For both the CGSR powders (without planetary milling) and the ball milled ZnNiSn

powders, approximately 2 grams of powder per specimen were PECS processed (Model 10, Series 4 by Thermal Technologies LLC, Santa Rosa, CA) in a 12.7 mm diameter graphite die with grafoil covering each of the punch faces. The sintering temperatures, peak pressures and times are summarized in Table 11.1.

For each of the PECS processed specimens, the heating and cooling ramp rates were 10^{o}C/min and the pressure ramp rate was 22.5 MPa/min. The specimens fabricated from the CGSR powders (without planetary milling) were labeled as HH-X (X = the sintering temperature), and the specimens fabricated from ball milled powders were labeled as HH-BM-Y (Y = the sintering temperature).

2.3 Microstructural analysis

The CGSR powders, the ball milled powders, and fractured surfaces of specimens HH-1000, 800 and HH-BM-1000 were observed using a scanning electron microscope (SEM, Carl Zeiss Microscopy, LLC, Thornwood, NY) with an accelerating voltage of 20 kV and a working distance of 5 mm.

Crystallographic phase analysis was performed using a Rigaku Ultima III diffractometer with CuKα radiation with 2θ between 20^{o} and 70^{o}. X-ray diffraction (XRD) was performed on specimens HH-900 and HH-950.

The PECS processed disk-shaped specimens were then polished using diamond paste with grit sizes ranging from 90 μm to 1 μm. The specimens were then cut into bars (Table 11.1) for microstructural analysis, as well as elastic modulus and hardness measurements. The mean grain sizes of the densified ZrNiSn specimens were determined using a linear

intercept method with 150 to 200 intercepts per SEM micrograph and a stereographic projection factor of 1.5 [Underwood 1968, Case 1981].

2.4. Elastic modulus measurement

The room temperature elastic moduli of the ZrNiSn specimens included in this study were measured using the resonant ultrasound spectroscopy (RUS) technique [Miglori 1997]. A commercial resonant ultrasound spectroscopy device (RUSpec, Magnaflux Quasar, Albuquerque, NM) was used in which the specimen is placed on a tripod of piezoelectric transducers. One transducer excites mechanical vibrations in the test specimen while the other two transducers detect the vibrations. In this study, the frequency for the driving transducer was swept from 20 kHz to 600 kHz in 29,999 steps. The elastic moduli are then calculated based on the mechanical resonance frequencies, the mass, dimensions and geometry of the specimens [Miglori 1997] using commercial software (RPModel, Magnaflux Quasar, Albuquerque, NM).

2.5. Hardness measurements

Prior to the room temperature hardness measurements on the ZrNiSn specimens, the Vickers indenter (Shimazdu HMV 2000, Kyoto, Japan) was calibrated using a standard hardness calibration block (HV 790 steel standard calibration block, Yamamoto Scientific Tools Lab Co. LTD, Chiba, Japan). The hardness, H, was calculated from the average of at least 10 indentations per specimen using [Wachtman 2009]

$$H = \zeta \frac{1.8544F}{(2a)^2} \quad (1)$$

Table 11.1. For each cut and polished specimen included in this study, the PECS temperature, T, and the relative porosity, P, the mass and dimensions. For each specimen, the PECS pressure was 50 MPa, with a holding time of 20 minutes except for specimen HH-900, whose holding time was 10 minutes.

Specimen label	PECS T (^{o}C)	Mass (g)	Dimensions (cm x cm x cm)	Relative porosity, P
HH-800	800	0.704	0.81 x 0.60 x 0.24	0.24
HH-850	850	0.656	0.84 x 0.62 x 0.20	0.23
HH-900	900	0.856	0.83 x 0.62 x 0.25	0.15
HH-950	950	0.742	0.80 x 0.61 x 0.23	0.14
HH-975	975	0.685	0.82 x 0.59 x 0.20	0.09
HH-1000	1000	0.542	0.81 x 0.59 x 0.14	0.01
HH-1025	1025	0.634	0.81 x 0.61 x 0.17	0.04
HH-BM-800	800	0.829	0.91 x 0.60 x 0.22	0.13
HH-BM-850	850	0.796	0.90 x 0.65 x 0.19	0.09
HH-BM-900	900	0.837	0.85 x 0.64 x 0.20	0.04
HH-BM-1000	1000	0.699	0.90 x 0.60 x 0.17	0.04

where the dimensionless constant, ζ, is the calibration factor obtained from the indentation of the calibration block, F is the applied indentation load and a is half of the diagonal length of the indentation impression.

3. Results and Discussion

3.1 Microstructure and phase analysis

Micrographs of CGSR powder showed a wide distribution of particle size, from sub-micron, a few microns to roughly 40 to 50 μm (Figures 11.1 a). After ball milling, the powders were reduced to particle sizes from sub-micron to roughly 20 μm (Figures 11.1b).

On the fractured surface of HH-800 (Figure 11.2a), a matrix of small grains with distributed large grains was observed. The average grain size of the small matrix grains ranged from roughly 1 μm to 5 μm, with large grains in the 10 μm to 30 μm range (Figure 11.2a). Roughly half of the area of the fractured surface is occupied by large grains(Figure 11.2a). For the specimen HH-BM-800 (Figure 11.2b), about one third of the fractured surface are occupied by large grains at the size of 10 – 15 μm, and no grains larger than ~ 20 μm were observed.

For the densified HH specimens, the volume fraction porosity, P, for the specimens ranged from 0.24 to 0.01, with the highest porosity for specimen HH-800 and lowest porosity for specimen HH-1000 (Table 11.1). For specimens densified using the same PECS condition but from different powders, namely the CGSR powders and the ball milled powders, the final porosities are different. For example, the final porosity for HH-800 was 0.24, while for HH-BM-800 was 0.13. The lower final porosity for

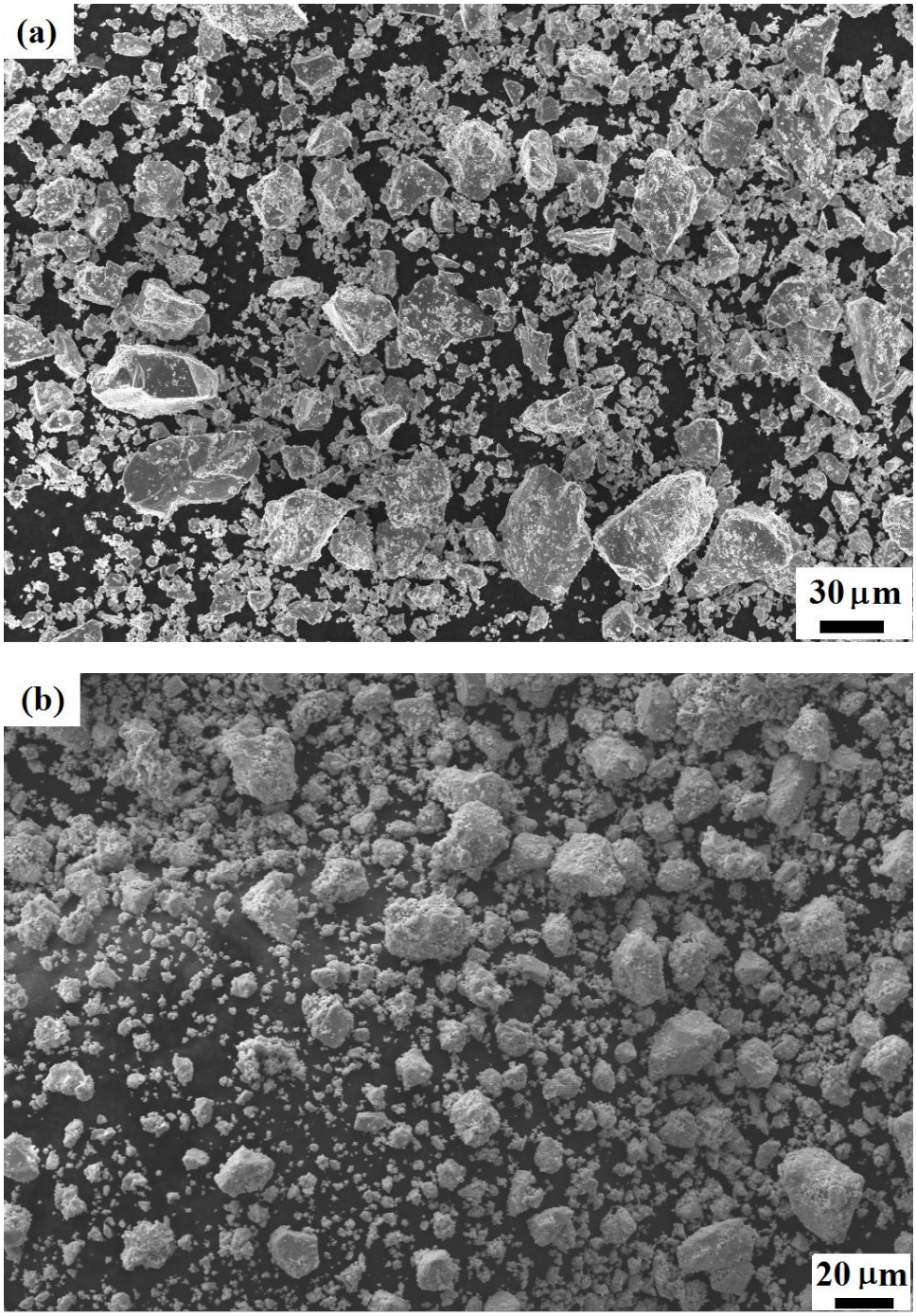

Figure 11.1. SEM micrographs of powder processed ZrNiSn, for (a) CGSR powders, (b) ball milled powders.

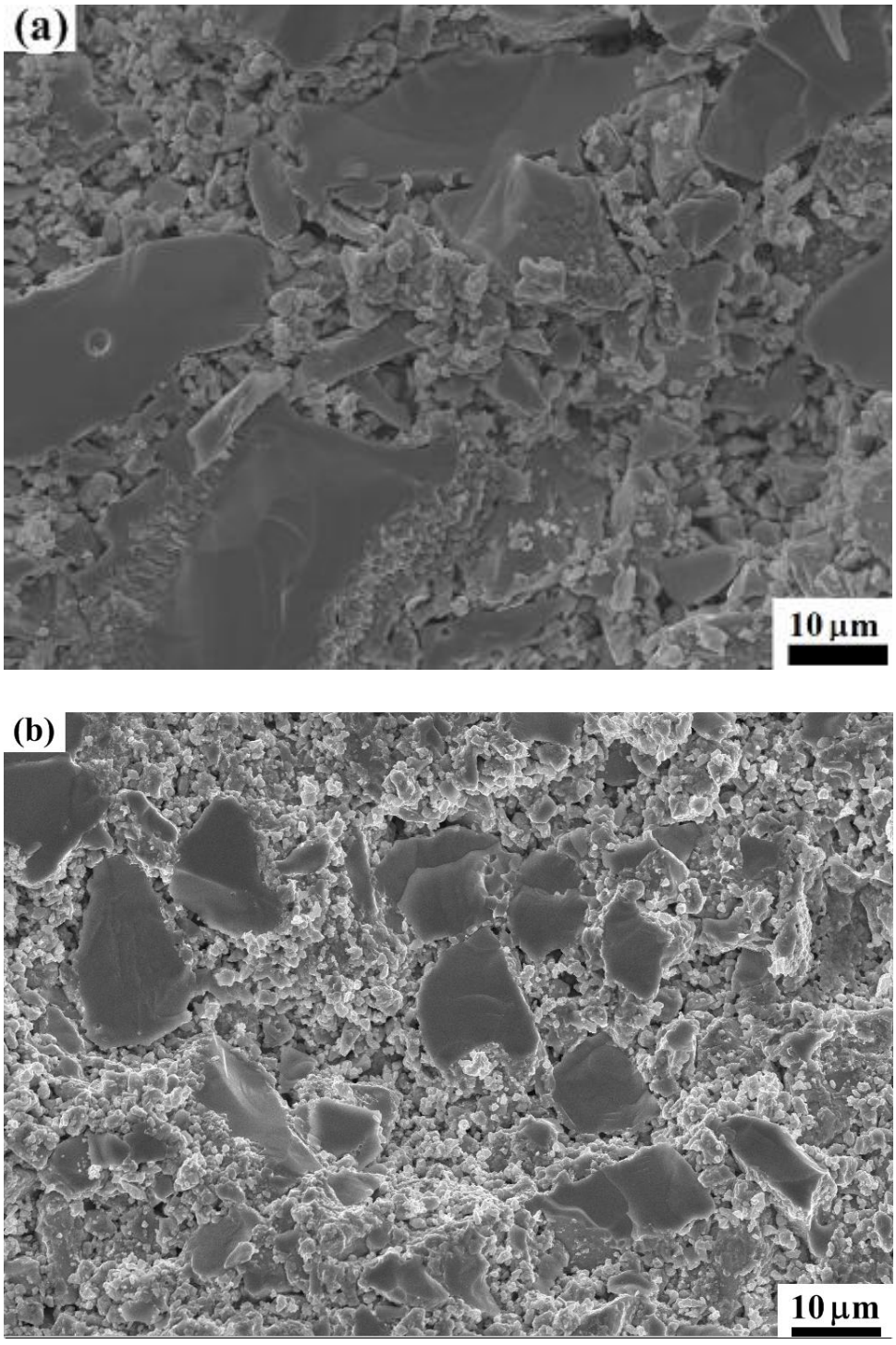

Figure 11.2. SEM micrographs of fractured surface for (a) HH-800, and (b) HH-BM-1000.

HH-BM-800 is due to smaller starting powder particle size and the relatively narrow particle size distribution [Barsoum 1997].

An XRD analysis showed that the specimen was relatively pure ZrNiSn (Figure 11.3). However, a faint peak indicated by the arrow (Figure 11.3) is not yet identified.

3.2 Elastic modulus measurement

Elastic moduli were measured on the polished, bar-shaped specimens. Details on the number of resonant peaks, rms error and elastic moduli are listed in Table 11.2.

The porosity dependence of the elastic moduli (Figure 11.4) is described well by the empirical relation [Rice 1998, Fan 2012b]

$$A = A_0 \exp(-b_A P) \quad (2)$$

where A represents the elastic moduli (Young's modulus, E, shear modulus, G and Poisson's ratio, ν), A_0 is the elastic moduli at P = 0 and b_A is a unitless, material-dependent constant that is proportional to the rate of decrease in A with increasing P.

As reviewed by Rice [Rice 1998], for volume fraction porosities, P, greater than a critical porosity, P_C, the experimentally-determined elastic modulus sometimes decrease much faster with increasing P than is predicted by equation 2. Often P_C is from roughly 0.3 to 0.4 [Rice 1998, Fan 2013]. For the range of P included in this study ($0.01 < P < 0.24$), equation 2 does describe the modulus-porosity relationship quite well. For example, the least-squares fits of the E, G, and ν data to equation (2) yielded $E_0 = 214.0 \pm 6.8$ GPa, $b_E = 4.1 \pm 0.3$; $G_0 = 85.1 \pm 2.9$ GPa, $b_G = 4.0 \pm 0.3$; $\nu_0 = 0.262 \pm 0.004$, $b_\nu = 0.87 \pm 0.10$, with coefficients of

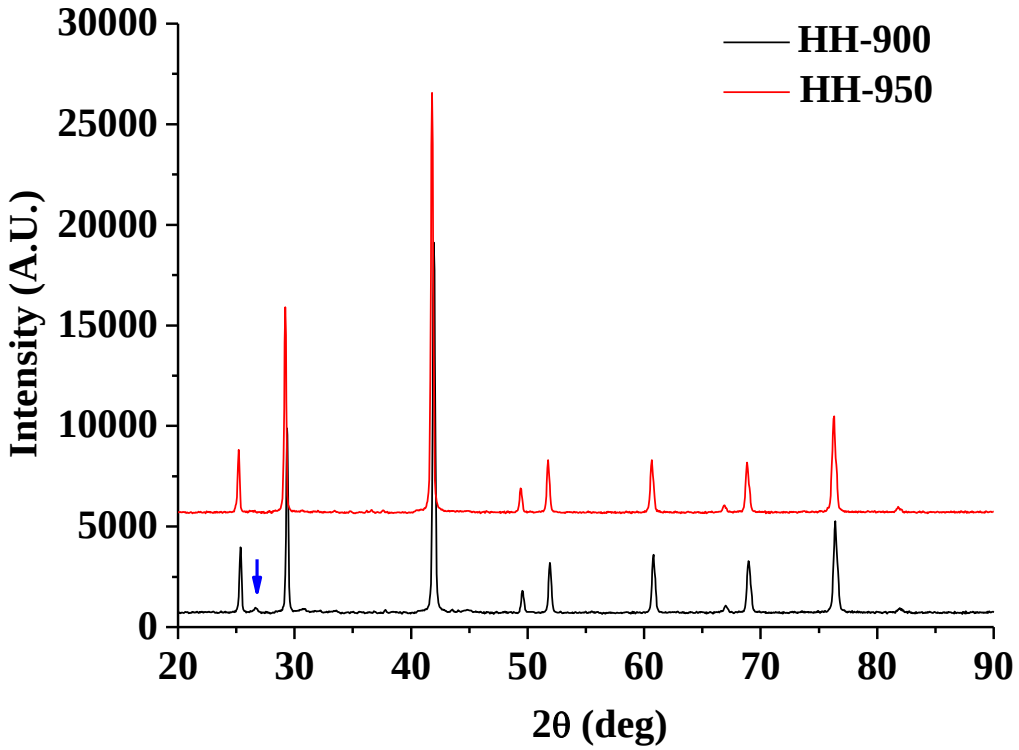

Figure 11.3. XRD spectra for specimens HH-900 and HH-950. The faint peak indicated by the blue arrow is not yet identified.

Table 11.2. For RUS analysis for each specimen, the number of resonant peaks, N, the rms error, the Young's modulus, E, the shear modulus, G, the bulk modulus, B, and Poisson's ratio, υ.

Specimen label	N	rms error	E (GPa)	G (Gpa)	B (Gpa)	υ
HH-800	19	0.49%	76.7	31.5	45.1	0.216
HH-850	27	0.45%	73.8	30.2	44.0	0.220
HH-900	26	0.47%	121.9	49.8	73.5	0.224
HH-950	24	0.36%	115.5	47.2	69.8	0.224
HH-975	28	0.48%	154.5	61.8	102.9	0.250
HH-1000	22	0.40%	191.6	75.9	134.4	0.262
HH-1025	23	0.21%	188.0	74.9	128.5	0.256
HH-BM-800	25	0.39%	116.5	47.1	73.7	0.236
HH-BM-850	22	0.39%	150.32	60.56	96.7	0.241
HH-BM-900	22	0.37%	189.3	76.4	120.4	0.238
HH-BM-1000	21	0.49%	187.4	75.8	125.7	0.251

determination, R^2, of 0.970, 0.970 and 0.912, respectively.

3.3 Hardness measurement

The Vickers hardness, H, was measured on the polished surfaces using five different loads, namely 0.98 N, 2.94 N, 4.9 N, 9.8 N and 19.6 N (Figure 11.5). The H values were nearly independent of load ranging from 2.94 N to 19.6 N for selected HH specimens. The slightly higher hardness values obtained for the indentation load of 0.98 N may be due to the avoidance of indentation on porous areas. For lower loads such as 0.98 N, the indentation impression is too small to read if was placed in the porous areas.

Hardness-porosity relations were investigated indented at load of 4.9 N. Hardness-porosity data were fit to the empirical relationship

$$H = H_0 \exp(-b_H P) \quad (3)$$

where H is hardness, H_0 is the hardness at zero porosity and b_H is a unitless constant (Figure 11.6). Least-squares fits of H values for all the specimens to equation (3) yielded $H_0 = 9.7 \pm 0.9$ GPa, $b_H = 5.6 \pm 1.1$ and $R^2 = 0.812$. The low R^2 value indicated that equation (3) did not fit the hardness data as a function of porosity well.

3.4 Comparison to literature values for elastic moduli and hardness

In the literature (Table 11.3), there are some theoretical simulations of half-Heusler compounds such as NiTiSn [Hichour 2012], CoVSn [Hichour 2012], IrMnAl [Hamidani 2009], IrMnSn [Hamidani 2009], IrMnSb [Hamidani 2009], and intermetallic compound of Fe-Al-Ti [Krein 2010]. The calculated Young's modulus of NiTiSn [Hichour 2012], CoVSn [Hichour 2012], IrMnAl [Hamidani 2009] and intermetallic compound of Fe-Al-Ti [Krein

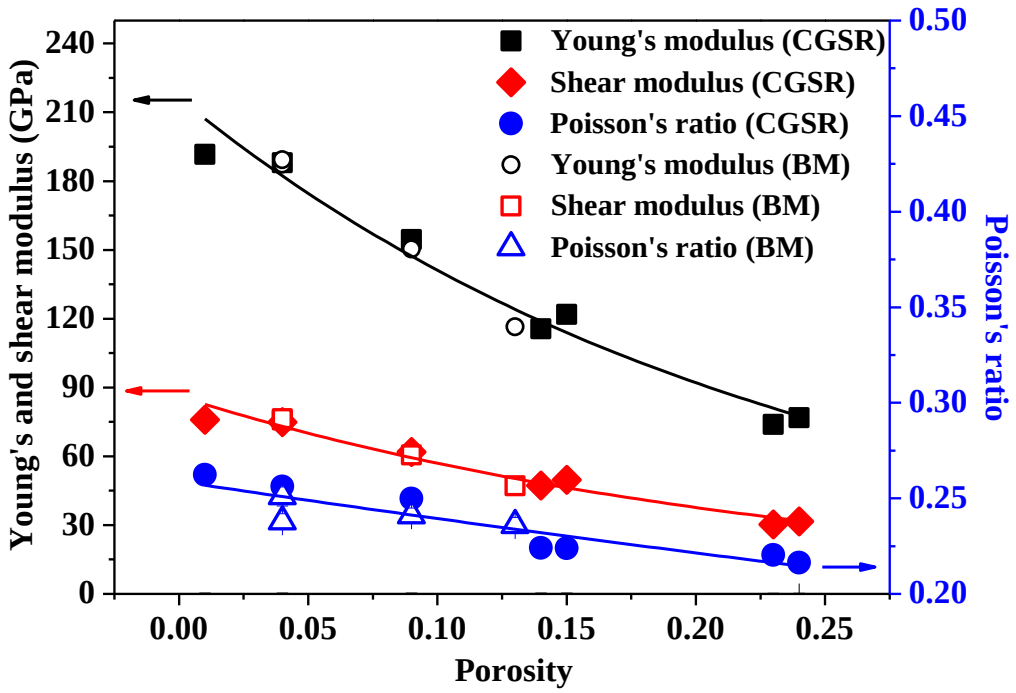

Figure 11.4. Young's modulus, shear modulus and Poisson's ratio versus porosity for specimens fabricated from CGSR powders (solid symbols) and specimen fabricated from ball milled powders (open symbols). The solid curves for each data set represent the least-squares fit to equation 2.

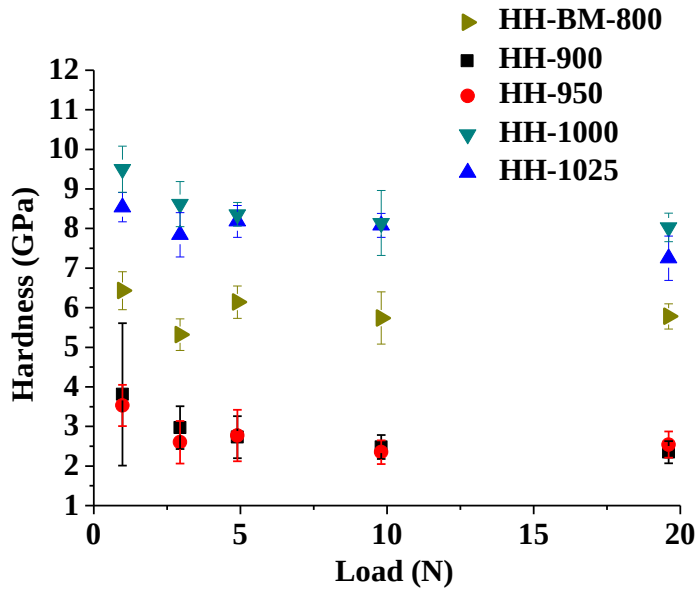

Figure 11.5. Hardness as a function of load for specimens fabricated from CGSR powders and ball milled powders.

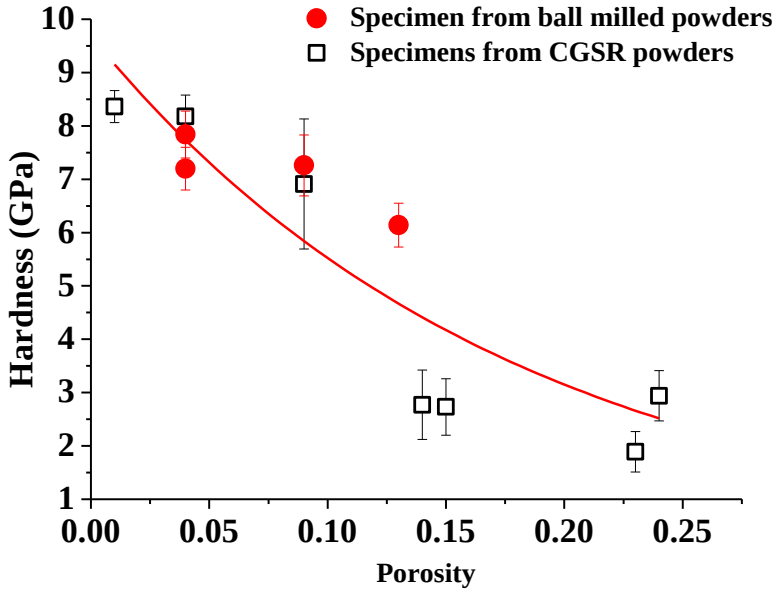

Figure 11.6. Hardness vs. P for specimens fabricated from CGSR powders (open symbol) and specimen fabricated from ball milled powders (solid symbol) indented at load = 4.9N.

2010] are comparable to the E value for the ZrNiSn in this study, except for IrMnSn [Hamidani 2009], IrMnSb [Hamidani 2009] which have lower E values. Germond [2010] obtained elastic moduli of ZrNiSn using indentation technique. The Young's modulus of 223.5 GPa and 241.1 GPa [Germond 2010] are somewhat higher than the value for the specimens in this study (E_0 = 215 GPa). However, indentation method is a static technique, and measures the Young's modulus of a localized area, while RUS used in this study is a dynamic method that measures the elastic response of the bulk specimen. Elastic modulus for Fe-Al-Ti compound measured by the indentation method [Prakash 2001] showed comparable E values to the HH specimens in this study.

Table 11.4 gives hardness data from the literature for two half-Heusler compounds [Verges 2011, Germond 2010] along with the specimen fabrication technique, relative density and grain size. The specimens from the study by Verges [2011] had a relative density of 95%. Using the hardness values obtained from HH specimen with a relative density of 96%, it is found that the hardness value in this study (H = 8.54 $\pm$ 0.37 GPa) is comparable to that in the study by Verges (H = 9.2 $\pm$ 0.4 GPa) [Verges 2011] However, the grain size of the specimens in Verges's study [Verges 2011] was not stated, and the composition was different from this study. For the specimens from Germond's study [Germond 2010], the composition is the same as in this study. The hardness values were ~14 GPa [Germond 2010], which are higher than the values in this study. However, the relative density of the specimens were not given [Germond 2010]. The hardness value (~14 GPa) measured by Germond [Germond 2010] is even higher than the extrapolation value obtained from the hardness-porosity plot

Table 11.3. Comparison of the Young's modulus, shear modulus and Poisson's ratio data from this study to data for intermetallic compounds from the literature.

References	Material	Young's modulus (GPa)	Shear modulus (GPa)	Poisson's ratio	P	Measurement /calculation method
This study	ZrNiSn	187.4	75.8	0.251	0.01	Resonant ultrasound spectroscopy
Germond 2010	ZrNiSn - PECS	223.5	NS[a]	NS	NS	Depth sensing indentation techniques
	ZrNiSn – Hot pressed	241.1	NS	NS	NS	
Hichour 2012	NiTiSn	219.96	87.84	0.25	0[b]	Theoretical calculation by full-potential linear muffin-tin orbital (FP-LMTO) method
	CoVSn	243.24	95.69	0.27	0[b]	
Hamidani 2009	IrMnAl	231.15	92.66	0.247	0[b]	Theoretical calculation by full potential linearized augmented plane wave method
	IrMnSn	79.19	28.61	0.331	0[b]	
	IrMnSb	135.65	50.94	0.383	0[b]	
Prakash 2001	Fe-(10-27.5) at.%Al-(10-30) at.%Ti	"just above 200"	NS	NS	NS	Indentation depth as a function of applied load during loading and unloading of Vickers indentation
Krein 2010	Fe-25Al	178	NS	NS	0[b]	Ab initio calculation
	Fe-25Al-6Ti	200	NS	NS	0[b]	
	Fe-25Al-25Ti	265	NS	NS	0[b]	
	Fe-25Al-20Ti-4Cr	240	NS	NS	NS	Dynamic measurement device

[a] Not stated by the authors.

[b] Theoretical calculation assume dense materials (P = 0).

Table 11.4. Comparison of the hardness data from this study to data for half-Huesler compounds from the literature.

Reference and material	Powder preparation & specimen fabrication	Load (N)	Vickers Hardness (GPa)	Relative density	Grain size
This study ZrNiSn	PECS at 900^{o}C and 50 MPa for 10 min	0.98	8.54 ± 0.37	96 %	Need to give a grain size
Verges 2011 $Zr_{0.5}Hf_{0.5}NiSn_{0.99}Sb_{0.01}$	Hot pressed at 100 MPa and 820^{o}C for 1 h	1.96	9.2 ± 0.4	95%	NS[a]
Germond 2010 ZrNiSn	Mechanical alloying Hot pressed at 850 ^{o}C for 60 min, 100 MPa for 180 min	0.49	14.15	N/A	43 nm
	Mechanical alloying SPS at 825^{o}C for 7 min	0.49	13.69	N/A	39 nm

[a] Not stated by the authors.

(Figure 11.6). It is important to note that the grain size for Germond's HH specimens is in the nano regime, from 39 nm to 43 nm [Germond 2010]. For the specimens in this study, the grain sizes are much larger (with grain size from roughly 1 – 30 μm) than Germond's HH specimens [Germond 2010]. As indicated by the Hall-Petch relationship [Rice 2000], the hardness values increase with decreasing grain size, for grain size greater than the grain size, usually around 10 nm. Hall-Petch relationship can be expressed as [Rice 2000]

$H = H_c + k\,(GS)^{-0.5}$

where H_c is the H value in the single crystal limit, k is the Petch parameter and GS is the grain size.

4. Summary and Conclusions

Arc melted ZrNiSn ingots were powder processed and densified by PECS over a temperature range from 800°C to 1025°C in order to intentionally induce a range of porosity, P, from about 0.01 to 0.24 in the specimens. The porosity-dependent elastic moduli (Young's modulus, shear modulus, Poisson's ratio) were measured via RUS and the hardness was determined by Vickers indentation.

Over the range of porosity included in this study, the Young's and shear modulus versus porosity as well as the hardness versus porosity were relatively well described by the empirical exponential relationship $A(P) = A_0\exp(-b_A P)$, which is also the porosity dependence that been reported in the literature for a wide range of brittle materials. In addition, the elastic modulus and hardness values compare favorably with the corresponding literature values.

Acknowledgements

The authors acknowledge the financial support of the Department of Energy, “Revolutionary Materials for Solid State Energy Conversion Center,” an Energy Frontiers Research Center funded by the U.S. Department of Energy, Office of Science, Office of Basic energy Sciences under award number DE-SC0001054.

REFERENCES

REFERENCES

[Case 1981] E. D. Case, J. R. Smyth, and V. Monthei, Grain-size determinations, Journal of the American Ceramic Society, 64, C24-C25, 1981.

[Case 2012] E. D. Case, Thermal fatigue and waste heat recovery via thermoelectrics, Journal of Electronic Materials, 41, 1811-1819, 2012.

[Fan 2012a] X. Fan, E. D. Case, M. J. Baumann, The effect of indentation-induced microcracks on the elastic modulus of hydroxyapatite, Journal of Materials Science, 47, 6333–6345, 2012.

[Fan 2012b] X. Fan, E. D. Case, F. Ren, Y. Shu and M. J. Baumann, Part II: Fracture strength and elastic modulus as a function of porosity for hydroxyapatite and other brittle materials, Journal of the Mechanical Behavior of Biomedical Materials, 8, 99-110, 2012.

[Fan 2013] X. Fan, E. D.Casen, Q.Yang, J. D. Nicholas, Room temperature elastic properties of gadolinia-doped ceria as a function of porosity, Ceramics International, 39, 6877-6886, 2013.

[Fu 2013] C.G. Fu, H.H. Xie, Y.T. Liu, T.J. Zhu, J. Xie, X.B. Zhao, Thermoelectric properties of FeVSb half-Heusler compounds by levitation melting and spark plasma sintering Intermetallics, 32, 39 – 43, 2013.

[Germond 2010] J. D Germond, Structural characterization and thermoelectric performance of ZrNiSn half-heusler compound synthesized by mechanical alloying, 2010. Department of Mechanical Engineering, University of New Orleans, M.S. thesis.

[Hamidani 2009] A. Hamidani, B. Bennecer, B. Boutarfa,Structural and elastic properties of the half-Heusler compounds IrMnZ (Z = Al, Sn and Sb), Materials Chemistry and Physics 114, 732 – 735, 2009.

[Hichour 2012] M. Hichour, D.Rached, R.Khenata, M.Rabah, M.Merabet, A.H.Reshak, S. BinOmran, R.Ahmed, Theoretical investigations of NiTiSn and CoVSn compounds, Journal of Physics and Chemistry of Solids 73, 975–981, 2012.

[Hoepfner 2003] T. P. Hoepfner, E. D. Case, The influence of the microstructure on the hardness of sintered hydroxyapatite, Ceramics International. Ceram. Int. 29, 699 – 706, 2003.

[Kamboj 2003] R.K. Kamboj, S. Dhara, P. Bhargava, Machining behaviour of green gelcast ceramics, J. Eur. Ceram. Soc. 23, 1005–1011, 2003.

[Kallel 2012] A. Kallel, G. Roux, T. Derycke, C. L. Martin, M. Marinova, C. Cayron,

Microstructure and Thermoelectric Properties of Bulk and Porous N-type Silicon-Germanium Alloy Prepared by HUP, AIP Conf. Proc. 1449, 409-412, 2012.

[Kim 2002] S.W. Kim, Y. Mishima, D.C. Cho, Effect of process conditions on the thermoelectric properties of CoSi, Intermetallics 10, 177–184, 2002.

[Kim 2013] J.Y. Kim, T. Athar, S.J. Kim, W.S. Seo, K. Park, Electrical conductivity and thermoelectric power studies of solution-combustion-processed $Ca_{2.76}Cu_{0.24}Co_4O_9$, Ceramics International 39, 1397–1402, 2013.

[Kong 2012] F. Kong, Y. Hu, H. Hou, Y. Liu, B. Wang, L.Wang, Thermoelectric and thermodynamic properties of half-Heulser alloy YPdSb from first principles calculations, Journal of Solid State Chemistry, 196, 511–517, 2012.

[Krakhmalev 2006] P.V. Krakhmalev, J. Bergstrom, Tribological behavior and wear mechanisms of MoSi2-base composites sliding against AA6063 alloy at elevated temperature, Wear 260, 450–457, 2006.

[Krein 2010] R. Krein, M. Friak, J. Neugebauer, M. Palm, M. Heilmaier, L21-ordered Fe–Al–Ti alloys, Intermetallics 18, 1360–1364, 2010.

[Lee 2010] H. Lee, D. Vashaee, D. Z. Wang, M. S. Dresselhaus, Z. F. Ren, G. Chen, Effects of nanoscale porosity on thermoelectric properties of SiGe, Journal of Applied Physics, 107, 094308, 2010.

[Martin 1973] H.C. Martin, G.F. Carey, Introduction to Finite Element Analysis, McGraw-Hill, New York, 1973.

[Migliori 1997] A. Migliori, J.L. Sarrao, Resonant ultrasound spectroscopy applications to physics, materials measurements and nondestructive evaluation, Wiley-Interscience, Hoboken, NJ, USA, 1997.

[Ohtaki 2011] M. Ohtaki, K.F. Araki, Thermoelectric properties and thermopower enhancement of Al-doped ZnO with nanosized pore structure, J. Ceram. Soc. Jpn. 119, 813-816, 2011.

[Pilchak 2007] A. L. Pilchak, F. Ren, E. D. Case, E.J. Timm, H.J. Schock, C-I Wu, T.P. Hogan, Characterization of dry milled powders of LAST (lead-antimony-silver-tellurium) thermoelectric material, Phil. Mag. 87, 4567-4591, 2007.

[Populoh 2012] S. Populoh, M.H. Aguirre, O.C. Brunko, K. Galazka, Y. Lu, A. Weidenkaff, High figure of merit in (Ti,Zr,Hf)NiSn half-Heusler alloys, Scripta Materialia, 66, 1073–1076, 2012.

[Prakash 2001] U. Prakash, G. Sautho, Structure and properties of Fe-Al-Ti intermetallic alloys, Intermetallics 9, 107-112, 2001.

[Rice 1998] R.W. Rice, Porosity of Ceramics, Marcel-Dekker, Inc., New York. 1998.

[Shen 2001] Q. Shen, L. Chen, T. Goto, T. Hirai, J. Yang, G. P. Meisner, C. Uher, Effects of partial substitution of Ni by Pd on the thermoelectric properties of ZrNiSn-based half-Heusler compounds, Appl. Phys. Lett. 79, 4165-4167, 2001.

[Underwood 1968] E.E. Underwood, A.R. Colcord, R.C. Waugh, Quantitative Relationships for Random Microstructures, in: R.M. Fulrath, J.A. Pask (Eds.) Ceramic Microstructures, John Wiley & Sons, New York, 1968.

[Vandeperre 2004] L. J. Vandeperre, J. Wang, W. J. Clegg, Effects of porosity on the measured fracture energy of brittle materials, Philos. Mag. 84, 3689-3704, 2004.

[Verges 2011] M. A. Verges, P. J. Schilling, P. Upadhyay, W. K. Miller, R. Yaqub, K. L. Stokes, P. F. P. Poudeu, Young's modulus and hardness of $Zr_{0.5}Hf_{0.5}Ni_xPd_{1-x}Sn_{0.99}Sb_{0.01}$ half-heusler compounds, Science of Advanced Materials 3, 659–666, 2011.

[Wachtman 2009] J.B. Wachtman, W.R. Cannon, M.J. Matthewson, Mechanical Properties of Ceramics, 2nd edition, John Wiley & Sons, Inc., New York, 2009.

[Yu 2009] C. Yu, T.J. Zhu, R.Z. Shi, Y. Zhang, X.B. Zhao, J. He, High-performance half-Heusler thermoelectric materials Hf1−x ZrxNiSn1−ySby prepared by levitation melting and spark plasma sintering, Acta Materialia, 57, 2757–2764, 2009.

[Zou 2013] M. Zou, J.F. Li, T. Kita, Thermoelectric properties of fine-grained FeVSb half-Heusler alloys tuned to p-type by substituting vanadium with titanium, Journal of Solid State Chemistry, 198, 125–130, 2013.

CHAPTER 12

SUMMARY AND CONCLUSIONS

In this study, the mechanical properties of hydroxyapatite (HA), gadolina doped ceria (GDC10) and thermoelectric materials ($Cu_{10}Zn_2As_4S_{13}$ - $Cu_{12}Sb_4S_{13}$and ZrNiSn) were characterized as a function of microstructure and/or composition.

For HA specimens, unimodal porosity ranging from 0.08 to 0.62 was induced by partial sintering. A total of more than 500 specimens were fabricated, whose elastic moduli were measured by resonant ultrasound spectroscopy, and then fractured by biaxial flexure testing. The porosity, P, dependence of the mean fracture strength, $<\sigma_f>$, and the Young's modulus, E, for the HA specimens are power law functions of the degree of densification, ϕ, where $\phi = 1 - P/P_G$ and P_G is the green porosity (Chapter 5). The Weibull modulus, m, was studied along with data from the literature that represent eight different materials and more than 1500 specimens. The m versus P plot including all the data set showed a "U - shaped" trend with a wide band of m values for $P < 0.1$ and $P > 0.55$, and a narrower band in the intermediate porosity region of $0.1 < P < 0.55$ (Chapter 4).

The limited range of Weibull modulus values ($\sim 4 < m < 11$) for all the data set in the porosity range of $0.1 < P < 0.55$ regardless of the composition, grain size, testing techniques or surface finish of the specimens has important implications since porosity of the majority of the applications of porous brittle materials fall within this range (Chapter 4). A medium to high scatter in the fracture strength is to be expected, thus requiring the designers of such

components to include high safety factors in their designs. The fracture strength and Young's modulus are crucial to the design of brittle components too. The power law functions of the degree of densification for fracture strength and Young's modulus can be applied to many partially sintered brittle materials (Chapter 5).

As a follow-up study, about 300 HA specimens with high porosity from 0.59 to 0.62 were fabricated at sintering T from 350^{o}C to 1025^{o}C. The fracture strength decreased monotonically with decreasing T_{sinter}, from 4.8 MPa for specimens sintered at 1025^{o}C to 0.66 MPa for specimens sintered at 350^{o}C (Chapter 7). The decrease in fracture strength with limited porosity increase is due to the neck growth during initial sintering stage. The Weibull modulus remained surprisingly high, ranging from 6.6 to 15.5 (Chapter 7).

This study (Chapter 7) is the first research on Weibull modulus for highly porous materials (near green density). Despite their low strength, the surprisingly high Weibull modulus implied high mechanical reliability, which may indicate to designers that new, practical applications are possible for highly porous materials.

The effect of microcracking on the reductions of the Young's modulus, E, and Poisson's ratio, υ, was studied by inducing an array of Vickers indentation microcracks on the surfaces of HA specimens (Chapter 6). Both E and υ decreased approximately linearly with increasing microcrack damage. The results agreed with the theoretical predictions on the microcracking-elastic moduli relations.

This study (Chapter 6) validated the theoretical work by direct measurements of crack number density and crack length. The agreement of this study and a study on alumina [Kim

1993] supported the conclusion that the linear elastic modulus – microcrack damage trend may apply to a wide variety of brittle materials.

For the gadolinia doped ceria ($Ce_{0.9}Gd_{0.1}O_{1.95}$ or GDC10), the room temperature elastic properties (Chapter 8) and hardness (Chapter 9) were measured as a function of porosity. GDC10 specimens with porosities from 0.07 to 0.60 were produced by hard die pressing and partial sintering. The room temperature Young's modulus, shear modulus, bulk modulus and Poisson's ratio decreased exponentially with increasing porosity (Chapter 8). The Vickers hardness also decreased with increasing P exponentially in porosity range of $0.08 < P < 0.60$ (Chapter 9). For Vickers indentation loads of 0.98 N to 9.8 N, hardness showed no dependence with regard to the applied load.

The knowledge of elastic moduli of GDC10 at different porosity levels is essential to model the response of the SOFCs to internal or external stresses and to design more reliable SOFCs with longer service life (Chapter 8). In addition, hardness, H, is related to a material's wear resistance and machinability, which are two essential factors for fabrication and mechanical stability in application (Chapter 9).

For thermoelectric solid solution system $Cu_{10}Zn_2As_4S_{13}$ - $Cu_{12}Sb_4S_{13}$, the room temperature elastic moduli, hardness and fracture toughness were investigated as a function of (i) composition and (ii) ball milling time. The composition dependence of the Young's modulus, E, shear modulus, G and hardness, H were described well by the parabolic relationship (Chapter 10), in agreement with the trends observed for the elastic moduli and hardness of a number of solid solution systems in the literature. The fracture toughness, Kc,

is independent of the composition change. For the study on ball milling time, the grain size decreased with increasing milling time, and reached to a steady state after 4 hours of milling. The elastic moduli and Poisson's ratio are essentially independent of milling time. The scatter in the H and Kc make it difficult to discern a trend as a function of milling time (Chapter 10).

For the half-Heusler compound ZrNiSn prepared from arc melted ingots followed by powder processing and densified by pulsed electric current sintering, the room temperature Young's modulus, shear modulus, Poisson's ratio and hardness were studied (Chapter 11). Both porosity dependence of the elastic moduli and the hardness can be described well by the empirical exponential relationship $A(P) = A_0\exp(-b_A P)$ where A is the porosity-dependent mechanical property, A_0 is the value of A at P = 0, and b_A is a measure of the rate of decrease in A with increasing P (Chapter 11).

In waste heat recovery applications, thermoelectrics will undergo thermal and mechanical stresses arising from thermal gradient, thermal transient and mechanical loading. The elastic moduli and Poisson's ratio are required for the analysis of stress and strain by analytical or numerical simulations. The knowledge of hardness and fracture toughness is also crucial to successful design and application of such components.

Mechanical properties reflect how a component subjected to various thermal or mechanical stresses will respond. Studying the mechanical property – microstructure relationships is essential for a better understanding of the material's response under different circumstances. The knowledge of the mechanical properties will guide us to design and fabricate more reliable components with longer service life and higher safety factor.

REFERENCES

REFERENCES

[Kim 1993] Y. Kim, E.D. Case, S. Gaynor, The effect of surface-limited microcracks on the effective youngs modulus of ceramics .3. Experiments, J. Mater. Sci. 38,1910 – 1918, 1993.

CHAPTER 13

FUTURE WORK

In this study, the effect of total volume fraction porosity on elastic moduli, fracture strength and Weibull modulus of hydroxyapatite was explored. However, the effect of pore size, pore morphology and pore size distribution on the mechanical properties is not clear. Bimodal pore distribution is of great importance for hydroxyapatite application as bone scaffolds since the bimodal pores are biologically and physiologically essential for bone ingrowth and blood/nutrient circulations. Strategies of incorporating bimodal pores include burning out sacrificial fugitives (corn starch, polymer beads, etc.) and direct forming of gas bubbles. Future studies should focus on fabricating specimens with bimodal pore size distribution, and studying how the bimodal pores affect the mechanical properties. In addition, studying the porosity effect on other brittle materials could also be done.

In the current study, the room temperature elastic modulus, hardness and fracture toughness were studied for thermoelectric (TE) materials and solid oxide fuel cell (SOFC) materials. In commercial applications, these materials will be operated under cyclic temperatures and possible mechanical loading. Knowing the Young's modulus and Poisson's ratio at elevated temperature would be critical to model the thermal stress and strain using analytical or numerical simulations. Thus, future work needs to be done to measure the elasticity as a function of temperature for the TE and SOFC materials. Moreover, the mechanical integrity of these materials is essential in applications. Thermal fatigue testing is capable to evaluate whether the material could withstand a number of thermal cycles. In the future, thermal fatigue testing can be done on the TE and SOFC materials. Path towards improving thermal fatigue resistance for these materials needs to be considered. Porosity has

been proved to enhance thermal fatigue resistance for thermal barrier coatings. Future studies aiming to improve thermal fatigue resistance for the TE and SOFC materials can incorporate an engineered porosity ranging from 0.1 to 0.2. Besides working on the materials, future studies could also be done to investigate mechanical integrity of the entire thermoelectric module and the whole SOFC system.